Andreev and Majorana bound states in low-dimensional systems

INAUGURALDISSERTATION

zur

Erlangung der Würde eines Doktors der Philosophie

vorgelegt der

Philosophisch-Naturwissenschaftlichen Fakultät

der Universität Basel

von

Richard Gerhard Hess

Basel, 2024

Genehmigt von der Philosophisch-Naturwissenschaftlichen Fakultät auf Antrag von

Erstbetreuerin: Prof. Dr. Jelena Klinovaja

Zweitbetreuer: Prof. Dr. Daniel Loss

Externe Expertin: Prof. Dr. Annica Black-Schaffer

Basel, den 14. November 2023

Prof. Dr. Marcel Mayor
Dekan

To my parents, who always believe in me.

Summary

The discovery of the quantum Hall effect [1] and its explanation in terms of topology opened up a new field in condensed matter theory [2–5]. Topology, in the original context of mathematics, classifies geometric structures and studies whether an object can be continuously deformed into another one. If such a continuous deformation exists, then the two objects belong to the same topological class. Different topological classes are distinguished by the value of a topological invariant. For example, the tea cup and the torus both have one hole and therefore share the same topology. The topological invariant is in this example the number of holes which is called genus [6–9].

In 1982, Thouless, Kohmoto, Nightingale, and den Nijs related the quantized Hall conductance to a topological invariant [2]. This work among others [4, 10–13] paved the way towards the research of topological insulators (TIs) and superconductors (TSCs), which has become one of the most active research fields in condensed matter physics [6–8, 14–16]. TIs and TSCs are characterized by an energy gap in the bulk and subgap states at the surface/edge. The analogue of the continuous deformation of a geometrical object is here the continuous deformation of the Hamiltonian, under which the energy gap of the bulk does not close.

The quantum Hall system is one example of a TI, and it requires an external magnetic field, which explicitly breaks time reversal symmetry (TRS). Another class, namely time-reversal invariant TIs based on spin-orbit interaction (SOI), has been intensively studied in theory [10–13, 17] and experiment [18, 19]. The next important step in the research field of TIs was the description [20–23] and discovery [24–26] of three-dimensional topological insulators.

Topological superconductors have more exotic edge states, so-called Majorana modes, named after Ettore Majorana who proposed the existence of a particle that is its own antiparticle in the context of particle physics [27]. In two dimensions, chiral Majorana modes move around the one-dimensional boundary of the TSC, similar to the conducting edge states in a quantum Hall sample. A pair of vortices, in contrast, can host a pair of Majorana bound states (MBSs), with one MBS in each vortex [28–31]. These states with exactly zero energy are their own antiparticles and, even more interestingly, they obey non-Abelian braiding statistics [30, 32, 33]. This makes them highly attractive for quantum computation, since information could be protected against local perturbations due to the topology of the system. Usual Majorana qubit proposals rely on fermion parity conservation. One pair of MBSs forms a nonlocal fermionic state, which can be empty or occupied by one fermion. Therefore, two pairs of MBSs, so in total four MBSs, can define a qubit with conserved fermion parity [30, 32]: If only one fermion is present, then it can

either occupy the first or the second pair of MBSs and the fermion parity does not change when the fermion is transferred from one pair of MBSs to the other one.

Another famous system hosting MBSs apart from vortices in two-dimensional $p_x + ip_y$ superconductors is the Kitaev chain [34], which is a one-dimensional spinless p-wave superconductor. In this model, the MBSs appear at the ends of the chain and are topologically protected against disorder, as long as the length of the chain is much longer than the localization length of the MBSs. In the opposite limit, the MBSs lose their topological protection, however, they can still exist for a fine-tuned choice of parameters. Some works on so-called Poor Man's MBSs, namely MBSs which are not topologically protected, propose how to realize this short length limit of the Kitaev chain in real systems, for example with the help of strong local magnetic fields that polarize electrons of two quantum dots along different axes [35, 36]. First experiments on Poor Man's MBSs agree to some extent with the theory [37].

Most proposals for the realization of MBSs in experiments are based on the interplay of several ingredients which can mediate an effective superconducting p-wave pairing. One prominent example of an engineered platform is the Rashba nanowire [38, 39], in which the interplay of spin-orbit interaction, an external Zeeman field, and conventional s-wave superconductivity gives rise to an effective p-wave pairing. In 2012, Mourik et al. performed the first experiment looking for MBSs on this platform and reported zero-energy states at one end of the nanowire, in agreement with the theory predicting MBSs [40]. Many subsequent differential conductance experiments using different materials and slightly changed device designs confirmed the existence of the zero bias peak (ZBP) [41–45]. However, soon it was realized that also trivial states like Andreev bound states (ABSs) can accidentally appear at zero energy [46–54]. Therefore, the measurement of a single ZBP is not a sufficient indicator for the presence of an MBS. Subsequently, in order to clarify the origin of the ZBPs, other signatures were under consideration, for example, oscillations of the MBS energy as a function of the magnetic field [55], an almost quantized differential conductance value of $2e^2/h$ [56] and the simultaneous appearance of ZBPs on both ends of the nanowire [57]. However, it turned out that trivial ABSs can mimic all these features, and the problem remained unsolved [57–60]. More recently, non-local conductance has been proposed as another indicator revealing the bulk gap closing and reopening which accompanies a topological phase transition [61, 62]. Potential braiding experiments that could confirm the non-Abelian braiding statistic of MBSs, however, go beyond the current experimental capabilities.

Another platform for MBSs is based on chains of magnetic impurities deposited on s-wave superconductors [63–76]. The exchange coupling between the magnetic moments of the impurities and the itinerant electrons plays a similar role as the external magnetic field in the Rashba nanowire. Scanning tunneling microscopy (STM) measurements reported ZBPs at the ends of such impurity chains [77–80]. However, this platform has a limited tunability compared to the Rashba nanowire, since the exchange coupling is fixed. Therefore, and because trivial subgap states might cause similar signatures in experiments, the unambiguous identification of MBS remains challenging also in this platform.

Josephson junctions [81] are also a promising platform for the observation of MBSs, the phase difference between two superconductors serves here as an additional control knob which can drive the system into the topological phase [82–87]. The original proposal for Josephson junctions hosting MBSs requires an external magnetic field which is in-plane, in contrast to the usual out-of-plane configuration for topological superconductivity in two dimensions [88]. In fact, in SNSNS junctions, with three superconducting sections (S) and two normal sections (N), a magnetic field is not required for the realization of MBSs, if the Fermi velocity at the inner and outer Fermi surface differ [89, 90].

In general, the application of topology in condensed matter physics goes far beyond TIs and TSCs. For example, the fractional quantum Hall effect has an intrinsic topological order due to strongly correlated electrons [91, 92]. Moreover, magnetic textures like skyrmions [93–96] have a non-trivial topology in the sense that their local magnetization wraps one time around a sphere such that one can assign a topological invariant, also called topological charge, to this winding [97]. This real-space topology in combination with manipulation schemes based on external fields, currents, and temperature makes skyrmions good candidates for future information carriers [98–101].

This thesis is organized as follows: in the introduction, chapter 1 of this thesis, we recapitulate the concept of symmetry protected topological order and discuss it using the examples of the Kitaev chain, the Rashba nanowire, and magnetic chains deposited on superconductors. Moreover, we summarize the scattering matrix formalism in the context of differential conductance simulations. In chapter 2, we study the local and non-local conductance in short Rashba nanowires. In particular, we show that a single Andreev bound state can lead to ZBPs at both ends of the nanowire, if the length of the nanowire is comparable to the localization length of the Andreev bound state. Next, in chapter 3, we propose a mechanism based on overlapping Andreev bound states, that can lead to a signature reminiscent of the bulk gap closing and reopening of a topological phase transition in non-local conductance. In chapter 4, we study trivial zero-energy states in helical spin chains. In particular, we analyze spin configurations in which the angle between adjacent spins smoothly changes close to the ends of the chain. Last, in chapter 5, we analyze the superconducting diode effect for magnetic domain walls and skyrmions moving on a racetrack that is sandwiched by two superconductors forming a Josephson junction. Additionally, we classify magnetic textures and predict which textures support a superconducting diode effect without the need for an extra Rashba SOI in the two-dimensional electron gas beneath the Josephson junction.

Publication List

1. Richard Hess, Henry F. Legg, Daniel Loss, and Jelena Klinovaja,
   "Local and nonlocal quantum transport due to Andreev bound states in finite Rashba nanowires with superconducting and normal sections",
   Phys. Rev. B **104**, 075405 (2021).

2. Felix Küster, Sascha Brinker, Richard Hess, Daniel Loss, Stuart Parkin, Jelena Klinovaja, Samir Lounis, Paolo Sessi,
   "Non-Majorana modes in diluted spin chains proximitized to a superconductor",
   PNAS 119 (42) e2210589119 (2022)

3. Richard Hess, Henry F. Legg, Daniel Loss, and Jelena Klinovaja
   "Prevalence of trivial zero-energy sub-gap states in non-uniform helical spin chains on the surface of superconductors",
   Phys. Rev. B **106**, 104503 (2022)

4. Richard Hess, Henry F. Legg, Daniel Loss, and Jelena Klinovaja
   "Trivial Andreev Band Bimicking Topological Bulk Gap Reopening in the Nonlocal Conductance of Long Rashba Nanowires",
   Phys. Rev. Let. **130**, 207001 (2023)

5. Richard Hess, Henry F. Legg, Daniel Loss, and Jelena Klinovaja,
   "Josephson transistor from the superconducting diode effect in domain wall and skyrmion magnetic racetracks",
   Phys. Rev. B **108**, 174516 (2023)

6. Jung-Ching Liu, Chao Li, Richard Hess, Hongyan Chen, Carl Drechsel, Ping Zhou, Robert Häner, Ulrich Aschauer, Thilo Glatzel, Silvio Decurtins, Daniel Loss, Jelena Klinovaja, Shi-Xia Liu, Wulf Wulfhekel, Ernst Meyer, Rémy Pawlak,
   "Gate-tunable topological superconductivity in a supramolecular electron spin lattice",
   arXiv:2310.18134 (2023)

Note: only first-author articles are printed in this thesis.

Contents

CHAPTER 1

Introduction

1.1 Symmetry protected topological order

In this section, we briefly review the concepts of topology in condensed matter physics with a focus on *symmetry protected topological order* (SPTO). SPTO, in contrast to *topological order* (TO), describes systems that are only stable against perturbations that respect the symmetry protecting the systems [102–105]. Topological insulators [6–8, 14] and topological superconductors [15, 16] belong to this group of SPTO and have been extensively studied in recent years. In general, topological insulators are characterized by an insulating bulk, which means that the system is gapped at the Fermi level, and the existence of conducting surface states [6, 8]. Perturbations that respect the underlying symmetries of the system and which are not strong enough to close the bulk-gap cannot remove the surface states. In fact, only a topological phase transition, which is accompanied by the closing and reopening of the bulk-gap, can change the number of surface states. This phase transition is described by a topological order parameter, which changes its integer value when the system is driven through the phase transition. In contrast to the local order parameters used in the Landau theory [106, 107] to describe phase transitions in the framework of spontaneous symmetry breaking, the topological order parameter is a *global* order parameter. Usually, the topological order parameter is calculated in translationally invariant systems and its integer value is linked to the number of topologically protected surface states via the *bulk boundary correspondence*. If a system is of dimension d, then the surface states are of dimension $d-1$. More general theories discuss also higher-order topological insulators and superconductors, with edge states of lower dimensions [108–112], these theories are, however, not main subject of this thesis.

The topological insulators and topological superconductors are classified by time reversal symmetry (TRS), particle hole symmetry (PHS), and chiral symmetry (CS) [113, 114]. TRS inverts the direction of time t as $t \to -t$. This operation leaves, for example, the position of a particle or its energy unaffected. Many other physical quantities are, however, not invariant under this transformation. For instance, TRS flips the direction of momentum, spin, and magnetic field. The action of the time reversal operator $\mathcal{T}$ on the position-momentum commutator,

$$\mathcal{T} i\hbar \mathcal{T}^{-1} = \mathcal{T}[\hat{x}, \hat{p}]\mathcal{T}^{-1} = -[\hat{x}, \hat{p}] = -i\hbar, \tag{1.1}$$

shows that the action of the operator involves a complex conjugation. In general, the TRS operator is anti-unitary and takes in matrix representation the form $\mathcal{T} = U_\mathcal{T}\mathcal{K}$, where $U_\mathcal{T}$ is a unitary matrix and $\mathcal{K}$ denotes complex conjugation [114]. If $\mathcal{T}$ commutes with the Hamiltonian H as $\mathcal{T}H\mathcal{T}^{-1} = H$, then the system described by H is invariant under time reversal. Applying the operator twice to a state should return this original state up to a phase factor φ as [115]

$$\begin{aligned}\mathcal{T}\mathcal{T} =& U_\mathcal{T}\mathcal{K}U_\mathcal{T}\mathcal{K} = U_\mathcal{T}U_\mathcal{T}^* = U_\mathcal{T}[U_\mathcal{T}^T]^{-1} = \varphi && (1.2)\\ \Leftrightarrow\ & U_\mathcal{T} = \varphi U_\mathcal{T}^T && (1.3)\\ \Leftrightarrow\ & U_\mathcal{T}^T = U_\mathcal{T}\varphi, && (1.4)\end{aligned}$$

where we used $U^\dagger U = (U^T)^* U = 1 \Leftrightarrow U^* U^T = 1 \Leftrightarrow U^* = [U^T]^{-1}$ which holds for any unitary matrix U. Here, the superscripts T, $*$, and $\dagger$ denote the transpose, the complex conjugate and the hermitian conjugate, respectively. Inserting the expression for U^T from Eq. (1.4) into Eq. (1.3) yields

$$U_\mathcal{T} = \varphi U_\mathcal{T}\varphi, \tag{1.5}$$

which is satisfied for the choice $\varphi = \pm\mathbb{I}$, where $\mathbb{I}$ is the identity matrix. Consequently, the time reversal symmetry operator squares to ± 1. In the case of integer spin particles (bosons) the time reversal symmetry operator squares to $+1$, while for half integer spin particles (fermions) the time reversal operator squares to -1. If $\mathcal{T}^2 = -1$, then the time-reversed state $|\mathcal{T}v\rangle$ is orthogonal to the original single particle state $|v\rangle$ since [115]

$$\langle v|\mathcal{T}v\rangle = \left\langle \mathcal{T}^2 v\middle|\mathcal{T}v\right\rangle = -\langle v|\mathcal{T}v\rangle\,. \tag{1.6}$$

Here, we used the anti-unitary property $\langle \mathcal{T}u|\mathcal{T}v\rangle = \langle v|u\rangle$ of the time reversal operator and introduced the bra-ket notation for convenience. So far, the discussion has focused on a single particle state which can be generated with the usual creation operator $c^\dagger_{m,\nu}$ acting on the vacuum $|0\rangle$ as $|m,\nu\rangle = c^\dagger_{m,\nu}|0\rangle$, with m denoting an arbitrary quantum number and with $\nu \in \{\uparrow,\downarrow\}$ the spin quantum number of a spin-$\frac{1}{2}$-system with a quantization axis along the z-direction. In general, the operator transforms under time-reversal as [115]

$$\mathcal{T}c_{m,\uparrow}\mathcal{T}^{-1} = c_{m,\downarrow} \tag{1.7}$$

and

$$\mathcal{T}c_{m,\downarrow}\mathcal{T}^{-1} = -c_{m,\uparrow} \tag{1.8}$$

so that acting twice with the time reversal operator on the annihilation operator yields

$$\mathcal{T}^2 c_{m,\nu}[\mathcal{T}^2]^{-1} = -c_{m,\nu}. \tag{1.9}$$

Going beyond the single particle picture, one can create an n particle state like

Table 1.1: *Table of topological insulators and superconductors*: The different classes distinguish systems by the presence or absence of TRS, PHS, and CS. Moreover, the classification differentiates whether the TRS or PHS operator squares to $+1$ or -1. Systems without PHS belong to the A classes (A, AI, AII, AIII), while systems with $\mathcal{P}^2 = -1$ and $\mathcal{P}^2 = +1$ belong to the C (C, CI, CII) or D (D, DIII, BDI) classes. The topological invariant of each class varies as a function of the dimension d. If this invariant is zero, then the corresponding system is trivial and cannot enter the topological phase. In contrast, systems with a $\mathbb{Z}$ or $\mathbb{Z}_2$ topological invariant have also non-trivial phases.

				d							
Class	$\mathcal{T}^2$	$\mathcal{P}^2$	$\mathcal{S}$	1	2	3	4	5	6	7	8
A	0	0	0	0	$\mathbb{Z}$	0	$\mathbb{Z}$	0	$\mathbb{Z}$	0	$\mathbb{Z}$
AIII	0	0	1	$\mathbb{Z}$	0	$\mathbb{Z}$	0	$\mathbb{Z}$	0	$\mathbb{Z}$	0
AI	1	0	0	0	0	0	$\mathbb{Z}$	0	$\mathbb{Z}_2$	$\mathbb{Z}_2$	$\mathbb{Z}$
BDI	1	1	1	$\mathbb{Z}$	0	0	0	$\mathbb{Z}$	0	$\mathbb{Z}_2$	$\mathbb{Z}_2$
D	0	1	0	$\mathbb{Z}_2$	$\mathbb{Z}$	0	0	0	$\mathbb{Z}$	0	$\mathbb{Z}_2$
DIII	-1	1	1	$\mathbb{Z}_2$	$\mathbb{Z}_2$	$\mathbb{Z}$	0	0	0	$\mathbb{Z}$	0
AII	-1	0	0	0	$\mathbb{Z}_2$	$\mathbb{Z}_2$	$\mathbb{Z}$	0	0	0	$\mathbb{Z}$
CII	-1	-1	1	$\mathbb{Z}$	0	$\mathbb{Z}_2$	$\mathbb{Z}_2$	$\mathbb{Z}$	0	0	0
C	0	-1	0	0	$\mathbb{Z}$	0	$\mathbb{Z}_2$	$\mathbb{Z}_2$	$\mathbb{Z}$	0	0
CI	1	-1	1	0	0	$\mathbb{Z}$	0	$\mathbb{Z}_2$	$\mathbb{Z}_2$	$\mathbb{Z}$	0

$c^\dagger_{n,\nu} c^\dagger_{n-1,\nu} ... c^\dagger_{1,\nu} |0\rangle = \Omega |0\rangle$. The operator Ω is here composed of n creation operators and it transforms under $\mathcal{T}^2$ as [115]

$$\mathcal{T}^2 \Omega [\mathcal{T}^2]^{-1} = (-1)^n \Omega. \tag{1.10}$$

Consequently, the action of the square of the time reversal operator on a multi-fermion state is a function of the total number of fermions: Only in the case of a state with an odd number of fermions the transformation gives a minus sign. This, in combination with Eq. (1.6), leads to the famous Kramers theorem [116], which states that every eigenstate in a system with an odd number of half-integer spin particles has a time-reversed partner with the same energy if TRS is a symmetry of the system. A concrete example of an application of the Kramers theorem is the Anderson theorem: potential disorder does not break TRS in s-wave superconductors. Therefore, pairs of time-reversed states can still form Cooper pairs [117].

Particle hole symmetry, which exchanges single particle creation and annihilation operators [118], is also described by an anti-unitary operator as $\mathcal{P} = U_\mathcal{P} \mathcal{K}$, where $U_\mathcal{P}$ is a unitary matrix. Due to its anti-unitary character, the PHS operator squares also as $\mathcal{P}^2 = \pm 1$ [114, 119]. We note that the Bogoliubov-de Gennes (BdG) formalism in superconductors requires PHS by definition: the Hamiltonian is designed to have PHS. Therefore, PHS is a constraint in the BdG description of superconductors and cannot break down.

Last, chiral symmetry, also sometimes called sublattice symmetry, is the product of TRS and PHS. The corresponding operator $\mathcal{S}$ is unitary, and its matrix representation is given by $\mathcal{S} = U_{\mathcal{S}}$, where $U_{\mathcal{S}}$ denotes a unitary matrix. In fact, if a Hamiltonian H has chiral symmetry, then its matrix representation can be transformed to a block off-diagonal matrix like

$$\tilde{H} = \begin{pmatrix} 0 & h_B \\ h_B^\dagger & 0 \end{pmatrix}, \tag{1.11}$$

where h_B is a block matrix [114, 119].

The combination of these three symmetries provides a classification scheme leading to the 10-fold table of topological insulators and superconductors, see Table 1.1 [113, 114, 120]. The first column contains the names of the different classes, the second to third columns indicate the square of the TRS and PHS operators, while the fourth column indicate the presence (1) or absence (0) of chiral symmetry. The last eight columns describe the form of the topological order parameter for the dimensions $d = 1$ to $d = 8$. A topological order parameter of 0 indicates that the system is trivial, while $\mathbb{Z}$ and $\mathbb{Z}_2$ indicate that the order parameter is an integer or takes only two integer values, with one value corresponding to the trivial phase. This table repeats for higher dimensions and is therefore also called a periodic table. Last, we note that the table can be generalized for nodal systems or additional spatial symmetries [121–125]. Spatial symmetries are, however, often considered to be *weak* in the sense that they can easily be broken.

1.2 The Kitaev chain

So far, we have introduced the basic ideas of topology in condensed matter physics. Here, we will focus on topological superconductors and in particular on their edge states, so-called Majorana modes, which are named after the Italian physicist Ettore Majorana, who proposed the existence of a particle with the peculiar property of being its own antiparticle in the context of particle physics [27]. So far, this particle, the *Majorana fermion*, has not been experimentally identified in particle/high-energy physics, despite intense efforts. However, many years after the proposal of the Majorana fermion, it was realized that the basic concept of a particle being self-adjoint also applies to special quasiparticles, the Majorana bound states (MBSs), in condensed matter theory [29, 30, 34, 126–128]. Apart from the fact that MBSs are their own antiparticles, the MBSs, however, differ greatly from the original Majorana fermion. For instance, the MBSs obey non-Abelian braiding statistics, which makes them highly attractive for quantum computation [29, 30, 32, 33, 126, 129].

One of the most studied toy models for topological superconductivity and MBSs was proposed by Alexei Kitaev [34]: a one-dimensional spinless p-wave supercon-

Figure 1.1: *Kitaev chain with five fermionic sites*: (a) If the hopping amplitude and the superconducting pairing potential are set to zero, then only Majorana modes (blue dots) from the same fermionic site (black rectangle) are paired. (b) In contrast, if the system is tuned to the limit of vanishing chemical potential and a pairing potential that is equal to the hopping amplitude, then only Majorana operators from different sites couple. This means for a chain with open boundary conditions that the Majorana mode at the very left (γ_1) and the very right (γ_{10}) remain unpaired and together form a nonlocal fermionic state.

ductor, which is described via the lattice Hamiltonian

$$H_{KC} = \sum_{j=1}^{N-1} \left[-t(c_j^\dagger c_{j+1} + c_{j+1}^\dagger c_j) + \Delta c_j c_{j+1} + \Delta^* c_{j+1}^\dagger c_j^\dagger \right] - \sum_{j=1}^{N} \mu c_j^\dagger c_j, \tag{1.12}$$

where t and μ denote the nearest neighbor hopping amplitude and the chemical potential, respectively, while $\Delta = |\Delta| e^{i\varphi}$ denotes the superconducting pairing potential with the phase φ. Moreover, N is the total number of sites, and the chain has open boundary conditions. The fermionic creation and annihilation operator $c_j^\dagger$ and c_j can be expressed in terms of the MBS operators γ_{2j-1} and γ_{2j} as [34]

$$c_j = \frac{1}{2} e^{-i\frac{\varphi}{2}} \gamma_{2j-1} + \frac{i}{2} e^{-i\frac{\varphi}{2}} \gamma_{2j} \qquad c_j^\dagger = \frac{1}{2} e^{i\frac{\varphi}{2}} \gamma_{2j-1} - \frac{i}{2} e^{i\frac{\varphi}{2}} \gamma_{2j}, \tag{1.13}$$

while the inverse transformation reads

$$\gamma_{2j-1} = e^{i\frac{\varphi}{2}} c_j + e^{-i\frac{\varphi}{2}} c_j^\dagger \qquad \gamma_{2j} = -ie^{i\frac{\varphi}{2}} c_j + ie^{-i\frac{\varphi}{2}} c_j^\dagger. \tag{1.14}$$

Here, we note that the Majorana operators anti-commute like usual fermion operators, however, they square to one instead of zero [32]. Colloquially speaking, this transformation splits the fermionic operator corresponding to one lattice site into two Majorana operators. Rewriting the Hamiltonian in terms of the new operators results in [34]

$$\tilde{H}_{KC} = \frac{i}{2} \left\{ \sum_{j=1}^{N} -\mu \gamma_{2j-1} \gamma_{2j} + \sum_{j=1}^{N-1} \left[(t + |\Delta|) \gamma_{2j} \gamma_{2j+1} + (-t + |\Delta|) \gamma_{2j-1} \gamma_{2j+2} \right] \right\}. \tag{1.15}$$

In the limit $t = |\Delta| = 0$ the Hamiltonian in Majorana representation simplifies to [34]

$$\tilde{H}_{KC}(t = \Delta = 0) = -\frac{i}{2} \mu \sum_{j=1}^{N} \gamma_{2j-1} \gamma_{2j}, \tag{1.16}$$

which means that only Majorana modes from the same site are coupled, namely γ_{2j-1} and γ_{2j}, see Fig. 1.1a. In contrast, if the chemical potential is set to $\mu = 0$, and hopping and superconducting pairing satisfy the condition $t = |\Delta| > 0$, then the Hamiltonian reads [34]

$$\tilde{H}_{KC}(t = \Delta > 0, \mu = 0) = it \sum_{j=1}^{N-1} \gamma_{2j}\gamma_{2j+1}. \tag{1.17}$$

This Hamiltonian involves only products of γ_{2j} with γ_{2j+1} and therefore it exclusively couples Majorana operators from different fermionic sites. Due to the open boundary conditions, two Majorana operators, namely γ_1 and γ_{2N}, remain unpaired at the ends of the chain, see Fig. 1.1b. We note that, in this fine-tuned limit, the number of sites is not relevant for the emergence of unpaired MBSs, as long as $N \geq 2$, since the MBSs are fully localized at the first and last site of the chain. This particular choice of the system parameters, $t = |\Delta| > 0$, is unrealistic; however, MBSs appear also in less fine-tuned systems, see Fig. 1.2a showing the energy spectrum of H_{KC} as a function of the chemical potential in the limit $|\Delta| \ll t$. In this case, the wave functions are not localized on single sites, see Fig. 1.2b, causing an exponentially suppressed overlap of the left and the right MBS. Consequently, the energy of the MBSs is not exactly zero anymore. The longer the chain, the better the spatial separation of the MBSs and, therefore, the smaller their energy. A local perturbation cannot affect the energy of the MBSs, if they are sufficiently separated. This stability of the MBSs is attributed to the topology of the system: Let us consider a fixed phase φ of the superconducting order parameter. In this case, the TRS operator has to be defined for this particular choice of φ as $\mathcal{T} = U(\varphi)\mathcal{K}$ [115]. Changing the superconducting phase to φ' will therefore require an adjustment to the TRS operator. If, for simplicity, the superconducting order parameter is real and if the system is only exposed to perturbations that are invariant under time reversal symmetry, then the Kitaev chain belongs to the class BDI with a $\mathbb{Z}$ topological invariant W which takes the values $-1, 0, 1$ [119, 130]. The system is in the trivial phase for $W = 0$ and topological otherwise. In particular, $W = -1$ [$W = 1$] corresponds to the case $\Delta < 0$ [$\Delta > 0$]. Please note that a gauge transformation would break the TRS, which was defined for the system with the originally real superconducting order parameter. Therefore, in order to stay in the class BDI, the superconducting gap has to close and reopen to go from one topological phase with $\Delta < 0$ to the other one with $\Delta > 0$.

In contrast, if TRS is broken, then the system belongs to class D [34] and the corresponding $\mathbb{Z}_2$ topological invariant Q is defined as [82, 89, 130]

$$Q = \text{sgn}\left\{\text{Pf}\left[H_{KC}(k = 0)\mathcal{P}\right]\right\} \text{sgn}\left\{\text{Pf}\left[H_{KC}(k = \pi)\mathcal{P}\right]\right\}, \tag{1.18}$$

where Pf[] and sgn{} denote the Pfaffian and the sign function. The momentum-dependent Hamiltonian density $H_{KC}(k)$ entering Eq. 1.18 can be written as

$$H_{KC}(k) = [-2t\cos(k) - \mu]\tau^z + 2\Delta\sin(k)\tau^y \tag{1.19}$$

in the basis $\Psi_K^\dagger(k) = \begin{pmatrix} c_k^\dagger & c_{-k} \end{pmatrix}$. Here, τ^z and τ^y are Pauli matrices acting in particle-hole space. Moreover, the operator $c_k^\dagger$ [c_k] creates [annihilates] an electron with momentum k. We note that only the high symmetry points $k = 0$ and $k = \pi$ enter the expression of Q. This considerably simplifies the calculation of Q which is given by

$$Q = \text{sgn}\left\{[-2t - \mu]\right\} \text{sgn}\left\{[2t - \mu]\right\}. \tag{1.20}$$

Consequently, $Q = +1$ for $|\mu| > 2t$, as shown in Fig. 1.2c. However, this limit corresponds to an insulator since the chemical potential drops out of the band: This means that the system remains gapped at the Fermi energy when the superconducting pairing strength is set to zero. In the opposite regime, $|\mu| < 2t$, the value $Q = -1$ indicates the topological phase. Last, we numerically perform the Majorana decomposition of the wave functions, see Fig. 1.2d. This calculation reveals that one MBS is localized on the left side while the second MBS is localized on the right side.

1.3 Rashba nanowire

In the previous section, we introduced the Kitaev chain and showed that MBSs can emerge at the ends of this chain for certain parameter regimes. A major drawback of this model, however, is that it relies on p-wave superconductivity, which has not been identified in nature. Sr_2RuO_4 has been considered as a candidate for chiral p-wave superconductivity. However, the experimental data does not fully agree with theoretical predictions and remains inconclusive [131–139].

Most superconductors have been identified as s-wave type while a few are of d-wave symmetry[140–143]. A solution to this lack of natural p-wave superconductors relies on the combination of multiple ingredients available in nature, like normal s-wave superconductivity, Rashba spin orbit interaction (SOI) [144], and magnetic fields [38, 39, 88, 145], which allows generating an effective p-wave pairing in a single band. A prominent example with these ingredients is the semiconducting Rashba nanowire proximitized by a superconductor and exposed to a magnetic field [38, 39], which can be described via the Hamiltonian

$$H = \int \Psi^\dagger \left[\left(-\frac{\hbar^2}{2m}\frac{\partial^2}{\partial x^2} - \mu \right) \tau^z + \Delta_Z \boldsymbol{\sigma} \cdot \mathbf{S} + \Delta \tau^x - i\alpha \frac{\partial}{\partial x} \sigma^y \tau^z \right] \Psi \mathrm{d}x, \tag{1.21}$$

where the Nambu vector

$$\Psi^\dagger = \begin{pmatrix} \psi_{x,\uparrow}^\dagger & \psi_{x,\downarrow}^\dagger & \psi_{x,\downarrow} & -\psi_{x,\uparrow} \end{pmatrix} \tag{1.22}$$

is constructed out of field operators $\psi_{x,\nu}^\dagger$ [$\psi_{x,\nu}$] which create [annihilate] electrons with spin $\nu \in \{\uparrow, \downarrow\}$ at the coordinate x. Moreover, Δ_Z and Δ denote the Zeeman coupling strength and the superconducting pairing potential, while α denotes the SOI strength. The direction of the Zeeman field is set by the vector $\mathbf{S}$ which couples to the Pauli matrix vector $\boldsymbol{\sigma} = (\sigma^x, \sigma^y, \sigma^z)$, where the Pauli matrices σ^j act in spin

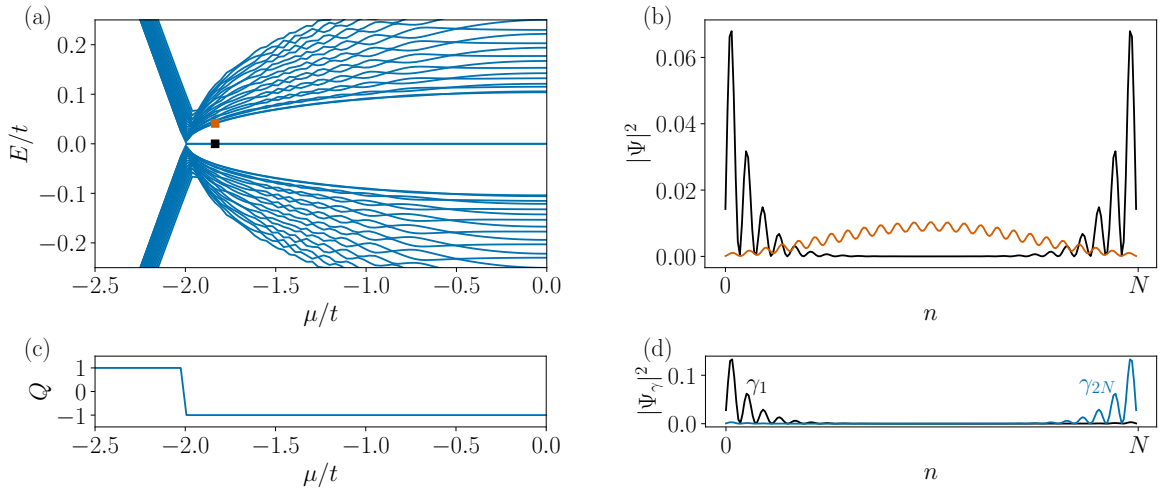

Figure 1.2: *Numerical analysis of the Kitaev chain*: (a) Eigenvalues of the Kitaev chain as a function of the chemical potential. Here, we show only the 40 lowest eigenvalues and measure the chemical potential from half filling. The spectrum reveals a zero-energy state in the topological regime. (b) Probability density of the wave functions associated with the energies marked with the black and orange squares in panel (a). The probability density of the lowest energy eigenstate has weights on both ends of the chain and decays into the bulk. In contrast, the second eigenstate has most of its weight in the bulk of the chain and vanishes at the ends. (c) The topological invariant Q, which is calculated in an infinite system, changes its sign when the system undergoes a topological phase transition. If $Q = -1$, then MBSs are present. We note that the choice $|\mu| > 2$ corresponds to the transition to an insulator and is only shown to illustrate the change of the sign of Q. (d) A decomposition of the lowest eigenvector [corresponding to the black line in panel (b)] into the Majorana contributions reveals that one MBS is fully localized at the left end, while a second MBS is localized on the right side. The chosen parameters are: $t = 1$, $\Delta = 0.05$, $N = 200$.

space. In contrast, the Pauli matrices τ^j act in particle-hole space. Last, $-\frac{\hbar^2}{2m}\frac{\partial^2}{\partial x^2}$ describes the kinetic term, with m the effective mass of the electrons in the semiconductor and μ is the chemical potential. If this one-dimensional system is translationally invariant in x-direction, then the momentum k along the nanowire serves as a good quantum number, and the Fourier transformed Hamiltonian is given by $H' = \sum_k \Psi_k^\dagger H(k) \Psi_k$ with [39]

$$H(k) = \left(\frac{\hbar^2 k^2}{2m} - \mu\right)\tau^z + \Delta_Z \boldsymbol{\sigma}\cdot\mathbf{S} + \Delta\tau^x + \alpha k \sigma^y \tau^z \tag{1.23}$$

in the basis $\Psi_k^\dagger = \begin{pmatrix} c_{k,\uparrow}^\dagger & c_{k,\downarrow}^\dagger & c_{-k,\downarrow} & -c_{-k,\uparrow} \end{pmatrix}$. Here $c_{k,\nu}^\dagger[c_{k,\nu}]$ with $\nu \in \{\uparrow,\downarrow\}$ creates [annihilates] an electron with momentum k and spin ν. If the direction of the magnetic field is perpendicular to the direction of the spin-orbit interaction, for example,

if it is oriented in the x-direction, then the energies are given by [39, 146]

$$E(k) = \pm \left[\Delta_Z^2 + (\alpha k)^2 + \Delta^2 + \epsilon_k^2 \pm 2\sqrt{\Delta_Z^2 \left(\Delta^2 + \epsilon_k^2\right) + (\alpha k \epsilon_k)^2} \right]^{1/2} \tag{1.24}$$

with the abbreviation

$$\epsilon_k = \frac{\hbar^2 k^2}{2m} - \mu. \tag{1.25}$$

In order to understand the whole system, it is useful to examine the impact of the individual ingredients. First, we will disregard superconductivity by choosing $\Delta = 0$. In this limit, it is sufficient to study the electron block with the spin degree of freedom. If the external magnetic field is turned off and SOI is absent, then the Hamiltonian is given by $H_{k,1} = \epsilon_k \sigma^0$ and the bands are parabolic, as shown in Fig. 1.3a. Moreover, the bands are degenerate since no spin-splitting term appears. The addition of Rashba SOI to the Hamiltonian yields $H_{k,2} = \epsilon_k \sigma^0 + \alpha k \sigma^z$ which is still diagonal in spin space. Calculating the energies by completing the square for spin up and down sectors yields $E_{H_{k,2},\pm}(k) = \frac{\hbar^2}{2m}(k \pm k_{so})^2 - \mu - E_{so}$, with the SOI momentum $k_{so} = m\alpha/\hbar^2$ and the SOI energy $E_{so} = (\hbar k_{so})^2/(2m) = m\alpha^2/(2\hbar^2)$. Consequently, the SOI shifts the apex of the parabolas differently for the spin up and the spin down bands, see Fig 1.3b. A magnetic field perpendicular to the Rashba SOI vector lifts the degeneracy at $k = 0$ and splits the two bands, see Fig. 1.3c. Next, we take superconductivity into account: the superconducting pairing potential couples the electron and hole sectors and can open a gap in the energy spectrum at the chemical potential. The magnitude of this gap is a function of Δ_Z. In particular, it is given by $E_g = 2\Delta$ at $\Delta_Z = 0$, see Fig. 1.3d, it decreases in the interval $0 < \Delta_Z < \Delta_Z^c$ until it vanishes at $\Delta_Z = \Delta_Z^c$, see Fig. 1.3e, and finally reopens for field strengths $\Delta_Z > \Delta_Z^c$ if SOI is present in the system, see Fig. 1.3f. This closing and reopening is associated with a topological phase transition from the trivial to the topological phase, like in the Kitaev chain. The critical Zeeman field strength Δ_Z^c of the phase transition is determined by the condition $E(k = 0) = 0$, see Eq. (1.24), which yields [33]

$$\Delta_Z^c = \pm\sqrt{\Delta^2 + \mu^2}. \tag{1.26}$$

The Rashba SOI does not explicitly enter this expression, however, the SOI is still required for the topological phase since it enforces the reopening of the gap at $\Delta_Z > \Delta_Z^c$. In fact, if SOI was absent, then superconductivity would break down at $\Delta_Z > \Delta$ according to the Pauli limit, in which the Zeeman field overcomes the binding energy of the Cooper pairs and splits them [147–149].

Next, we discretize the model from Eq. (1.21) and generalize it for position-dependent chemical potential μ_n, superconducting pairing Δ_n, and Zeeman field

$\Delta_{Z,n}$:

$$H_L = \sum_{n=1}^{N} \left(\sum_{\nu,\nu'} c_{n,\nu}^{\dagger} \left[\left(-t\delta_{\nu,\nu'} + i\alpha_L \sigma_{\nu,\nu'}^{y} \right) c_{n+1,\nu'} + \frac{1}{2} \left([2t - \mu_n]\delta_{\nu,\nu'} + \Delta_{Z,n}\sigma_{\nu,\nu'}^{x} \right) c_{n,\nu'} \right] + \Delta_n c_{n,\downarrow}^{\dagger} c_{n,\uparrow}^{\dagger} + \text{H.c.} \right). \tag{1.27}$$

Here, $c_{n,\nu}^{\dagger}$ [$c_{n,\nu}$] creates [annihilates] an electron with spin $\nu \in \{\uparrow, \downarrow\}$ at the lattice site n. The hopping amplitude is given by $t = \frac{\hbar^2}{2ma^2}$, where a denotes the lattice constant. Similar, the lattice version α_L of the SOI coefficient is related to the continuum version α as $\alpha_L = \frac{\alpha}{2a}$. Moreover, N denotes the total number of sites in the chain. In this section, we consider the simple case of position-independent parameters like $\mu_n = \mu$, $\Delta_n = \Delta$ and $\Delta_{Z,n} = \Delta_Z$ and numerically diagonalize the Hamiltonian H_L for hard-wall boundary conditions. The eigenvalue spectrum reveals a closing and reopening of the superconducting gap in agreement with the predictions from the bulk system, see Fig. 1.4a. Moreover, the reopening is accompanied by the appearance of low-energy subgap states. These subgap states are identified as MBSs. Their energy is shifted away from zero and oscillates as a function of the Zeeman field strength due to an overlap of the wave functions, see the black line in Fig. 1.4b. The wave functions are mainly localized at the ends of the nanowire and decay exponentially into the bulk. Additionally the wave function is modulated by an oscillation whose period is roughly set by the Fermi wave length [146, 150]. In contrast, the first excited state, see the red line in Fig. 1.4b, is mainly localized in the bulk of the system and decays at the boundaries of the system.

1.4 Transport

Many experiments have been searching MBSs in Rashba nanowires [40–45, 57], however, despite these great efforts, the experimental data remains ambiguous. One of the most common experiments relies on the measurement of differential conductance curves, like for example the seminal work of Mourik et al. [40]: a semiconducting nanowire with strong SOI, for instance InAs or InSb, is proximitized by a grounded superconductor, usually Al or NbTiN [41–45]. Moreover, a normal lead is attached to one side of the semiconducting nanowire, for example, the left side, and a tunnel gate, mounted to the semiconducting nanowire close to the normal lead, allows a tuning of the barrier potential between the normal lead and the proximitized nanowire. The experiment measures the current response to a voltage that is applied between the normal lead and the grounded superconductor. This experimental setup, known as a two-terminal device, is suited for local differential conductance measurements. Here, locality is meant in the sense that the differential conductance measurements detect only states which have a finite weight close to the normal lead. In an ideal topological nanowire, MBSs appear at the ends of the nanowire and would therefore lead to a zero-bias peak in the differential conductance curve. The two-terminal device can be extended to a three-terminal geometry

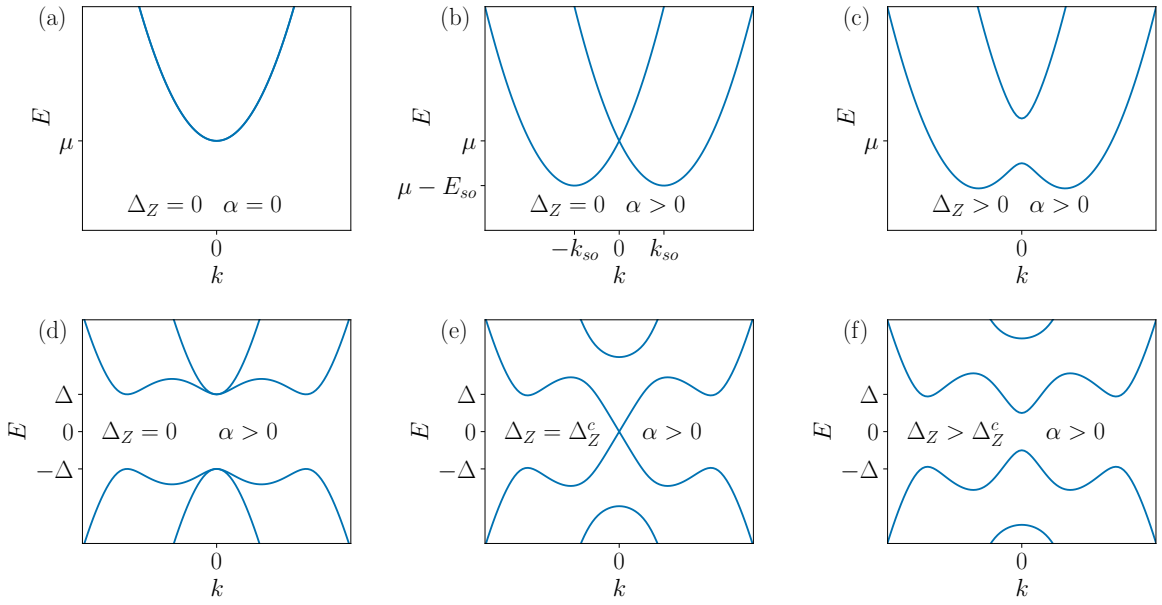

Figure 1.3: *Energy spectra in the Rashba nanowire*. First row: Rashba nanowire. Second row: proximitized Rashba nanowire. (a) The energy spectrum is parabolic and doubly degenerate due to the spin degree of freedom in the absence of a Zeeman field. (b) A Rashba term shifts the parabolas different for spin up and spin down and an additional Zeeman term (c) removes the degeneracy and opens a "gap" at $k = 0$. (d) The proximity effect opens a gap at the chemical potential. (e) If the Zeeman field strength Δ_Z reaches the critical value Δ_Z^c, then the energy gap closes, (f) but it reopens at higher field strengths indicating the topological phase transition. The parameters are $\hbar^2/(2m) = 1$, $\mu = 0$, $\Delta = 0.01$, $\alpha = 0.2$, (c) $\Delta_Z = 0.005$, (e) $\Delta_Z = 0.01$, (f) $\Delta_Z = 0.015$.

by attaching a second normal lead at the other end of the nanowire. Depending on the voltage-current configuration, it is now possible to measure not only local differential conductance on both ends of the nanowire but also the so-called nonlocal differential conductance. The latter can detect extended states, namely states that connect the two normal leads.

Here, we calculate the local and nonlocal differential conductance via the python package Kwant [151], which is based on the scattering matrix (S-matrix) formalism [152, 153]. For the actual computation, we implement the tight-binding Hamiltonian of the nanowire, see Eq. (1.27), with a position-dependent chemical potential as

$$\mu_n = \mu - (\gamma_L + \mu)\Theta(N_{B,L} - n) - (\gamma_R + \mu)\Theta(n - [N - N_{B,R}]), \tag{1.28}$$

where γ_L [γ_R] and $N_{B,L}$ [$N_{B,R}$] denote the barrier strength and barrier length in terms of sites on the left [right] end of the nanowire. Moreover, $\Theta(n')$ denotes the Heaviside step function with the definition $\Theta(0) = 1$. The profile of the supercon-

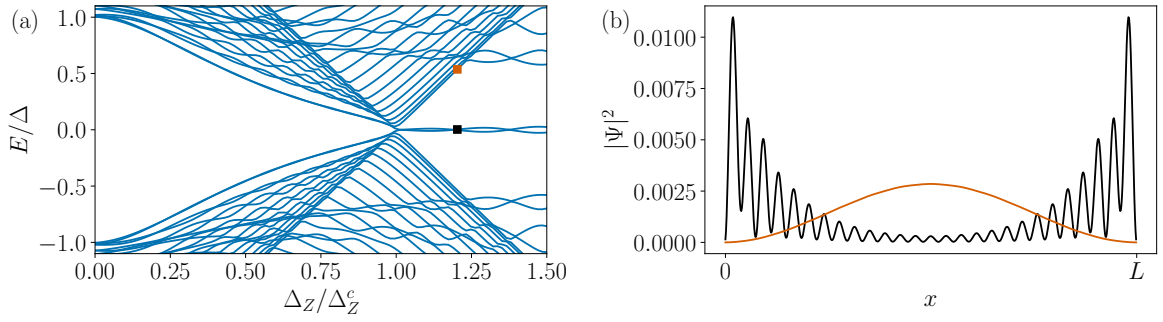

Figure 1.4: *Energies and wave functions in the finite Rashba nanowire*: (a) Energies (blue) as a function of the Zeeman field strength Δ_Z. The spectral gap is maximal at $\Delta_Z = 0$, decreases in the region $0 < \Delta_Z < \Delta_Z^c$ until it vanishes at the critical value Δ_Z^c, and reopens for $\Delta_Z > \Delta_Z^c$. This reopening is accompanied by the appearance of MBSs close to zero energy, which are energetically separated from the bulk states of the nanowire. (b) Probability density of the lowest and second-lowest state in the topological phase. The lowest state (black) reveals an accumulation of the probability density at the ends of the nanowire and decays exponentially into the bulk of the nanowire. This decay is modulated by oscillations, whose period is determined by the Fermi wave length. The second lowest state (red) is mainly localized in the bulk of the nanowire and vanishes at the ends. The value of the Zeeman field and the energies associated with the wave functions are indicated in panel (a) with the black and red squares. The chosen parameters are $a = 5$ nm, $\alpha_L = 2$ meV, $\Delta = 0.25$ meV, $L = Na = 700a = 3500$ nm, $t \approx 102$ meV, and $\mu = 0.6$ meV.

ducting gap is given by

$$\Delta_n = \Delta\{1 - \Theta(N_{B,L} - n) - \Theta(n - [N - N_{B,R}])\}, \tag{1.29}$$

while we choose the Zeeman field to be constant in space $\Delta_{Z,n} = \Delta_Z$. For the transport calculation, we attach two leads to both ends of the nanowire. These leads are also described by Eq. (1.27) with spatially uniform parameter profiles such that the Hamiltonians of the leads are translationally invariant. In particular, the superconducting pairing vanishes in the leads $\Delta \to 0$, and the chemical potential in the lead can differ from the value in the nanowire, meaning that $\mu_{\text{Lead}} \neq \mu$. In addition, we choose the same SOI strength α_L and Zeeman field strength Δ_Z in the lead as in the nanowire. This choice, however, is not crucial and modifications of the SOI strength or the Zeeman field strength in the lead do not affect the qualitative results. The most important step of the differential conductance computation, namely the calculation of the S-matrix, is internally handled by Kwant.

In general, the S-matrix for a three-terminal device is defined as

$$S = \begin{pmatrix} S_{LL} & S_{RL} \\ S_{LR} & S_{RR} \end{pmatrix}, \tag{1.30}$$

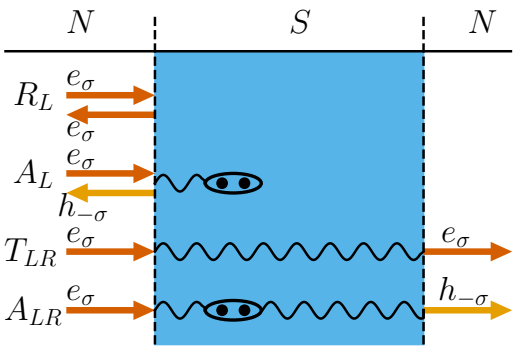

Figure 1.5: *Scattering processes in a NSN junctions:* In total, four scattering processes take place in a NSN junction. First, an electron coming, for example, from the left normal region can be reflected at the first NS interface with an amplitude of R_L. Second, the electron can undergo Andreev reflection with a probability amplitude A_L, meaning that the electron enters the superconductor (blue) and forms a Cooper pair with another electron under the retro-reflection of a hole with opposite spin. Moreover, there is a finite probability amplitude T_{LR} that an electron tunnels from the left normal region through the superconductor to the right normal region. Last, an incident electron can undergo crossed Andreev reflection, described by the amplitude A_{LR}, meaning that the electron entering the superconductor from the left normal region can form a Cooper pair with another electron while at the same time creating a hole in the right normal region. The red and yellow arrows describe the propagation directions of electrons and holes with spin σ, respectively, while the two dots encircled by the ellipse represent a Cooper pair. The dashed vertical lines separate the normal regions, denoted by N, from the superconductor, denoted by S.

where the sub-blocks $S_{\alpha\beta}$ with $\alpha, \beta \in \{L, R\}$ are given by

$$S_{\alpha\beta} = \begin{pmatrix} S^{ee}_{\alpha\beta} & S^{eh}_{\alpha\beta} \\ S^{he}_{\alpha\beta} & S^{hh}_{\alpha\beta} \end{pmatrix}. \tag{1.31}$$

Here, for example, S^{eh}_{LR} describes the scattering process that involves an incident electron from the left lead and an outgoing hole in the right lead. In order to understand the scattering and therefore the local and nonlocal differential conductance, which is set by combinations of the scattering matrix elements, we recapitulate all scattering processes appearing in a normal-superconductor-normal (NSN) junction, see Fig. 1.5. First, we note that the energy spectrum in the superconductor is gapped; consequently, an incident electron coming from a normal metal cannot just enter the superconductor at energies below the superconducting gap. Instead, the electron can be normal-reflected or Andreev-reflected, with the probability amplitudes $R_\eta = S^{ee}_{\eta\eta}$ and $A_\eta = S^{eh}_{\eta\eta}$, which determine the local differential conductance at zero temperature as

$$G_{\eta\eta}(\omega) = N_\eta - R_\eta(\omega) + A_\eta(\omega), \tag{1.32}$$

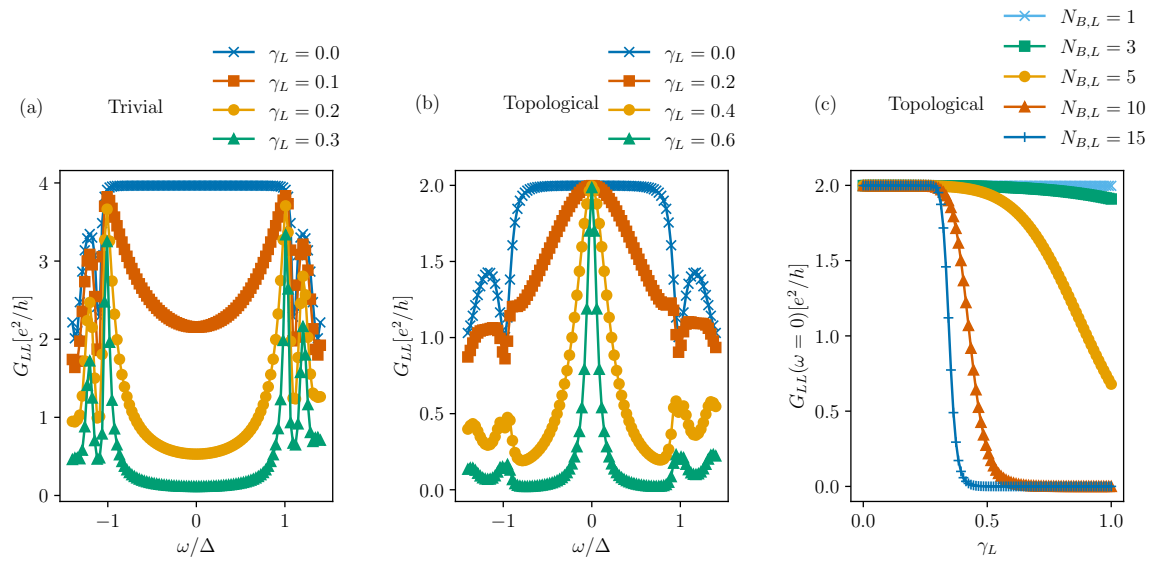

Figure 1.6: *Local differential conductance in the finite-size Rashba nanowire*: (a) Left local differential conductance in the trivial regime ($\Delta_Z = 0$) as a function of energy ω. If the strength of the barrier is set to zero, $\gamma_L = 0$, then perfect Andreev reflection takes place (blue x-shaped markers) at energies inside the gap. Therefore, the differential conductance is $4e^2/h$. However, a finite barrier strength gives rise to normal reflection processes, and consequently, G_{LL} is reduced. In the regime of realistic barrier strengths (green triangle markers), the differential conductance is strongly suppressed inside the gap and is peaked at the gap edge. (b) Left local differential conductance in the topological regime ($\Delta_Z = 0.2 > \Delta_Z^c \approx 0.103$) as a function of energy. The maximal differential conductance is $2e^2/h$ since only one band contributes to the Andreev reflection. Increasing the barrier strength reduces the width of the zero-energy peak. (c) Zero-energy left local differential conductance in the topological regime as a function of the left barrier strength. At low barrier strength, the differential conductance at zero energy remains close to $2e^2/h$, as shown also in (b). For strong barrier strength, however, $G_{LL}(\omega = 0)$ deviates from the quantized value. The longer the barrier, here measured in terms of sites, the faster the decay of $G_{LL}(\omega = 0)$. The chosen parameters are $a = 1$, $\alpha_L = 0.2$, $\Delta = 0.025$, $N = 201 + N_{B,L}$, $t = 1$, and $\mu = 0.1$, $\mu_{\text{Lead}} = 0.1$, $\gamma_R = 0$, $N_{B,R} = 1$. Moreover, in (a) and (b) $N_{B,L} = 3$. These calculations are done for the temperature $T = 0$ K.

with $\eta \in \{L, R\}$ and N_η the number of channels [154–156]. Moreover, ω denotes the energy of the ingoing electron. The Andreev reflection describes a process in which the electron combines with a second electron to form a Cooper pair under the retro-reflection of a hole into the metallic lead from which the original electron came. If no barrier is present between the normal lead and the superconductor, then Andreev reflection is favored over normal reflection. In the absence of further processes, a charge of $2e$ per spin degree of freedom is transferred, explaining the differential conductance value of $4e^2/h$ in the limit of perfect Andreev reflection. This value of

differential conductance decreases with growing barrier potential since the normal reflection comes into play, as shown in Fig. 1.6a. If the Andreev reflection vanishes, then the local differential conductance is zero inside the gap.

Multiple Andreev reflections in systems with a spatially varying superconducting order parameter, like an SNS junction, lead to the formation of subgap states, the so-called Andreev bound states (ABSs). These non-topological subgap states are localized in the region in which the superconducting order parameter varies. The energy of these trivial ABSs is a function of all system parameters and can be tuned to zero [46–54]. A measurement of a zero-energy state is consequently not a sufficient indicator to unambiguously identify MBSs. Subgap states close to the normal leads change the scattering processes. The current and therefore the differential conductance is suppressed for moderate barriers in fully gapped systems. In contrast, if subgap states are present, then the differential conductance becomes finite at the energies of these subgap states. This is because an electron can tunnel through the barrier and the subgap state mediates the Andreev reflection.

An MBS has equal weights of electron and hole charge, which is the precondition for the zero-bias differential conductance peak quantization in an idealized system: The normal lead serves as an electron and a hole lead, as a result of the absence of superconductivity in the lead, the electron and hole sectors do not mix. Consequently, one can theoretically split the lead into two separate leads, namely one electron and one hole lead. If an electron in the electron lead propagates towards the NS interface, then it tunnels into the MBS with a tunneling amplitude t. The MBS with its vanishing charge mediates the Andreev reflection process, and the resulting hole can again tunnel through the barrier into the hole lead. This second tunneling process is described by the same tunneling amplitude t since the hole has to tunnel through the same barrier [56]. The whole process is therefore similar to a resonant tunneling process, which describes an electron tunneling through two subsequent barriers at an energy of a state which is localized between the double barrier [157]. If the two barriers are of the same strength and if the shape of the barriers is given by delta-potentials, then the tunneling probability of the electron is almost independent of the barrier strength, and the transmission coefficient is quantized to one. Back in the picture of the MBSs, we note that in the topological phase, the superconductor gaps out only one band since the second band is shifted to much higher energies and is essentially unaffected by the superconductor and, therefore, the MBS zero-bias differential conductance peak is "quantized" to $2e^2/h$, see Fig. 1.6b. However, this quantization is based on idealized assumptions and breaks down in any realistic system: first, in a finite-size nanowire, the two MBSs from opposite ends overlap and split from zero energy; consequently, they cannot mediate perfect Andreev reflection anymore, and the differential conductance decreases as a function of the barrier strength, see Fig. 1.6c. The longer the barrier, the faster the local differential conductance decays. Moreover, temperature broadens the peak and lowers the differential conductance value. Last, the lead itself causes a broadening of the peak, but the barrier lowers the coupling to the lead and therefore the peaks become sharper, see Fig. 1.6b. This width of the peak, however, also

sets the timescale that it takes an electron to tunnel into this state. An increase of the barrier height means, therefore, that the tunneling time increases, and in the limit of very strong barriers, the process would exceed any realistic measurement time.

Apart from normal reflection and Andreev reflection also nonlocal processes take place in the three-terminal device. First, an electron can tunnel from the left normal lead through the entire proximitized nanowire and enter the right normal lead, see Fig. 1.5. This process, also known as co-tunneling, is described by the transmission coefficient $T_{LR} = S^{ee}_{LR}$. Finally, an electron incident from the left onto the NSN junction can undergo crossed Andreev reflection (CAR), meaning that the electron combines with another electron to form a Cooper pair, similar to normal Andreev reflection, but this time a hole is created in the right lead, see Fig. 1.5. This process is described by the CAR coefficient $A_{LR} = S^{eh}_{LR}$. In general, such nonlocal processes are exponentially suppressed at subgap energies via $\exp(-L/\xi)$, where L is the length of the superconducting section and ξ the superconducting coherence length [158]. Consequently, usual subgap states do not show up in nonlocal processes in the limit $L \gg \xi$, therefore finite amplitudes of nonlocal processes are often an indicator for bulk states. The nonlocal differential conductance from left to right lead ($\eta = L, \eta' = R$) and right to left lead ($\eta = R, \eta' = L$) at zero temperature is given by [154–156, 158]

$$G_{\eta\eta'}(\omega) = A_{\eta\eta'}(\omega) - T_{\eta\eta'}(\omega) \tag{1.33}$$

and therefore the local and nonlocal differential conductance can be fully described in terms of the scattering processes in superconductors. In general, local and nonlocal differential conductance are not completely independent of each other. More precisely, the antisymmetric (with respect to ω) component of the local differential conductance $G^o_{\eta,\eta}$ is related to the antisymmetric component of the nonlocal differential conductance $G^o_{\eta\bar{\eta}}$ with $\bar{\eta} \neq \eta$ as [156, 159]

$$G^o_{\eta\eta}(\omega) = -G^o_{\eta\bar{\eta}}(\omega). \tag{1.34}$$

We illustrate this relation in Fig. 1.7, where $G^o_{\eta\eta}$, shown as the red solid line, exactly matches with $-G^o_{\eta\bar{\eta}}$ shown as blue dots.

Last, we extend our model and include potential disorder, which we describe via a Gaussian distribution centered at the value of the chemical potential and with a standard deviation κ [160–163]. We add this type of disorder to every site, except the sites of the barriers. Here, we choose moderate disorder, such that the system does not enter the Anderson localization regime [164]. We plot G_{LL} and G_{LR} in Figs. 1.8a and 1.8b as a function of the Zeeman field strength and the energy. The left local differential conductance reveals all states on the left side of the nanowire, including a signature stemming from the MBSs when $\Delta_Z > \Delta^c_Z$, see Fig. 1.8a. In contrast, the nonlocal differential conductance reveals only the extended states, such that the bulk gap closing and reopening is well visible, see Fig. 1.8b. We test the MBS stability with another stronger disorder configuration, see Fig 1.8c. The MBS is still visible, but its differential conductance deviates from the perfect quantization. Moreover, the nonlocal differential conductance is slightly suppressed, and

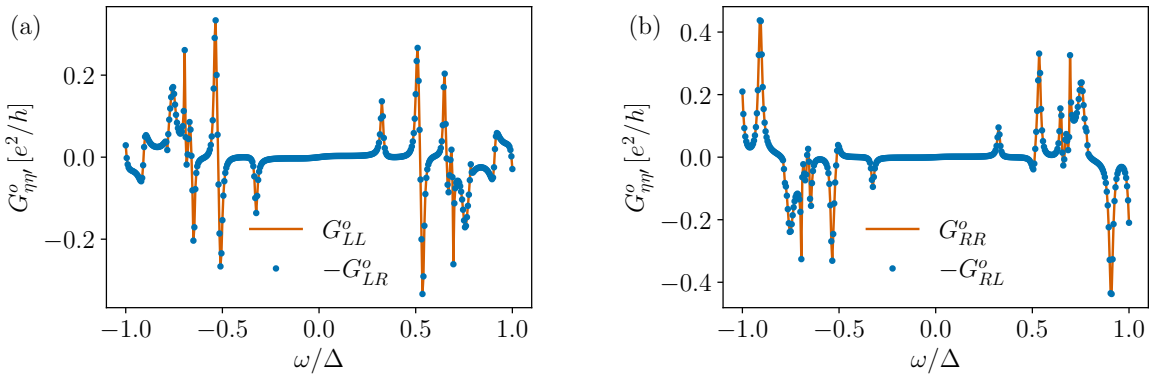

Figure 1.7: *Symmetry relations of local and nonlocal differential conductance*: (a) [(b)] The antisymmetric part of the local differential conductance G^o_{LL} [G^o_{RR}], shown as the red solid line, is equal to the negative of the antisymmetric part of the nonlocal differential conductance G^o_{LR} [G^o_{RL}] shown by the blue dots. The chosen parameters are $a = 5$ nm, $\alpha_L = 2$ meV, $\Delta = 0.25$ meV, $N = 700 + N_{B,L} + N_{B,R}$, $t = 102$ meV, $\mu = 0.6$ meV, $\mu_{\text{Lead}} = 25$ meV, $\gamma_L = \gamma_R = 10$ meV, $N_{B,L} = N_{B,R} = 4$, $\kappa = \Delta$. These calculations are done for the temperature $T = 0$ K.

the closing and reopening signature is less clear. In particular, the gap does not close at a single value of the Zeeman field; instead, there is a range of Zeeman energies at which the system is gapless, roughly from $\Delta_Z = 2\Delta$ to $\Delta_Z = 3\Delta$. This calculation illustrates to some extent the topological protection of the MBSs: the chosen disorder does not break the symmetry of class D (PHS) and consequently, the disorder does not remove the MBSs. This statement, however, is oversimplified since sufficiently strong disorder can close the superconducting gap and drive the system into the trivial phase. In this regime, the nonlocal differential conductance is strongly suppressed since strong disorder causes a localization of the originally extended states [161].

1.5 Yu-Shiba-Rusinov states

In the previous section, we introduced ABSs, however, other mechanisms than Andreev reflection can also lead to subgap states in superconductors. A magnetic impurity, for example, does not obey the Anderson theorem [117], locally suppresses the superconducting order parameter, and gives rise to a subgap state, the so-called Yu-Shiba-Rusinov [165–168] (YSR) state. The physics of this system is described via the Hamiltonian [166]

$$H_{YSR} = \int \Psi^\dagger(\mathbf{r}) \left[\left(-\frac{\hbar^2}{2m}\boldsymbol{\nabla}^2_{\mathbf{r}} - \mu \right) \tau^z + J\delta(\mathbf{r}-\mathbf{r}_0)\boldsymbol{\sigma}\cdot\mathbf{S} + \Delta\tau^x \right] \Psi(\mathbf{r})\mathrm{d}r, \tag{1.35}$$

which is written in the basis presented in Eq. (1.22). Here we replaced the original one-dimensional coordinate x, used in Eq. (1.21), with the spatial coordinate $\mathbf{r}$,

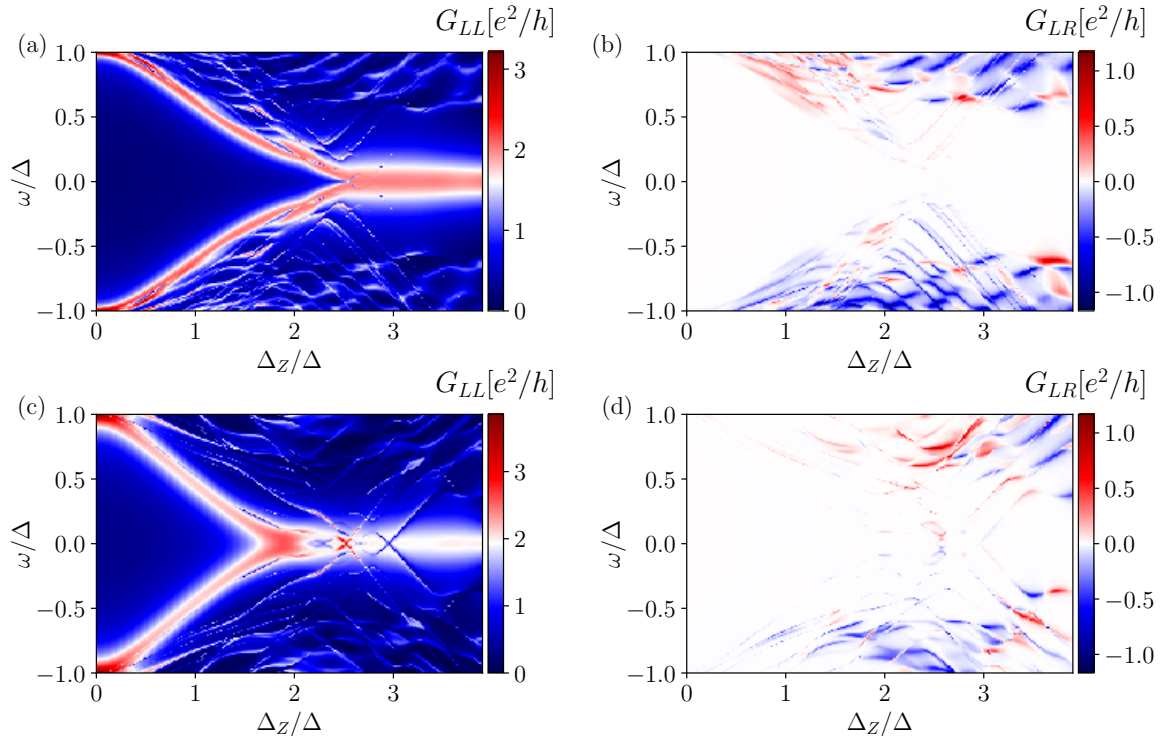

Figure 1.8: *Local and nonlocal differential conductance in the presence of disorder as a function of the Zeeman field strength Δ_Z and the energy ω*: (a,c) local differential conductance G_{LL} (b,d) nonlocal differential conductance G_{LR}. The local differential conductance elements reveal the closing and reopening of the superconducting gap as a function of the Zeeman energy. Moreover, in the topological phase, the MBSs are visible as ZBPs with a differential conductance maximum close to $2e^2/h$ at $\omega = 0$. In contrast, the nonlocal differential conductance does not show the MBSs since they are well separated and do not form an extended state that connects the two normal leads. The first row corresponds to moderate disorder $\kappa = 1\Delta$, while the second row corresponds to strong disorder $\kappa = 5\Delta$. The stronger the disorder, the less clear is the closing and reopening of the bulk gap in nonlocal differential conductance. The chosen parameters are $a = 5$ nm, $\alpha_L = 2$ meV, $\Delta = 0.25$ meV, $N = 700 + N_{B,L} + N_{B,R}$, $t = 102$ meV, $\mu = 0.6$ meV, $\mu_{\text{Lead}} = 25$ meV, $\gamma_L = \gamma_R = 10$ meV, and $N_{B,L} = N_{B,R} = 4$. These calculations are done for the temperature $T = 0$ K.

which can account for different dimensions of the system. Additionally $\mathbf{r}_0$ denotes the position of the impurity and J denotes the exchange coupling strength between the classical magnetic moment of the magnetic impurity and the spin of the itinerant electrons.

In the classical limit $\mathbf{S} \gg 1$, the energy of this YSR state can be calculated via the

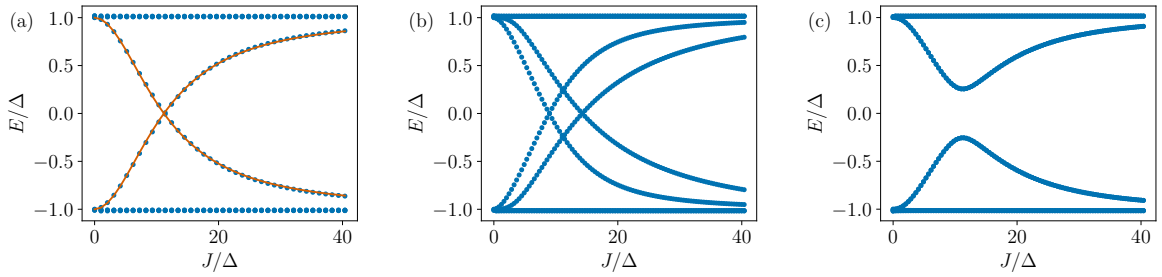

Figure 1.9: *YSR state energies in a one-dimensional system as a function of the exchange coupling*: (a) energy of a YSR state associated with a single magnetic impurity. The analytic solution (red solid line) for the impurity-induced subgap state [Eq. (1.36)] agrees well with the numerical result (blue circular markers). (b) If two magnetic impurities are ferromagnetically aligned, then the two associated YSR states hybridize and split in energy. (c) In contrast, if the two magnetic impurities have an antiferromagnetic ordering, then the energies of the two subgap states are degenerate. For the numerical calculation, we use the tight-binding model presented in Eq. (1.27) with $a = 1$, $\Delta = 0.08$, $N = 200$, $\alpha_L = 0$, $t = 1$, and $\mu = 0.2$. Moreover, in panel (a), we set $\Delta_{Z,n} = J\delta_{n,n_{\mathrm{Imp}}}$ with the Kronecker delta δ_{n_1,n_2} and the impurity position $n_{\mathrm{Imp}} = 100$. Similar, we chose $\Delta_{Z,n} = J\delta_{n,n_{\mathrm{Imp}}} + [-]J\delta_{n,n_{\mathrm{Imp}}+d_I}$ in (b) [(c)], where d_I denotes the distance between the two impurities, which is set to $d_I = 12$. Additionally, we chose $n_{\mathrm{Imp}} = 94$ in panels (b) and (c).

T-matrix formalism and is approximately given by

$$E_{YSR} = \pm\Delta\frac{1-\gamma^2}{1+\gamma^2}, \tag{1.36}$$

where $\gamma = \pi v_0 J|\mathbf{S}|$ [166]. Here, v_0 denotes the density of states of the normal (not superconducting) system at the Fermi energy [169]. In the absence of an exchange coupling, there is no subgap state, however, a small but finite exchange coupling introduces a subgap state close to the gap edge. The energy of this state decreases with increasing exchange coupling and crosses zero energy at $\gamma = \pm 1$, as shown in Fig. 1.9a for a one-dimensional system. This zero-energy crossing is accompanied by a quantum phase transition [170], during which the spin quantum number of the ground state changes from 0 to $1/2$ since the magnetic impurity binds a quasiparticle [170–174]. Moreover, self-consistent calculations of the superconducting gap show a sign change of the superconducting order parameter at the position of the impurity [169, 175, 176].

The electron and hole component $\Psi_\pm$ of the wave function of a YSR state are given by

$$\Psi_\pm = \frac{1}{\sqrt{N\pi k_F r}}\sin\left(k_F r - \frac{\pi}{4} + \delta^\pm\right)e^{-\Delta\sin\left(\delta^+-\delta^-\right)r/(\hbar v_F)} \tag{1.37}$$

in two dimensions and by

$$\Psi_{\pm} = \frac{1}{\sqrt{N}k_F r} \sin\left(k_F r + \delta^{\pm}\right) e^{-\Delta \sin\left(\delta^{+} - \delta^{-}\right) r/(\hbar v_F)} \tag{1.38}$$

in three dimensions [167, 177]. Here, k_F and v_F denote the Fermi momentum and Fermi velocity, respectively. Moreover, r denotes the distance from the impurity, N is a normalization factor, and

$$\tan\left(\delta^{\pm}\right) = \mu_0 v_0 \pm v_0 JS/2, \tag{1.39}$$

where μ_0 is an additional non-magnetic potential of the impurity. The main difference is given by the $1/r$ vs. the $1/\sqrt{r}$ decay.

If two impurities with the same direction of magnetic moments are placed close to each other, then the two YSR states might overlap and form a bonding and antibonding state such that their energy splits similar to the energies of overlapping states in a double quantum dot [178], see Fig. 1.9b. In general, the energy splitting is a function of the relative orientation of the two magnetic moments and the distance between the impurities [179, 180]. For example, if the magnetic moments are aligned antiferromagnetically along the z-axis, then the magnetic impurities trap a spin up and a spin down quasiparticle and the energies of the two subgap states remain degenerate since the quasiparticles differ in the spin quantum number, see Fig. 1.9c. In contrast, every deviation from the antiferromagnetic ordering causes a finite energy splitting, as long as the inter-impurity distance is not much larger than the decay length of the YSR wave functions [179].

Based on these considerations, an alternative platform for MBSs has been proposed: the one-dimensional impurity chain. More specifically, a one-dimensional array of magnetic impurities deposited on a superconductor gives rise to overlapping YSR states, which form an energy band inside the gap, the so-called Shiba band. This band can support MBSs if the magnetic moments of the impurity adatoms are ferromagnetically aligned and if, in addition, Rashba SOI is present in the superconductor. Alternatively, the magnetic moments can form a spiral, meaning that the spins along the chain rotate in a plane. In the latter case Rashba SOI is not required for the appearance of MBSs [63–76, 181]. In fact, it was shown that a unitary transformation [182] maps the spiral of magnetic moments in one dimension to a constant ferromagnetic impurity chain with Rashba spin orbit interaction. A spiral ordering could be mediated via Rudermann-Kittel-Kasuya-Yosida (RKKY) [183–185] interaction or Dzyaloshinskii–Moriya interaction (DMI) [186, 187]. The former mechanism orders the spins such that the rotation period of the spins is set by π/k_F, where k_F denotes the Fermi momentum. Spin-polarized scanning tunneling microscopy (STM) measurements have already shown ferromagnetic ordering, antiferromagnetic ordering, and helical ordering [188–191]. In general, the alignment of the magnetic moments depends on the element used as the magnetic adatom, the growth direction of the chain, and the distance between adjacent impurities. In the direct comparison of the two platforms, the exchange coupling in the impurity

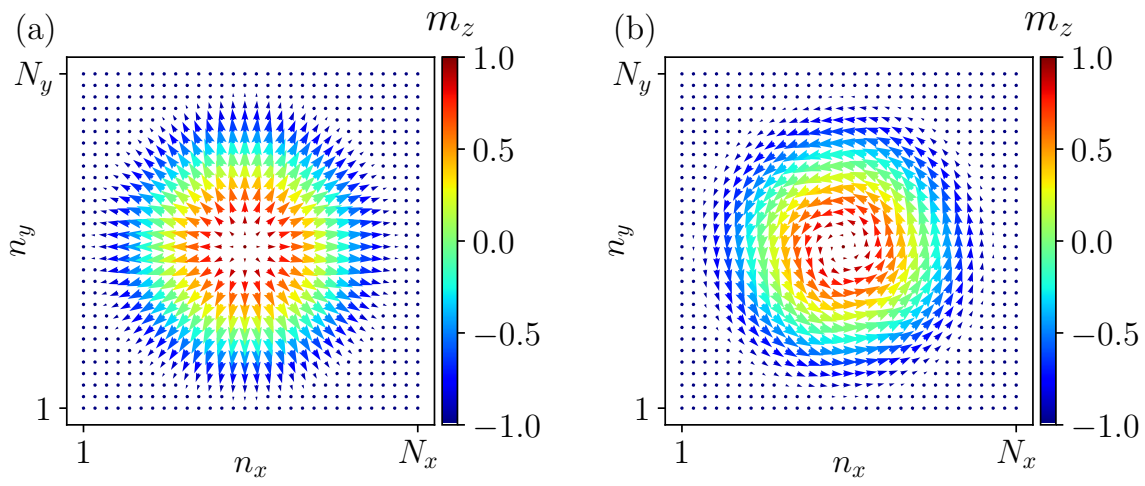

Figure 1.10: *Magnetic texture of a Neel and a Bloch skyrmion*: schematic illustration of (a) [(b)] a Neel [Bloch] skyrmion embedded in a ferromagnetic background. The arrows indicate the in-plane component of the normalized vector $\mathbf{m}(\mathbf{r})$, while the color code indicates the out-of-plane component. Here, we used a lattice of $N_x \times N_y = 30 \times 30$ sites in x and y-direction, respectively. The skyrmion radius is set to 14 sites.

chain plays a similar role as the external Zeeman field in the Rashba nanowire. The fixed exchange coupling strength of the magnetic moments, however, reduces the tunability of the system compared to the Rashba nanowire. On the other hand, STM measurements enable the study of the local density of states at arbitrary positions, while the differential conductance measurements in the Rashba nanowire only provide local information at the fixed positions of the leads. Moreover, the single atom manipulation technique [192–196] enables building magnetic chains atom by atom such that the level of disorder is strongly reduced. To date, various experiments have reported zero-energy modes at the ends of atomic chains [77, 197, 198]. However, there is still no clear evidence that these features originate from MBSs, since trivial mechanisms might cause similar signatures.

1.6 Skyrmions

In the previous section, we discussed the formation of helical spin chains based on RKKY interaction or DMI. DMI, which is also called anisotropic exchange interaction, is described by the term $\mathbf{D} \cdot \mathbf{S}_n \times \mathbf{S}_m$, where $\mathbf{D}$ is the DMI vector. In general, DMI can locally tilt the magnetization such that the ground state of a magnetic texture is neither ferromagnetic nor antiferromagnetic. In fact, DMI can mediate the formation of magnetic quasiparticles like skyrmions [93–96]. In Fig. 1.10, we show the magnetic textures of a Néel skyrmion [199] and a Bloch skyrmion [200] with a ferromagnetic background in a two-dimensional magnet. If the magnetic texture

of such a simple skyrmion is mapped on the unit sphere, then it wraps one time around this sphere, in contrast to a ferromagnetic texture. Based on these considerations, one can define a real space topological invariant Q_S, also called topological charge

$$Q_S = \frac{1}{4\pi} \int_{\mathbf{A}} \mathbf{m}(\mathbf{r}) \cdot \left[\frac{\partial \mathbf{m}(\mathbf{r})}{\partial r} \times \frac{\partial \mathbf{m}(\mathbf{r})}{\partial \varphi} \right] \mathrm{d}\mathbf{A}. \tag{1.40}$$

Here $\mathbf{m}(\mathbf{r}) = \mathbf{S}(\mathbf{r})/|\mathbf{S}(\mathbf{r})|$ is the normalized magnetization at the coordinate $\mathbf{r} = \begin{bmatrix} r\cos(\varphi) & r\sin(\varphi) \end{bmatrix}$ with r and φ the usual polar coordinates [97]. Moreover, $\mathbf{A}$ denotes the surface over which the integration runs. We note that the topological charge is related to the Chern number, which serves as a topological invariant for some classes of topological insulators and superconductors [201, 202]. As an example, we can calculate the topological charge for axially symmetric magnetic textures, as modeled by

$$\mathbf{m}(\mathbf{r}) = \begin{pmatrix} \sin[\mathbf{\Theta}(\mathbf{r})]\cos[\mathbf{\Phi}(\mathbf{r})] & \sin[\mathbf{\Theta}(\mathbf{r})]\sin[\mathbf{\Phi}(\mathbf{r})] & \cos[\mathbf{\Theta}(\mathbf{r})] \end{pmatrix}, \tag{1.41}$$

where the angle $\mathbf{\Theta}(\mathbf{r})$ $[\mathbf{\Phi}(\mathbf{r})]$ is independent of the polar coordinate φ $[r = |\mathbf{r}|]$. Inserting this expression of the local magnetization into the definition of the topological charge yields [97]

$$Q_S = -\frac{1}{4\pi} [\mathbf{\Phi}(\varphi)]_{\varphi=0}^{\varphi=2\pi} [\cos\{\mathbf{\Theta}(r)\}]_{r=0}^{r=\infty}. \tag{1.42}$$

The choices $\mathbf{\Theta}(r) = \pi\tanh(r)$ and $\mathbf{\Phi}(\varphi) = \varphi + \varphi_0$, where φ_0 is a constant, can parametrize both the Néel and the Bloch skyrmion and yield $Q_S = -1$. We can easily flip the sign of the topological charge by changing $\mathbf{\Phi}(\varphi) \to -\varphi + \varphi_0$. In contrast, a ferromagnet with magnetization in z-direction, as described via $\mathbf{\Theta}(r) = 0$, has a vanishing topological charge $Q_S = 0$.

The real-space topology, which guarantees the stability of the skyrmion, in combination with manipulation techniques that provide great control, makes skyrmions attractive for new types of computer hardware. For instance, skyrmions could be used to build future racetrack memories [98, 203–209]. Moreover, magnetic quasiparticles are considered as an alternative potential platform for MBSs. A simple skyrmion with $Q_S = \pm 1$ proximitized by a superconductor can usually not host an MBS [210], except if the skyrmion is coupled to a superconducting vortex [211]. Such a combined structure [212–216] has the advantage over simple vortices that it can be moved via the usual skyrmion manipulation techniques [99–101] and, therefore, it enables in principle real space braiding of MBSs [217]. Alternatively, elongated skyrmions [218] or skyrmions with multiple windings [210, 211] can support the formation of MBSs without the need for vortices. Therefore, skyrmions are not only interesting magnetic quasiparticles with a real-space topology, but they are also potential building blocks of future technologies.

Bibliography

[1] K. v. Klitzing, G. Dorda, and M. Pepper. "New Method for High-Accuracy Determination of the Fine-Structure Constant Based on Quantized Hall Resistance". In: Phys. Rev. Lett. 45 (6 Aug. 1980), pp. 494–497.

[2] D. J. Thouless et al. "Quantized Hall Conductance in a Two-Dimensional Periodic Potential". In: Phys. Rev. Lett. 49 (6 Aug. 1982), pp. 405–408.

[3] B. I. Halperin. "Quantized Hall conductance, current-carrying edge states, and the existence of extended states in a two-dimensional disordered potential". In: Phys. Rev. B 25 (4 Feb. 1982), pp. 2185–2190.

[4] R. B. Laughlin. "Quantized Hall conductivity in two dimensions". In: Phys. Rev. B 23 (10 May 1981), pp. 5632–5633.

[5] David J Thouless. "Topological Quantum Numbers in Nonrelativistic Physics". In: (1998).

[6] M. Z. Hasan and C. L. Kane. "Colloquium: Topological insulators". In: Rev. Mod. Phys. 82 (4 Nov. 2010), pp. 3045–3067.

[7] Xiao-Liang Qi and Shou-Cheng Zhang. "Topological insulators and superconductors". In: Rev. Mod. Phys. 83 (4 Oct. 2011), pp. 1057–1110.

[8] Yoichi Ando. "Topological Insulator Materials". In: Journal of the Physical Society of Japan 82.10 (2013), p. 102001.

[9] Mikio Nakahara. "Geometry,Topology and Physics". In: CRC Press (2017).

[10] F. D. M. Haldane. "Model for a Quantum Hall Effect without Landau Levels: Condensed-Matter Realization of the "Parity Anomaly"". In: Phys. Rev. Lett. 61 (18 Oct. 1988), pp. 2015–2018.

[11] Shuichi Murakami, Naoto Nagaosa, and Shou-Cheng Zhang. "Dissipationless Quantum Spin Current at Room Temperature". In: Science 301.5638 (2003), pp. 1348–1351.

[12] Shuichi Murakami, Naoto Nagaosa, and Shou-Cheng Zhang. "Spin-Hall Insulator". In: Phys. Rev. Lett. 93 (15 Oct. 2004), p. 156804.

[13] C. L. Kane and E. J. Mele. "Quantum Spin Hall Effect in Graphene". In: Phys. Rev. Lett. 95 (22 Nov. 2005), p. 226801.

[14] Yoichi Ando and Liang Fu. "Topological Crystalline Insulators and Topological Superconductors: From Concepts to Materials". In: Annual Review of Condensed Matter Physics 6.1 (2015), pp. 361–381.

[15] Masatoshi Sato and Yoichi Ando. "Topological superconductors: a review". In: Reports on Progress in Physics 80.7 (May 2017), p. 076501.

[16] M M Sharma et al. “Comprehensive review on topological superconducting materials and interfaces”. In: Superconductor Science and Technology 35.8 (July 2022), p. 083003.

[17] B. Andrei Bernevig and Shou-Cheng Zhang. “Quantum Spin Hall Effect”. In: Phys. Rev. Lett. 96 (10 Mar. 2006), p. 106802.

[18] Markus König et al. “Quantum Spin Hall Insulator State in HgTe Quantum Wells”. In: Science 318.5851 (2007), pp. 766–770.

[19] Andreas Roth et al. “Nonlocal Transport in the Quantum Spin Hall State”. In: Science 325.5938 (2009), pp. 294–297.

[20] Liang Fu and C. L. Kane. “Topological insulators with inversion symmetry”. In: Phys. Rev. B 76 (4 July 2007), p. 045302.

[21] Liang Fu, C. L. Kane, and E. J. Mele. “Topological Insulators in Three Dimensions”. In: Phys. Rev. Lett. 98 (10 Mar. 2007), p. 106803.

[22] J. E. Moore and L. Balents. “Topological invariants of time-reversal-invariant band structures”. In: Phys. Rev. B 75 (12 Mar. 2007), p. 121306.

[23] Xiao-Liang Qi, Taylor L. Hughes, and Shou-Cheng Zhang. “Topological field theory of time-reversal invariant insulators”. In: Phys. Rev. B 78 (19 Nov. 2008), p. 195424.

[24] D. Hsieh et al. “A topological Dirac insulator in a quantum spin Hall phase”. In: Nature 452.7190 (2008), pp. 970–974.

[25] Y. L. Chen et al. “Experimental Realization of a Three-Dimensional Topological Insulator, Bi¡sub¿2¡/sub¿Te¡sub¿3¡/sub¿”. In: Science 325.5937 (2009), pp. 178–181.

[26] Y. Xia et al. “Observation of a large-gap topological-insulator class with a single Dirac cone on the surface”. In: Nature Physics 5.6 (2009), pp. 398–402.

[27] Ettore Majorana. “Teoria simmetrica dell’elettrone e del positrone”. In: Il Nuovo Cimento (1924-1942) 14.4 (1937), pp. 171–184.

[28] G. E. Volovik. “Fermion zero modes on vortices in chiral superconductors”. In: Journal of Experimental and Theoretical Physics Letters 70.9 (1999), pp. 609–614.

[29] N. Read and Dmitry Green. “Paired states of fermions in two dimensions with breaking of parity and time-reversal symmetries and the fractional quantum Hall effect”. In: Phys. Rev. B 61 (15 Apr. 2000), pp. 10267–10297.

[30] D. A. Ivanov. “Non-Abelian Statistics of Half-Quantum Vortices in p-Wave Superconductors”. In: Phys. Rev. Lett. 86 (2 Jan. 2001), pp. 268–271.

[31] Kristofer Björnson and Annica M. Black-Schaffer. “Probing vortex Majorana fermions and topology in semiconductor/superconductor heterostructures”. In: Phys. Rev. B 91 (21 June 2015), p. 214514.

[32] C. W. J. Beenakker. “Search for non-Abelian Majorana braiding statistics in superconductors”. In: SciPost Phys. Lect. Notes (2020), p. 15.

[33] Jason Alicea. "New directions in the pursuit of Majorana fermions in solid state systems". In: Reports on Progress in Physics 75.7 (June 2012), p. 076501.

[34] A Yu Kitaev. "Unpaired Majorana fermions in quantum wires". In: Phys. Usp. 44.10S (Oct. 2001), pp. 131–136.

[35] Martin Leijnse and Karsten Flensberg. "Parity qubits and poor man's Majorana bound states in double quantum dots". In: Phys. Rev. B 86 (13 Oct. 2012), p. 134528.

[36] Athanasios Tsintzis, Rubén Seoane Souto, and Martin Leijnse. "Creating and detecting poor man's Majorana bound states in interacting quantum dots". In: Phys. Rev. B 106 (20 Nov. 2022), p. L201404.

[37] Tom Dvir et al. "Realization of a minimal Kitaev chain in coupled quantum dots". In: Nature 614.7948 (2023), pp. 445–450.

[38] Roman M. Lutchyn, Jay D. Sau, and S. Das Sarma. "Majorana Fermions and a Topological Phase Transition in Semiconductor-Superconductor Heterostructures". In: Phys. Rev. Lett. 105 (7 Aug. 2010), p. 077001.

[39] Yuval Oreg, Gil Refael, and Felix von Oppen. "Helical Liquids and Majorana Bound States in Quantum Wires". In: Phys. Rev. Lett. 105 (17 Oct. 2010), p. 177002.

[40] V. Mourik et al. "Signatures of Majorana Fermions in Hybrid Superconductor-Semiconductor Nanowire Devices". In: Science 336.6084 (2012), pp. 1003–1007.

[41] Satoshi Sasaki et al. "Topological Superconductivity in $\mathrm{Cu}_x\mathrm{Bi}_2\mathrm{Se}_3$". In: Phys. Rev. Lett. 107 (21 Nov. 2011), p. 217001.

[42] M. T. Deng et al. "Anomalous Zero-Bias Conductance Peak in a Nb–InSb Nanowire–Nb Hybrid Device". In: Nano Lett. 12 (12 Dec. 2012), pp. 6412–6419.

[43] Anindya Das et al. "Zero-bias peaks and splitting in an Al–InAs nanowire topological superconductor as a signature of Majorana fermions". In: Nat. Phys. 8 (12 2012), pp. 887–895.

[44] H. O. H. Churchill et al. "Superconductor-nanowire devices from tunneling to the multichannel regime: Zero-bias oscillations and magnetoconductance crossover". In: Phys. Rev. B 87 (24 June 2013), p. 241401.

[45] S. M. Albrecht et al. "Exponential protection of zero modes in Majorana islands". In: Nature 531.7593 (2016), pp. 206–209.

[46] G. Kells, D. Meidan, and P. W. Brouwer. "Near-zero-energy end states in topologically trivial spin-orbit coupled superconducting nanowires with a smooth confinement". In: Phys. Rev. B 86 (10 Sept. 2012), p. 100503.

[47] Shuo Mi et al. "X-shaped and Y-shaped Andreev resonance profiles in a superconducting quantum dot". In: Journal of Experimental and Theoretical Physics 119.6 (2014), pp. 1018–1027.

[48] Jorge Cayao et al. “SNS junctions in nanowires with spin-orbit coupling: Role of confinement and helicity on the subgap spectrum”. In: Phys. Rev. B 91 (2 Jan. 2015), p. 024514.

[49] Chun-Xiao Liu et al. “Andreev bound states versus Majorana bound states in quantum dot-nanowire-superconductor hybrid structures: Trivial versus topological zero-bias conductance peaks”. In: Phys. Rev. B 96 (7 Aug. 2017), p. 075161.

[50] Christopher Reeg et al. “Zero-energy Andreev bound states from quantum dots in proximitized Rashba nanowires”. In: Phys. Rev. B 98 (24 Dec. 2018), p. 245407.

[51] Fernando Peñaranda et al. “Quantifying wave-function overlaps in inhomogeneous Majorana nanowires”. In: Phys. Rev. B 98 (23 Dec. 2018), p. 235406.

[52] Adriaan Vuik et al. “Reproducing topological properties with quasi-Majorana states”. In: SciPost Phys. 7 (2019), p. 061.

[53] Oladunjoye A. Awoga, Jorge Cayao, and Annica M. Black-Schaffer. “Supercurrent Detection of Topologically Trivial Zero-Energy States in Nanowire Junctions”. In: Phys. Rev. Lett. 123 (11 Sept. 2019), p. 117001.

[54] Elsa Prada et al. “From Andreev to Majorana bound states in hybrid superconductor–semiconductor nanowires”. In: Nature Reviews Physics 2.10 (2020), pp. 575–594.

[55] S. Das Sarma, Jay D. Sau, and Tudor D. Stanescu. “Splitting of the zero-bias conductance peak as smoking gun evidence for the existence of the Majorana mode in a superconductor-semiconductor nanowire”. In: Phys. Rev. B 86 (22 Dec. 2012), p. 220506.

[56] K. T. Law, Patrick A. Lee, and T. K. Ng. “Majorana Fermion Induced Resonant Andreev Reflection”. In: Phys. Rev. Lett. 103 (23 Dec. 2009), p. 237001.

[57] P. Yu et al. “Non-Majorana states yield nearly quantized conductance in proximatized nanowires”. In: Nature Physics 17.4 (2021), pp. 482–488.

[58] Zhan Cao et al. “Decays of Majorana or Andreev Oscillations Induced by Steplike Spin-Orbit Coupling”. In: Phys. Rev. Lett. 122 (14 Apr. 2019), p. 147701.

[59] Haining Pan et al. “Generic quantized zero-bias conductance peaks in superconductor-semiconductor hybrid structures”. In: Phys. Rev. B 101 (2 Jan. 2020), p. 024506.

[60] Haining Pan, Jay Deep Sau, and Sankar Das Sarma. “Random matrix theory for the robustness, quantization, and end-to-end correlation of zero-bias conductance peaks in a class D ensemble”. In: Phys. Rev. B 106 (11 Sept. 2022), p. 115413.

[61] D. Puglia et al. “Closing of the induced gap in a hybrid superconductor-semiconductor nanowire”. In: Phys. Rev. B 103 (23 June 2021), p. 235201.

[62] Morteza Aghaee et al. “InAs-Al hybrid devices passing the topological gap protocol”. In: Phys. Rev. B 107 (24 June 2023), p. 245423.

[63] T.-P. Choy et al. "Majorana fermions emerging from magnetic nanoparticles on a superconductor without spin-orbit coupling". In: Phys. Rev. B 84 (19 Nov. 2011), p. 195442.

[64] Falko Pientka, Leonid I. Glazman, and Felix von Oppen. "Topological superconducting phase in helical Shiba chains". In: Phys. Rev. B 88 (15 Oct. 2013), p. 155420.

[65] Ivar Martin and Alberto F. Morpurgo. "Majorana fermions in superconducting helical magnets". In: Phys. Rev. B 85 (14 Apr. 2012), p. 144505.

[66] Jelena Klinovaja et al. "Topological Superconductivity and Majorana Fermions in RKKY Systems". In: Phys. Rev. Lett. 111 (18 Nov. 2013), p. 186805.

[67] Bernd Braunecker and Pascal Simon. "Interplay between Classical Magnetic Moments and Superconductivity in Quantum One-Dimensional Conductors: Toward a Self-Sustained Topological Majorana Phase". In: Phys. Rev. Lett. 111 (14 Oct. 2013), p. 147202.

[68] S. Nadj-Perge et al. "Proposal for realizing Majorana fermions in chains of magnetic atoms on a superconductor". In: Phys. Rev. B 88 (2 July 2013), p. 020407.

[69] M. M. Vazifeh and M. Franz. "Self-Organized Topological State with Majorana Fermions". In: Phys. Rev. Lett. 111 (20 Nov. 2013), p. 206802.

[70] Andreas Heimes, Panagiotis Kotetes, and Gerd Schön. "Majorana fermions from Shiba states in an antiferromagnetic chain on top of a superconductor". In: Phys. Rev. B 90 (6 Aug. 2014), p. 060507.

[71] Hoi-Yin Hui et al. "Majorana fermions in ferromagnetic chains on the surface of bulk spin-orbit coupled s-wave superconductors". In: Scientific Reports 5.1 (2015), p. 8880.

[72] Falko Pientka, Leonid I. Glazman, and Felix von Oppen. "Unconventional topological phase transitions in helical Shiba chains". In: Phys. Rev. B 89 (18 May 2014), p. 180505.

[73] I. Reis, D. J. J. Marchand, and M. Franz. "Self-organized topological state in a magnetic chain on the surface of a superconductor". In: Phys. Rev. B 90 (8 Aug. 2014), p. 085124.

[74] Yang Peng et al. "Strong Localization of Majorana End States in Chains of Magnetic Adatoms". In: Phys. Rev. Lett. 114 (10 Mar. 2015), p. 106801.

[75] Andreas Heimes, Daniel Mendler, and Panagiotis Kotetes. "Interplay of topological phases in magnetic adatom-chains on top of a Rashba superconducting surface". In: New Journal of Physics 17.2 (Feb. 2015), p. 023051.

[76] Andreas Theiler, Kristofer Björnson, and Annica M. Black-Schaffer. "Majorana bound state localization and energy oscillations for magnetic impurity chains on conventional superconductors". In: Phys. Rev. B 100 (21 Dec. 2019), p. 214504.

[77] Stevan Nadj-Perge et al. “Observation of Majorana fermions in ferromagnetic atomic chains on a superconductor”. In: Science 346.6209 (2014), pp. 602–607.

[78] Michael Ruby et al. “End States and Subgap Structure in Proximity-Coupled Chains of Magnetic Adatoms”. In: Phys. Rev. Lett. 115 (19 Nov. 2015), p. 197204.

[79] Rémy Pawlak et al. “Probing atomic structure and Majorana wavefunctions in mono-atomic Fe chains on superconducting Pb surface”. In: npj Quantum Information 2.1 (2016), p. 16035.

[80] Lucas Schneider et al. “Precursors of Majorana modes and their length-dependent energy oscillations probed at both ends of atomic Shiba chains”. In: Nature Nanotechnology 17.4 (2022), pp. 384–389.

[81] B.D. Josephson. “Possible new effects in superconductive tunnelling”. In: Physics Letters 1.7 (1962), pp. 251–253.

[82] Falko Pientka et al. “Topological Superconductivity in a Planar Josephson Junction”. In: Phys. Rev. X 7 (2 May 2017), p. 021032.

[83] Michael Hell, Martin Leijnse, and Karsten Flensberg. “Two-Dimensional Platform for Networks of Majorana Bound States”. In: Phys. Rev. Lett. 118 (10 Mar. 2017), p. 107701.

[84] F. Setiawan, Ady Stern, and Erez Berg. “Topological superconductivity in planar Josephson junctions: Narrowing down to the nanowire limit”. In: Phys. Rev. B 99 (22 June 2019), p. 220506.

[85] Benedikt Scharf et al. “Tuning topological superconductivity in phase-controlled Josephson junctions with Rashba and Dresselhaus spin-orbit coupling”. In: Phys. Rev. B 99 (21 June 2019), p. 214503.

[86] André Melo, Sebastian Rubbert, and Anton R. Akhmerov. “Supercurrent-induced Majorana bound states in a planar geometry”. In: SciPost Phys. 7 (2019), p. 039.

[87] Melina Luethi et al. “Planar Josephson junctions in germanium: Effect of cubic spin-orbit interaction”. In: Phys. Rev. B 107 (3 Jan. 2023), p. 035435.

[88] Masatoshi Sato, Yoshiro Takahashi, and Satoshi Fujimoto. “Non-Abelian Topological Order in s-Wave Superfluids of Ultracold Fermionic Atoms”. In: Phys. Rev. Lett. 103 (2 July 2009), p. 020401.

[89] Omri Lesser, Yuval Oreg, and Ady Stern. “One-dimensional topological superconductivity based entirely on phase control”. In: Phys. Rev. B 106 (24 Dec. 2022), p. L241405.

[90] Melina Luethi et al. “Majorana Bound States in Germanium Josephson Junctions via Phase Control”. In: arXiv:2304.12689 (2023).

[91] D. C. Tsui, H. L. Stormer, and A. C. Gossard. “Two-Dimensional Magnetotransport in the Extreme Quantum Limit”. In: Phys. Rev. Lett. 48 (22 May 1982), pp. 1559–1562.

[92] X. G. Wen and Q. Niu. "Ground-state degeneracy of the fractional quantum Hall states in the presence of a random potential and on high-genus Riemann surfaces". In: Phys. Rev. B 41 (13 May 1990), pp. 9377–9396.

[93] A. Neubauer et al. "Topological Hall Effect in the A Phase of MnSi". In: Phys. Rev. Lett. 102 (18 May 2009), p. 186602.

[94] K. Everschor-Sitte et al. "Perspective: Magnetic skyrmions - Overview of recent progress in an active research field". In: Journal of Applied Physics 124.24 (2018). Cited by: 329; All Open Access, Bronze Open Access.

[95] C Back et al. "The 2020 skyrmionics roadmap". In: Journal of Physics D: Applied Physics 53.36 (June 2020), p. 363001.

[96] Kang Wang et al. "Fundamental physics and applications of skyrmions: A review". In: Journal of Magnetism and Magnetic Materials 563 (2022), p. 169905.

[97] Yoshinori Tokura and Naoya Kanazawa. "Magnetic Skyrmion Materials". In: Chemical Reviews 121.5 (Mar. 2021), pp. 2857–2897.

[98] Albert Fert, Vincent Cros, and João Sampaio. "Skyrmions on the track". In: Nature Nanotechnology 8.3 (2013), pp. 152–156.

[99] S. L. Zhang et al. "Manipulation of skyrmion motion by magnetic field gradients". In: Nature Communications 9.1 (2018), p. 2115.

[100] Arianna Casiraghi et al. "Individual skyrmion manipulation by local magnetic field gradients". In: Communications Physics 2.1 (2019), p. 145.

[101] Koudai Migita, Keisuke Yamada, and Yoshinobu Nakatani. "Controlling skyrmion motion in an angelfish-type racetrack memory by an AC magnetic field". In: Applied Physics Express 13.7 (July 2020), p. 073003.

[102] Xie Chen et al. "Symmetry protected topological orders and the group cohomology of their symmetry group". In: Phys. Rev. B 87 (15 Apr. 2013), p. 155114.

[103] Xiao-Gang Wen. "Symmetry-protected topological invariants of symmetry-protected topological phases of interacting bosons and fermions". In: Phys. Rev. B 89 (3 Jan. 2014), p. 035147.

[104] T. Senthil. "Symmetry-Protected Topological Phases of Quantum Matter". In: Annual Review of Condensed Matter Physics 6.1 (2015), pp. 299–324.

[105] Xiao-Gang Wen. "Colloquium: Zoo of quantum-topological phases of matter". In: Rev. Mod. Phys. 89 (4 Dec. 2017), p. 041004.

[106] LD Landau. "On the theory of phase transitions". In: Zh. Eksp. Teor. Fiz. 7 (1937), pp. 19–32.

[107] V. L. Ginzburg and L. D. Landau. "On the Theory of superconductivity". In: Zh. Eksp. Teor. Fiz. 20 (1950), pp. 1064–1082.

[108] Zhida Song, Zhong Fang, and Chen Fang. "$(d-2)$-Dimensional Edge States of Rotation Symmetry Protected Topological States". In: Phys. Rev. Lett. 119 (24 Dec. 2017), p. 246402.

[109] Josias Langbehn et al. “Reflection-Symmetric Second-Order Topological Insulators and Superconductors”. In: Phys. Rev. Lett. 119 (24 Dec. 2017), p. 246401.

[110] Frank Schindler et al. “Higher-order topological insulators”. In: Science Advances 4.6 (2018), eaat0346.

[111] Yanick Volpez, Daniel Loss, and Jelena Klinovaja. “Second-Order Topological Superconductivity in π-Junction Rashba Layers”. In: Phys. Rev. Lett. 122 (12 Mar. 2019), p. 126402.

[112] Katharina Laubscher, Pim Keizer, and Jelena Klinovaja. “Fractional second-order topological insulator from a three-dimensional coupled-wires construction”. In: Phys. Rev. B 107 (4 Jan. 2023), p. 045409.

[113] Shinsei Ryu et al. “Topological insulators and superconductors: tenfold way and dimensional hierarchy”. In: New Journal of Physics 12.6 (June 2010), p. 065010.

[114] Ching-Kai Chiu et al. “Classification of topological quantum matter with symmetries”. In: Rev. Mod. Phys. 88 (3 Aug. 2016), p. 035005.

[115] B. Andrei Bernevig. Topological Insulators and Topological Superconductors. Princeton: Princeton University Press, 2013.

[116] Hendrik Anthony Kramers. “Théorie générale de la rotation paramagnétique dans les cristaux”. In: Proc. Koninkl. Akad. Wet. (1930), pp. 959–972.

[117] P.W. Anderson. “Theory of dirty superconductors”. In: Journal of Physics and Chemistry of Solids 11.1 (1959), pp. 26–30.

[118] Martin R. Zirnbauer. “Particle–hole symmetries in condensed matter”. In: Journal of Mathematical Physics 62.2 (Feb. 2021), p. 021101.

[119] Pasquale Marra. “Majorana nanowires for topological quantum computation”. In: Journal of Applied Physics 132.23 (Dec. 2022), p. 231101.

[120] Alexander Altland and Martin R. Zirnbauer. “Nonstandard symmetry classes in mesoscopic normal-superconducting hybrid structures”. In: Phys. Rev. B 55 (2 Jan. 1997), pp. 1142–1161.

[121] Timothy H. Hsieh et al. “Topological crystalline insulators in the SnTe material class”. In: Nature Communications 3.1 (2012), p. 982.

[122] Y. Tanaka et al. “Experimental realization of a topological crystalline insulator in SnTe”. In: Nature Physics 8.11 (2012), pp. 800–803.

[123] Ken Shiozaki and Masatoshi Sato. “Topology of crystalline insulators and superconductors”. In: Phys. Rev. B 90 (16 Oct. 2014), p. 165114.

[124] Andreas P Schnyder and Philip M R Brydon. “Topological surface states in nodal superconductors”. In: Journal of Physics: Condensed Matter 27.24 (May 2015), p. 243201.

[125] Qing-Ze Wang and Chao-Xing Liu. “Topological nonsymmorphic crystalline superconductors”. In: Phys. Rev. B 93 (2 Jan. 2016), p. 020505.

[126] Gregory Moore and Nicholas Read. "Nonabelions in the fractional quantum hall effect". In: Nucl. Phys. B 360.2 (1991), pp. 362–396.

[127] Liang Fu and C. L. Kane. "Superconducting Proximity Effect and Majorana Fermions at the Surface of a Topological Insulator". In: Phys. Rev. Lett. 100 (9 Mar. 2008), p. 096407.

[128] Yukio Tanaka, Takehito Yokoyama, and Naoto Nagaosa. "Manipulation of the Majorana Fermion, Andreev Reflection, and Josephson Current on Topological Insulators". In: Phys. Rev. Lett. 103 (10 Sept. 2009), p. 107002.

[129] Chetan Nayak et al. "Non-Abelian anyons and topological quantum computation". In: Rev. Mod. Phys. 80 (3 Sept. 2008), pp. 1083–1159.

[130] Sumanta Tewari and Jay D. Sau. "Topological Invariants for Spin-Orbit Coupled Superconductor Nanowires". In: Phys. Rev. Lett. 109 (15 Oct. 2012), p. 150408.

[131] Y. Maeno et al. "Superconductivity in a layered perovskite without copper". In: Nature 372.6506 (1994), pp. 532–534.

[132] J. A. Duffy et al. "Polarized-Neutron Scattering Study of the Cooper-Pair Moment in Sr_2RuO_4". In: Phys. Rev. Lett. 85 (25 Dec. 2000), pp. 5412–5415.

[133] Andrew Peter Mackenzie and Yoshiteru Maeno. "The superconductivity of Sr_2RuO_4 and the physics of spin-triplet pairing". In: Rev. Mod. Phys. 75 (2 May 2003), pp. 657–712.

[134] H. Murakawa et al. "101Ru Knight Shift Measurement of Superconducting Sr_2RuO_4 under Small Magnetic Fields Parallel to the RuO_2 Plane". In: Journal of the Physical Society of Japan 76.2 (2007), p. 024716.

[135] C Kallin and A J Berlinsky. "Is Sr2RuO4 a chiral p-wave superconductor?" In: Journal of Physics: Condensed Matter 21.16 (Mar. 2009), p. 164210.

[136] Catherine Kallin. "Chiral p-wave order in Sr2RuO4". In: Reports on Progress in Physics 75.4 (Mar. 2012), p. 042501.

[137] Clifford W. Hicks et al. "Strong Increase of T_c of Sr_2RuO_4 Under Both Tensile and Compressive Strain". In: Science 344.6181 (2014), pp. 283–285.

[138] Alexander Steppke et al. "Strong peak in T_c of Sr_2Ru0_4 under uniaxial pressure". In: Science 355.6321 (2017), eaaf9398.

[139] Daniel F. Agterberg. "The symmetry of superconducting Sr2RuO4". In: Nature Physics 17.2 (2021), pp. 169–170.

[140] F. Steglich et al. "Superconductivity in the Presence of Strong Pauli Paramagnetism: $CeCu_2Si_2$". In: Phys. Rev. Lett. 43 (25 Dec. 1979), pp. 1892–1896.

[141] J. G. Bednorz and K. A. Müller. "Possible highTc superconductivity in the Ba-La-Cu-O system". In: Zeitschrift für Physik B Condensed Matter 64.2 (1986), pp. 189–193.

[142] Manfred Sigrist and Kazuo Ueda. "Phenomenological theory of unconventional superconductivity". In: Rev. Mod. Phys. 63 (2 Apr. 1991), pp. 239–311.

[143] Manfred Sigrist. "Introduction to Unconventional Superconductivity". In: AIP Conference Proceedings 789.1 (Sept. 2005), pp. 165–243.

[144] Yu A Bychkov and E I Rashba. "Oscillatory effects and the magnetic susceptibility of carriers in inversion layers". In: Journal of Physics C: Solid State Physics 17.33 (Nov. 1984), p. 6039.

[145] Karsten Flensberg, Felix von Oppen, and Ady Stern. "Engineered platforms for topological superconductivity and Majorana zero modes". In: Nature Reviews Materials 6.10 (2021), pp. 944–958.

[146] Katharina Laubscher and Jelena Klinovaja. "Majorana bound states in semiconducting nanostructures". In: Journal of Applied Physics 130 (8 2021), p. 081101.

[147] B. S. Chandrasekhar. "A Note on the Maximum Critical Field of High-Field Superconductors". In: Applied Physics Letters 1.1 (Dec. 2004), pp. 7–8.

[148] A. M. Clogston. "Upper Limit for the Critical Field in Hard Superconductors". In: Phys. Rev. Lett. 9 (6 Sept. 1962), pp. 266–267.

[149] Kazumi Maki and Toshihiko Tsuneto. "Pauli Paramagnetism and Superconducting State". In: Progress of Theoretical Physics 31.6 (June 1964), pp. 945–956.

[150] Jelena Klinovaja and Daniel Loss. "Composite Majorana fermion wave functions in nanowires". In: Phys. Rev. B 86 (8 Aug. 2012), p. 085408.

[151] Christoph W Groth et al. "Kwant: a software package for quantum transport". In: New Journal of Physics 16.6 (June 2014), p. 063065.

[152] G. E. Blonder, M. Tinkham, and T. M. Klapwijk. "Transition from metallic to tunneling regimes in superconducting microconstrictions: Excess current, charge imbalance, and supercurrent conversion". In: Phys. Rev. B 25 (7 Apr. 1982), pp. 4515–4532.

[153] C. W. J. Beenakker. "Quantum transport in semiconductor-superconductor microjunctions". In: Phys. Rev. B 46 (19 Nov. 1992), pp. 12841–12844.

[154] Benjamin M. Fregoso, Alejandro M. Lobos, and S. Das Sarma. "Electrical detection of topological quantum phase transitions in disordered Majorana nanowires". In: Phys. Rev. B 88 (18 Nov. 2013), p. 180507.

[155] Alejandro M Lobos and S Das Sarma. "Tunneling transport in NSN Majorana junctions across the topological quantum phase transition". In: New Journal of Physics 17.6 (June 2015), p. 065010.

[156] Jeroen Danon et al. "Nonlocal Conductance Spectroscopy of Andreev Bound States: Symmetry Relations and BCS Charges". In: Phys. Rev. Lett. 124 (3 Jan. 2020), p. 036801.

[157] R. Tsu and L. Esaki. "Tunneling in a finite superlattice". In: Applied Physics Letters 22.11 (Oct. 2003), pp. 562–564.

[158] T. Ö. Rosdahl et al. "Andreev rectifier: A nonlocal conductance signature of topological phase transitions". In: Phys. Rev. B 97 (4 Jan. 2018), p. 045421.

[159] Andrea Maiani, Max Geier, and Karsten Flensberg. "Conductance matrix symmetries of multiterminal semiconductor-superconductor devices". In: Phys. Rev. B 106 (10 Sept. 2022), p. 104516.

[160] Diego Rainis et al. "Towards a realistic transport modeling in a superconducting nanowire with Majorana fermions". In: Phys. Rev. B 87 (2 Jan. 2013), p. 024515.

[161] Haining Pan, Jay D. Sau, and S. Das Sarma. "Three-terminal nonlocal conductance in Majorana nanowires: Distinguishing topological and trivial in realistic systems with disorder and inhomogeneous potential". In: Phys. Rev. B 103 (1 Jan. 2021), p. 014513.

[162] Haining Pan and S. Das Sarma. "Disorder effects on Majorana zero modes: Kitaev chain versus semiconductor nanowire". In: Phys. Rev. B 103 (22 June 2021), p. 224505.

[163] Sankar Das Sarma and Haining Pan. "Disorder-induced zero-bias peaks in Majorana nanowires". In: Phys. Rev. B 103 (19 May 2021), p. 195158.

[164] P. W. Anderson. "Absence of Diffusion in Certain Random Lattices". In: Phys. Rev. 109 (5 Mar. 1958), pp. 1492–1505.

[165] L.Yu. "Bound State in Superconductors with Paramagnetic Impurities". In: Acta. Phys. Sin 21 (1965), p. 75.

[166] Hiroyuki Shiba. "Classical Spins in Superconductors". In: Prog. Theor. Phys. 40.3 (Sept. 1968), pp. 435–451.

[167] A I Rusinov. "Superconductivity near a Paramagnetic Impurity". In: JETP Letters 9 (2 Jan. 1969).

[168] A. I. Rusinov. "On the Theory of Gapless Superconductivity in Alloys Containing Paramagnetic Impurities". In: Sov. Phys. JETP 29 (1969), p. 1101.

[169] Tobias Meng et al. "Superconducting gap renormalization around two magnetic impurities: From Shiba to Andreev bound states". In: Phys. Rev. B 92 (6 Aug. 2015), p. 064503.

[170] Akio Sakurai. "Comments on Superconductors with Magnetic Impurities". In: Progress of Theoretical Physics 44.6 (Dec. 1970), pp. 1472–1476.

[171] Michael E. Flatté and Jeff M. Byers. "Local Electronic Structure of a Single Magnetic Impurity in a Superconductor". In: Phys. Rev. Lett. 78 (19 May 1997), pp. 3761–3764.

[172] M. I. Salkola, A. V. Balatsky, and J. R. Schrieffer. "Spectral properties of quasiparticle excitations induced by magnetic moments in superconductors". In: Phys. Rev. B 55 (18 May 1997), pp. 12648–12661.

[173] A. V. Balatsky, I. Vekhter, and Jian-Xin Zhu. "Impurity-induced states in conventional and unconventional superconductors". In: Rev. Mod. Phys. 78 (2 May 2006), pp. 373–433.

[174] Felix von Oppen and Katharina J. Franke. "Yu-Shiba-Rusinov states in real metals". In: Phys. Rev. B 103 (20 May 2021), p. 205424.

[175] Andrzej Ptok, Szczepan Głodzik, and Tadeusz Doma ński. "Yu-Shiba-Rusinov states of impurities in a triangular lattice of $NbSe_2$ with spin-orbit coupling". In: Phys. Rev. B 96 (18 Nov. 2017), p. 184425.

[176] Szczepan Głodzik and Andrzej Ptok. "Quantum Phase Transition Induced by Magnetic Impurity". In: Journal of Superconductivity and Novel Magnetism 31.3 (2018), pp. 647–650.

[177] Gerbold C. Ménard et al. "Coherent long-range magnetic bound states in a superconductor". In: Nature Physics 11.12 (2015), pp. 1013–1016.

[178] Michael E. Flatté and David E. Reynolds. "Local spectrum of a superconductor as a probe of interactions between magnetic impurities". In: Phys. Rev. B 61 (21 June 2000), pp. 14810–14814.

[179] Silas Hoffman et al. "Impurity-induced quantum phase transitions and magnetic order in conventional superconductors: Competition between bound and quasiparticle states". In: Phys. Rev. B 92 (12 Sept. 2015), p. 125422.

[180] Oindrila Deb et al. "Yu-Shiba-Rusinov states and ordering of magnetic impurities near the boundary of a superconducting nanowire". In: Phys. Rev. B 103 (16 Apr. 2021), p. 165403.

[181] Oladunjoye A. Awoga, Kristofer Björnson, and Annica M. Black-Schaffer. "Disorder robustness and protection of Majorana bound states in ferromagnetic chains on conventional superconductors". In: Phys. Rev. B 95 (18 May 2017), p. 184511.

[182] Bernd Braunecker et al. "Spin-selective Peierls transition in interacting one-dimensional conductors with spin-orbit interaction". In: Phys. Rev. B 82 (4 July 2010), p. 045127.

[183] M. A. Ruderman and C. Kittel. "Indirect Exchange Coupling of Nuclear Magnetic Moments by Conduction Electrons". In: Phys. Rev. 96 (1 Oct. 1954), pp. 99–102.

[184] Tadao Kasuya. "A Theory of Metallic Ferro- and Antiferromagnetism on Zener's Model". In: Prog. Theor. Phys. 16.1 (July 1956), pp. 45–57.

[185] Kei Yosida. "Magnetic Properties of Cu-Mn Alloys". In: Phys. Rev. 106 (5 June 1957), pp. 893–898.

[186] I. Dzyaloshinsky. "A thermodynamic theory of "weak" ferromagnetism of antiferromagnetics". In: Journal of Physics and Chemistry of Solids 4.4 (1958), pp. 241–255.

[187] Tôru Moriya. "Anisotropic Superexchange Interaction and Weak Ferromagnetism". In: Phys. Rev. 120 (1 Oct. 1960), pp. 91–98.

[188] Roland Wiesendanger. "Spin mapping at the nanoscale and atomic scale". In: Rev. Mod. Phys. 81 (4 Nov. 2009), pp. 1495–1550.

[189] Oswald Pietzsch and Roland Wiesendanger. "Non-collinear magnetic order in nanostructures investigated by spin-polarized scanning tunneling microscopy". In: Pure and Applied Chemistry 83.11 (2011), pp. 1981–1988.

[190] Manuel Steinbrecher et al. “Non-collinear spin states in bottom-up fabricated atomic chains”. In: Nature Communications 9.1 (2018), p. 2853.

[191] Lucas Schneider et al. “Atomic-scale spin-polarization maps using functionalized superconducting probes”. In: Science Advances 7.4 (2021), eabd7302.

[192] A. Kamlapure et al. “Engineering the spin couplings in atomically crafted spin chains on an elemental superconductor”. In: Nature Communications 9.1 (2018), p. 3253.

[193] Lucas Schneider et al. “Controlling in-gap end states by linking nonmagnetic atoms and artificially-constructed spin chains on superconductors”. In: Nature Communications 11.1 (2020), p. 4707.

[194] Felix Friedrich et al. “Coupling of Yu-Shiba-Rusinov states in one-dimensional chains of Fe atoms on Nb(110)”. In: Phys. Rev. B 103 (23 June 2021), p. 235437.

[195] Felix Küster et al. “Long range and highly tunable interaction between local spins coupled to a superconducting condensate”. In: Nature Communications 12.1 (2021), p. 6722.

[196] Martina O. Soldini et al. “Two-dimensional Shiba lattices as a possible platform for crystalline topological superconductivity”. In: Nature Physics (2023).

[197] Howon Kim et al. “Toward tailoring Majorana bound states in artificially constructed magnetic atom chains on elemental superconductors”. In: Science Advances 4.5 (2018), eaar5251.

[199] Stefan Heinze et al. “Spontaneous atomic-scale magnetic skyrmion lattice in two dimensions”. In: Nature Physics 7.9 (2011), pp. 713–718.

[200] X. Z. Yu et al. “Real-space observation of a two-dimensional skyrmion crystal”. In: Nature 465.7300 (2010), pp. 901–904.

[201] Kristofer Björnson and Annica M. Black-Schaffer. “Skyrmion spin texture in ferromagnetic semiconductor–superconductor heterostructures”. In: Phys. Rev. B 89 (13 Apr. 2014), p. 134518.

[202] Karin Everschor-Sitte and Matthias Sitte. “Real-space Berry phases: Skyrmion soccer (invited)”. In: Journal of Applied Physics 115.17 (Apr. 2014), p. 172602.

[203] Stuart S. P. Parkin, Masamitsu Hayashi, and Luc Thomas. “Magnetic Domain-Wall Racetrack Memory”. In: Science 320.5873 (2008), pp. 190–194.

[204] Kwang-Su Ryu et al. “Chiral spin torque at magnetic domain walls”. In: Nature Nanotechnology 8.7 (2013), pp. 527–533.

[205] Stuart Parkin and See-Hun Yang. “Memory on the racetrack”. In: Nature Nanotechnology 10.3 (2015), pp. 195–198.

[206] X. Z. Yu et al. “Skyrmion flow near room temperature in an ultralow current density”. In: Nature Communications 3.1 (2012), p. 988.

[207] J. Sampaio et al. “Nucleation, stability and current-induced motion of isolated magnetic skyrmions in nanostructures”. In: Nature Nanotechnology 8.11 (2013), pp. 839–844.

[208] R. Tomasello et al. “A strategy for the design of skyrmion racetrack memories”. In: Scientific Reports 4.1 (2014), p. 6784.

[209] Jan Mueller. “Magnetic skyrmions on a two-lane racetrack”. In: New J. Phys. 19 (2017), p. 025002.

[210] Guang Yang et al. “Majorana bound states in magnetic skyrmions”. In: Phys. Rev. B 93 (22 June 2016), p. 224505.

[211] Stefan Rex, Igor V. Gornyi, and Alexander D. Mirlin. “Majorana bound states in magnetic skyrmions imposed onto a superconductor”. In: Phys. Rev. B 100 (6 Aug. 2019), p. 064504.

[212] Kjetil M. D. Hals, Michael Schecter, and Mark S. Rudner. “Composite Topological Excitations in Ferromagnet-Superconductor Heterostructures”. In: Phys. Rev. Lett. 117 (1 June 2016), p. 017001.

[213] J. Baumard et al. “Generation of a superconducting vortex via Néel skyrmions”. In: Phys. Rev. B 99 (1 Jan. 2019), p. 014511.

[214] Samme M. Dahir, Anatoly F. Volkov, and Ilya M. Eremin. “Interaction of Skyrmions and Pearl Vortices in Superconductor-Chiral Ferromagnet Heterostructures”. In: Phys. Rev. Lett. 122 (9 Mar. 2019), p. 097001.

[215] Raıé M. Menezes et al. “Manipulation of magnetic skyrmions by superconducting vortices in ferromagnet-superconductor heterostructures”. In: Phys. Rev. B 100 (1 July 2019), p. 014431.

[216] A. P. Petrovi ć et al. “Skyrmion-(Anti)Vortex Coupling in a Chiral Magnet-Superconductor Heterostructure”. In: Phys. Rev. Lett. 126 (11 Mar. 2021), p. 117205.

[217] Jonas Nothhelfer et al. “Steering Majorana braiding via skyrmion-vortex pairs: A scalable platform”. In: Phys. Rev. B 105 (22 June 2022), p. 224509.

[218] Utkan Güngördü, Shane Sandhoefner, and Alexey A. Kovalev. “Stabilization and control of Majorana bound states with elongated skyrmions”. In: Phys. Rev. B 97 (11 Mar. 2018), p. 115136.

CHAPTER 2

Local and nonlocal quantum transport due to Andreev bound states in finite Rashba nanowires with superconducting and normal sections

Adapted from:
Richard Hess, Henry F. Legg, Daniel Loss, and Jelena Klinovaja,
"Local and nonlocal quantum transport due to Andreev bound states in finite Rashba nanowires with superconducting and normal sections",
Phys. Rev. B **104**, 075405 (2021).

We analyze Andreev bound states (ABSs) that form in normal sections of a Rashba nanowire that is only partially covered by a superconducting layer. These ABSs are localized close to the ends of the superconducting section and can be pinned to zero energy over a wide range of magnetic field strengths even if the nanowire is in the non-topological regime. For finite-size nanowires (typically $\lesssim 1$ μm in current experiments), the ABS localization length is comparable to the length of the nanowire. The probability density of an ABS is therefore non-zero throughout the nanowire and differential-conductance calculations reveal a correlated zero-bias peak (ZBP) at both ends of the nanowire. When a second normal section hosts an additional ABS at the opposite end of the superconducting section, the combination of the two ABSs can mimic the closing and reopening of the bulk gap in local and non-local conductances accompanied by the appearance of the ZBP. These signatures are reminiscent of those expected for Majorana bound states (MBSs) but occur here in the non-topological regime. Our results demonstrate that conductance measurements of correlated ZBPs at the ends of a typical superconducting nanowire or an apparent closing and reopening of the bulk gap in the local and non-local conductance are not conclusive indicators for the presence of MBSs.

2.1 Introduction

Majorana bound states (MBSs) have been of significant interest in condensed matter physics for over two decades, largely due to their potential application as topological qubits [1–7]. The prospective utilization of MBSs in quantum computation stems from their non-Abelian braiding statistics [8–15]. Despite this intense interest there has been no conclusive experimental observation of these exotic properties to date.

The most mature experimental platform expected to host MBSs are Rashba nanowire (see Fig. 2.1), where the key differential-conductance signature associated with MBSs is a zero-bias peak (ZBP) that is stable for a wide range of magnetic field strengths. A ZBP is, however, by itself not a unique fingerprint of MBSs. Previously it was suggested that additional local conductance features can clarify the origin of such a ZBP, namely the quantization of the peak height at $2e^2/h$ [16–20] and oscillations around zero energy that originate from the overlap of the two MBS wave functions at either end of the nanowire [21–25]. The ZBPs and their oscillations have been observed in past experiments [26–32], while quantization of the ZBP has not been observed. Recently it has been suggested [33, 34] that the next generation of Rashba nanowire systems, three-terminal devices, could elucidate whether a given ZBP stems from the presence of MBSs by observing additional auxiliary features in the local and non-local differential conductances. For example, such devices could observe correlations between ZBPs at both ends of the nanowire and the closing and reopening of the bulk-gap that should accompany the transition to topological superconductivity.

Additional signatures of MBSs beyond a simple ZBP are necessary because topologically trivial states such as Andreev bound states (ABSs) [35–42] can generate conductance features similar to those expected from MBSs and therefore strongly challenge the interpretation of experimental observations [42–57]. For instance, it has been shown that the energy of an ABS in a non-topological system can be pinned close to zero over a wide range of magnetic field strengths when a resonance condition for the strength of the spin-orbit interaction (SOI) is fulfilled [48]. In transport experiments, this resonance is broadened by finite temperature and the coupling to external leads. Such ABSs can therefore produce ZBP features in the conductance even in systems that are topologically trivial at all magnetic field strengths. The pinning of trivial ABSs close to zero energy can also originate from smooth parameter profiles of the chemical potential and the superconducting gap [49–51], such that a short section of the nanowire is nominally in the topological regime. Such zero-energy states, observed in the trivial phase of the bulk of the nanowire, are known as quasi-Majorana bound states (quasi-MBSs) and their zero-bias pinning is in fact also stable against changes of SOI strength or tunnel barrier gate voltage.

Previous devices focused on local measurements on a single end of a nanowire. Such measurements can already provide additional indicators that could clarify the origin of a ZBP. One example is the oscillations around zero energy expected due to the hybridization of MBSs at either end of a finite nanowire [21–24]. Such oscillations should have an increasing amplitude when magnetic field strength is

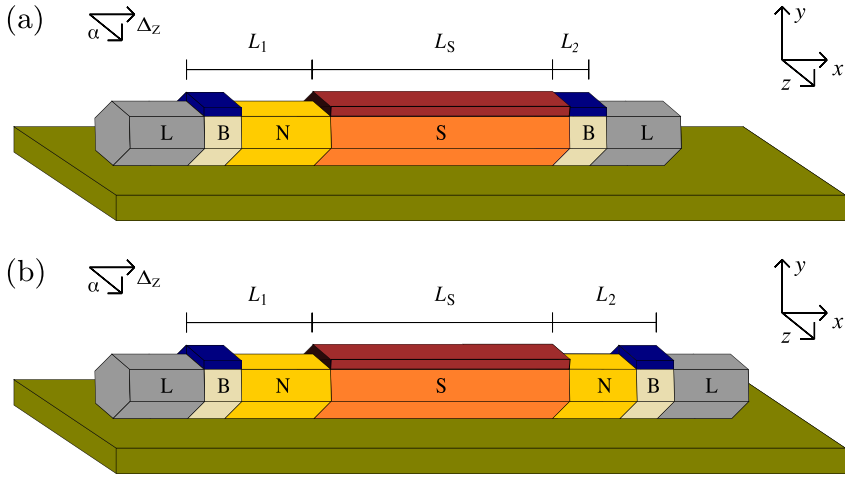

Figure 2.1: Different configurations of a nanowire setup considered in this work: The semiconducting nanowire is aligned along the x-axis. The Rashba vector points in z-direction and the applied magnetic field in x-direction. A grounded s-wave superconductor (dark red) covers a section of length L_S (orange), locally inducing superconductivity via the proximity effect. (a) Only a left section (yellow) or (b) both left and right sections on both ends of length L_1 and L_2 are uncovered by the superconductor and remain normal. Leads (gray) are attached on the left and right end to measure the differential conductance of the system. Tunnel barriers (beige) at the ends of the normal sections can be used to control differential conductance, the height of these tunnel barriers is tuned by local contacts (dark blue).

increased or nanowire length decreased. In contrast to this expectation, several experiments observed oscillations with an amplitude which decays as the magnetic field is increased [31, 58, 59]. Although there are proposed explanations for this behavior such as orbital effects [24] or a step-like profile of the Rashba SOI strength [60], even in such scenarios the parameter window for a decay in the amplitude of oscillations is rather small and therefore the experimentally observed behavior is likely the result of trivial states. In addition, recent theoretical works have shown that even the quantization of a ZBP at one end of the nanowire is not an exclusive property of MBSs [51, 61]. As such, while conductance oscillations and even quantization can provide limited additional evidence for the potential presence of MBSs, they are not sufficient for an unambiguous identification of topologically protected states.

Given the ambiguous origins of previous experimental observations from the single end of a nanowire, in the absence of braiding experiments, further signatures in conductance are necessary to improve the classification of ZBPs in the next generation of Rashba nanowire systems. For instance, this can be achieved by considering non-local correlation properties of MBSs in three-terminal devices [33, 34, 62–68]. MBSs should be localized at the opposite ends of a superconducting Rashba nanowire and therefore conductance measurements on both ends should reveal ZBPs. Furthermore, three-terminal experiments enable the measurement of

non-local conductances which can indicate the bulk-gap closing and reopening and therefore go beyond local properties. Recently, it was highlighted in Ref. [33] that the exponential decay of sub-gap states into the bulk of the nanowire makes the non-local conductance an ideal tool for distinguishing between trivial and topological phases in nanowires which are much longer than the localization length of such sub-gap states. Recent experiments have been performed on three-terminal devices [69–71] but so far did not find clear signatures of MBSs.

In this paper we focus mainly on *non-topological* three-terminal junctions consisting of a partially proximitized Rashba nanowire where the normal sections can host an ABS. We consider normal-superconducting (NS) and normal-superconducting-normal (NSN) junction setups. In contrast to previous works, we examine the case where the ratio between the length of the superconducting section and the localization length of ABSs is small. This regime is of present experimental relevance and the nanowire lengths as well as the superconducting gaps we consider will be comparable to current setups where typical lengths are between 0.4 μm [71] and 1 μm [70]. The nanowire length is limited by the requirement of working in the ballistic regime to avoid disorder effects, which were shown to be harmful for the observation of topological phases. In the short-nanowire regime the wave function of a trivial ABS leaks from one end of the nanowire to the opposite end. When the parameters of the ABS are close to the resonance condition from Ref. [48], the energy of the ABS is pinned close to zero over a wide range of magnetic field strengths. Our calculation of the differential conductance confirms that in such a scenario correlated ZBPs of a trivial origin appear at both ends of the nanowire. We find that the same effect can occur for quasi-MBSs in topological nanowires.

We also examine the consequences of the presence of a second normal section hosting an additional ABS on the other side of the superconducting section. Such NSN junctions with two normal sections are expected to naturally occur in three-terminal devices available experimentally. We find that the appearance of the second ABS can further complicate the interpretation of experimental signatures. Not only is the second ABS also visible in the non-local conductance but the combination of the two ABSs at either end of the nanowire can generate a conductance feature that is reminiscent of the bulk-gap edge undergoing a closing and reopening process that should accompany a topological phase transition.

Our findings show that, while three-terminal devices can potentially provide additional insights into the origins of ZBPs, correlated zero-bias peaks at both ends of superconducting sections of Rashba nanowires and the apparent observation of the closing and reopening of the bulk band gap with increasing magnetic field strength do not suffice as unambiguous additional indicators for the presence of MBSs in nanowires of the lengths used in current experimental devices.

The paper is organized as follows. In Sec. 4.2 we define the model to describe a non-topological and a topological nanowire containing trivial zero-energy ABSs or quasi-MBSs, respectively. In Sec. 2.3, we discuss features in the differential conductance arising due to the presence of a single ABS hosted in the, say, left normal section of a non-topological nanowire. Here we show that as the ratio between the length of the superconducting section and the localization length of the ABS is decreased, the probability density of the ABS on the right side of the nanowire in-

creases and, as a result, the ABS also becomes visible in the local conductance measured at the right end of the nanowire. Moreover, we examine the case of an NSN junction with two normal sections, one at each end of the non-topological proximitized nanowire, and show that this setup can mimic the signatures of a topological phase transition in transport measurements, despite the trivial nature of the ABSs. Section 2.4 focuses on the topological nanowire and addresses features arising due to the presence of quasi-MBSs in the left and right local conductance. It is shown again that if the ratio between the superconducting section and the localization length of the quasi-MBS is small, then correlated zero-bias peaks appear at both ends. Furthermore, we examine the non-local differential conductance via the bulk states undergoing the bulk-gap closing and reopening process when two normal sections at each end of the topological nanowire both host quasi-MBSs. Finally, we discuss the impact of our results on the interpretation of present-day three-terminal experiments in Sec. 5.6. In App. 2.A we describe numerical approaches used to model transport experiments. We compare the conductance pattern of the non-topological nanowire with the conductance pattern of a uniform topological nanowire in App. 2.B. The effect of strong broadening of finite-energy peaks is discussed in App. 2.C. In App. 2.D we study the bulk wave functions of a topological nanowire with quasi-MBSs on both ends. Finally, App. 2.E deals with the conductance pattern of a nanowire hosting quasi-MBSs on the left end and an ABS on the right end.

2.2 Model of the nanowire

We consider a one-dimensional (1D) semiconducting nanowire aligned along the x-direction. The system is subjected to a magnetic field, which is applied parallel to the nanowire axis. This magnetic field results in a Zeeman energy of strength $\Delta_Z(x)$. The nanowire is partially covered by an s-wave superconductor, resulting in a proximity-induced superconducting gap $\Delta(x)$ in a section of length L_S. This grounded superconducting section is centered between a left and a right normal section of length L_1 and L_2, respectively. The Rashba SOI of strength $\alpha(x)$ is position-dependent and the corresponding SOI vector points in the z-direction. The effective 1D lattice Hamiltonian is given by

$$\begin{aligned} H = \sum_{n=1}^{N} \Bigg[& \sum_{\sigma,\sigma'} c^\dagger_{n,\sigma} (\{t_{n+\frac{1}{2}} + t_{n-\frac{1}{2}} - \mu_n + \gamma_n\}\delta_{\sigma\sigma'} + \Delta_{Z,n}\sigma^x_{\sigma\sigma'}) c_{n,\sigma'} \\ & - \left(\sum_{\sigma,\sigma'} c^\dagger_{n,\sigma} \left\{ t_{n+\frac{1}{2}}\delta_{\sigma\sigma'} - i\alpha_{n+\frac{1}{2}}\sigma^z_{\sigma\sigma'} \right\} c_{n+1,\sigma'} + \Delta_n c^\dagger_{n,\downarrow} c^\dagger_{n,\uparrow} + \text{H.c.} \right) \Bigg], \end{aligned} \tag{2.1}$$

where $c^\dagger_{n,\sigma}$ and $c_{n,\sigma}$ creates and annihilates an electron of spin $\sigma = \uparrow, \downarrow$ at the lattice site n, respectively. The total number of sites is given by $N = N_1 + N_S + N_2$, where $N_1 = L_1/a$, $N_2 = L_2/a$, and $N_S = L_S/a$, where a is an effective lattice constant. In addition, t_n and μ_n denote the nearest neighbor tunneling matrix element and the chemical potential, respectively. Furthermore, $\delta_{\sigma\sigma'}$ denotes the Kronecker delta.

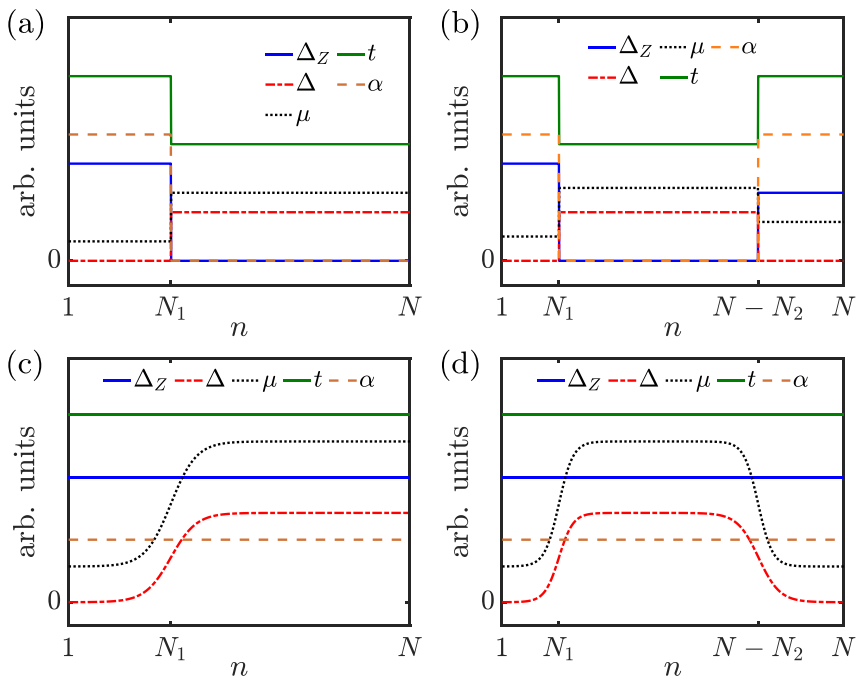

Figure 2.2: Parameter profiles in the nanowire: superconducting gap Δ (dashed-dotted red), chemical potential μ (dotted black), Zeeman energy Δ_Z (solid blue), SOI strength α (dashed orange), and tunneling matrix element t (green) in arbitrary units. Non-topological nanowire (first row): both the SOI and the Zeeman energy are suppressed in the superconducting section. When a resonance condition in the normal part is satisfied, the lowest ABS is pinned to zero energy. Topological nanowire (second row): smooth parameter profiles lead to a zero-energy pinning of the lowest ABS in the topologically trivial bulk-phase. Left column: NS-junction. Right column: NSN-junction.

Normal leads are attached on the left and right ends of the nanowire. The leads are modeled by the same Hamiltonian as the normal sections. The chemical potentials μ_L and μ_R of the left and right normal leads are adjusted to account for a possible difference between lead and nanowire. Additionally, we introduce tunnel barriers between the leads and the nanowire: these barriers of length $L_{B,1}$ and $L_{B,2}$ are constituent parts of the normal sections of length L_1 and L_2, see Fig. 2.1b. The height γ_n of the tunnel barrier at site n is used to control the coupling between the system and the leads; it therefore controls the conductance value. We will focus on two setups, which we refer to as the 'non-topological' and 'topological' nanowire. Both of these systems can host ABSs that are pinned to zero energy, however, the mechanism fixing the ABS energy to zero is different for the two nanowire types. These specific parameter configurations for the non-topological and topological cases are described in Secs. 2.2 and 2.2.

Non-topological nanowire

In this section we specify the profiles of the parameters that enter the Hamiltonian, H, given in Eq. (4.2) for the non-topological nanowire. We define the boundary between the left normal section (N_1) and the superconducting section (S) as $N_b = N_1 + 1/2$ and similarly the boundary between S and the right normal section (N_2) as $N_b' = N_1 + N_S + 1/2$. The non-uniform system parameters entering the Hamiltonian H have the following structures: The tunneling matrix element is defined as

$$t_n = t_1\Theta(N_b - n) + t_S\left[\Theta(n - N_b) - \Theta(n - N_b')\right] + t_2\Theta(n - N_b') \tag{2.2}$$

and is constructed out of the tunneling matrix elements $t_1 = t_2$ in N_1 and N_2 and the tunneling matrix element t_S in S. We define the Heaviside function $\Theta(n)$ with $\Theta(0) = 1/2$ throughout. The difference between the tunneling matrix elements of the superconducting and the normal sections arises due to the mass renormalization inside the superconducting section caused by metallization effects induced by the thin superconducting shell [72–77]. The chemical potential has a similar structure

$$\mu_n = \mu_1\Theta(N_b - n) + \mu_s\left[\Theta(n - N_b) - \Theta(n - N_b')\right] + \mu_2\Theta(n - N_b'), \tag{2.3}$$

where μ_1 and μ_2 denote the chemical potential in the normal sections and μ_S the chemical potential in the superconducting section. Since the magnetic field suppresses the bulk-gap of the parent superconductor, the superconducting gap decreases with increasing Zeeman energy and vanishes at the critical field strength Δ_Z^c:

$$\Delta = \Delta_0\sqrt{1 - (\Delta_Z/\Delta_Z^c)^2}, \tag{2.4}$$

where the maximal value is given by Δ_0. Therefore, the superconducting gap has the following profile

$$\Delta_n = \Delta\left[\Theta(n - N_b) - \Theta(n - N_b')\right]. \tag{2.5}$$

The superconducting gap is zero in N_1 and N_2. In contrast, the Zeeman energy and Rashba SOI are non-zero only in the normal sections and are defined as

$$\Delta_{Z,n} = \Delta_Z\Theta(N_b - n) + \Delta_Z\Theta(n - N_b'), \tag{2.6}$$

$$\alpha_n = \alpha_1\Theta(N_b - n) + \alpha_2\Theta(n - N_b'). \tag{2.7}$$

Here, the SOI strengths α_1 and α_2 could be different [78]. The SOI energy is given by $E_{\mathrm{so},i} = \alpha_i^2/t_i$. In Fig. 2.2 we show examples of the profiles of the superconducting gap, the Zeeman energy, the chemical potential, the tunneling matrix element, and the Rashba SOI strength for an NS and an NSN junction. Tunnel barriers are described by

$$\gamma_n = \gamma_1\Theta(N_{B,b} - n) + \gamma_2\Theta(n - N_{B,b}'), \tag{2.8}$$

where γ_1 and γ_2 denote the height of the left and right tunnel barriers and $N_{B,b} = N_{B,1} + 1/2$ and $N_{B,b}' = N - N_{B,2} + 1/2$ are the positions at which the left tunnel barrier ends and the right tunnel barrier starts, respectively. Here we defined $N_{B,i}$ via $L_{B,i} = N_{B,i}a$. We note that the topological phase cannot be achieved in this setup because the Zeeman energy and the Rashba SOI vanish in the superconducting section. We therefore refer to this system as *non-topological nanowire*.

Topological nanowire

The second system under consideration is a nanowire in which the chemical potential and the superconducting gap change smoothly. These smooth parameter variations can generate an ABS which, as in the non-topological nanowire, sticks to zero energy over a wide range of Zeeman energies in the trivial regime inside the superconducting section [43, 49–51]. In this case, nominally, the system enters the topological phase locally at the short segment between the normal and superconducting sections. However, the length of this segment is much shorter than the localization length of potential MBSs, such that only quasi-MBSs can appear in the spectrum if certain conditions are satisfied. The spatial dependence of parameters is modelled by the function

$$\Omega_\lambda(n, N_i) = 1/2[1 + \tanh(\{n - N_i\}/\lambda)], \tag{2.9}$$

where λ parametrizes the smoothness (see Figs. 2.2c-d). The exact form of the function is not relevant for the appearance of quasi-MBSs rather it is the smoothness itself that determines the presence of quasi-MBSs. The superconducting gap (chemical potential) profile is characterized by the parameter $\lambda_{S,L/R}$ ($\lambda_{L/R}$), which can take different values on the left and the right sides of the nanowire:

$$\Delta_n = \Delta_0 \left[\Omega_{\lambda_{S,L}}(n, N_1) - \Omega_{\lambda_{S,R}}(n, N_1 + N_S + 1)\right], \tag{2.10}$$

$$\mu_n = \mu_1 + (\mu_S - \mu_1)\Omega_{\lambda_L}(n, N_1) + (\mu_2 - \mu_S)\Omega_{\lambda_R}(n, N_1 + N_S + 1). \tag{2.11}$$

In contrast to the previous section, here, we use a superconducting gap that is independent of the Zeeman energy. For the case of a single normal section on the left and a tunnel barrier only on the right, we choose the profiles:

$$\Delta_n = \Delta_0 \Omega_{\lambda_{S,L}}(n, N_1)\Theta(N'_{B,b} - n), \tag{2.12}$$

$$\mu_n = \left[\mu_1 + (\mu_S - \mu_1)\Omega_{\lambda_L}(n, N_1)\right]\Theta(N'_{B,b} - n) + \mu_2\Theta(n - N'_{B,b}). \tag{2.13}$$

The tunnel barriers are modeled in the same manner as in the non-topological system, see Eq. (3.2). The remaining parameters are chosen to be uniform:

$$t_n = t, \quad \alpha_n = \alpha, \quad \Delta_{Z,n} = \Delta_Z. \tag{2.14}$$

In Figs. 2.2c and 2.2d, we show examples of profiles for the superconducting gap, the Zeeman energy, the chemical potential, the tunneling matrix element, and the Rashba SOI strength in an NS and an NSN junction. This system can enter a topological phase hosting MBSs, however, we will mainly focus on the trivial regime which can host only quasi-MBSs.

2.3 ABS in Non-topological nanowires

ABS in the left normal section

In this section we study ABSs in non-topological nanowires as defined in Sec. 2.2. We start our investigation with the setup shown in Fig. 2.1a but without tunnel

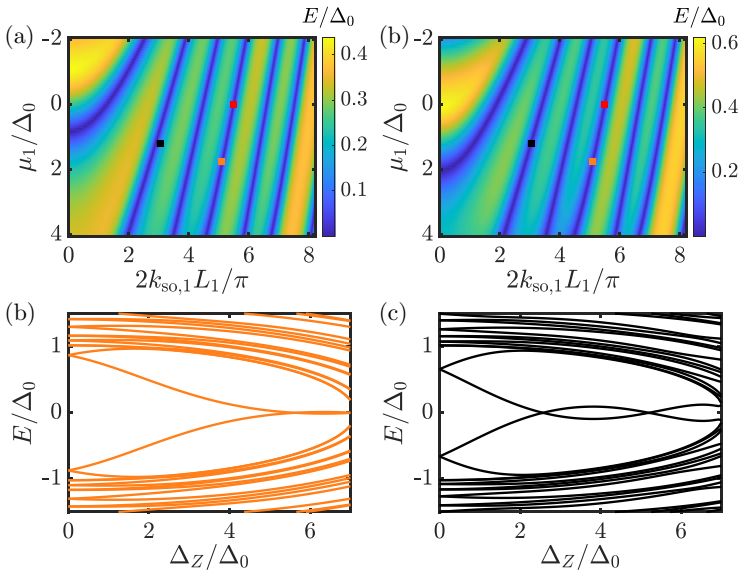

Figure 2.3: Non-topological nanowire with an ABS in the left normal section [see Fig. 2.1a]: The energy of the ABS oscillates as a function of the chemical potential μ_1 and the SOI wavevector k_{so} for the fixed Zeeman energy: (a) $\Delta_Z = 0.9\Delta_Z^c$ and (b) $\Delta_Z = 0.75\Delta_Z^c$. If the minima of the lowest energy (blue regions), which determine the numerical resonance condition, appear at the same values of SOI strength and chemical potential (the red and the orange square) for the different Zeeman energies, then the ABS stays at zero energy for some range of Δ_Z, see panel (c) and Fig. 2.4a. Otherwise (the black square), the ABS energy is not strictly pinned to zero as shown in (d). These ABS levels are, however, broadened by finite temperature and by coupling to external leads in a transport experiment such that one can still observe an apparent ZBP, see App. 2.C. The parameters are listed in Table 2.1 in App. 2.F.

barriers or leads. The left (right) normal section can host ABSs localized close to N_1 (N_2). The ratio $2\alpha_i a/L_i$ determines the ABS level spacing and therefore the number of ABSs in the left ($i = 1$) and right ($i = 2$) normal sections. If this ratio is large in comparison to Δ_0 as is in our case, then the system hosts only a few or a single ABS. The energy of the ABS is pinned to zero if the parameters approximately fulfill the resonance condition

$$\cos(2k_{\mathrm{so,i}}L_i) = 0, \tag{2.15}$$

where $k_{\mathrm{so,i}} = 2m_i a\alpha_i/\hbar^2$ denotes the SOI momentum and $m_i = \hbar^2/(2t_i a^2)$ denotes the effective electron mass inside the normal section [48]. The resonance condition is derived for a chemical potential equal to zero in the normal section, where it is calculated from the SOI energy. The ABS energy, however, can also be pinned to zero in the case of a non-zero chemical potential inside the normal section as we will demonstrate below numerically. In particular, we discuss both the energy spectrum as well as wave functions of the ABS. The wave function contains information about the spatial distribution of the ABS, which is important for understanding the

local and non-local differential conductance of ABSs in three-terminal devices. The parameter profiles for the NS junction are shown in Fig. 2.2a. We examine the case of small ratios $q(\Delta_Z) = L_S/\xi(\Delta_Z)$ between the length L_S of the superconducting section and the localization length ξ of the ABSs,

$$\xi(\Delta_Z) = \hbar v_F/\Delta. \tag{2.16}$$

Here, the renormalized Fermi velocity is defined as $v_F \approx \sqrt{2\mu_S/m_S}$ with $m_S = \hbar^2/(2t_S a^2)$ being the effective mass in the superconducting section and the dependence of Δ on Δ_Z is defined in Eq. (2.4). The value of q is small for a short superconducting section or for a small superconducting gap Δ_0. The latter is associated with a large localization length since ξ is inverse proportional to Δ.

In Figs. 2.3a and 2.3b we plot the energy of the lowest ABS as a function of the SOI momentum $k_{\text{so},1}$ and of the chemical potential μ_1 with the Zeeman energy being fixed close to Δ_Z^c. For $\mu_1 = 0$ the ABS energy exhibits an oscillatory behavior that approximately matches the resonance condition from Eq. (2.15). The oscillatory behavior is preserved for $\mu_1 \neq 0$ and there are still recurring points at which the energy is close to zero (blue). Tuning the system to one of these resonance points also for finite values of the chemical potential (e.g. the orange or red square), we find a zero-energy pinning (see Figs. 2.3c and 2.4a). If the resonance points do not coincide for the different Zeeman energies (see the black square), then the energy is not strictly pinned to zero, see Fig. 2.3d. In a transport experiment, however, such small deviations from zero energy could be masked by, for example, finite temperature, resulting in a broadened ZBP (see App. 2.C).

When the ratio between the length of the superconducting section and the localization length is large ($q \gg 1$), the exponential decay of the ABS wave function in the superconducting section means that the ABS is essentially entirely localized on the left side of the nanowire, see Fig. 2.4b. We extract the localization length of the ABS from the numerically calculated probability density, see Fig. 2.4b, and find that the numerical value of ξ agrees well with the prediction of the analytic expression from Eq. (2.16). A smaller q can be achieved by choosing a smaller superconducting gap (see Figs. 2.4c and 2.4d) or decreasing the length of the superconducting section (see Figs. 2.4e and 2.4f). As the parameter q approaches one, the exponential suppression becomes less pronounced. This results in a small but finite probability density on the right end of the nanowire. We note that the probability density of the ABS on the right side is always non-zero for large values of the Zeeman energy when the superconducting gap is suppressed, see Fig. 2.4h. This behavior is explained by the dependence of the localization length on the Zeeman energy. The localization length increases for large Zeeman energies and therefore the parameter q approaches the value $q \sim 1$. In addition, we note that the extended wave function of the ABS in nanowires with small values of q can be expected to generate a signature in the local conductance measurements on both ends of the nanowire. These local signals on the left and right ends would be correlated since they correspond to the same ABS. Experiments may therefore not be able to distinguish between this correlated ABS signatures and MBS signatures, when the parameter q is small.

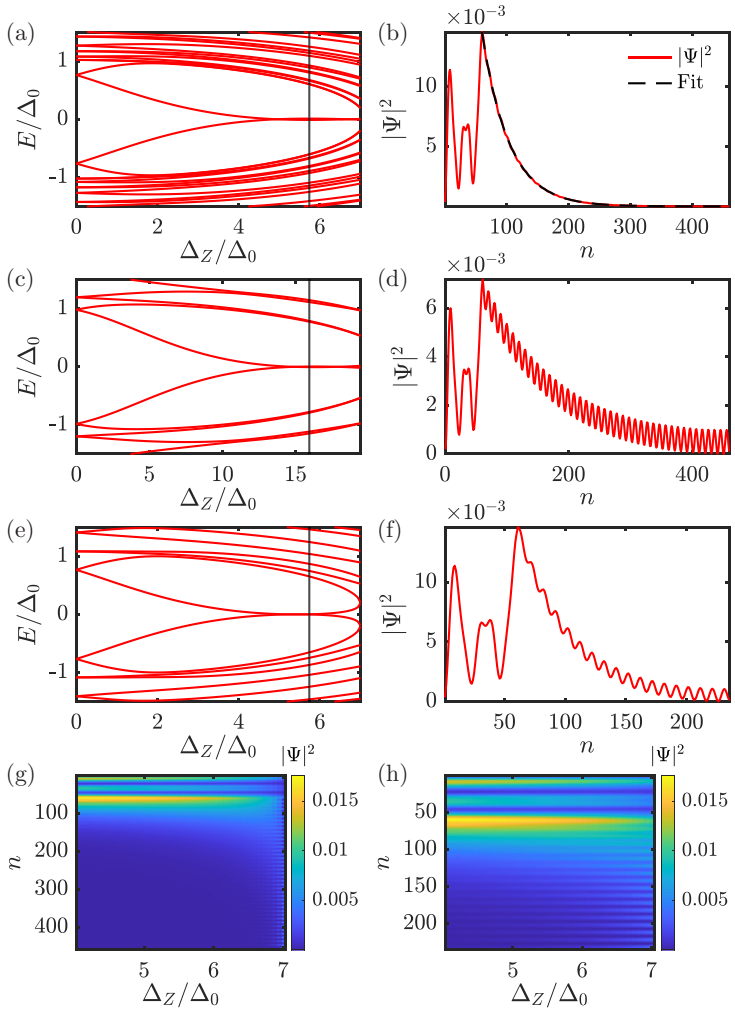

Figure 2.4: (a,c,e) Energy spectrum and (b,d,f) probability density of the ABS, $|\Psi|^2$, at $\Delta_{Z,0} = 5.74\Delta_0$ (indicated by the black line in the left panels) for different values of $q = L_S/\xi$. First row: In the case of a long superconducting section $L_S \gg \xi$ [$q(\Delta_{Z,0}) = 4.5$], the ABS probability density is only non-zero on the left end of the nanowire and decays exponentially inside the superconducting section. We extract the numerical localization length of the ABS by fitting an exponential function (black dashed line) to the probability density. This numerically calculated localization length $\xi = 438$ nm agrees well with the analytic result $\xi = 442$ nm. Second (third) row corresponds to a small value of Δ_0 (of L_S) with $q(\Delta_{Z,0}) = 1.63$ [$q(\Delta_{Z,0}) = 1.98$]. In this case, $|\Psi|^2$ has a finite value on the right end of the nanowire. Generally, as one approaches Δ_Z^c, the ABS probability density also has a finite weight on the right end of the nanowire. For fixed Δ_0, this effect is more pronounced in (h) short than in (g) long nanowires. The parameters are listed in Table 2.1 in App. 2.F.

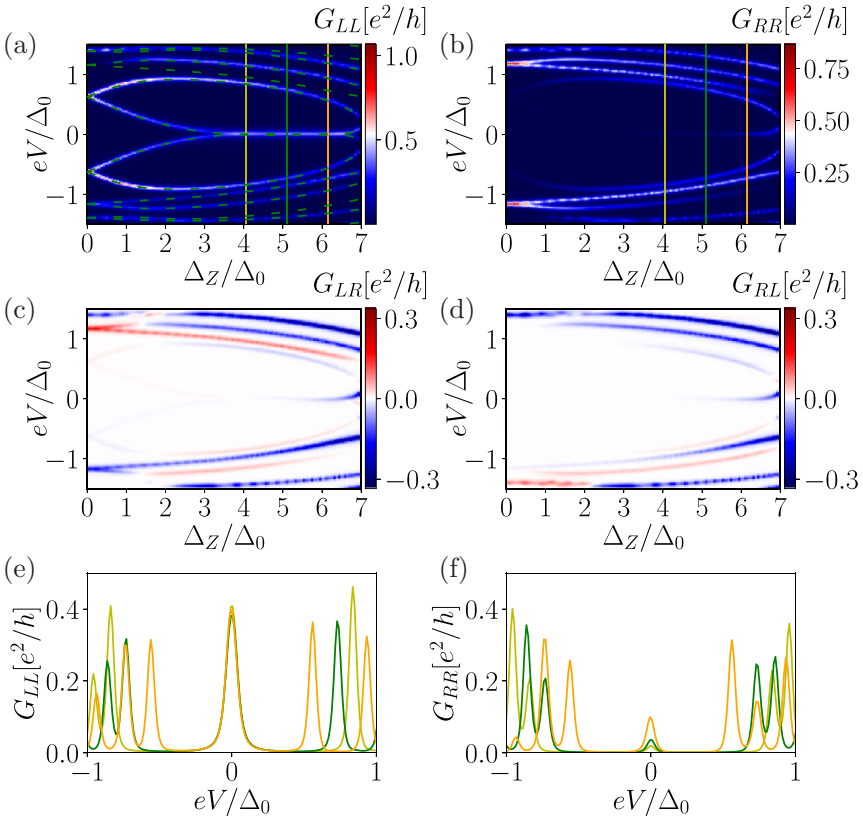

Figure 2.5: Differential conductance in a non-topological nanowire containing one ABS on the left end that extends up to the right end. Both local conductances (a) G_{LL} and (b) G_{RR} exhibit a ZBP due to the extended nature of the ABS wave function. The conductance of the ABS is not quantized to $2e^2/h$ due to the shape of barriers chosen. This conductance pattern agrees well with the energy spectrum, indicated by the dark green dashed lines. The yellow, dark green, and orange solid line indicate line cuts of (e) G_{LL} and (f) G_{RR} at the Zeeman energies $\Delta_Z = \{4.01, 5.11, 6.16\}\Delta_0$. The non-local conductances (c) G_{LR} and (d) G_{RL} contain signatures of the extended ABSs and of the bulk-gap closing at Δ_Z^c. The parameters are listed in Table 2.1 in App. 2.F.

Next, we calculate numerically the differential-conductance matrix elements

$$G_{\alpha\beta} = dI_\alpha/dV_\beta, \tag{2.17}$$

which are the derivative of the total current (which includes both spin contributions) I_α in lead α flowing into the nanowire with respect to the voltage bias V_β at lead β (we follow the notation of Ref. [66], see App. 2.A). To account for tunnel barriers and leads at both ends, see Fig. 2.1a, we choose a slightly longer normal section L_1 than before. The local conductance G_{LL} on the left end exhibits very similar features as the energy spectrum, which we plot for comparison as dark green dashed lines, see Fig. 2.5a. The ABS is visible for all Zeeman energies and is pinned close to zero for a wide range of Δ_Z but the conductance is not quantized to $G = 2e^2/h$

at zero bias and depends on the tunnel barrier properties such as its strength and length, which would be also a case for MBSs. Current experiments do not observe the quantized value, $2e^2/h$, of the ZBP expected for an MBS, thus, experiments cannot easily distinguish between this trivial feature and an MBS signature. A weaker ZBP also appears in G_{RR} for $\Delta_Z \approx 4\Delta_0$ and stays stable until the superconducting gap is suppressed at Δ_Z^c, see also the line-cuts in Fig. 2.5f. This ZBP only appears for large Zeeman energies when the wave function starts to leak through the superconducting section. An equivalent signature could also be expected for the MBS case, for instance, when the two tunnel barriers are of different strength.

The non-local conductances G_{LR} and G_{RL} are similar to each other and exhibit the bulk-gap closing at $\Delta_Z = \Delta_Z^c$ as well as the ZBP, see Fig. 2.5. This ZBP in the non-local conductance is not present in long nanowires but it is visible in short wires due to the extension of the ABS over the entire superconducting section. We note that non-zero non-local conductances indicate that the local conductances G_{LL} and G_{RR} are not symmetric with respect to the bias, since electrons might tunnel directly between the normal leads, see Refs. [66, 67]. The sum of all differential-conductance matrix elements, however, is symmetric with respect to the bias. The antisymmetric part of the local conductance G_{LL}^a (G_{RR}^a) corresponds to the negative value of the antisymmetric part of the non-local conductance G_{LR}^a (G_{RL}^a), see Ref. [66].

The ZBP in our setup is robust against changes of the Zeeman energy but not against fluctuations of the tunnel barrier strength γ_1. Indeed, tuning γ_1 to slightly different values removes the perfect zero-energy pinning. Parenthetically we note that in short topological nanowires, the MBS wave functions overlap, and so, similar to the behavior of our ABSs, it is anyway expected that MBSs are not fixed to zero energy in short wires. Furthermore, broadening effects, for example due to temperature, affect the differential conductance. If the energy is not perfectly pinned to zero and the broadening is large enough then a conductance measurement can not resolve a small finite energy splitting and will reveal only a single peak, which actually consists of two single merged peaks around zero bias, see App. 2.C. Although our system is not designed to explain the data from any specific experiment, we note that our results are similar to the experimental data from Ref. [71]. In particular, a ZBP appears in the left conductance for a specific value of the tunnel barrier gate voltage whereas a ZBP appears in the right conductance at larger Zeeman energies.

We conclude that such an ABS mimics certain key properties of an MBS, which, in turn, presents a challenge for an unambiguous interpretation of experimental observations. If the ratio between the length of the superconducting section and the localization length is small, then the ABS-ZBPs can even be correlated at the left and right ends of the nanowire. The ABS requires some tuning and is not universally stable against fluctuations in the SOI strength or the tunnel barrier strength. We again note that, by construction, the system considered in this section cannot enter the topological phase and so all features we have found here are due to trivial ABSs.

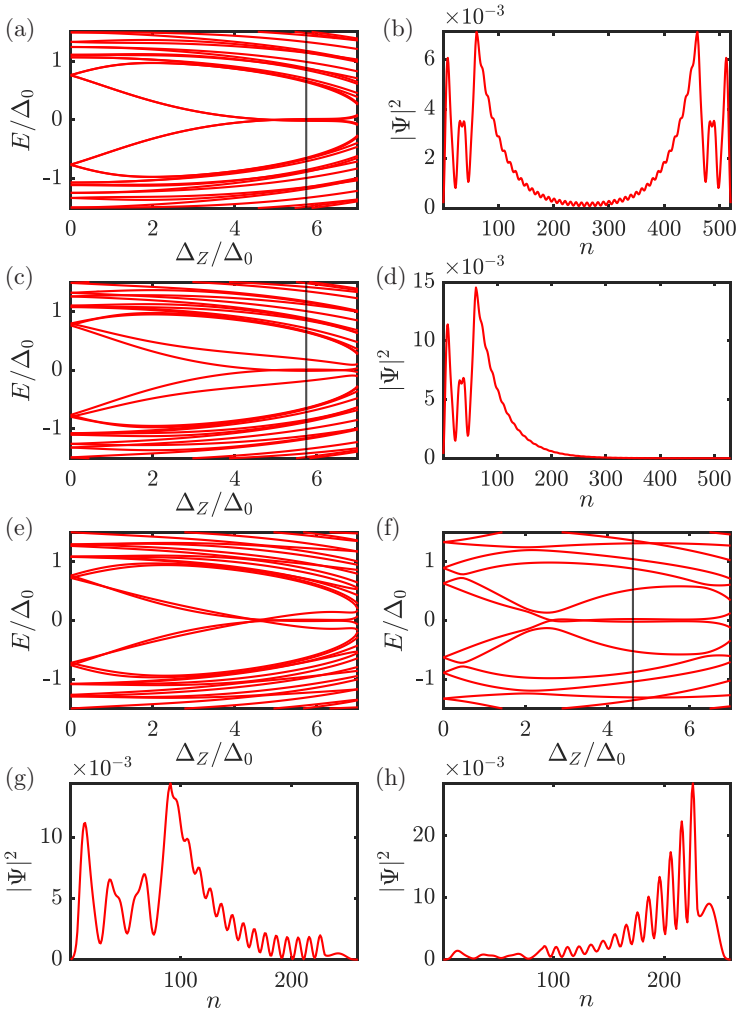

Figure 2.6: Non-topological nanowire with two ABSs: one ABS in the left and a second one in the right normal section. (a,c,e,f) Energy spectrum and (b,d,g,h) probability densities of the ABSs at $\Delta_Z = 5.74\Delta_0$ and $\Delta_Z = 4.62\Delta_0$ (indicated by the black line in the panels with the energy spectra). First row: Both ABSs in N_1 and N_2 are tuned to zero energy, therefore, the ABSs in the left and right normal sections are degenerate but essentially uncorrelated. Tuning the parameters of the right ABS away from the resonance condition (second row), one lifts the degeneracy. The left ABS stays pinned to zero energy, see (d). Third row: The right ABS mimics the behavior of the edge of a bulk-gap in (e) long and (f) short nanowires. The probability density of the (g) left and (h) right ABS, corresponding to the panel (f), has a finite value throughout the entire nanowire. The parameters are listed in Table 2.1 in App. 2.F.

ABS in the left and right normal sections

In this section, we examine the non-topological nanowire with two normal sections hosting two ABSs: one on the left and another one on the right side of the nanowire, see Fig. 2.1b. As before, we begin without tunnel barriers and without the leads. If

the resonance condition is fulfilled simultaneously in the left and the right normal sections of the long nanowire, then the two ABSs become degenerate. The probability density shows peaks at both ends of the nanowire, see Fig. 2.6b. For long wires there is no correlation between the ABS on the left end and the ABS on the right end: both are independent of each other and the overlap of their wave functions is approximately zero. As can be expected from the previous section, this is not the case for shorter wires and correlations can occur when the ratio q is small.

In general, a topological phase transition is accompanied by a bulk-gap closing and reopening. Here, we show that such a gap behavior can also be mimicked by two ABSs in non-topological nanowires. We tune the parameters of the right normal section away from the resonance condition by changing the length of N_2. The degeneracy is lifted and the energy of the right ABS is different from that of the left ABS, see Fig. 2.6c. The parameters α_2 and N_2 do not affect the zero-energy pinning of the left ABS and can be chosen independently to control the behavior of the right ABS in dependence of the Zeeman energy. We then tune the right ABS such that it crosses the zero energy at the same value of the magnetic field at which the zero-energy pinning of the left ABS starts to take place. The resulting energy spectrum is shown in Fig. 2.6e and is reminiscent of what one might expect close to the topological phase transition, however, we stress that here all these features occur due to the presence of trivial ABSs in non-topological nanowires.

The nanowire examined in Fig. 2.6e is relatively long with a large value of the parameter $q \approx 4.5$; it is therefore not expected that the left ABS is visible in the local conductance on the right end of the nanowire. If instead we choose a similar parameter set as in Fig. 2.5, corresponding to a short nanowire and, in addition, account for a tunnel barrier (see Fig. 2.1b), we find the energy spectrum shown in Fig. 2.6f. The energy spectrum in Fig. 2.6f strongly resembles the gap closing and reopening one expects from a topological phase transition, but is again entirely due to ABSs. Additionally, the wave function of the left ABS now spreads from the left to the right end and vice versa for the wave function of the right ABS, see Figs. 2.6g and 2.6h.

The local conductances G_{LL} and G_{RR} reveal that the ABS localized more on the left (right) is still visible at the opposite right (left) end, see Fig. 2.7. The left (right) ABS has a smaller conductance value on the right (left) end and the conductance is not quantized. In the absence of quantized conductances, however, this behavior significantly complicates the interpretation of future experimental data: The local conductance on the left and right end exhibits a correlated ZBP and this is accompanied by a signature reminiscent of a bulk-gap closing and reopening. In addition, the non-local conductance also exhibits the correlated left and right ABS-ZBP as well as a signature similar to a bulk-gap closing and reopening during a topological phase transition. All these features could be misinterpreted as signatures of MBSs but appear here in a nanowire that is, by design, topologically trivial at all magnetic field strengths. The complementary scenario in short topological nanowires is discussed in App. 2.B.

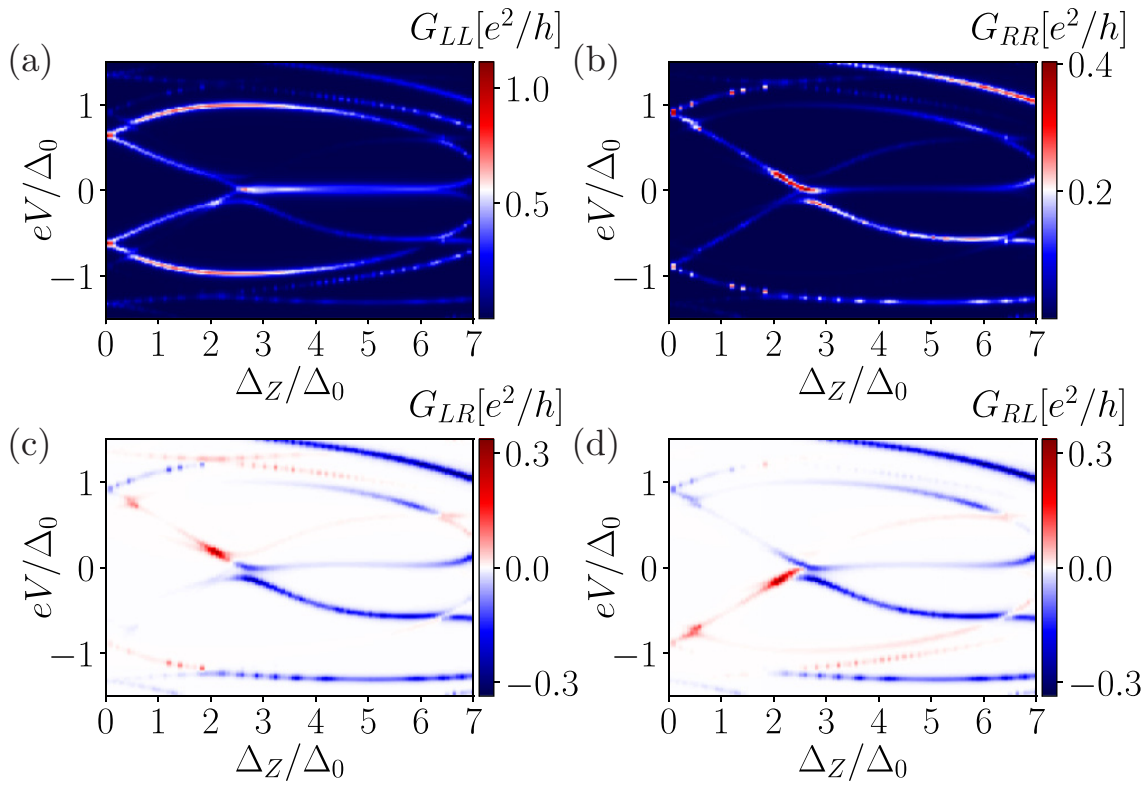

Figure 2.7: Differential-conductance patterns corresponding to the energy spectrum of a non-topological nanowire from Fig. 2.6f. Both local conductances (a) G_{LL} and (b) G_{RR} exhibit a ZBP due to the extended left ABS wave function, see Fig. 2.6g. Although entirely trivial in origin, the local conductance is reminiscent of what is expected for MBSs, containing both correlated ZBPs and an apparent gap closing and reopening process. The non-local conductances (c) G_{LR} and (d) G_{RL} contain signatures of both the bulk states and the extended ABSs, which are similar to those expected for MBSs. The parameters are listed in Table 2.1 in App. 2.F.

2.4 quasi-MBS in topological nanowires

Quasi-MBS in the left normal section

In this section, we consider topological nanowires in configurations shown in Fig. 2.1a with parameter profiles shown in Fig. 2.2c. Such nanowires host quasi-MBSs even if the superconducting section is in the trivial phase as discussed in Sec. 2.2. In Fig. 2.8, we compare the energy spectrum and probability density of systems with long and short superconducting sections. Quasi-MBSs at approximately zero energy exist in the trivial phase and evolve into MBSs at stronger magnetic fields. The phase transition takes place approximately at the critical value $\Delta_Z^T = \sqrt{\Delta_0^2 + \mu_S^2}$, indicated by the green line, and is accompanied by a bulk-gap closing and reopening. Changing the shape of Δ_n and μ_n to step-like functions shifts quasi-MBSs to higher energies, whereas MBSs in the topological phase are not affected. The wave functions of the quasi-MBSs only have support on the left

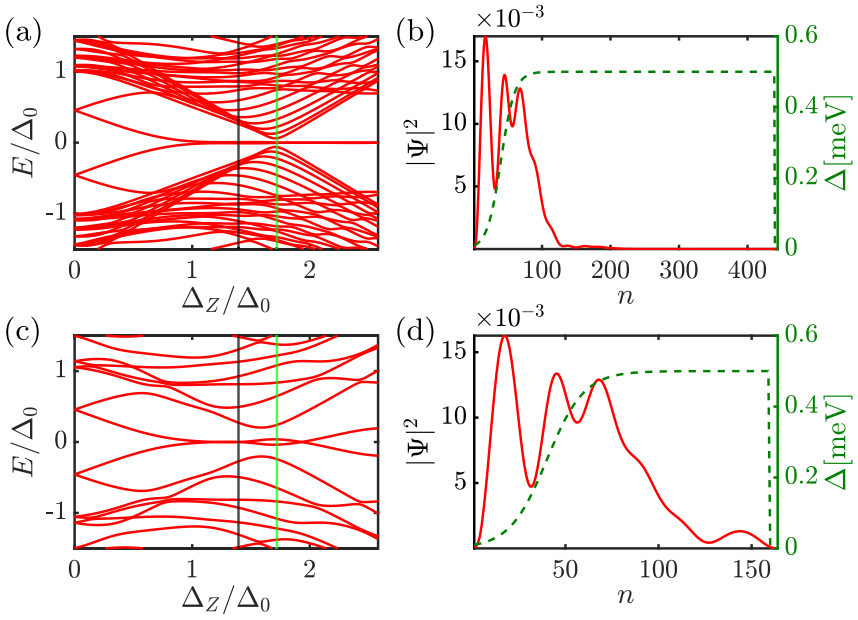

Figure 2.8: Topological nanowire with quasi-MBSs on the left end: (a,c) Energy spectrum and (b,d) probability densities of the quasi-MBS at $\Delta_Z = 1.39\Delta_0$ (indicated by the black line in the left panels) and profile of the superconducting gap (dark green dashed line). First row: In the case of a long superconducting section $L_S \gg \xi$, the quasi-MBS probability density is only non-zero on the left end of the nanowire and decays inside the superconducting section. The second row corresponds to a smaller value of L_S and in this case the probability density has a finite value at the right end of the nanowire. The topological phase transition from quasi-MBSs to MBSs takes place at $\Delta_Z = 1.73\Delta_0$ (indicated by the green line in the left panels). The parameters are listed in Table 2.2 in App. 2.F.

end of the nanowire and decay inside the superconducting section. Therefore, the probability density is only non-zero also on the right end of the nanowire when MBSs appear. The quasi-MBSs still exist in short nanowires with a small ratio q and, in this case, the wave function spreads through the superconducting section to the right end, see Fig. 2.8d. In contrast to ABSs in the non-topological nanowire system considered above [see Sec. 2.3], quasi-MBSs in a nanowire with smooth parameter profiles are more stable against fluctuations of the tunnel-barrier strength. For long wires quasi-MBSs can appear over a wide range of SOI strengths. In short nanowires, however, the quasi-MBSs are only pinned to zero for a narrow interval of the SOI strength.

Within this setup we first study the transport properties of long topological nanowires that host quasi-MBSs, see Fig. 2.9. As is expected for MBSs, the conductance of these quasi-MBSs is nearly quantized to $2e^2/h$ for some set of parameters, as discussed in earlier works [49]. Deviations from this value are due to line broadening effects. In long nanowires quasi-MBSs are only visible in the local conductance on the left end, G_{LL}, the corresponding region is encircled by an ellipse in Figs. 2.9a and 2.9b; see also Figs. 2.9e and 2.9f for line-cuts of the local conductances

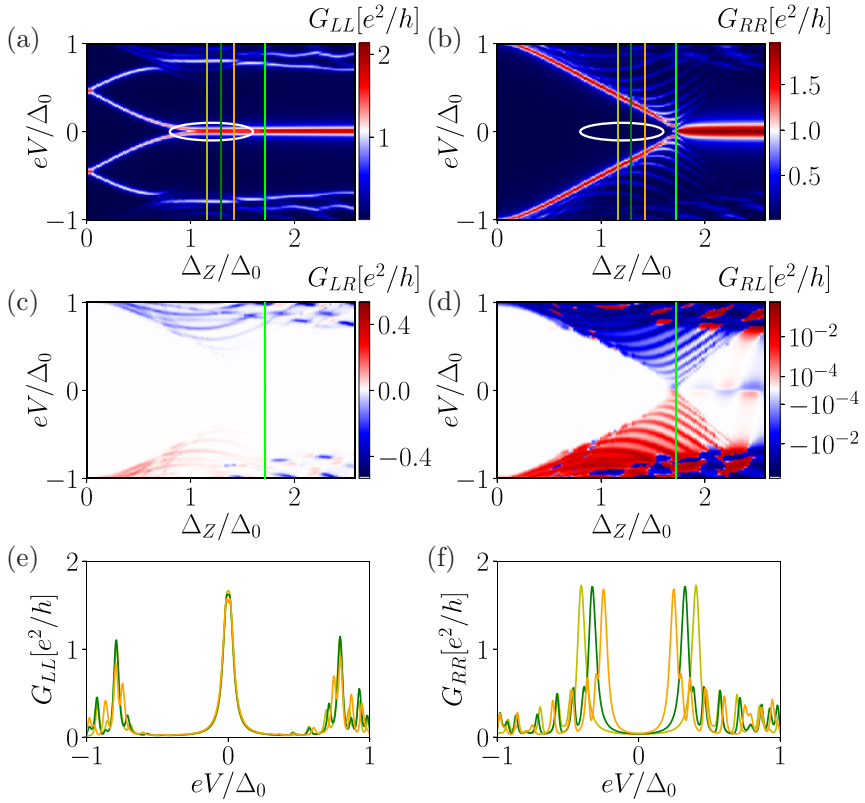

Figure 2.9: Differential-conductance patterns reproduce the energy spectrum of the topological nanowire, see Fig. 2.8a. The system undergoes a topological phase transition at $\Delta_Z \approx 1.73\Delta_0$ as indicated by the green line. The local conductance (a) G_{LL} and (b) G_{RR} of the MBSs are nearly quantized close to the value $2e^2/h$. The parameter region of potential quasi-MBSs is encircled by the white ellipse. Only G_{LL} exhibits a ZBP of quasi-MBS: this local conductance is also quantized close to $2e^2/h$, deviations from this value are due to thermal broadening. The non-local conductances (c) G_{LR} and (d) G_{RL} contain only signatures coming from the bulk states. Line cuts (e,f) of the local conductance G_{LL} and G_{RR} at the Zeeman energies $\Delta_Z = \{1.16, 1.29, 1.42\}\Delta_0$ [indicated by the yellow, dark green and orange lines in (a,b)] confirm that the quasi-MBS-ZBP appears only on the left end. The parameters are listed in Table 2.2 in App. 2.F.

G_{LL} and G_{RR} at certain Zeeman energies. This behavior can be understood from the fact that the quasi-MBS wave function is localized on the left end of the nanowire. The bulk-gap closing and reopening is only weakly pronounced in G_{LL} because the bulk states are mainly localized within the superconducting section and the left lead is relative far away from this region. As a result, G_{LL} primarily probes the quasi-MBS (which is localized in N_1) but not the bulk states. It should be noted that the bulk states can become more visible using a logarithmic color scale (see Fig. 2.9d). The normal section on the right end is shorter and so the right local conductance is a better probe of the bulk states. The bulk-gap closing and reopening in the non-local conductances G_{LR} and G_{RL}, shown in Figs. 2.9c and 2.9d, respectively, is less

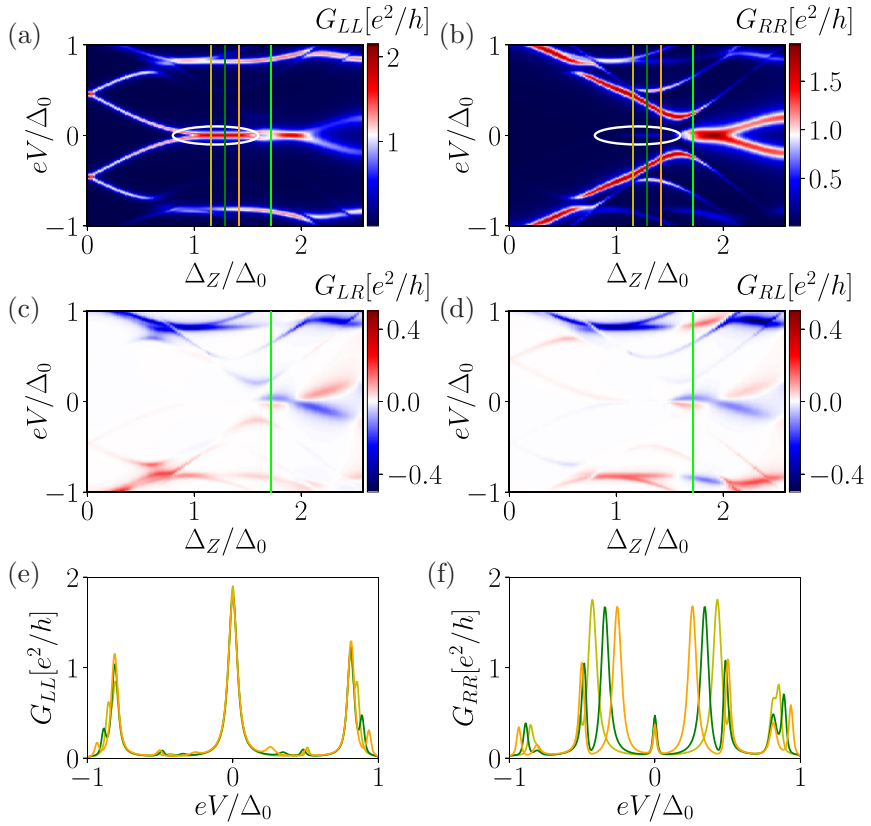

Figure 2.10: The same as in Fig. 2.9 but for a short nanowire. The corresponding energy spectrum is shown in Fig. 2.8c. Both local conductances (a) G_{LL} and (b) G_{RR} exhibit a ZBP coming from quasi-MBSs (highlighted by the white ellipse). The conductance of the quasi-MBSs is close to the quantization value of $2e^2/h$ on the left end but not on the right end. The non-local conductances (c) G_{LR} and (d) G_{RL} contain signatures of the bulk states as well as of the quasi-MBSs and MBSs. Line cuts (e,f) of the local conductance G_{LL} and G_{RR} at the Zeeman energies $\Delta_Z = \{1.16, 1.29, 1.42\}\Delta_0$ [indicated by the yellow, dark green, and orange lines in (a,b)] confirm that the quasi-MBS-ZBP appears on both ends of the nanowire. The parameters are listed in Table 2.2 in App. 2.F.

clear compared to nanowires with uniform parameters as well as the quasi-MBSs and the MBSs are not visible in the non-local conductances. The right local conductance, G_{RR}, takes larger values close to the bulk-gap edge in the trivial regime (see Fig. 2.9b) since there is an 'intrinsic' ABS just at the gap edge, see Refs. [79, 80].

Next, we consider short superconducting sections. The conductance value of the quasi-MBS and its zero-bias pinning is essentially unaffected by the change of length, see Fig. 2.10. In contrast, the MBSs that occur in the topological phase are pushed away from zero energy. In short nanowires quasi-MBSs are visible in G_{RR}: this region is indicated by the white ellipse in Figs. 2.10a and 2.10b. The quasi-MBS-ZBP appearing in G_{RR} is not quantized and much smaller than that in G_{LL}, see also Figs. 2.10e and 2.10f for a line cut of the conductance. The right local conductance,

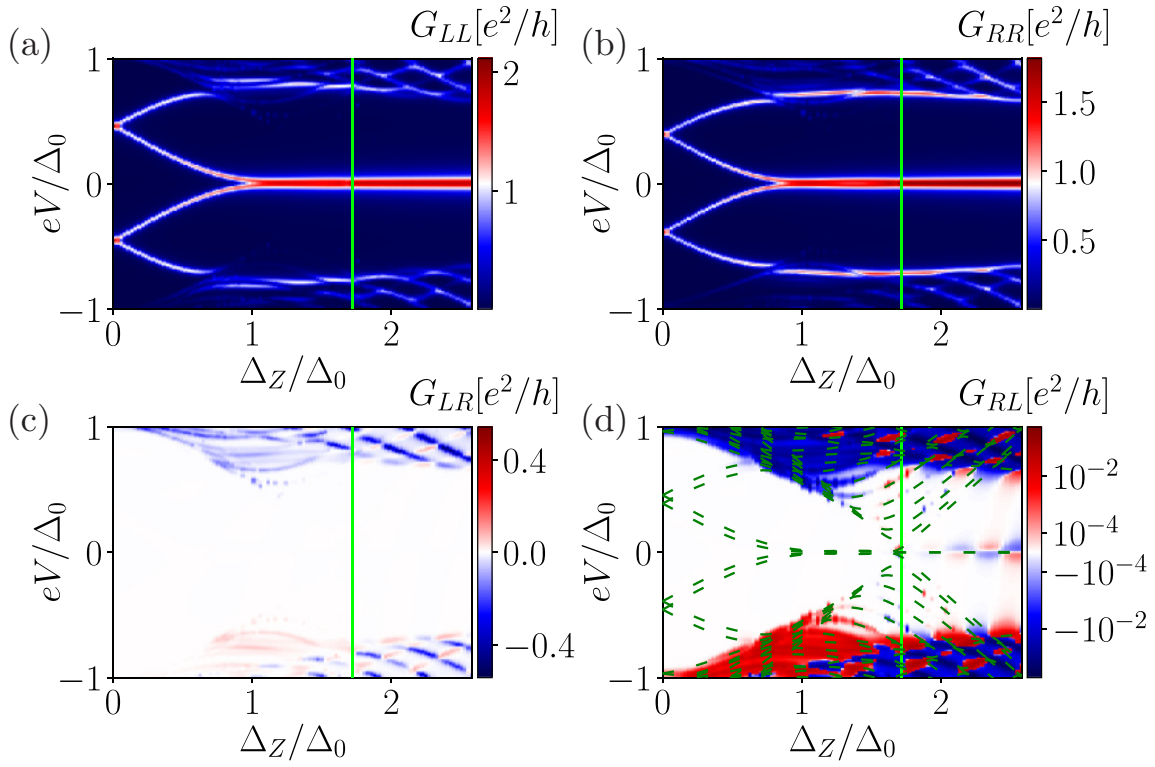

Figure 2.11: A long topological nanowire, as in Fig. 2.9a, with quasi-MBSs present at both nanowire ends. The local conductance (a) G_{LL} and (b) G_{RR} of the MBSs and the quasi-MBSs is close to the quantization value of $G = 2e^2/h$, deviations from this value are due to thermal broadening. The non-local conductances (c) G_{LR} and (d) G_{RL} contain only signatures of the bulk states, and the bulk-gap closing and reopening is only weakly pronounced. The parameters are listed in Table 2.2 in App. 2.F.

however, exhibits a small ZBP and this peak is correlated to the one on the left end. Furthermore, while the quasi-MBSs and the MBSs generate a signal in the non-local conductances, G_{LR} and G_{RL}, the bulk-gap closing and reopening is not as clear as in the case of the long superconducting section.

Quasi-MBSs in the left and right normal sections

The final setup we consider is a topological nanowire with normal sections on both ends, see Fig. 2.1b, with parameter profiles specified in Fig. 2.2d. Such a system can host zero-energy quasi-MBSs at both ends of the nanowire in the topologically trivial regime. In App. 2.D, we discuss the energy spectrum and the wave functions of bulk states, the latter is important for the understanding of the non-local conductances. The conductance patterns of the nanowire, depicted in Fig. 2.11, exhibit features coming from the left and right localized quasi-MBSs. As found previously, their conductance value is quantized close to $2e^2/h$. The bulk-gap closing and reopening is only weakly pronounced in the non-local conductance G_{RL}, although a

logarithmic color scale can reveal this process, see Fig. 2.11d. We note that even on the logarithmic scale the bulk states are poorly visible compared to Fig. 2.9d, whereas the energy spectrum (dark green dashed lines) clearly shows the bulk-gap closing and reopening. This reduction of the non-local conductance signature of the bulk-gap closing and reopening by normal sections has been noted but not explained in Ref. [68]. The reason for this reduction is that the bulk states have no support in the normal sections and especially the low energy states are confined to the middle of the superconducting section and, therefore, these bulk states have only very weak features in the local and non-local conductances. Other states are extended throughout the whole nanowire and thus contribute more strongly to the non-local conductances, see App. 2.B.

This suppression of the visibility of the bulk-gap closing in the non-local conductance can be somewhat offset by decreasing the step height of the chemical potential at the interface between the normal and superconducting section. Nonetheless, three-terminal experiments will require a very high resolution to measure the bulk-gap closing and reopening in superconducting nanowires with normal sections on both ends. If this gap behavior cannot be resolved experimentally, then it will also not be possible to distinguish MBSs from quasi-MBSs, even in long nanowires.

2.5 Conclusions

We analyzed transport properties of non-topological Rashba nanowires with normal sections that host ABSs. When the parameters of a normal section are close to a resonance condition and the ratio between the length of the superconductor and the ABS localization length is small, an ABS is pinned to zero energy over a wide range of Zeeman energies and has a finite probability density on both ends of the nanowire. The same effect occurs for the case of smooth spatial variation of system parameters such as chemical potential and superconducting gap. As such, even though their origin is topologically trivial, calculations of local and non-local conductances reveal correlated ZBPs on the left and the right ends of the nanowire due to the ABSs. We conclude therefore that the measurement of correlated ZBPs on both ends of a superconducting nanowire is not an unambiguous indicator for the presence of MBSs.

The observation of the closing and reopening of the bulk-gap in the local and non-local conductances that should accompany a topological phase transition has also been considered in previous works as an additional indicator for the topological phase. However, we find here that a second ABS at the other end of the nanowire can mimic the edge of the bulk-gap, when the ratio between the length of superconducting section and the localization length of the ABS is small. Therefore, local and non-local conductance measurements of ZBPs on each end with an apparent closing and reopening of the bulk-gap is also not an unambiguous indicator for the presence of MBSs.

We conclude that, while next generation three-terminal experimental devices will have access to additional auxiliary features that can help clarify the origins of ZBPs, trivial ABSs can also generate conductance features similar to those expected

from MBSs when such devices do not have long superconducting sections. In particular, we find that ABSs can produce correlated ZBPs and a feature reminiscent of a bulk-gap closing and reopening in local and non-local conductances. Our results therefore suggest that it is essential to perform measurements in systems with long superconducting sections and over a large region of parameter space if one wishes to gain confidence in a purported MBS signature. That said, ballistic transport experiments favor short nanowires since presently the production of devices with long mean free paths is challenging. It is therefore questionable whether current state-of-the-art or near-term Rashba nanowire devices will be able to conclusively rule out the effects of extended ABSs. Alternatively, these three-terminal detection methods should be supplemented by additional signatures observable in the bulk [81–86] and related to the topological phase transition, such as the inversion of spin polarization in the lowest energy bulk states [87, 88].

2.6 Acknowledgements

This project has received funding from the European Union's Horizon 2020 research and innovation programme under Grant Agreement No 862046 and under Grant Agreement No 757725 (the ERC Starting Grant). This work was supported by the Georg H. Endress Foundation and the Swiss National Science Foundation.

2.A Energy and Transport calculation

To obtain the energy spectrum and wave functions, we diagonalize numerically the Hamiltonian H. For differential conductance calculations we use the Python package Kwant [89], which is based on the Blonder Tinkham Klapwijk (BTK) formalism [90]. Kwant is used to compute the differential conductance $G_{\alpha\beta} = dI_\alpha/dV_\beta$ of the three-terminal device consisting of a nanowire with a grounded superconducting section and two normal leads at the left and right end. In particular, we utilise Kwant to numerically calculate the S-matrix and extract the transmission and reflection coefficients that determine the Andreev conductance matrix at zero temperature

$$\begin{aligned} G_0 &= \begin{pmatrix} G_{LL,0} & G_{LR,0} \\ G_{RL,0} & G_{RR,0} \end{pmatrix} \\ &= \frac{e^2}{h} \begin{pmatrix} N_L - R^e_L(-eV_L) + A^e_L(-eV_L) & -T^e_{LR}(-eV_R) + A^e_{LR}(-eV_R) \\ -T^e_{RL}(-eV_L) + A^e_{RL}(-eV_L) & N_R - R^e_R(-eV_R) + A^e_R(-eV_R) \end{pmatrix}, \end{aligned} \tag{2.18}$$

where N_L (N_R) and $V_{L[R]}$ denote the number of channels and the gate voltage on the left (right) lead, respectively, R_α and A_α are the probabilities of an electron in lead α to be reflected as an electron or hole, respectively, and similarly, the coefficients $T_{\alpha\beta}$ and $A_{\alpha\beta}$ are the probabilities of an electron from lead β to transmit as an electron or hole to lead α, respectively. The sign of the non-local conductance reveals whether the crossed Andreev reflection, described by the transmission coefficient $A_{\alpha\beta}$, or

the electron co-tunneling, described by the coefficient $T_{\alpha\beta}$, is a dominant contribution for the non-local differential conductance. The differential-conductance matrix elements [63, 66, 91] at finite temperature T are given by

$$G_{LL} = -\frac{e^2}{h}\int_{-\infty}^{\infty} \mathrm{d}\omega \frac{\mathrm{d}f_L(\omega)}{\mathrm{d}\omega}\left[N_L - R_L^e(\omega) + A_L^e(\omega)\right], \tag{2.19a}$$

$$G_{LR} = \frac{e^2}{h}\int_{-\infty}^{\infty} \mathrm{d}\omega \frac{\mathrm{d}f_R(\omega)}{\mathrm{d}\omega}\left[T_{LR}^e(\omega) - A_{LR}^e(\omega)\right], \tag{2.19b}$$

$$G_{RL} = \frac{e^2}{h}\int_{-\infty}^{\infty} \mathrm{d}\omega \frac{\mathrm{d}f_L(\omega)}{\mathrm{d}\omega}\left[T_{RL}^e(\omega) - A_{RL}^e(\omega)\right], \tag{2.19c}$$

$$G_{RR} = -\frac{e^2}{h}\int_{-\infty}^{\infty} \mathrm{d}\omega \frac{\mathrm{d}f_R(\omega)}{\mathrm{d}\omega}\left[N_R - R_R^e(\omega) + A_R^e(\omega)\right], \tag{2.19d}$$

where $f_{L[R]}(\omega) = f(\omega + eV_{L[R]})$ denotes the Fermi distribution function $f(\omega) = [\exp[\omega/(k_BT)] + 1]^{-1}$, with k_B being the Boltzmann constant. The temperature T broadens peaks in the differential conductance. In this work, we perform the calculations using the temperature $T = 40$ mK throughout, unless stated otherwise. Further details about the BTK formalism in three-terminal devices and the numerical implementation can be found in Refs. [33, 34, 63, 66, 68, 89, 91].

Conventional Andreev reflection describes the process of an incoming electron with spin σ incident on the interface of a normal-superconductor junction from the normal material side. The electron can form a Cooper pair with another electron under retro-reflection of a hole with opposite spin $-\sigma$ [36, 38, 92]. On the other hand, in topological superconductors, selective equal-spin Andreev reflection is possible [93] and leads to the reflection of a hole with the same spin polarization as the incoming electron. In this manuscript, however, we include SOI and a Zeeman term in the normal leads, similar for example to Ref. [47]. As a result the spin in the lead is not a good quantum number and a projection onto the conventional Andreev reflection channel or the selective equal-spin Andreev reflection channel is not possible.

2.B Short uniform topological nanowire

In this section, we compute the differential conductance of a short uniform nanowire, which enters a topological phase at $\Delta_Z = \Delta_0$, see Fig. 2.12. This conductance behavior is well known and is presented here in order to compare with that of a short non-topological nanowire which can exhibit similar signatures, see Fig. 2.7. The left and right conductance patterns exhibit features coming from the MBSs after the topological phase transition. The MBSs overlap since their localization length is comparable to the system length and, therefore, the non-local conductance also contains a weak MBS signature in this regime, see Figs. 2.12c and 2.12d. A logarithmic scale can, however, reveal these weak MBS signatures in the non-local conductance, for example, see also Fig. 2.11d.

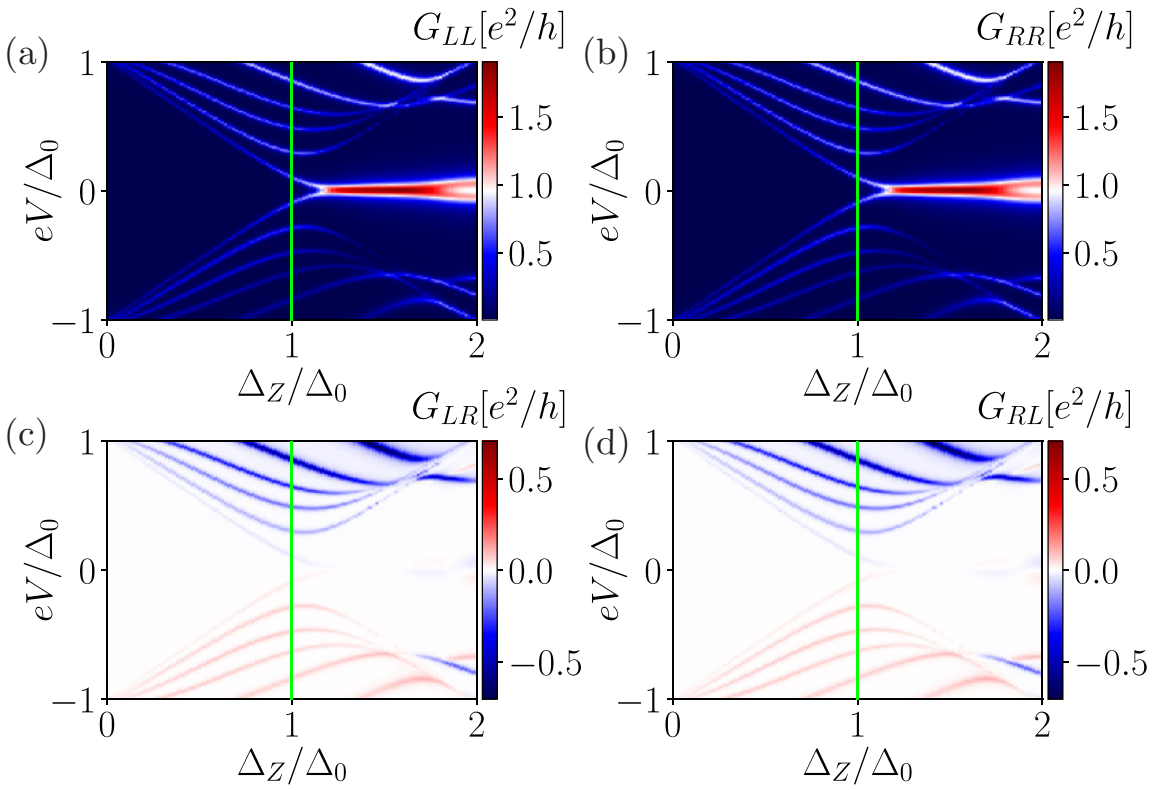

Figure 2.12: Differential-conductance patterns in a short topological nanowire with uniform parameter profiles. The local conductances (a) G_{LL} and (b) G_{RR} are identical and exhibit ZBPs coming from the MBS in the topological phase. The height of this ZBP is a bit smaller than $2e^2/h$ due to thermal broadening. The non-local conductance (c) G_{LR} and (d) G_{RL} exhibit the non-local bulk-gap closing and reopening process, close to the Zeeman energy $\Delta_Z = \Delta_0$, indicated by the green line. Furthermore, the non-local conductance exhibits features around zero energy originating from overlapping MBSs. The parameters are listed in Table 2.2 in App. 2.F.

In short nanowires only a few states contribute to conductance at low biases close to the bulk-gap closing and reopening point. For instance, in the example shown in Fig. 2.12, only three states contribute. This should be compared to the conductance of the non-topological nanowire shown in Fig. 2.7, which hosts one state that mimics the bulk states undergoing a topological phase transition and is very similar to the behavior found in topological nanowires. In longer nanowires the energy level spacing between the bulk states decreases. As such, many states contribute to the conductance close to the bulk-gap closing and reopening point and therefore it is easier to distinguish between the bulk and bound states.

We note that the ZBP of the MBSs in the short topological nanowire is not quantized, which is also the case for the ZBP in the trivial nanowire. Experimentally, the robust quantization has not been observed so far. All in all, a distinction between topological and trivial states in short nanowires via a local and non-local conductance measurement is therefore challenging.

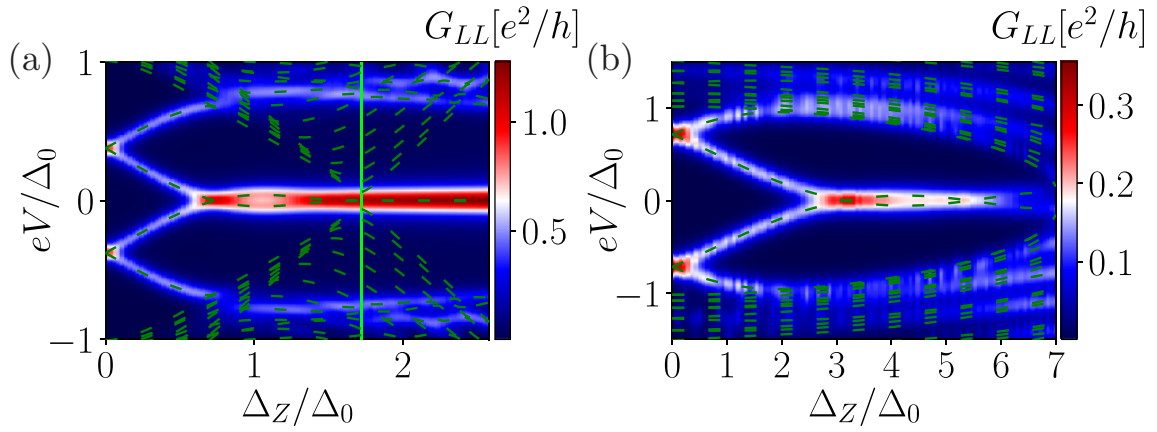

Figure 2.13: Strong broadening of the ZBP in a long (a) topological and (b) non-topological nanowire hosting an ABS. The differential conductance peaks are in general broadened by different mechanisms such as strong coupling between leads and nanowire, external perturbations due to the environment, and high temperatures; here we effectively take these broadening mechanisms into account via a large effective temperature of $T = 150$ mK. (a) The left local conductance exhibits only a single ZBP, in contrast, the energies of the ABS (shown in dashed green lines) are not well pinned to zero. The strong broadening merges the two finite-energy peaks together to a single ZBP. The topological phase transition is indicated by the green vertical line. (b) The same effect is present in the non-topological system. The parameters are listed in Table 2.2 in App. 2.F.

2.C Broadening of ZBP

We note that the calculated conductance peaks are relatively sharp. In contrast, experiments usually show broadened conductance patterns. Different mechanisms such as the strong coupling between leads and nanowire, external perturbations due to environment effects, and high temperatures lead to a broadening of the conductance peaks. In this section we consider long topological and non-topological nanowires, hosting nearly zero-energy ABSs in the left normal section, and calculate the local conductance G_{LL}, see Fig. 2.13. All broadening mechanisms are taken into account effectively via thermal effects, i.e., by choosing a relatively high temperature of $T = 150$ mK. The resulting conductance is less sharp and is therefore in better agreement with the broader conductance features found in experiments. Furthermore, broadening prevents a high resolution mapping of the energy spectrum. The left local conductance G_{LL} cannot resolve the fact that the ABS has a finite energy (in Fig. 2.13 energies are shown as green dashed lines for comparison). The conductance peaks of the finite-energy ABS and its particle-hole partner are merged together into a single conductance peak at zero energy. As such, even in systems where ABSs are not perfectly tuned to zero energy, for example, if the resonance condition is fulfilled only approximately, an apparent ZBP in the conductance can still emerge.

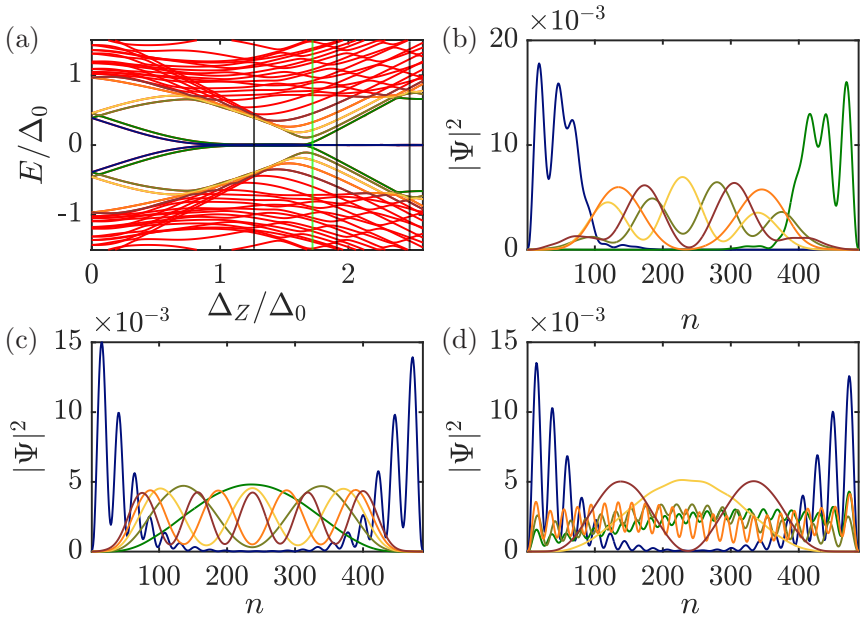

Figure 2.14: Topological nanowire hosting quasi-MBSs on both ends. (a) Energy spectrum and (b,c,d) probability densities of the quasi-MBSs and of the lowest bulk states at $\Delta_Z = \{1.26, 1.91, 2.48\}\Delta_0$ [indicated by the black lines in panel (a)]. The topological phase transition takes place at $\Delta_Z = 1.73\Delta_0$ [indicated by the green line in panel (a)]. The color of the energy states in panel (a) determines the color-code for their probability densities in the remaining panels. (b) In the trivial phase, the quasi-MBSs are well localized at the left and right ends. The first four bulk states (khaki green, yellow, orange, dark red) are mainly localized in the superconducting section of the nanowire. (c) Shortly after the topological phase transition, the wave functions of the energetically lowest bulk states are still mainly localized within the superconducting section. (d) Deeply in the topological phase transition, the lowest bulk states (dark green and khaki green) are extended over the entire nanowire. These extended states are more visible in the non-local conductance (see Fig. 2.11) than the bulk states shown in panel (b) and (c). The parameters are listed in Table 2.2 in App. 2.F.

2.D Absence of the signature of the bulk-gap closing in conductance

In this section we consider topological nanowires which host quasi-MBSs at both ends and analyze the suppression of signatures of the topological phase transition in the conductance. Our discussion focusses on long nanowires, for which elements of the corresponding conductance matrix are shown in Fig. 2.11. The non-local conductances, G_{RL} and G_{LR}, show only weak bulk-gap features at lower biases, despite the fact that the energy spectrum exhibits a clear bulk-gap closing and reopening consistent with the topological phase transition, see Fig. 2.14. The phase transition is indicated by the green vertical line. This puzzle can be resolved by looking at the

bulk wave functions, see Fig. 2.14. The non-uniform chemical potential is responsible for confining the lowest energy bulk sub-gap states within the superconducting section. When the bulk gap closes in the superconducting section, the normal sections still nominally have a gap for states with nearly zero momentum originating from the interior branches of the spectrum. In the trivial phase (see Fig. 2.14b), the quasi-MBSs (blue, dark green) are well localized at the left and right ends of the nanowire. As a result, they couple strongly to the leads. In contrast, the energetically lowest bulk states (khaki green, yellow, orange and dark red) are mainly localized within the superconducting section. Thus, there is hardly any coupling to the leads and, as such, these bulk states only weakly contribute to the non-local conductance of the trivial phase.

Right after the topological phase transition (see Fig. 2.14c), the wave functions of the energetically lowest bulk states are also mainly localized within the superconducting section and not in the normal sections. This results in a similar absence of a corresponding non-local conductance signal as occurred in the trivial phase. In general, we find the lower the energy of the bulk state the more it is localized within the superconducting section. For example, the energetically lowest state (dark green) is more localized than the fifth bulk state (dark red). Furthermore, these bulk states are spatially separated from the left and right ends of the nanowire, so that a local conductance measurement also can not resolve such states. In contrast, the MBSs (dark blue) are mainly localized in the normal sections and decay into the superconductor making them highly visible in local conductance measurements.

Deep inside the topological phase (see Fig. 2.14d), the lowest bulk states (dark green and khaki green) originating from the exterior branches of the spectrum (from finite Fermi momentum) are extended over the entire nanowire. These delocalized states couple strongly to the leads and do contribute to the non-local conductance. In contrast, some of the energetically higher states (such as the yellow and dark red) originating from the interior branches of the spectrum (from nearly zero Fermi momentum), – which are related to the states discussed in Fig. 2.14c – remain confined in the superconducting section and therefore contribute less to the non-local conductance.

The absence of a clear bulk-gap closing and reopening signal in such a setup makes it essentially impossible to determine the location of the topological phase transition measuring local and non-local conductances and therefore it is also not possible to conclusively determine whether the system hosts MBSs or two quasi-MBSs. Although discussed here for long topological nanowires, this behavior also occurs in short topological nanowires.

2.E Interplay between quasi-MBSs at the left end and ABS at the right end of a short topological nanowire

Finally, we consider a short topological nanowire with quasi-MBSs on the left end and an ABS on the right end. The ABS is again tuned so that it mimics a bulk-gap

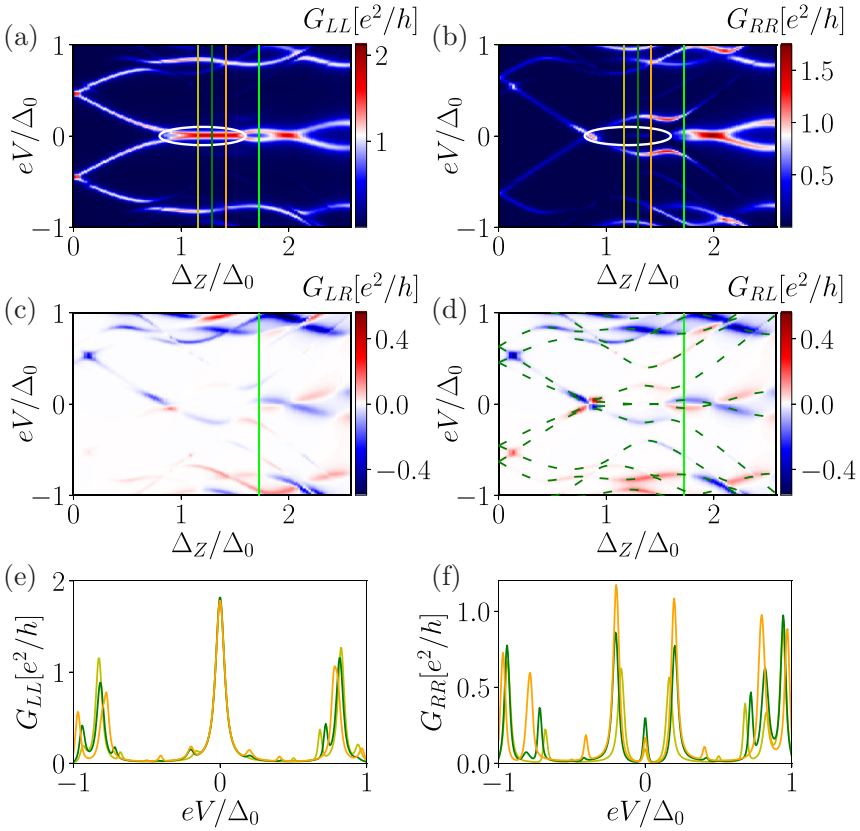

Figure 2.15: Same as Fig. 2.10 but for the nanowire containing an additional right normal section hosting an ABS, which mimics a bulk-gap closing and reopening in the non-local conductances close to $\Delta_Z \approx 0.9\Delta_0$. The left quasi-MBSs are visible in the local conductances (a) G_{LL} and (b) G_{RR}. However, in G_{RR} they are less pronounced. The non-local conductances (c) G_{LR} and (d) G_{RL} contain features coming from the lowest bulk states as well as from the right ABS, which leaks through the superconducting section. Line cuts (e,f) of the local conductances G_{LL} and G_{RR} at the Zeeman energies $\Delta_Z = \{1.16, 1.29, 1.42\}\Delta_0$ [indicated by the yellow, dark green and orange lines in (a,b)] both contain features coming from the left quasi-MBSs. The parameters are listed in Table 2.2 in App. 2.F.

undergoing a topological phase transition. The parameter profiles of superconducting gap and chemical potential are not identical in two normal sections. We choose a smooth parameter profile at the interface between N_1 and S, and a step-like profile at the interface between S and N_2. The elements of the conductance matrix are shown in Fig. 2.15. The energy spectrum (dark green dashed lines) agrees well with features in the non-local conductance G_{RL}. The left quasi-MBSs leak through the superconducting section and generates a small ZBP in the right conductance G_{RR}, see Fig. 2.15b. This behavior is similar to the one of the setup shown in Fig. 2.10 and is again explained by the extended nature of wave functions. The ZBP originating from the left quasi-MBSs in the right local conductance is more pronounced in line cuts, see Fig. 2.15f. The energy of the right ABS decreases with increasing Zeeman

energy until it is nearly zero at the same values of the magnetic field at which the quasi-MBSs begin to be pinned to zero energy ($\Delta_Z \approx 0.9\Delta_0$). At stronger magnetic fields ($0.9\Delta_0 < \Delta_Z < 1.4\Delta_0$), the right ABS moves away from zero energy, mimicking the reopening of the bulk gap. The true topological phase transition, however, takes place only around $\Delta_Z \approx 1.74\Delta_0$. The right ABS is not only visible in G_{RR} but also in the non-local conductances, see Figs. 2.15c and 2.15d. Additionally, this ABS generates a small feature in G_{LL} which is only visible in the line cut shown in Fig. 2.15e. We note that the height of this right ABS peak in G_{LL} is comparable with the one of the energetically lowest bulk state. We conclude that, in experiments, an ABS on the right end could easily mask a topological phase transition.

2.F Parameter values

In this section, we list all parameters used in each figure, see Table 2.1 and Table 2.2. The hyphen in the table indicates that the respective parameter was not included in the calculation: For example the nanowire considered in Fig. 2.4a does not include a second normal section to the right of the superconducting section. Furthermore, the asterisks $*$ indicates that the corresponding parameter runs over a finite interval which is indicated in the figure. The parameters from Figs. 2.4g and 2.4h are the same as the ones from Figs. 2.4a and 2.4e. We choose a temperature of $T = 40$ mK in all plots except in Fig. 2.13, where we take $T = 150$ mK. Furthermore, the effective lattice constant is $a = 5$ nm in all plots. All energy values in the following tables are given in units of meV.

Table 2.1: Parameters used to model non-topological nanowires

Fig.	N_1	N_2	N_S	$N_{B,1}$	$N_{B,2}$	t_1	t_2	t_S	μ_1	μ_2	μ_S	Δ_0	Δ_Z	Δ_Z^c	α_1	$E_{so,1}$	α_2	$E_{so,2}$	γ_1	γ_2	μ_L	μ_R
2.3a	60	-	400	-	-	100	-	20	$*$	-	2	0.25	1.58	1.75	$*$	$*$	-	-	-	-	-	-
2.3b	60	-	400	-	-	100	-	20	$*$	-	2	0.25	1.31	1.75	$*$	$*$	-	-	-	-	-	-
2.3c	60	-	400	-	-	100	-	20	0.44	-	2	0.25	$*$	1.75	13.35	1.78	-	-	-	-	-	-
2.3d	60	-	400	-	-	100	-	20	0.3	-	2	0.25	$*$	1.75	7.97	0.63	-	-	-	-	-	-
2.4a	60	-	400	-	-	100	-	20	0	-	2	0.25	$*$	1.75	14.35	2.06	-	-	-	-	-	-
2.4c	60	-	400	-	-	100	-	20	0	-	2	0.09	$*$	1.75	14.35	2.06	-	-	-	-	-	-
2.4e	60	-	175	-	-	100	-	20	0	-	2	0.25	$*$	1.75	14.35	2.06	-	-	-	-	-	-
2.5	90	7	140	7	7	100	100	20	0	0	2	0.25	$*$	1.75	13.75	1.89	13.75	1.89	10	10	20	20
2.6a	60	60	400	-	-	100	100	20	0	0	2	0.25	$*$	1.75	14.35	2.06	14.35	2.06	-	-	-	-
2.6c	60	70	400	-	-	100	100	20	0	0	2	0.25	$*$	1.75	14.35	2.06	14.35	2.06	-	-	-	-
2.6e	60	40	400	-	-	100	100	20	0	0	2	0.25	$*$	1.75	14.35	2.06	10.33	1.07	-	-	-	-
2.6f	90	30	140	7	7	100	100	20	0	0	2	0.25	$*$	1.75	13.75	1.89	2.75	0.08	10	10	-	-
2.7	90	30	140	7	7	100	100	20	0	0	2	0.25	$*$	1.75	13.75	1.89	2.75	0.08	10	10	20	20
2.13b	60	7	400	7	7	100	100	20	0.3	0	2	0.25	$*$	1.75	8.80	0.77	8.80	0.77	10	5	5	5

Table 2.2: Parameters used to model topological nanowires

Fig.	N_1	N_2	N_S	$N_{B,1}$	$N_{B,2}$	t	μ_1	μ_2	μ_S	Δ_0	Δ_Z^c	α	E_{so}	γ_1	γ_2	μ_L	μ_R	$\lambda_{S,L}$	$\lambda_{S,R}$	λ_L	λ_R
2.8a	40	4	400	4	4	102	0.2	0.2	0.7	0.5	-	3.5	0.12	10	10	-	-	20	-	20	-
2.8c	40	4	120	4	4	102	0.2	0.2	0.7	0.5	-	3.5	0.12	10	10	-	-	20	-	20	-
2.9	40	4	400	4	4	102	0.2	0.2	0.7	0.5	-	3.5	0.12	10	10	20	20	20	-	20	-
2.10	40	4	120	4	4	102	0.2	0.2	0.7	0.5	-	3.5	0.12	10	10	20	20	20	-	20	-
2.11	40	48	400	4	4	102	0.2	0.1	0.7	0.5	-	3.5	0.12	10	10	20	20	20	24	20	24
2.12	4	4	140	4	4	102	0	0	0	0.7	-	3.5	0.12	10	10	20	20	-	-	-	-
2.13a	40	4	400	4	4	102	0.2	0.2	0.7	0.5	-	3.5	0.12	10	10	20	20	10	-	20	-
2.14	40	48	400	4	4	102	0.2	0.1	0.7	0.5	-	3.5	0.12	10	10	-	-	20	24	20	24
2.15	40	32	120	4	4	102	0.2	0.2	0.7	0.5	-	3.5	0.12	10	10	20	20	20	-	20	-

Bibliography

[1] A Yu Kitaev. "Unpaired Majorana fermions in quantum wires". In: Phys. Usp. 44.10S (Oct. 2001), pp. 131–136.

[2] Satoshi Fujimoto. "Topological order and non-Abelian statistics in noncentrosymmetric s-wave superconductors". In: Phys. Rev. B 77 (22 June 2008), p. 220501.

[3] Masatoshi Sato, Yoshiro Takahashi, and Satoshi Fujimoto. "Non-Abelian Topological Order in s-Wave Superfluids of Ultracold Fermionic Atoms". In: Phys. Rev. Lett. 103 (2 July 2009), p. 020401.

[4] G.E. Volovik. "Fermion zero modes at the boundary of superfluid 3He-B". In: JETP Lett. 90.5 (2009), p. 398.

[5] Yuval Oreg, Gil Refael, and Felix von Oppen. "Helical Liquids and Majorana Bound States in Quantum Wires". In: Phys. Rev. Lett. 105 (17 Oct. 2010), p. 177002.

[6] Roman M. Lutchyn, Jay D. Sau, and S. Das Sarma. "Majorana Fermions and a Topological Phase Transition in Semiconductor-Superconductor Heterostructures". In: Phys. Rev. Lett. 105 (7 Aug. 2010), p. 077001.

[7] Masatoshi Sato, Yoshiro Takahashi, and Satoshi Fujimoto. "Non-Abelian topological orders and Majorana fermions in spin-singlet superconductors". In: Phys. Rev. B 82 (13 Oct. 2010), p. 134521.

[8] Gregory Moore and Nicholas Read. "Nonabelions in the fractional quantum hall effect". In: Nucl. Phys. B 360.2 (1991), pp. 362–396.

[9] G. E. Volovik. "Fermion zero modes on vortices in chiral superconductors". In: Journal of Experimental and Theoretical Physics Letters 70.9 (1999), pp. 609–614.

[10] N. Read and Dmitry Green. "Paired states of fermions in two dimensions with breaking of parity and time-reversal symmetries and the fractional quantum Hall effect". In: Phys. Rev. B 61 (15 Apr. 2000), pp. 10267–10297.

[11] T. Senthil and Matthew P. A. Fisher. "Quasiparticle localization in superconductors with spin-orbit scattering". In: Phys. Rev. B 61 (14 Apr. 2000), pp. 9690–9698.

[12] D. A. Ivanov. "Non-Abelian Statistics of Half-Quantum Vortices in p-Wave Superconductors". In: Phys. Rev. Lett. 86 (2 Jan. 2001), pp. 268–271.

[13] Chetan Nayak et al. "Non-Abelian anyons and topological quantum computation". In: Rev. Mod. Phys. 80 (3 Sept. 2008), pp. 1083–1159.

[14] Jason Alicea. "New directions in the pursuit of Majorana fermions in solid state systems". In: Rep. Prog. Phys. 75.7 (June 2012), p. 076501.

[15] C.W.J. Beenakker. "Search for Majorana Fermions in Superconductors". In: Annu. Rev. Condens. Matter Phys. 4.1 (2013), pp. 113–136.

[16] K. T. Law, Patrick A. Lee, and T. K. Ng. "Majorana Fermion Induced Resonant Andreev Reflection". In: Phys. Rev. Lett. 103 (23 Dec. 2009), p. 237001.

[17] A. R. Akhmerov, Johan Nilsson, and C. W. J. Beenakker. "Electrically Detected Interferometry of Majorana Fermions in a Topological Insulator". In: Phys. Rev. Lett. 102 (21 May 2009), p. 216404.

[18] Karsten Flensberg. "Tunneling characteristics of a chain of Majorana bound states". In: Phys. Rev. B 82 (18 Nov. 2010), p. 180516.

[19] M Wimmer et al. "Quantum point contact as a probe of a topological superconductor". In: New J. Phys. 13.5 (May 2011), p. 053016.

[20] Denis Chevallier and Jelena Klinovaja. "Tomography of Majorana fermions with STM tips". In: Phys. Rev. B 94 (3 July 2016), p. 035417.

[21] Elsa Prada, Pablo San-Jose, and Ramón Aguado. "Transport spectroscopy of NS nanowire junctions with Majorana fermions". In: Phys. Rev. B 86 (18 Nov. 2012), p. 180503.

[22] S. Das Sarma, Jay D. Sau, and Tudor D. Stanescu. "Splitting of the zero-bias conductance peak as smoking gun evidence for the existence of the Majorana mode in a superconductor-semiconductor nanowire". In: Phys. Rev. B 86 (22 Dec. 2012), p. 220506.

[23] Diego Rainis et al. "Towards a realistic transport modeling in a superconducting nanowire with Majorana fermions". In: Phys. Rev. B 87 (2 Jan. 2013), p. 024515.

[24] Olesia Dmytruk and Jelena Klinovaja. "Suppression of the overlap between Majorana fermions by orbital magnetic effects in semiconducting-superconducting nanowires". In: Phys. Rev. B 97 (15 Apr. 2018), p. 155409.

[25] C. Fleckenstein et al. "Decaying spectral oscillations in a Majorana wire with finite coherence length". In: Phys. Rev. B 97 (15 Apr. 2018), p. 155425.

[26] Satoshi Sasaki et al. "Topological Superconductivity in $\mathrm{Cu}_x\mathrm{Bi}_2\mathrm{Se}_3$". In: Phys. Rev. Lett. 107 (21 Nov. 2011), p. 217001.

[27] V. Mourik et al. "Signatures of Majorana Fermions in Hybrid Superconductor-Semiconductor Nanowire Devices". In: Science 336.6084 (2012), pp. 1003–1007.

[28] M. T. Deng et al. "Anomalous Zero-Bias Conductance Peak in a Nb–InSb Nanowire–Nb Hybrid Device". In: Nano Lett. 12 (12 Dec. 2012), pp. 6412–6419.

[29] Anindya Das et al. "Zero-bias peaks and splitting in an Al–InAs nanowire topological superconductor as a signature of Majorana fermions". In: Nat. Phys. 8 (12 2012), pp. 887–895.

[30] H. O. H. Churchill et al. "Superconductor-nanowire devices from tunneling to the multichannel regime: Zero-bias oscillations and magnetoconductance crossover". In: Phys. Rev. B 87 (24 June 2013), p. 241401.

[31] S. M. Albrecht et al. "Exponential protection of zero modes in Majorana islands". In: Nature 531.7593 (2016), pp. 206–209.

[32] Lucas Schneider et al. "Precursors of Majorana modes and their length-dependent energy oscillations probed at both ends of atomic Shiba chains". In: Nature Nanotechnology 17.4 (2022), pp. 384–389.

[33] T. Ö. Rosdahl et al. "Andreev rectifier: A nonlocal conductance signature of topological phase transitions". In: Phys. Rev. B 97 (4 Jan. 2018), p. 045421.

[34] Dmitry I. Pikulin et al. "Protocol to identify a topological superconducting phase in a three-terminal device". In: arXiv:2103.12217 (2021).

[35] P.G. de Gennes and D. Saint-James. "Elementary excitations in the vicinity of a normal metal-superconducting metal contact". In: Phys. Lett. 4.2 (1963), pp. 151–152.

[36] A. F. Andreev. "The thermal conductivity of the intermediate state in superconductors". In: Sov. Phys. JETP 19 (5 Nov. 1964), p. 1228.

[37] C. Caroli, P.G. De Gennes, and J. Matricon. "Bound Fermion states on a vortex line in a type II superconductor". In: Phys. Lett. 9.4 (1964), pp. 307–309.

[38] A. F. Andreev. "Electron Spectrum of the Intermediate State of Superconductors". In: Sov. Phys. JETP 22 (5 Feb. 1966), p. 455.

[39] Hiroyuki Shiba. "Classical Spins in Superconductors". In: Prog. Theor. Phys. 40.3 (Sept. 1968), pp. 435–451.

[40] A. I. Rusinov. "On the Theory of Gapless Superconductivity in Alloys Containing Paramagnetic Impurities". In: Sov. Phys. JETP 29 (1969), p. 1101.

[41] J. A. Sauls. "Andreev bound states and their signatures". In: Phil. Trans. R. Soc. 376 (2125 June 2018).

[42] Elsa Prada et al. "From Andreev to Majorana bound states in hybrid superconductor–semiconductor nanowires". In: Nature Reviews Physics 2.10 (2020), pp. 575–594.

[43] G. Kells, D. Meidan, and P. W. Brouwer. "Near-zero-energy end states in topologically trivial spin-orbit coupled superconducting nanowires with a smooth confinement". In: Phys. Rev. B 86 (10 Sept. 2012), p. 100503.

[44] Eduardo J. H. Lee et al. "Zero-Bias Anomaly in a Nanowire Quantum Dot Coupled to Superconductors". In: Phys. Rev. Lett. 109 (18 Oct. 2012), p. 186802.

[45] Jorge Cayao et al. "SNS junctions in nanowires with spin-orbit coupling: Role of confinement and helicity on the subgap spectrum". In: Phys. Rev. B 91 (2 Jan. 2015), p. 024514.

[46] Andrzej Ptok, Aksel Kobiałka, and Tadeusz Doma ński. "Controlling the bound states in a quantum-dot hybrid nanowire". In: Phys. Rev. B 96 (19 Nov. 2017), p. 195430.

[47] Chun-Xiao Liu et al. "Andreev bound states versus Majorana bound states in quantum dot-nanowire-superconductor hybrid structures: Trivial versus topological zero-bias conductance peaks". In: Phys. Rev. B 96 (7 Aug. 2017), p. 075161.

[48] Christopher Reeg et al. "Zero-energy Andreev bound states from quantum dots in proximitized Rashba nanowires". In: Phys. Rev. B 98 (24 Dec. 2018), p. 245407.

[49] Fernando Peñaranda et al. "Quantifying wave-function overlaps in inhomogeneous Majorana nanowires". In: Phys. Rev. B 98 (23 Dec. 2018), p. 235406.

[50] Christopher Moore, Tudor D. Stanescu, and Sumanta Tewari. "Two-terminal charge tunneling: Disentangling Majorana zero modes from partially separated Andreev bound states in semiconductor-superconductor heterostructures". In: Phys. Rev. B 97 (16 Apr. 2018), p. 165302.

[51] Adriaan Vuik et al. "Reproducing topological properties with quasi-Majorana states". In: SciPost Phys. 7 (2019), p. 061.

[52] Benjamin D. Woods et al. "Zero-energy pinning of topologically trivial bound states in multiband semiconductor-superconductor nanowires". In: Phys. Rev. B 100 (12 Sept. 2019), p. 125407.

[53] Chun-Xiao Liu et al. "Conductance smearing and anisotropic suppression of induced superconductivity in a Majorana nanowire". In: Phys. Rev. B 99 (2 Jan. 2019), p. 024510.

[54] J. Chen et al. "Ubiquitous Non-Majorana Zero-Bias Conductance Peaks in Nanowire Devices". In: Phys. Rev. Lett. 123 (10 Sept. 2019), p. 107703.

[55] David J. Alspaugh et al. "Volkov-Pankratov states in topological superconductors". In: Phys. Rev. Research 2 (2 May 2020), p. 023146.

[56] Christian Jünger et al. "Magnetic-Field-Independent Subgap States in Hybrid Rashba Nanowires". In: Phys. Rev. Lett. 125 (1 June 2020), p. 017701.

[57] Marco Valentini et al. "Nontopological zero-bias peaks in full-shell nanowires induced by flux-tunable Andreev states". In: Science 373.6550 (2021), pp. 82–88.

[58] E. C. T. O'Farrell et al. "Hybridization of Subgap States in One-Dimensional Superconductor-Semiconductor Coulomb Islands". In: Phys. Rev. Lett. 121 (25 Dec. 2018), p. 256803.

[59] Jie Shen et al. "Parity transitions in the superconducting ground state of hybrid InSb–Al Coulomb islands". In: Nat. Com. 9 (Nov. 2018), p. 4801.

[60] Zhan Cao et al. "Decays of Majorana or Andreev Oscillations Induced by Steplike Spin-Orbit Coupling". In: Phys. Rev. Lett. 122 (14 Apr. 2019), p. 147701.

[61] Haining Pan et al. "Generic quantized zero-bias conductance peaks in superconductor-semiconductor hybrid structures". In: Phys. Rev. B 101 (2 Jan. 2020), p. 024506.

[62] O. Entin-Wohlman, Y. Imry, and A. Aharony. "Conductance of superconducting-normal hybrid structures". In: Phys. Rev. B 78 (22 Dec. 2008), p. 224510.

[63] Alejandro M. Lobos and S Das Sarma. "Tunneling transport in NSN Majorana junctions across the topological quantum phase transition". In: New J. Phys. 17.6 (June 2015), p. 065010.

[64] J. Gramich, A. Baumgartner, and C. Schönenberger. "Andreev bound states probed in three-terminal quantum dots". In: Phys. Rev. B 96 (19 Nov. 2017), p. 195418.

[65] Hao Zhang et al. "Next steps of quantum transport in Majorana nanowire devices". In: Nat. Com. 10.1 (5 2019), p. 5128.

[66] Jeroen Danon et al. "Nonlocal Conductance Spectroscopy of Andreev Bound States: Symmetry Relations and BCS Charges". In: Phys. Rev. Lett. 124 (3 Jan. 2020), p. 036801.

[67] André Melo et al. "Conductance asymmetries in mesoscopic superconducting devices due to finite bias". In: SciPost Phys. 10 (2 2021), p. 37.

[68] Haining Pan, Jay D. Sau, and S. Das Sarma. "Three-terminal nonlocal conductance in Majorana nanowires: Distinguishing topological and trivial in realistic systems with disorder and inhomogeneous potential". In: Phys. Rev. B 103 (1 Jan. 2021), p. 014513.

[69] G. C. Ménard et al. "Conductance-Matrix Symmetries of a Three-Terminal Hybrid Device". In: Phys. Rev. Lett. 124 (3 Jan. 2020), p. 036802.

[70] D. Puglia et al. "Closing of the induced gap in a hybrid superconductor-semiconductor nanowire". In: Phys. Rev. B 103 (23 June 2021), p. 235201.

[71] P. Yu et al. "Non-Majorana states yield nearly quantized conductance in proximatized nanowires". In: Nat. Phys. 17.4 (2021), pp. 482–488.

[72] Christopher Reeg, Daniel Loss, and Jelena Klinovaja. "Finite-size effects in a nanowire strongly coupled to a thin superconducting shell". In: Phys. Rev. B 96 (12 Sept. 2017), p. 125426.

[73] Christopher Reeg, Daniel Loss, and Jelena Klinovaja. "Metallization of a Rashba wire by a superconducting layer in the strong-proximity regime". In: Phys. Rev. B 97 (16 Apr. 2018), p. 165425.

[74] Christopher Reeg, Daniel Loss, and Jelena Klinovaja. "Proximity effect in a two-dimensional electron gas coupled to a thin superconducting layer". In: Beilstein J. Nanotechnol 9 (2018), pp. 1263–1271.

[75] Benjamin D. Woods, Sankar Das Sarma, and Tudor D. Stanescu. "Electronic structure of full-shell InAs/Al hybrid semiconductor-superconductor nanowires: Spin-orbit coupling and topological phase space". In: Phys. Rev. B 99 (16 Apr. 2019), p. 161118.

[76] Georg W. Winkler et al. "Unified numerical approach to topological semiconductor-superconductor heterostructures". In: Phys. Rev. B 99 (24 June 2019), p. 245408.

[77] Thomas Kiendl, Felix von Oppen, and Piet W. Brouwer. "Proximity-induced gap in nanowires with a thin superconducting shell". In: Phys. Rev. B 100 (3 July 2019), p. 035426.

[78] Jelena Klinovaja and Daniel Loss. "Fermionic and Majorana bound states in hybrid nanowires with non-uniform spin-orbit interaction". In: Eur. Phys. J. B 88.3 (2015), p. 62.

[79] Yingyi Huang et al. "Metamorphosis of Andreev bound states into Majorana bound states in pristine nanowires". In: Phys. Rev. B 98 (14 Oct. 2018), p. 144511.

[80] Pavel P. Aseev, Jelena Klinovaja, and Daniel Loss. "Lifetime of Majorana qubits in Rashba nanowires with nonuniform chemical potential". In: Phys. Rev. B 98 (15 Oct. 2018), p. 155414.

[81] Tobias Gulden et al. "Universal Finite-Size Scaling around Topological Quantum Phase Transitions". In: Phys. Rev. Lett. 116 (2 Jan. 2016), p. 026402.

[82] Marcel Serina, Daniel Loss, and Jelena Klinovaja. "Boundary spin polarization as a robust signature of a topological phase transition in Majorana nanowires". In: Phys. Rev. B 98 (3 July 2018), p. 035419.

[83] Fan Yang, Shao-Jian Jiang, and Fei Zhou. "Robust cusps near topological phase transitions: Signatures of Majorana fermions and interactions with fluctuations". In: Phys. Rev. B 100 (5 Aug. 2019), p. 054508.

[84] Shun Tamura, Shintaro Hoshino, and Yukio Tanaka. "Odd-frequency pairs in chiral symmetric systems: Spectral bulk-boundary correspondence and topological criticality". In: Phys. Rev. B 99 (18 May 2019), p. 184512.

[85] Doru Sticlet, Cătălin Paşcu Moca, and Balázs Dóra. "All-electrical spectroscopy of topological phases in semiconductor-superconductor heterostructures". In: Phys. Rev. B 102 (7 Aug. 2020), p. 075437.

[86] Mahdi Mashkoori et al. "Identification of topological superconductivity in magnetic impurity systems using bulk spin polarization". In: Phys. Rev. B 102 (10 Sept. 2020), p. 104501.

[87] Paweł Szumniak et al. "Spin and charge signatures of topological superconductivity in Rashba nanowires". In: Phys. Rev. B 96 (4 July 2017), p. 041401.

[88] Denis Chevallier et al. "Topological phase detection in Rashba nanowires with a quantum dot". In: Phys. Rev. B 97 (4 Jan. 2018), p. 045404.

[89] Christoph W Groth et al. "Kwant: a software package for quantum transport". In: New Journal of Physics 16.6 (June 2014), p. 063065.

[90] G. E. Blonder, M. Tinkham, and T. M. Klapwijk. "Transition from metallic to tunneling regimes in superconducting microconstrictions: Excess current, charge imbalance, and supercurrent conversion". In: Phys. Rev. B 25 (7 Apr. 1982), pp. 4515–4532.

[91] Benjamin M. Fregoso, Alejandro M. Lobos, and S. Das Sarma. "Electrical detection of topological quantum phase transitions in disordered Majorana nanowires". In: Phys. Rev. B 88 (18 Nov. 2013), p. 180507.

[92] Grzegorz Michałek et al. "Interplay between direct and crossed Andreev reflections in hybrid nanostructures". In: Phys. Rev. B 88 (15 Oct. 2013), p. 155425.

[93] James J. He et al. "Selective Equal-Spin Andreev Reflections Induced by Majorana Fermions". In: Phys. Rev. Lett. 112 (3 Jan. 2014), p. 037001.

CHAPTER 3

Trivial Andreev band mimicking topological bulk gap reopening in the non-local conductance of long Rashba nanowires

Adapted from:
Richard Hess, Henry F. Legg, Daniel Loss, and Jelena Klinovaja
"Trivial Andreev Band Bimicking Topological Bulk Gap Reopening in the Nonlocal Conductance of Long Rashba Nanowires",
Phys. Rev. Let. **130**, 207001 (2023)

We consider a one-dimensional Rashba nanowire in which multiple Andreev bound states in the bulk of the nanowire form an Andreev band. We show that, under certain circumstances, this trivial Andreev band can produce an apparent closing and reopening signature of the bulk band gap in the non-local conductance of the nanowire. Furthermore, we show that the existence of the trivial bulk reopening signature (BRS) in non-local conductance is essentially unaffected by the additional presence of trivial zero-bias peaks (ZBPs) in the local conductance at either end of the nanowire. The simultaneous occurrence of a trivial BRS and ZBPs mimics the basic features required to pass the so-called 'topological gap protocol'. Our results therefore provide a topologically trivial minimal model by which the applicability of this protocol can be benchmarked.

3.1 Introduction

Majorana bound states (MBSs) are predicted to appear in the cores of vortices or at boundaries of topological superconductors [1–5]. The non-Abelian statistics of MBSs make them highly promising candidates for fault tolerant topological quantum computing [6–11]. However, so far, despite significant efforts, there has been no conclusive experimental observation of MBSs. The most heavily investigated platform purported to host MBSs are hybrid semiconductor-superconductor devices. These devices consist of a semiconductor nanowire with strong Rashba spin-orbit interaction (SOI) – for instance InSb or InAs – that has been brought into proximity with a superconductor – for instance NbTiN or Al [12–16]. Although the presence of zero-bias peaks (ZBPs) in local conductance measurements initially appeared promising evidence for MBSs in such devices [12–15, 17], it was subsequently realized that the same signature could be produced by trivial effects, for instance Andreev bound states (ABSs) [18–40].

Trivial mechanisms that mimic the expected experimental signatures of the topological superconducting phase have significantly complicated the search for MBSs. Several auxiliary features have been suggested to provide further clarity for the origin of a ZBP. Examples include, oscillations around zero energy due to the overlap of the MBSs in short nanowires [41–45], the flip of the lowest band spin polarization [46, 47], correlated ZBPs at either end of the nanowire, the superconducting diode effect [48, 49], and a quantized conductance peak with height $2e^2/h$ [50–54]. Although oscillations and correlated ZBPs have been experimentally observed [12–15, 17, 55, 56], these signatures can also be explained by trivial mechanisms [28, 57, 58].

Seperately, it has been proposed that non-local conductance measurements in three-terminal devices – for instance, as shown in Fig. a – can detect the bulk gap closing and reopening that is associated with the phase transition to topological superconductivity, potentially providing a signature for the bulk topology of the nanowire [59–68]. In particular, it is important that the length of the proximitized region in a device is much longer than the localization length of the induced superconductivity in the nanowire, otherwise a trivial bulk reopening signature (BRS) can arise simply due to the avoided crossing of close to zero-energy ABSs [37]. When arising due to a topological phase transition, the BRS in non-local conductance provides an upper bound for the size of the topological energy gap [67, 69]. Based on these ideas, a so-called *topological gap protocol* (TGP) has been proposed [67]. The basic features required to pass this protocol are correlated ZBPs at either end of the nanowire in combination with a BRS. Recently, state-of-the-art experimental devices were reported to have passed this protocol [69].

In this paper we consider trivial mechanisms that can mimic the basic features of the topological gap protocol in nanowire devices, where the length of the proximitized nanowire is significantly longer than the localization length of the induced superconductivity. While trivial origins of ZBPs have been discussed extensively in the literature [20–31, 33–38], trivial mechanisms that mimic the BRS are much less understood. First, we show that it is possible for multiple ABSs to form a band inside the superconducting gap. In particular, when approximately periodically

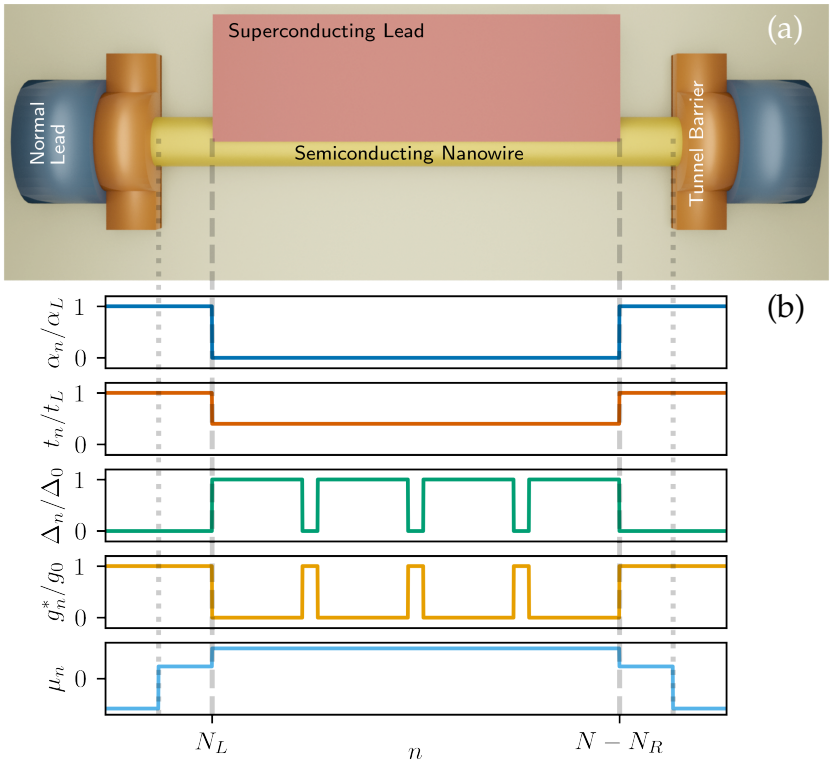

Figure 3.1: *Schematic sketch of a three-terminal device and a typical set of parameter profiles supporting the formation of an Andreev band.* (a) A grounded superconducting lead (red) is attached to a semiconducting nanowire (yellow). Normal leads (blue), connected to the ends of the nanowire and tunnel barriers (orange), control the transparency of the interface between the normal leads and the nanowire. Experimentally several different device architectures exist but the basic features for theoretical modeling remain the same in all cases. (b) Typical parameter profile used to model ABSs forming an Andreev band and the ZBPs at either end of the nanowire.

spatially distributed and at similar energies, the states within the Andreev band can have a finite support throughout the nanowire. As a result we find that this Andreev bandcan result in a non-local conductance signal reminiscent of a BRS. Furthermore, we combine this trivial BRS with known mechanisms for trivial ZBPs at each end of the nanowire and show that a trivial BRS and correlated ZBPs can occur independently. Finally, we discuss the consequences for future experimental probes of topological superconducting phases.

3.2 Model

The real-space Hamiltonian of the one-dimensional Rashba nanowire, brought into proximity with a superconductor and subject to an external magnetic field, is given

by [3, 4, 37]

$$H = \sum_{n=1}^{N} \Bigg(\sum_{\nu,\nu'} c_{n,\nu}^{\dagger} \Bigg[\left(-t_{n+\frac{1}{2}} \delta_{\nu\nu'} + i\alpha_{n+\frac{1}{2}} \sigma_{\nu\nu'}^{z} \right) c_{n+1,\nu'} + \frac{1}{2} \Big\{ \left(t_{n+\frac{1}{2}} + t_{n-\frac{1}{2}} - \mu_n \right) \delta_{\nu\nu'} + \Delta_{Z,n} \sigma_{\nu\nu'}^{x} \Big\} c_{n,\nu'} \Bigg] + \Delta_n c_{n,\downarrow}^{\dagger} c_{n,\uparrow}^{\dagger} + \text{H.c.} \Bigg), \tag{3.1}$$

where $c_{n,\nu}^{\dagger}$ ($c_{n,\nu}$) creates (annihilates) an electron at site n with spin $\nu = \uparrow, \downarrow$ in a one-dimensional chain with a total number of N sites. The Pauli matrices $\sigma_{\nu\nu'}^{l}$, with $l \in \{x, y, z\}$, act in spin space. All parameter profiles, namely hopping $t_{n\pm\frac{1}{2}}$, the proximity induced superconducting gap Δ_n, the chemical potential μ_n, the Rashba SOI strength α_n, and the Zeeman energy $\Delta_{Z,n}$ are assumed to be position dependent, indicated by the index n. A typical parameter profile is shown in Fig. b and the full mathematical expressions used can be found in the Supplemental Material (SM) [1].

Throughout we will distinguish between *interior* and *exterior* ABSs depending on whether a given ABS occurs in the bulk or at the ends of the nanowire, respectively. The position distinguishing the bulk and ends of the nanowires is indicated by gray dashed lines in Fig. b. Interior ABSs arise due to *interior normal sections* that are modeled by a vanishing local proximity gap and increase in g-factor at certain positions within the bulk of the nanowire. We consider distributions of interior normal sections over the full length of the nanowire that allow the formation of an Andreev band within the superconducting gap (see below). For simplicity ABSs are created using normal sections, but a modification of g-factor alone is sufficient to create the Andreev band that results in a trivial BRS (see SM [**Note1**]). Separately, in order to enable the nanowire to host zero-energy exterior ABSs at its ends we also model normal sections on the left and right end, which we call *exterior normal sections*, consisting of N_L and N_R sites, respectively.

3.3 The Andreev Band

We first develop a mechanism for the formation of a trivial band formed from Andreev bound states inside the superconducting gap based on the interplay of multiple ABSs. We will later consider the impact of this trivial band on non-local transport and trivial ZBPs. If individual ABSs are distributed in a quasi-periodic way and if, in addition, the separation between the ABSs is of the order of the superconducting coherence length, then the individual ABSs partially overlap and hybridize to form a band of Andreev states. In contrast to the individual ABSs, which are

[1] Supplemental Material. We present more details on the transport calculations, in particular, about the S-matrix and the topological visibility Q. We discuss disorder and scenarios in which the conditions for the appearance of the ABSs can be relaxed. Moreover, we consider an alternative mechanism for the formation of the Andreev band as an academic example and discuss the possibility of other trivial mechanisms leading to BRSs. Furthermore, we tabulate all parameter values used in the simulations. The Supplemental Material includes the additional Refs. [70–76], which do not appear in the main text.

well localized, the states within this band can have a finite support throughout the nanowire. As such, we will call this band of extended Andreev states an *Andreev band* due its strong similarity with the well studied Shiba band [77–79]. We emphasize that, unlike previous proposals for topological phases due to inhomogeneous superconductivity [80, 81], the system we consider here remains trivial for all values of magnetic field. In particular, this is ensured because the bulk g-factor is zero apart from in the normal sections that form the Andreev band and/or the SOI vanishes in the bulk of the nanowire.

Since the states in the Andreev band are extended they can connect the left and right normal lead and hence are visible in non-local differential conductances. The Andreev band emerges around the energy of the individual ABSs that form it and the bandwidth is determined by the overlap of the ABSs, which is related to the separation length between the ABSs. We note that, within our minimal model, the band width of the Andreev band is normally smaller than the size of the bulk superconducting gap such that there is usually a finite gap between bulk superconducting states and Andreev band states.

3.4 Trivial bulk reopening signature

To study the transport consequences of the delocalized states in the Andreev band, we first consider a profile with periodically distributed variations in the induced proximity gap and g-factor along the nanowire, as shown in Fig. a. ABSs created as a result of this profile have the majority of their weight in the normal sections and hybridize to form highly extended states, as shown by the probability densities in Fig. c. We note that, even though we do not consider zero-energy exterior ABSs here, short exterior normal sections are present in the model to provide tunnel barriers for the differential conductance computation, which we perform with the Python package Kwant [82].

Due to the variation in the g-factor between the normal and superconducting sections, the energies of states which form the Andreev band have a different slope as a function of Zeeman field than states with the majority of their weight in the superconducting sections, as shown in Fig. b. Here, the Zeeman field is defined as $\Delta_Z = g_0\mu_B B/2$, where μ_B is the Bohr magneton, B the magnetic field, and g_0 is the g-factor in the normal sections. Importantly, the larger g-factor means that the Andreev band states cross zero energy considerably before the closing of the bulk superconducting gap and therefore mimic a topological BRS in the energy spectrum. We note that for our model, the slope of the energies as a function of the Zeeman field is non-linear since we consider the superconducting gap to be a function of the Zeeman field and states leak into the regions with reduced g-factor, such that the average Zeeman field experienced by the ABSs is reduced.

The zero-energy crossing of the Andreev band states results in gapped regions of phase space that are entirely surrounded by regions that are essentially gapless, i.e. with a very small lowest energy state E_0, see Fig. d and also Sec. 3.G. This behaviour of the bulk spectrum is the same when there is a topological region. Nonlocal conductance, however, measures the transport gap since it is sensitive only to

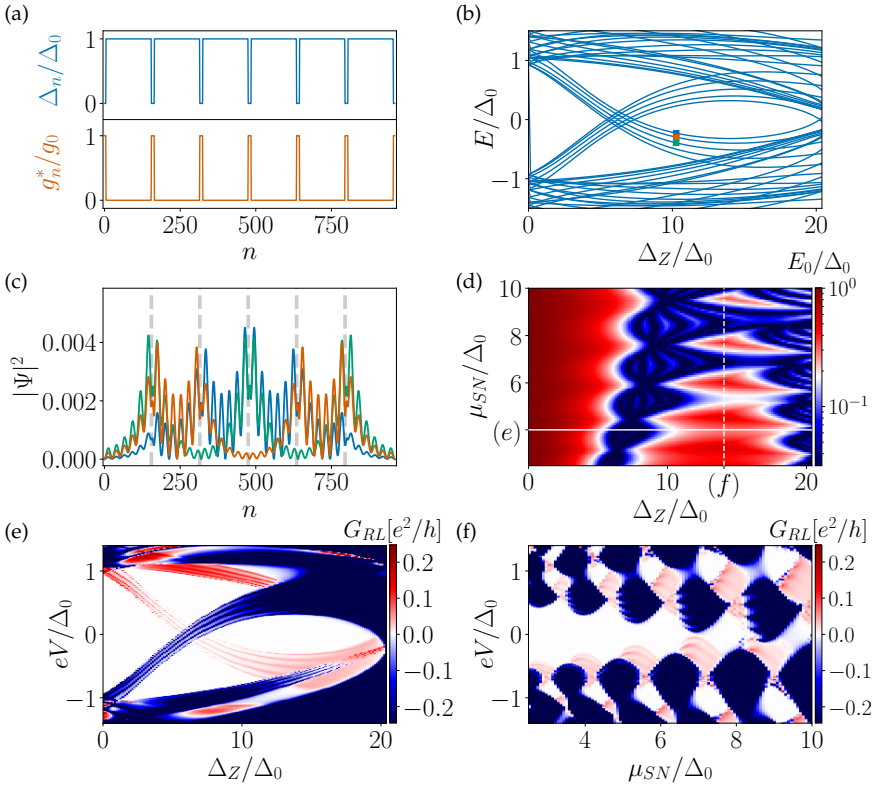

Figure 3.2: *Formation of the Andreev band*: (a) Spatial profiles of the induced superconducting gap and of the g-factor at zero Zeeman field in terms of their maximal zero-field values Δ_0 and g_0, respectively. The combination of the two profiles leads to the formation of an Andreev band inside the superconducting gap. (b) Energy spectrum of the Rashba nanowire, with Andreev band, as a function of Zeeman field. (c) Probability densities of the extended trivial Andreev states at the positions marked by the colored squares in panel (b). Gray dashed vertical lines indicate the position of the normal sections. Due to the hybridization of ABSs that form in the normal sections, the Andreev states extend throughout the nanowire. (d) Lowest energy as a function of Zeeman field and chemical potential. (e)[(f)] Non-local differential conductance G_{RL} as a function of Zeeman field [chemical potential] calculated at the chemical potential [Zeeman field] indicated by the white horizontal [vertical] line in panel (d). Parameters: $a = 4$ nm; $(N_L = N_R = N_{B,L} = N_{B,R}, N_S, N_N) = (5, 150, 10)$; $M = 6$; $(t_L = t_R = t_{SN}, \Delta_0, \Delta_Z^c, \alpha_L = \alpha_R, \gamma_L = \gamma_R, \mu_{Lead,L} = \mu_{Lead,R}) \approx (158, 0.6, 12.2, 0, 5, 5)$ meV; $T = 0$: see also Sec. 3.J.

states that connect left and right leads. As shown in Figs. e and f, the extended nature of the states that form the Andreev band means that these are indeed visible in the non-local conductance. Therefore, the zero-energy crossing of the Andreev band states can mimic the transport gap closing and reopening for regions of phase space, even though, by design, the system remains entirely trivial.

3.5 Combination of trivial effects

We now combine the trivial BRS due to an Andreev band with trivial ZBPs due to exterior ABSs at the ends of the nanowire, such zero-energy ABSs have previously been shown to be abundant in Rashba nanowires [20–38, 40]. Together, these trivial features mimic the key transport signatures of the topological gap protocol, namely, the exterior ABSs result in ZBPs on either end of the nanowire and the Andreev band results in a trivial BRS. To generate the ZBPs we tune the system to a certain resonance condition for SOI strength and the length of the normal sections, in order to pin the exterior ABSs to zero energy, see Refs. [25, 37] for more details. However, the particular mechanism causing ZBPs at the ends of the nanowire is not the main subject of this paper and this mechanism can be exchanged for any other that results in ZBPs, as long as the formation of the Andreev band is not affected. As previously, we set the Rashba SOI strength to zero in the superconducting sections of the nanowire which ensures the system is always in the trivial phase. In fact, the Rashba SOI is in our model only non-zero in the normal sections at the ends of the system to provide a control knob in the simulation for the zero-energy pinning of the exterior ABSs.

In Fig. a we show the energy spectrum of a system which combines the trivial BRS due to the Andreev band and trivial states with almost zero energy. Here, we tune the right exterior ABS slightly away from zero energy, in order to show that the exterior ABSs are independent of each other. In addition to the spectrum, we also calculate the topological visibility Q [83, 84], which is positive over the majority of the range of Zeeman field strengths, as expected since our system is always in the trivial phase, see Fig. b. We note that when Andreev band states cross zero energy then the unitary property of the reflection matrix breaks down and Q is ill-defined, see the Sec. 3.F.

Finally, the differential conductance matrix elements are shown in Figs. c-f. The trivial ZBPs due to the ABSs localized at both ends of the nanowire, are clearly visible in the local differential conductances, see Figs. c and d, but they do not appear in the non-local conductance, as expected for the ZBP signatures predicted for well separated MBSs in long nanowires [37, 66]. The Andreev band is visible in the non-local conductance and is also weakly pronounced in the local conductance. Hence, the Andreev band results in signature that mimics a topological BRS also in the case where trivial ZBPs occur at either end of the nanowire.

3.6 Experimental relevance and outlook

Our mechanism for a trivial BRS requires that a few ABSs occur at similar energies and are approximately equally spatially distributed within the bulk of the nanowire. Local conductance measurements on experimental state-of-the-art Rashba nanowire devices reveal many subgap states, indicating that many ABSs remain prevalent even in high quality devices [69]. We also note that, due to the long localization length of bound states in current nanowires (normally at least several 100 nm [69]), the distribution only needs to include a small number of ABSs, even

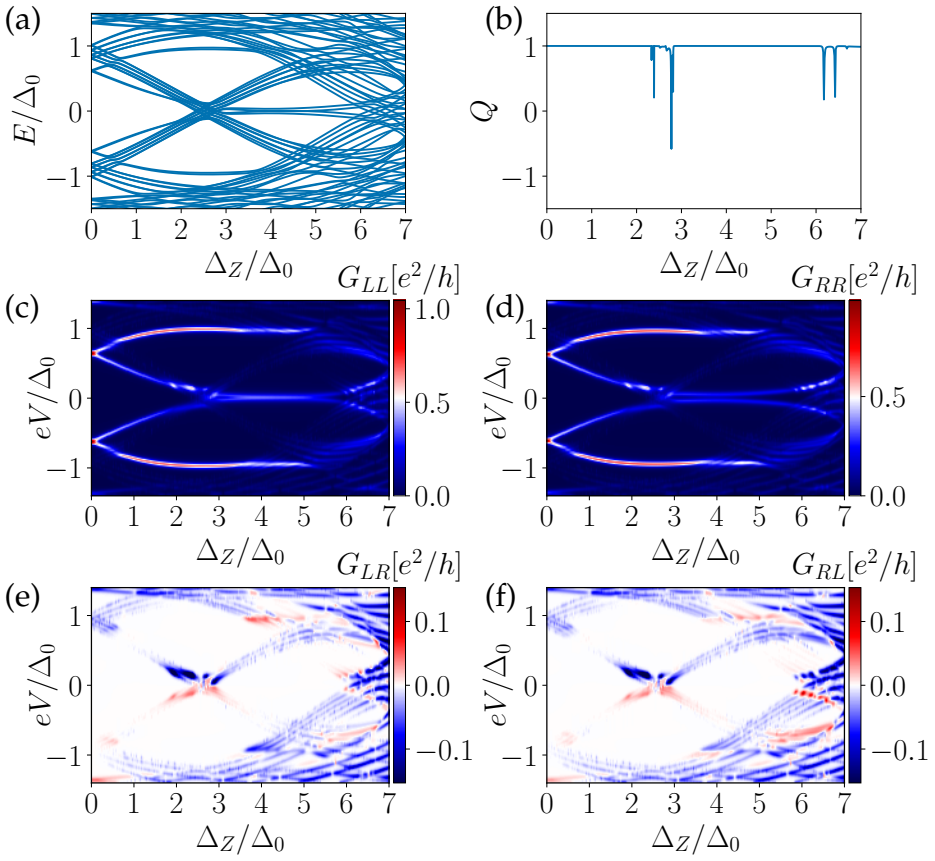

Figure 3.3: *Combination of the Andreev band with zero-energy states*: (a) Energy spectrum showing the Andreev band crossing zero energy at the Zeeman field strength at which exterior ABSs are pinned to zero energy. (b) The topological visibility indicates the trivial nature of the system for all Zeeman fields. (c,d) Local differential conductance calculated on the left and on the right end of the nanowire, showing pronounced ZBPs. (e,f) Non-local conductances showing that the BRS is essentially unaffected by the presence of the ZBPs. Parameters: $a = 5$ nm; $(N_L, N_R, N_S, N_N, N_{B,L} = N_{B,R}) = (90, 94, 140, 30, 7)a$; $M = 5$; $(t_L = t_R, t_{SN}, \mu_L = \mu_R, \mu_{SN}, \Delta_0, \Delta_Z^c, \alpha_L, \alpha_R, \gamma_L = \gamma_R, \mu_{Lead,L} = \mu_{Lead,R}) = (100, 20, 0, 2, 0.25, 1.75, 13.75, 13.20, 10, 40)$ meV; $T = 40$ mK. See also Sec. 3.J.

in nanowires with lengths of several micrometers. More precisely we find the Andreev band in systems with a length of $L \lesssim 10$ localization lengths can tolerate sizeable deviations from a periodic distribution, see Sec. 3.E for a systematic analysis. The prevalence of ABSs in current devices and the small number of ABSs required means that it is likely there are regions of parameter space in current devices where a trivial BRS can occur. Due to their independence, the probability of the combination of trivial ZBPs and trivial BRS occurring simultaneously, can be approximated from the number of occurrences of each individual signature.

We want to emphasize that the mechanism described above is much more general than the trivial BRS due to avoided crossing of ABSs in short nanowires described previously [37]. The Andreev band mechanism for a trivial BRS is relevant

for systems longer than the localization length. Additionally, the Andreev band contains many states that contribute to the trivial BRS and is therefore much more reminiscent of a bulk signature.

Our results suggest a roadmap to conclusively observe MBSs in nanowire devices. First, it remains crucial to determine the magnitude of the necessary parameters, such as SOI, in the presence of a superconductor where metallization effects can drastically reduce their values [85]. With this in mind, it might be desirable to switch device architecture or material platform to increase the phase space for MBSs and/or associated energy scales [86–88]. Second, the idea of combining multiple indicators, as suggested by TGP, can reduce the probability that trivial mechanisms simultaneously result in similar signatures as a topological phase transition for large continuous regions of phase space. In addition to local and non-local conductance, further auxiliary features (see the introduction [41–54]) could also be utilized to increase confidence that the topological phase transition is really being observed. Reducing disorder further lowers the probability of many trivial mechanisms for MBS indicators, including the trivial BRS discussed here. Finally, as discussed above, the trivial BRS becomes less likely when the length of the system is increased. Practically, this means that nanowires should be made with a length that is substantially longer than the superconducting coherence length, such that the probability of a trivial BRS in non-local conductance is suppressed, see Sec. 3.E.

3.7 Conclusion

We have shown here that, when approximately equally distributed throughout the nanowire and at similar energies, multiple ABSs can hybridize to form an Andreev band within the proximity induced superconducting gap of a Rashba nanowire. This Andreev band can cross zero-energy and therefore mimics a topological bulk closing and reopening signature. The trivial BRS discussed here can be easily combined with well-known mechanisms for trivial ZBPs since we find both phenomena are essentially independent of each other. Our simple model contains the basic features of the topological gap protocol [67, 69] and thus can serve as a basis for the applicability of this protocol. In particular, such a mechanism can provide a benchmark as to whether ZBPs in local conductance and a BRS in non-local conductance alone are sufficient to distinguish a trivial and topological phase, especially when these signatures occur in only a small region of phase space.

3.8 Acknowledgments

We thank Lucas Casparis, Leo Kouwenhoven, Yuval Oreg, Saulius Vaitiekėnas, and Marco Valentini for useful conversations. This project has received funding from the European Union's Horizon 2020 research and innovation programme under Grant Agreement No 862046 and under Grant Agreement No 757725 (the ERC Starting Grant). This work was supported by the Georg H. Endress Foundation and the Swiss National Science Foundation.

3.A Parameter profiles

We define the boundary between the left exterior normal section and the first section with induced superconductivity as $N_b = N_L + 1/2$. If the system has in total M sections each consisting of N_S lattice sites with induced superconductivity and $M-1$ interior normal sections with N_N lattice sites in between the superconducting sections, then we can define also a boundary between the last superconducting section, counting from left to right, and the exterior normal section on the right side as $N_b' = N_1 + (M-1)(N_S + N_N) + N_S + 1/2$. Finally, we define the hopping matrix elements t_n and the chemical potential μ_n via the auxiliary function

$$\eta_n = \eta_L \Theta(N_b - n) + \eta_{SN}\left[\Theta(n - N_b) - \Theta(n - N_b')\right] + \eta_R \Theta(n - N_b'),$$

where $\eta = \{t, \mu\}$. Here, t_L (t_R) [μ_L (μ_R)] denotes the hopping matrix element [chemical potential] in the exterior normal section on the left (right) side of the nanowire, $\Theta(n)$ is the Heaviside function with the definition $\Theta(0) = 1/2$, and t_{SN} [μ_{SN}] is the hopping matrix element [chemical potential] in the superconducting sections and the interior normal sections. We note that we do not change the hopping element (chemical potential) in the interior normal sections, since the difference $t_L - t_{SN}$ [$\mu_L - \mu_{SN}$] serves only the purpose of pinning the exterior ABSs to zero energy. In addition, we incorporate tunnel barriers

$$\gamma_n = (\gamma_L + \mu_L)\Theta(N_B - n) + (\gamma_R + \mu_R)\Theta(n - N_B'), \tag{3.2}$$

located at the ends of the nanowire, into the chemical potential via $\mu_n \to (\mu_n - \gamma_n)$. Here γ_L (γ_R) denotes the strength of the left (right) tunnel barrier and we defined $N_B = N_{B,L} + 1/2$ ($N_B' = N - N_{B,R} + 1/2$) for the left (right) tunnel barrier which consists of $N_{B,L}$ ($N_{B,R}$) lattice sites. We consider the SOI to be fully suppressed in the central region and to be non-zero only in the exterior normal sections with strength $\alpha_L(\alpha_R)$ on the left (right) side, the SOI strength profile is then given by

$$\alpha_n = \alpha_L \Theta(N_b - n) + \alpha_R \Theta(n - N_b'). \tag{3.3}$$

Additionally, we construct the profile of the induced superconducting gap as $\Delta_n = f_n \Delta$, where we used the auxiliary function

$$f_n = \sum_{j=0}^{j=M} \Lambda_n(N_L + j[N_S + N_N], N_L + j[N_S + N_N] + N_S), \tag{3.4}$$

which is constructed out of the rectangular function $\Lambda_n(n_1, n_2) = \Theta(n - n_1 - 1/2) - \Theta(n - n_2 - 1/2)$. We also make the assumption that superconductivity breaks down at a critical field strength $\Delta_Z = \Delta_Z^c$, such that $\Delta = \Delta_0\sqrt{1 - (\Delta_Z/\Delta_Z^c)^2}$, where Δ_0 is the pairing potential at zero magnetic field. Consequently, the profile of the induced superconducting gap Δ_n depends on the Zeeman field strength. Similarly to the induced superconducting gap, we define the spatially varying g-factor $g_n^*/g_0 = 1 - f_n$, which is suppressed in the sections with induced superconductivity, this can occur, for instance, due to the metallization effect [85]. Here g_0 denotes the g-factor

of the normal sections of the nanowire. This position dependent g-factor results in a Zeeman energy of the form $\Delta_{Z,n} = g_n^*/g_0\Delta_Z$, as in the main text $\Delta_Z = g_0\mu_B B/2$ is the strength of the Zeeman field, with μ_B and B denoting the Bohr magneton and the magnetic field, respectively.

3.B Minimal requirements for an Andreev band

In the main part of this paper, we considered a periodic distribution of interior normal sections, surrounded by superconducting sections. This structure of the induced gap was combined with an alternating g-factor, changing between zero and a maximal value. Here, we consider, instead, a spatial variation of the g-factor combined with a *constant* proximity induced superconducting gap, see Fig. a-d. If the g-factor is fully suppressed in certain sections of the nanowire but non-zero in short segments or at individual spatially separated lattice sites then the model can be mapped exactly on a system containing YSR states and consequently bound state appear for non-zero Zeeman fields [70, 77–79]. In this case our suggested mechanism for the formation of a band within the superconducting gap, based on overlapping ABSs, is equivalent to the well known Shiba band and an alternating g-factor alone is sufficient for the appearance of the trivial bulk reopening signature (BRS).

We note that the conditions for the Andreev band can be further relaxed: The g-factor can be non-zero in the whole nanowire as long as it takes much larger values at certain positions in space, as described via

$$g_n^*/g_0 = 1 - g_r f_n \tag{3.5}$$
$$\Delta_n = \Delta\Lambda_n(N_L, N - N_R), \tag{3.6}$$

where $g_r \in [0, 1]$ denotes the local reduction of the g-factor. The case of $g_r = 0.8$ is illustrated in Fig. e-h. In this case, the bulk states experience a non-zero Zeeman field and and the gap closes as a linear function of the Zeeman field strength. The crossing point, namely the value of the Zeeman strength, at which the Andreev band states are close to zero energy, is strongly affected by the chemical potential. In particular, the crossing point moves to smaller Zeeman strengths for decreasing chemical potential, since the localization length decreases and consequently the wave function localizes around the sections with larger g-factor and experience therefore a stronger Zeeman field.

3.C Impact of Rashba SOI on the Andreev band

So far we have neglected SOI in the nanowire in order to ensure that the system is always in the trivial phase. In this section we consider the impact of a finite Rashba SOI and show that the Andreev band can still result in a trivial BRS when SOI is present. We note that our main choice of parameters is also physically motivated by the metallization of a semiconducting nanowire due to being brought into proximity with a superconductor [85]. Metallization can strongly reduce properties such as

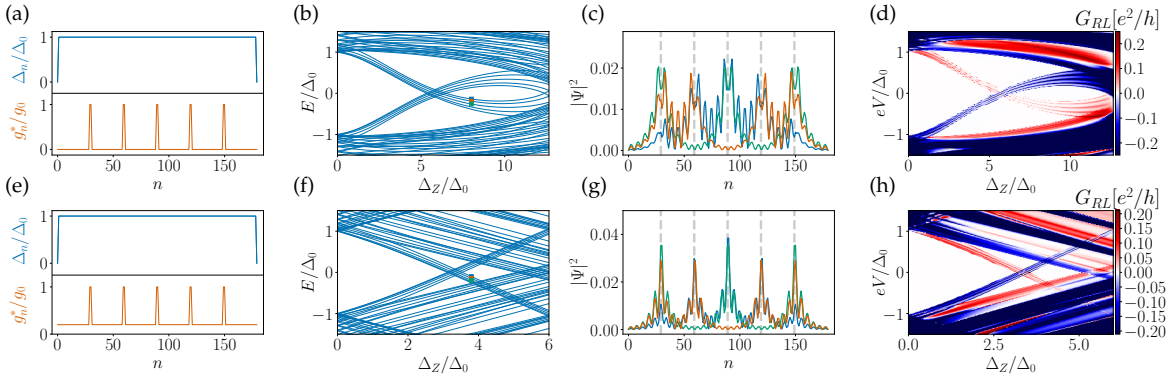

Figure 3.4: *Minimal requirements for an Andreev band*: The Andreev band appears also in case of an uniform induced superconducting gap, normal interior section are not required (First row). Moreover, the Andreev band forms also when the g-factor is non-zero in the entire nanowire, here it switches between 0.2 and 1 (Second row). (a,e) Spatial profiles of the induced superconducting gap and of the g-factor. (b,f) Energy spectra. (c,g) Extended wave functions of the states marked with the coloured squares in panel (b,f). The grey dashed vertical lines indicate the positions where the g-factor takes its maximum values. (d,h) Non-local differential conductance G_{RL}. The parameters are listed in table 3.1 and we note that we set $\Delta_Z^c \to \infty$ in the second row, which explains the linear behaviour due to the absence of SOI. The conditions on the parameter profiles, discussed in the main text, can be relaxed: The induced superconducting gap can be assumed to be constant and the g-factor does not need to vanish in any section of the proximitized nanowire, as long as it is modulated along the nanowire.

SOI energy and g-factors when the coupling between nanowire and superconductor is strong. Therefore, for instance, a spatial inhomogeneous coupling between nanowire and superconductor could result in a varying g-factor or SOI.

As shown in Fig. 3.5, the fundamental behavior that results in the Andreev band mimicking a topological BRS is not modified by the presence of Rashba SOI, although we note that SOI changes the slope of the Andreev band states with respect to the Zeeman field, especially in the vicinity of the band crossing point. Interestingly, a finite SOI in combination with the varying g-factor results in Shiba band physics [71, 77–79] such that the Andreev band actually becomes topological for a very small range of Zeeman fields close to the Andreev band crossing point. The overall spectrum, however, remains dominated by the closing and reopening of the Andreev band and our parameters – namely a large chemical potential – ensure the topological visibility is $Q = +1$ (trivial) for all Zeeman fields larger than the field associated with the Andreev band crossing point and smaller than the critical field, see Fig. f. Within the small range of Zeeman fields where the system is topological due to Shiba physics, well-localized MBSs do not occur since the effective Shiba chain is formed from only a few ABSs and the topological gap of the Shiba system is tiny compared to the gap defined by the Andreev band, see white ellipses in Figs. a

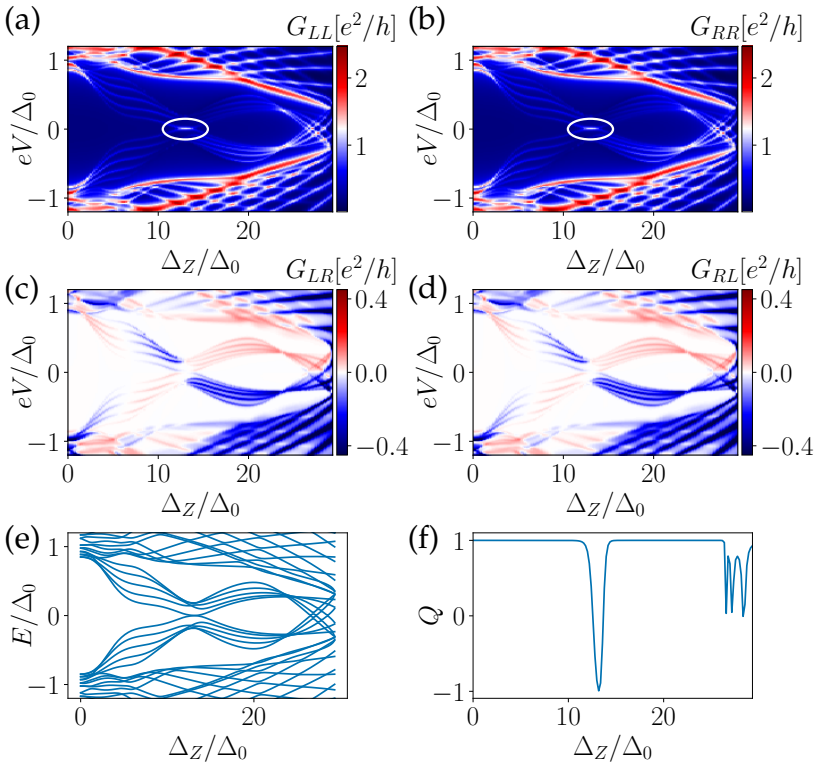

Figure 3.5: *Effect of Rashba SOI on the Andreev band*: The existence of a trivial BRS in the bulk spectrum of the nanowire is largely unaffected by the presence of a finite Rashba SOI. However, the combination of SOI, Zeeman field, and superconductivity results in Shiba physics that enables the system to enter a topological phase for a very small range of Zeeman energy close to the Andreev band crossing point. (a,b) Although local conductance remains essentially featureless, Shiba physics results in the appearance of close to zero-energy bias peaks in the local conductance for a very small range of Zeeman fields, see the regions encircled by the white ellipses. (c,d) As as in Fig. 2e of the main text, the non-local differential conductance exhibits an Andreev band that mimics a topological BRS, although SOI does change the slope of the Andreev band states with respect to the Zeeman field, especially in the vicinity of the band crossing point. (e) The energy spectrum as a function of the Zeeman field. (f) The topological visibility Q reveals the topological nature of the Andreev band in the small range of Zeeman energies close to the band crossing point where Shiba physics occurs, but also confirms the trivial nature in the vast majority of phase space. The parameters are listed in Table 3.1.

and b. The tiny size of the topological gap means that, in practice, this Shiba physics is highly unlikely to be clearly observed in experiments. In conclusion, the existence of a trivial BRS in the bulk spectrum of the nanowire is essentially unaffected by the presence of a small Rashba SOI.

3.D Alternative Ansatz for modeling the Andreev band

Here, we note that the reason for the appearance of ABSs is actually irrelevant for the formation of the Andreev band, as long as periodically distributed ABSs with similar energy exist in the system. An alternating phase of the superconducting order parameter along the nanowire, as described via

$$\Delta_n = \Delta\{[\Lambda_n(N_L, N - N_R) - f_n]e^{i\varphi} + f_n\}, \tag{3.7}$$

combined with a constant g-factor $g_n^*/g_0 = 1$ (see Fig. a-d), for example, also results in the appearance of ABSs in the Rashba nanowires and therefore enables the study of the formation of the Andreev band. This means that even if the ABSs in the experiment are caused by another mechanism than discussed in this paper, then the physics underlying the formation of the Andreev band and the corresponding requirements remain valid. Last we note that the parameter N_N which enters Eq. (3.7) via the auxiliary function f_n denotes here the number of sites in sections with different superconducting phase.

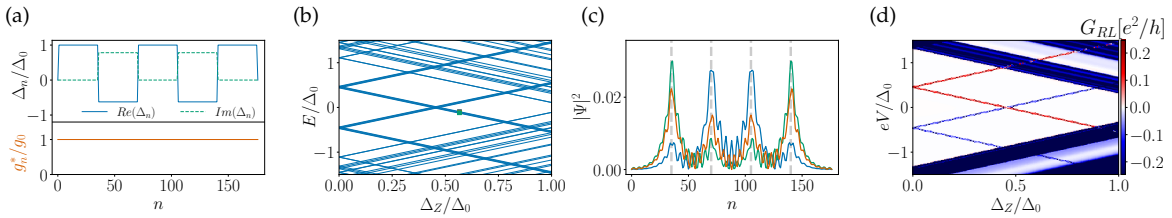

Figure 3.6: *Alternative mechanism causing the formation of the Andreev band*: We consider an induced superconducting gap with alternating phase combined with a uniform g-factor. (a) Spatial profiles of the induced superconducting gap and of the g-factor. (b) Energy spectra (c) Extended wave functions of the states marked with the coloured squares in panel (b). The grey dashed vertical lines indicate the positions where the phase of the superconductor changes (d) non-local differential conductance G_{RL}. The parameters are listed in table 3.1. We conclude that the specific profiles of induced superconducting gap and g-factor are not relevant for the formation of the Andreev band, as long as ABSs, with approximately equal energy, are approximately periodically distributed.

3.E Disorder

In this section, we study the effect of disorder on the formation of the Andreev band. Practically, ABSs will be randomly distributed over the whole length of the nanowire. If the energies of these ABSs differ strongly, then they do not form a band. However, if multiple ABSs are present and a subset of these ABSs are comparable in energy, then they can form a band under the condition that the remaining ABSs are sufficiently separated in space or in energy.

Based on the above considerations we will focus on the positional variation of ABSs with equal energies. In order to maximize the non-local conductance in the periodic case we place the first ABS approximately one localization length, ξ, away from the left end of the proximitized section. We note that we neglect a potential overlap of ABSs through the superconducting substrate [72]. The distance between two adjacent ABSs is set to roughly two localization lengths and the very right ABS (the last one) is separated by one localization length from the right end of the proximitized section. The proximitized section is described via Eq. (3.6) and the critical field strength Δ_Z^c is set to infinity so that $\Delta = \Delta_0$. All ABSs stem from the spatial variation of the g-factor which is modeled via

$$g_n = \sum_{j=1}^{j=M} \Lambda_n(n_{j,0}, n_{j,0} + N_N), \tag{3.8}$$

where $n_{j,0} = N_L + N_S/2 + jN_S + jN_N$ denotes the left position of the j-th section with non-zero g-factor, with $j \in \{1, 2, ..., M\}$ in case of a periodic distribution. The disordered position can be written as $n_{j,d} = n_{j,0} + \delta n$ where δn is randomly chosen from a Gaussian distributions with variance χ_δ and rounded to an integer number with the condition that the non-zero g-factor sections lie within the superconducting section. If $N_S/2$ is not an integer, then we round the value accordingly.

In order to study the effect of positional disorder systematically in the parameter space, we compute G_{RL} for different standard deviations χ_δ. The larger the standard deviation the more the ABS distribution deviates from the periodic case. Note that we use the python package Adaptive [73] to sample the peaks of the non-local conductance with a higher resolution for this particular study.

In addition to the variation of the standard deviation, we calculate G_{RL} for different numbers of ABSs, M, while keeping the density of ABSs fixed. In other words, a higher number of ABSs implies a longer nanowire. For example, we place two ABSs in a nanowire with a length of appproximately four times the localization length, while we place three ABSs in a nanowire of an approximate length of six localization lengths. We calculate G_{RL} for 40 disorder configurations of each combination of M and χ_δ, then obtain the finite temperature non-local conductance via a convolution with the derivative of the Fermi distribution. Finally, we extract the maximum of the absolute value of the finite temperature non-local conductance in the energy interval $[-0.9\Delta_0, 0.9\Delta_0]$ and average it over the 40 distributions yielding the quantity $\langle \max(|G_{RL}^{intra}|)\rangle$. We note that the choice of the energy interval, the g-factor profile, and Δ_Z^c ensure that the gap does not close as a function of the Zeeman field such that we indeed measure only non-local conductance due to Andreev band states.

In Figs. 3.7a and 3.7b, we present $\langle \max(|G_{RL}^{intra}|)\rangle$ and the corresponding standard deviation $\chi\langle \max(|G_{RL}^{intra}|)\rangle$. The non-local conductance is maximal in case of the periodic distribution of the ABSs and we note that the response is almost constant as a function of the number of ABSs M, meaning that the length of a periodic system has a rather small impact on the formation of the Andreev band and its signature in non-local conductance. If only two ABSs are present in the system, then it is not possible to define a period and consequently two ABSs of equal energy

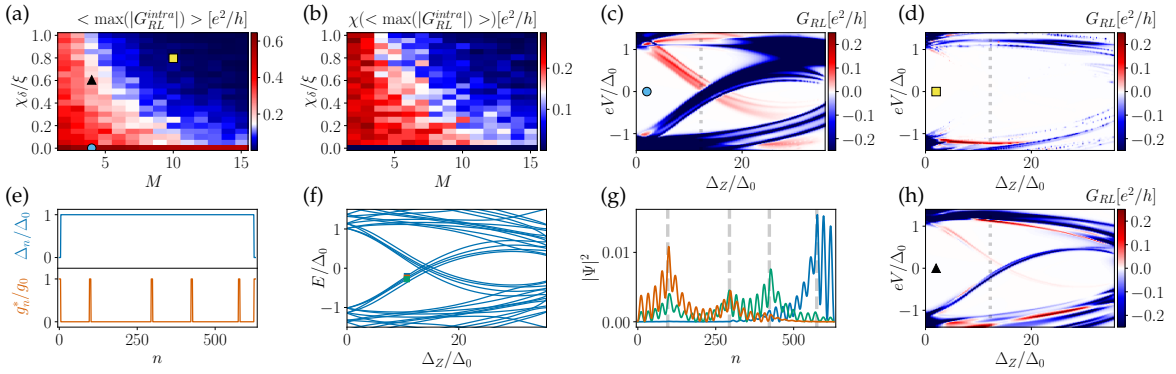

Figure 3.7: *Impact of positional disorder on the Andreev band*: (a) Averaged maximum $\langle \max(|G_{RL}^{intra}|)\rangle$ of the absolute value of the non-local conductance in the energy interval $eV \in [-0.9\Delta, 0.9\Delta]$, as a function of the standard deviation χ_δ from the periodic distribution and of the number of ABSs M. We made sure that we only pick non-local conductance signatures due to the Andreev band. (b) The standard deviation of $\langle \max(|G_{RL}^{intra}|)\rangle$ from its mean value. (c,d,h) G_{RL} as a function of the Zeeman field strength in case of (c) a periodic system, (d) a long nanowire with an ABS distribution strongly deviating from the periodic case, and (h) a nanowire with a length of eight times the localization length and with a moderate deviation from the periodic distribution. The dotted lines indicate the Zeeman strength used in (a). (e) Spatial profiles of the induced superconducting gap and the g-factor illustrating the deviation from periodicity. The configuration is associated to G_{RL} shown in (h). (f) The energy spectrum and (e) probability densities of the lowest states corresponding to the system from (e) and (h). These plots show that if the nanowire is short (a few times the localization length), then the Andreev band tolerates sizeable deviation from the periodic ABS distribution and it is still visible in non-local conductance. If, in contrast, the length of the nanowire is a several orders greater than the localization length, then the wave functions are strongly localized and consequently only a distribution close to the periodic case can maintain the Andreev band and its signature in non-local conductance. The parameters are listed in table 3.1.

hybridize well and mediate a signal in non-local conductance signal for many positional ABS distributions, as long as the nanowire length does not exceed four times the localization length. In contrast, in much longer nanowires with more ABSs, deviations from the spatial periodic distribution of ABSs lead to a localization of the wave functions (similar to Anderson localization in one-dimensional conductors with disorder), and therefore to a decrease of non-local conductance mediated by Andreev band states. We note, however, that in the experimental relevant regime of nanowires of a length between four and ten localization length, which corresponds to $2 \leq M \leq 5$, the non-local conductance signal is still sizeable for realistic deviations from the periodic distribution. In general, we find that the longer the nanowire the less deviation from the periodic distribution is tolerated by the Andreev band signature in non-local conductance. The standard deviation of $\chi\left[\langle \max(|G_{RL}^{intra}|)\rangle\right]$

shown in Fig. 3.7b reveals that the non-local conductance deviates much more in shorter systems and we note that the periodic system ($\chi_\delta = 0$) has zero standard deviation, since the positions of the ABSs are fixed.

Next, we choose three different system configurations, with lengths and standard deviations specified by the markers in Fig. 3.7a, and calculate the non-local conductance as a function of the Zeeman field strength. Here, in contrast to Figs. 3.7a and 3.7b, we use a finite value of Δ_Z^c in order to close the gap at a certain Zeeman field strength and we sample the non-local conductance on an equally spaced energy grid. First, we study a nanowire with spatial periodic ABSs, see the light blue circular marker in Fig. 3.7a and Fig. 3.7c. This distribution of ABSs supports the Andreev band, as discussed in the main text. Next, we analyse a long nanowire with ABSs deviating strongly from a periodic distribution. This deviation leads to the localization of the wave functions and non-local conductance is strongly reduced, compared to the periodic case, inside the gap independent of the values of the Zeeman field. Last, we study the experimental relevant case of a nanowire with a moderate deviation from the periodic distribution and with a length of eight times the localization length. The profiles of proximity gap and g-factor are shown in Fig. 3.7e, and the latter profile reveals the positional disorder of the ABSs. Figure 3.7f shows the energies associated with the ABS configuration and Fig. 3.7g shows the probability densities of the three lowest energies. The wave functions clearly begin to become localized but some of them have still a small support throughout the whole nanowire, explaining the reduced but finite non-local conductance signal shown in Fig. 3.7h.

3.F Impact of the Andreev band on the topological visibility Q

Here, we comment on the sharp negative dip of the topological visibility Q presented in Fig. 3b of the main text. Originally, $Q = \det[r(\omega = 0)]$ was suggested as a topological index in finite size systems of the symmetry class D [74–76, 83, 84]: In two-terminal devices two processes take place if an electron, with an energy smaller than the superconducting gap, is incident on the NS interface, namely normal reflection and Andreev reflection. The reflection matrix is unitary and particle-hole symmetric, therefore its determinant takes only the values $+1$ in case of normal reflection or -1 in case of perfect Andreev reflection [74–76, 83, 84]. The latter process can be mediated by MBSs, located at the interface, due to their equal electron and hole weights [50]. Fluctuations of the barrier strength or small disorder do not affect the unitary property of the reflection matrix and the value of the determinant does consequently not change. If the superconducting gap, however, closes, then an incident electron can enter the superconductor. This additional process leads to a break down of the unitary property of the reflection matrix and Q is therefore not necessarily ± 1 in gapless systems.

In this paper, we study a three terminal device, meaning that additional to the local processes of normal reflection and Andreev reflection also electron tunnelling (ET) and crossed Andreev reflection (CAR) between the two normal leads take

place. The Andreev band supports non-local conductance and therefore ET and CAR at certain sub-gap energies. If these processes occur at the Fermi energy, then the unitary property of the reflection matrix breaks down and enables changes of Q, consequently Q does not need to be precisely ± 1. In our simulations we find such a behaviour. For instance, see Fig. 3.8 which zooms into Fig. 3(b) of the main text: Q is only negative at a certain Zeeman strength for which a state of the Andreev band crosses the Fermi level. The value of Q is therefore not a good indicator of the topological phase if non-local conductance is non-zero close to zero energy. When, instead Q is calculated in a two-terminal configuration, by removing the right lead, the topological visibility is precisely $Q = +1$ in this case and does not show any dips, since non-local processes are not possible.

3.G Andreev bands as a function of the chemical potential

In this section, we study the trivial BRS as a function of the chemical potential, while we fix the barrier strength at the ends of the nanowire to a constant value. In Fig. 3.9, we show the lowest energies as a function of μ_{SN} and Δ_Z: a similar figure is shown in the main text (see Fig. 2d) with the difference that here the superconducting gap Δ is constant, which has an almost negligible impact as discussed in Fig. 3.4. In Fig. 3.9, the blue regions indicate gapless phases, while red indicates gapped phases. The gap closing and reopening at the lower values of the Zeeman field strength is caused by the Andreev band, while the second gap closing is set by the critical Zeeman field strength Δ_Z^c. The chemical potential is measured from the

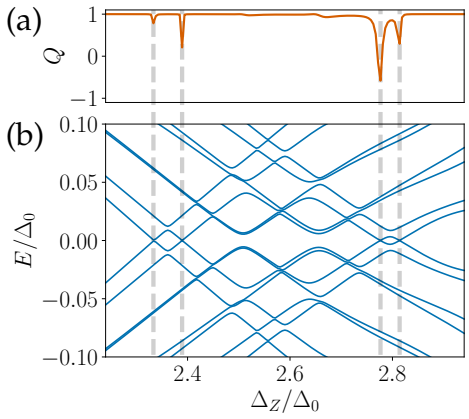

Figure 3.8: *Dips of the topological visibility* Q: (a) Q and (b) lowest eigenvalues as a function of the Zeeman field strength. Q has dips when the lowest state of the Andreev band crosses zero-energy, this can be explained via the breakdown of the unitary property of the reflection matrix due to the additional non-local processes. The grey dashed lines serve as guides for the eye to compare the position of the dips with the roots of the lowest energy. The parameters are the same as in Fig. 3 presented in the main text.

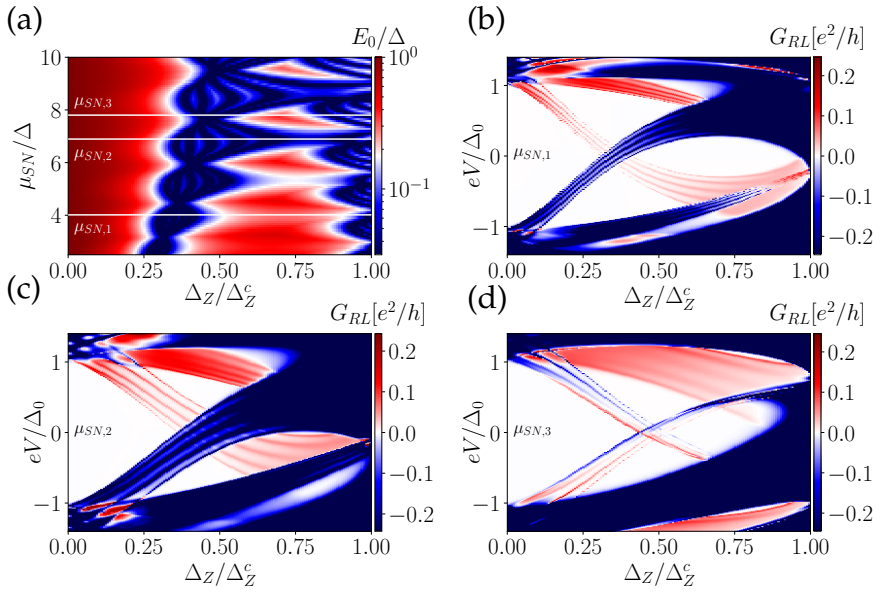

Figure 3.9: *Analysis of the Andreev band as a function of the chemical potential*: (a) Lowest energy, E_0, as a function of chemical potential μ_{SN} and Zeeman field Δ_Z. Here, we do not simulate trivial zero-energy states at the ends of the system and therefore the lowest energy reveals the energy of bulk states in the Andreev band. Consequently, the blue color indicates gapless regions while red color indicates gapped regions. (b-d) Non-local conductance as a function of the Zeeman field for three different values of the chemical potential: these values are indicated in panel (a) by the white horizontal lines. For certain choices of chemical potential the Andreev band gap does not reopen, see panel (c). As a result, gapped regions can be fully encircled by gapless regions. Same parameters as in Fig. 2 of the main text, except that we defined the superconducting gap via Eq. (3.6).

bottom of the band, meaning that the chemical potential can only take positive values and should be larger than the superconducting gap. We find that the Andreev band is relative stable against changes of the chemical potential. However, the value of the Zeeman field for which the Andreev band crosses zero-energy increases for growing chemical potential. Moreover, the Andreev band remains closed for certain values of the chemical potential, see the white horizontal line plotted at $\mu_{SN,2}$ and the associated Fig. 3.9c, which shows the non-local conductance. At higher chemical potentials the Andreev band is more narrow, see Fig. 3.9d. As such, the Andreev band leads to separated *gapped* regions that are surrounded by *gapless* regions, as expected also for a topological region of phase space.

In this paper, we focus mainly on the trivial BRS, which is why we omit in this section the simulation of trivial zero-energy states at the ends of the system. However, we have shown in the main text that trivial zero-energy states can appear simultaneously with the BRS. Moreover, trivial zero-energy states as a function of different system parameters have been discussed intensively in literature [20–38]. Therefore we conclude that the combination of the Andreev band and trivial zero-energy states lead in the phase space to gapped regions with zero-energy states

surrounded by Andreev band induced *gapless* regions, which are the main criteria of the topological gap protocol [67, 69].

3.H Alternative trivial bulk gap reopening mechanisms

In the main part of this paper, we discuss the Andreev band as a signature reminiscent of a gap reopening. Here for the sake of comparison we consider a considerably simpler mechanism: If the proximity effect itself is affected by the Zeeman field strength, then the induced gap might reach a local minimum at a Zeeman field strength $\Delta_{Z,\mathrm{min}}$ smaller than the critical field strength Δ_Z^{c} of the break-down of superconductivity or smaller than the critical field strength Δ_Z^T of a potential topological phase transition. Although speculative, such behaviour of the induced gap could be the result of the interplay of orbital effects in the parent superconductor, inter-facial disorder between the semiconducting nanowire and the superconductor, and/or the particular device geometry. We stress that we consider here a reduction of the induced gap $\Delta(\Delta_Z)$ at $\Delta_{Z,\mathrm{min}}$ and not of the gap of the parent superconductor. To model this we simply assume, without any detailed justification, that the induced gap could accidental behave as

$$\Delta(\Delta_Z) = \Delta_0 \left[1 - \kappa_1 e^{-\left(\frac{\Delta_Z - \Delta_{Z,\mathrm{min}}}{\kappa_2}\right)^2}\right], \tag{3.9}$$

where $\kappa_1 \in [0,1]$ determines the reduction of the gap and κ_2 sets the interval of Zeeman strength over which the gap is suppressed. The exact form of $\Delta(\Delta_Z)$ is not relevant, the main requirement for the closing and reopening is the presence of local minimum as described above.

This mechanism is, in general, independent of any ABSs which appear in the nanowire, we can therefore combine trivial zero-energy states, residing at the ends of the nanowire, with a gap reopening signature caused by a field-dependent proximity effect. Here, we consider only one trivial sub-gap state on the left end of the nanowire, however, it is, obviously, also possible to tune additionally a second trivial sub-gap state on the right end to zero-energy. In contrast to the main part of this paper, we model this time a nanowire which can undergo a topological phase transition since the Rashba SOI is chosen to be non-zero in the region with induced superconducting gap.

The hopping and SOI strength profiles are simplified as $t_n = t$ and $\alpha_n = \alpha$. Moreover, we use a smooth step functions of the superconducting gap and chemical potential, instead of tuning the system to a resonance condition, to pin the energy of an ABS to zero for Zeeman fields smaller than the critical field

$$\Delta_Z^T(\Delta_Z) = \sqrt{\left[\Delta(\Delta_Z)\right]^2 + \mu_{SN}^2}, \tag{3.10}$$

associated with the topological phase transition. We note here that this condition becomes explicitly dependent on the Zeeman field strength. The profile of the su-

perconducting gap and the chemical potential are modeled by

$$\Delta_n = \Delta(\Delta_Z) \begin{cases} \frac{1}{2}\left[1 + \tanh\left(\{n - N_L\}/\lambda\right)\right], & \text{if } N_{B,L} < n \leq N - N_{B,R} \\ 0, & \text{else} \end{cases} \tag{3.11}$$

and

$$\mu_n = \Delta(\Delta_Z) \begin{cases} \mu_L + (\mu_{SN} - \mu_L)\frac{1}{2}\left[1 + \tanh\left(\{n - N_L\}/\lambda\right)\right], & \text{if } N_{B,L} < n \leq N - N_{B,R} \\ 0, & \text{else,} \end{cases} \tag{3.12}$$

where λ controls the smoothness of the step function. A representative energy spectrum of such a system is shown in Fig. a. The gap of the system closes and reopens two times as a function of the Zeeman field: the first gap reopening is enforced via the relation defined in Eq. (3.9), and appears at $\Delta_{Z,\text{min}}$, while the second gap reopening appears at the topological phase transition and this second BRS would also emerge in case of a constant function $\Delta(\Delta_Z) = \Delta_0$. We plot the topological visibility Q in Fig. b. The system remains trivial between $\Delta_{Z,\text{min}}$ and Δ_Z^T. Q is only negative for Zeeman strength which are approximately given by $\Delta_Z > \Delta_Z^T$. A ZBP is clearly visible in the region $\Delta_{Z,\text{min}} < \Delta_Z < \Delta_Z^T$, see Fig. c. We choose a sufficiently large chemical potential so that the system remains trivial ($Q > 0$) for Zeeman field strengths in the vicinity of $\Delta_{Z,\text{min}}$.

Finally, we note that the gap closing corresponding to the topological phase transition is less pronounced in the non-local conductance than the enforced gap reopening at $\Delta_{Z,\text{min}}$, since the associated wave functions decay into the normal section on the left side.

3.I Transport calculations

We perform the transport calculations with the Python package Kwant [82]. In particular, we attach normal leads at the left and right end of the nanowire, as schematically shown in Fig. 1 in the main text, inject modes of certain energies and calculate the S-matrix. The parameters of the leads are chosen to be the same as in the neighbouring normal section, except the chemical potential, which is set to $\mu_{Lead,L}$ ($\mu_{Lead,R}$) in the left (right) lead. We construct the differential conductance matrix $G_{\alpha\beta}$ with $\alpha, \beta \in \{L, R\}$ from the reflection r, r' and transmission coefficients t, t' of the S-matrix

$$S = \begin{pmatrix} r & t \\ t' & r' \end{pmatrix}, \tag{3.13}$$

as explained in [37, 64, 82]. The transport calculations are performed for different temperatures T (see next section).

3.J System parameters

Here we provide the parameters used in our calculations. The hyphen in table 3.1 indicates that the corresponding parameter was not used in the calculation. We note

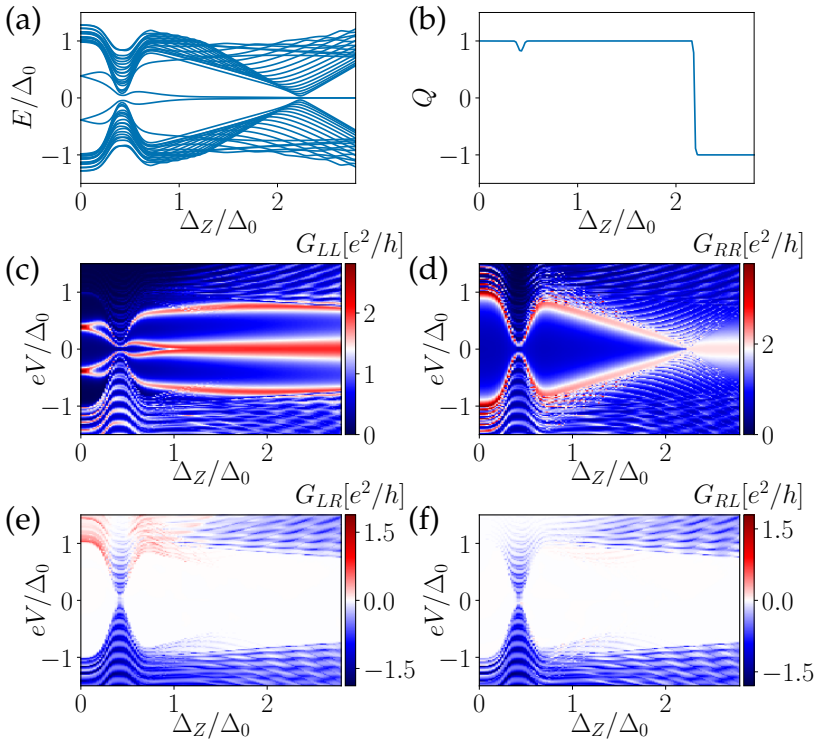

Figure 3.10: *Gap closing due to a Zeeman field dependent proximity effect*: (a) Energy spectrum showing the enforced closing due to a variation of the induced superconducting gap at $\Delta_{Z,\min} = 0.42\Delta_0$ in addition to the actual topological phase transition $\Delta_Z^T \approx 2.24\Delta_0$. (b) The topological visibility Q indicates that the system remains trivial after the first gap reopening (c,d) Local differential conductance calculated on the left and on the right end of the nanowire and (e,f) non-local conductances. The parameters are listed in Table 3.2. The trivial gap closing and reopening is visible in local and non-local conductance, while the single left ABS is only visible in left local conductance.

that we used Eq. (3.6) in a-d to model the induced superconducting gap, meaning that there are no interior normal sections. Moreover, we chose a constant value of the Rashba SOI along the nanowire $\alpha = const = \alpha_L = \alpha_R$ in Fig. 3.5a-3.5f.

Table 3.1: Parameter I

Fig.	N_L	N_R	N_S	N_N	M	$N_{B,L}$	$N_{B,R}$	t_L	t_R	t_{SN}	μ_L	μ_R	μ_{SN}	Δ_0	Δ_Z^c
3	90	94	140	30	5	7	7	100 meV	100 meV	20 meV	0 meV	0 meV	2 meV	0.25 meV	1.75 meV
2	5	5	150	10	6	5	5	158 meV	158 meV	158 meV	-	-	-	0.6 meV	12.2 meV
3.4a-3.4d	1	1	28	2	6	1	1	1	1	1	0.3	0.3	0.3	0.1	1.265
3.4e-3.4h	1	1	28	2	6	1	1	1	1	1	0.3	0.3	0.3	0.1	∞
3.5a-3.5f	10	10	300	50	6	10	10	635 meV	635 meV	635 meV	3 meV	3 meV	3 meV	0.6 meV	17.6 meV
3.6	1	1	35	35	3	1	1	1	1	1	0.4	0.4	0.4	0.1	∞
3.7a-3.7b	5	5	150	5	-	5	5	158 meV	158 meV	158 meV	3 meV	3 meV	3 meV	0.6 meV	∞
3.7c-3.7h	5	5	150	5	-	5	5	158 meV	158 meV	158 meV	3 meV	3 meV	3 meV	0.6 meV	21.4 meV

Fig.	α_L	α_R	γ_L	γ_R	$\mu_{Lead,L}$	$\mu_{Lead,R}$	T	a	g_r	φ
3	13.75 meV	13.20 meV	10 meV	10 meV	40 meV	40 meV	40 mK	5 nm	-	-
2	0 meV	0 meV	5 meV	5 meV	5 meV	5 meV	0 mK	4 nm	-	-
3.4a-3.4d	0	0	0.25	0.25	0.9	0.9	0	1	1	-
3.4e-3.4h	0	0	0.25	0.25	0.9	0.9	0	1	0.8	-
3.5a-3.5f	25 meV	25 meV	8 meV	8meV	5 meV	5meV	50 mK	2 nm	0.95	-
3.6	0	0	0.25	0.25	0.9	0.9	0	1	-	$\pi/1.4$
3.7a-3.7b	0 meV	0 meV	4 meV	4 meV	5 meV	5 meV	50 mK	4 nm	-	-
3.7c-3.7h	0 meV	0 meV	4 meV	4 meV	5 meV	5 meV	50 mK	4 nm	-	-

Table 3.2: Parameter II

Fig.	N_L	N_R	N_S	N_N	M	$N_{B,L}$	$N_{B,R}$	t	μ_L	μ_{SN}	Δ_0	κ_1	κ_2	a	λ	T	α	$\gamma_L = \gamma_R$	$\mu_{Lead,L} = \mu_{Lead,R}$
3.10	11	1	151	0	1	1	1	1	0	0.2	0.1	0.95	0.015	1	5	0	0.2	0.5	0.6

Bibliography

[1] A Yu Kitaev. "Unpaired Majorana fermions in quantum wires". In: Phys. Usp. 44.10S (Oct. 2001), pp. 131–136.

[2] Satoshi Fujimoto. "Topological order and non-Abelian statistics in noncentrosymmetric s-wave superconductors". In: Phys. Rev. B 77 (22 June 2008), p. 220501.

[3] Yuval Oreg, Gil Refael, and Felix von Oppen. "Helical Liquids and Majorana Bound States in Quantum Wires". In: Phys. Rev. Lett. 105 (17 Oct. 2010), p. 177002.

[4] Roman M. Lutchyn, Jay D. Sau, and S. Das Sarma. "Majorana Fermions and a Topological Phase Transition in Semiconductor-Superconductor Heterostructures". In: Phys. Rev. Lett. 105 (7 Aug. 2010), p. 077001.

[5] Masatoshi Sato, Yoshiro Takahashi, and Satoshi Fujimoto. "Non-Abelian topological orders and Majorana fermions in spin-singlet superconductors". In: Phys. Rev. B 82 (13 Oct. 2010), p. 134521.

[6] G. E. Volovik. "Fermion zero modes on vortices in chiral superconductors". In: Journal of Experimental and Theoretical Physics Letters 70.9 (1999), pp. 609–614.

[7] N. Read and Dmitry Green. "Paired states of fermions in two dimensions with breaking of parity and time-reversal symmetries and the fractional quantum Hall effect". In: Phys. Rev. B 61 (15 Apr. 2000), pp. 10267–10297.

[8] D. A. Ivanov. "Non-Abelian Statistics of Half-Quantum Vortices in p-Wave Superconductors". In: Phys. Rev. Lett. 86 (2 Jan. 2001), pp. 268–271.

[9] Chetan Nayak et al. "Non-Abelian anyons and topological quantum computation". In: Rev. Mod. Phys. 80 (3 Sept. 2008), pp. 1083–1159.

[10] Jason Alicea. "New directions in the pursuit of Majorana fermions in solid state systems". In: Rep. Prog. Phys. 75.7 (June 2012), p. 076501.

[11] Katharina Laubscher and Jelena Klinovaja. "Majorana bound states in semiconducting nanostructures". In: Journal of Applied Physics 130 (8 2021), p. 081101.

[12] V. Mourik et al. "Signatures of Majorana Fermions in Hybrid Superconductor-Semiconductor Nanowire Devices". In: Science 336.6084 (2012), pp. 1003–1007.

[13] M. T. Deng et al. "Anomalous Zero-Bias Conductance Peak in a Nb–InSb Nanowire–Nb Hybrid Device". In: Nano Lett. 12 (12 Dec. 2012), pp. 6412–6419.

[14] Anindya Das et al. "Zero-bias peaks and splitting in an Al–InAs nanowire topological superconductor as a signature of Majorana fermions". In: Nat. Phys. 8 (12 2012), pp. 887–895.

[15] H. O. H. Churchill et al. "Superconductor-nanowire devices from tunneling to the multichannel regime: Zero-bias oscillations and magnetoconductance crossover". In: Phys. Rev. B 87 (24 June 2013), p. 241401.

[16] P. Yu et al. "Non-Majorana states yield nearly quantized conductance in proximatized nanowires". In: Nat. Phys. 17.4 (2021), pp. 482–488.

[17] Satoshi Sasaki et al. "Topological Superconductivity in $\mathrm{Cu}_x\mathrm{Bi}_2\mathrm{Se}_3$". In: Phys. Rev. Lett. 107 (21 Nov. 2011), p. 217001.

[18] A. F. Andreev. "The thermal conductivity of the intermediate state in superconductors". In: Sov. Phys. JETP 19 (5 Nov. 1964), p. 1228.

[19] A. F. Andreev. "Electron Spectrum of the Intermediate State of Superconductors". In: Sov. Phys. JETP 22 (5 Feb. 1966), p. 455.

[20] G. Kells, D. Meidan, and P. W. Brouwer. "Near-zero-energy end states in topologically trivial spin-orbit coupled superconducting nanowires with a smooth confinement". In: Phys. Rev. B 86 (10 Sept. 2012), p. 100503.

[21] Eduardo J. H. Lee et al. "Zero-Bias Anomaly in a Nanowire Quantum Dot Coupled to Superconductors". In: Phys. Rev. Lett. 109 (18 Oct. 2012), p. 186802.

[22] Jorge Cayao et al. "SNS junctions in nanowires with spin-orbit coupling: Role of confinement and helicity on the subgap spectrum". In: Phys. Rev. B 91 (2 Jan. 2015), p. 024514.

[23] Andrzej Ptok, Aksel Kobiałka, and Tadeusz Doma ński. "Controlling the bound states in a quantum-dot hybrid nanowire". In: Phys. Rev. B 96 (19 Nov. 2017), p. 195430.

[24] Chun-Xiao Liu et al. "Andreev bound states versus Majorana bound states in quantum dot-nanowire-superconductor hybrid structures: Trivial versus topological zero-bias conductance peaks". In: Phys. Rev. B 96 (7 Aug. 2017), p. 075161.

[25] Christopher Reeg et al. "Zero-energy Andreev bound states from quantum dots in proximitized Rashba nanowires". In: Phys. Rev. B 98 (24 Dec. 2018), p. 245407.

[26] Fernando Peñaranda et al. "Quantifying wave-function overlaps in inhomogeneous Majorana nanowires". In: Phys. Rev. B 98 (23 Dec. 2018), p. 235406.

[27] Christopher Moore, Tudor D. Stanescu, and Sumanta Tewari. "Two-terminal charge tunneling: Disentangling Majorana zero modes from partially separated Andreev bound states in semiconductor-superconductor heterostructures". In: Phys. Rev. B 97 (16 Apr. 2018), p. 165302.

[28] Adriaan Vuik et al. "Reproducing topological properties with quasi-Majorana states". In: SciPost Phys. 7 (2019), p. 061.

[29] Benjamin D. Woods et al. "Zero-energy pinning of topologically trivial bound states in multiband semiconductor-superconductor nanowires". In: Phys. Rev. B 100 (12 Sept. 2019), p. 125407.

[30] Chun-Xiao Liu et al. "Conductance smearing and anisotropic suppression of induced superconductivity in a Majorana nanowire". In: Phys. Rev. B 99 (2 Jan. 2019), p. 024510.

[31] J. Chen et al. "Ubiquitous Non-Majorana Zero-Bias Conductance Peaks in Nanowire Devices". In: Phys. Rev. Lett. 123 (10 Sept. 2019), p. 107703.

[32] Oladunjoye A. Awoga, Jorge Cayao, and Annica M. Black-Schaffer. "Supercurrent Detection of Topologically Trivial Zero-Energy States in Nanowire Junctions". In: Phys. Rev. Lett. 123 (11 Sept. 2019), p. 117001.

[33] David J. Alspaugh et al. "Volkov-Pankratov states in topological superconductors". In: Phys. Rev. Research 2 (2 May 2020), p. 023146.

[34] Christian Jünger et al. "Magnetic-Field-Independent Subgap States in Hybrid Rashba Nanowires". In: Phys. Rev. Lett. 125 (1 June 2020), p. 017701.

[35] Marco Valentini et al. "Nontopological zero-bias peaks in full-shell nanowires induced by flux-tunable Andreev states". In: Science 373.6550 (2021), pp. 82–88.

[36] Elsa Prada et al. "From Andreev to Majorana bound states in hybrid superconductor–semiconductor nanowires". In: Nature Reviews Physics 2.10 (2020), pp. 575–594.

[37] Richard Hess et al. "Local and nonlocal quantum transport due to Andreev bound states in finite Rashba nanowires with superconducting and normal sections". In: Phys. Rev. B 104 (7 Aug. 2021), p. 075405.

[38] Roshni Singh and Bhaskaran Muralidharan. "Conductance Spectroscopy of Majorana Zero Modes in Superconductor-Magnetic Insulating Nanowire Hybrid Systems". In: arXiv:2203.08413 (2022).

[39] Pasquale Marra. "Majorana nanowires for topological quantum computation". In: Journal of Applied Physics 132.23 (Dec. 2022), p. 231101.

[40] Igor J. Califrer et al. "Proximity-induced zero-energy states indistinguishable from topological edge states". In: Phys. Rev. B 107 (4 Jan. 2023), p. 045401.

[41] Elsa Prada, Pablo San-Jose, and Ramón Aguado. "Transport spectroscopy of NS nanowire junctions with Majorana fermions". In: Phys. Rev. B 86 (18 Nov. 2012), p. 180503.

[42] S. Das Sarma, Jay D. Sau, and Tudor D. Stanescu. "Splitting of the zero-bias conductance peak as smoking gun evidence for the existence of the Majorana mode in a superconductor-semiconductor nanowire". In: Phys. Rev. B 86 (22 Dec. 2012), p. 220506.

[43] Diego Rainis et al. "Towards a realistic transport modeling in a superconducting nanowire with Majorana fermions". In: Phys. Rev. B 87 (2 Jan. 2013), p. 024515.

[44] Olesia Dmytruk and Jelena Klinovaja. "Suppression of the overlap between Majorana fermions by orbital magnetic effects in semiconducting-superconducting nanowires". In: Phys. Rev. B 97 (15 Apr. 2018), p. 155409.

[45] C. Fleckenstein et al. "Decaying spectral oscillations in a Majorana wire with finite coherence length". In: Phys. Rev. B 97 (15 Apr. 2018), p. 155425.

[46] Paweł Szumniak et al. "Spin and charge signatures of topological superconductivity in Rashba nanowires". In: Phys. Rev. B 96 (4 July 2017), p. 041401.

[47] Denis Chevallier et al. "Topological phase detection in Rashba nanowires with a quantum dot". In: Phys. Rev. B 97 (4 Jan. 2018), p. 045404.

[48] Henry F. Legg, Daniel Loss, and Jelena Klinovaja. "Superconducting diode effect due to magnetochiral anisotropy in topological insulators and Rashba nanowires". In: Phys. Rev. B 106 (10 Sept. 2022), p. 104501.

[49] Henry F. Legg et al. "Parity protected superconducting diode effect in topological Josephson junctions". In: arXiv.2301.13740 (2023).

[50] K. T. Law, Patrick A. Lee, and T. K. Ng. "Majorana Fermion Induced Resonant Andreev Reflection". In: Phys. Rev. Lett. 103 (23 Dec. 2009), p. 237001.

[51] A. R. Akhmerov, Johan Nilsson, and C. W. J. Beenakker. "Electrically Detected Interferometry of Majorana Fermions in a Topological Insulator". In: Phys. Rev. Lett. 102 (21 May 2009), p. 216404.

[52] Karsten Flensberg. "Tunneling characteristics of a chain of Majorana bound states". In: Phys. Rev. B 82 (18 Nov. 2010), p. 180516.

[53] M Wimmer et al. "Quantum point contact as a probe of a topological superconductor". In: New J. Phys. 13.5 (May 2011), p. 053016.

[54] Denis Chevallier and Jelena Klinovaja. "Tomography of Majorana fermions with STM tips". In: Phys. Rev. B 94 (3 July 2016), p. 035417.

[55] S. M. Albrecht et al. "Exponential protection of zero modes in Majorana islands". In: Nature 531.7593 (2016), pp. 206–209.

[56] Ji-Yin Wang et al. "Parametric exploration of zero-energy modes in three-terminal InSb-Al nanowire devices". In: Phys. Rev. B 106 (7 Aug. 2022), p. 075306.

[57] Zhan Cao et al. "Decays of Majorana or Andreev Oscillations Induced by Steplike Spin-Orbit Coupling". In: Phys. Rev. Lett. 122 (14 Apr. 2019), p. 147701.

[58] Haining Pan et al. "Generic quantized zero-bias conductance peaks in superconductor-semiconductor hybrid structures". In: Phys. Rev. B 101 (2 Jan. 2020), p. 024506.

[59] O. Entin-Wohlman, Y. Imry, and A. Aharony. "Conductance of superconducting-normal hybrid structures". In: Phys. Rev. B 78 (22 Dec. 2008), p. 224510.

[60] Alejandro M. Lobos and S Das Sarma. "Tunneling transport in NSN Majorana junctions across the topological quantum phase transition". In: New J. Phys. 17.6 (June 2015), p. 065010.

[61] J. Gramich, A. Baumgartner, and C. Schönenberger. "Andreev bound states probed in three-terminal quantum dots". In: Phys. Rev. B 96 (19 Nov. 2017), p. 195418.

[62] T. Ö. Rosdahl et al. "Andreev rectifier: A nonlocal conductance signature of topological phase transitions". In: Phys. Rev. B 97 (4 Jan. 2018), p. 045421.

[63] Hao Zhang et al. "Next steps of quantum transport in Majorana nanowire devices". In: Nat. Com. 10.1 (5 2019), p. 5128.

[64] Jeroen Danon et al. "Nonlocal Conductance Spectroscopy of Andreev Bound States: Symmetry Relations and BCS Charges". In: Phys. Rev. Lett. 124 (3 Jan. 2020), p. 036801.

[65] André Melo et al. "Conductance asymmetries in mesoscopic superconducting devices due to finite bias". In: SciPost Phys. 10 (2 2021), p. 37.

[66] Haining Pan, Jay D. Sau, and S. Das Sarma. "Three-terminal nonlocal conductance in Majorana nanowires: Distinguishing topological and trivial in realistic systems with disorder and inhomogeneous potential". In: Phys. Rev. B 103 (1 Jan. 2021), p. 014513.

[67] Dmitry I. Pikulin et al. "Protocol to identify a topological superconducting phase in a three-terminal device". In: arXiv:2103.12217 (2021).

[68] A. Banerjee et al. "Local and Nonlocal Transport Spectroscopy in Planar Josephson Junctions". In: arXiv:2205.09419 (2022).

[69] Morteza Aghaee et al. "InAs-Al Hybrid Devices Passing the Topological Gap Protocol". In: arXiv:2207.02472 (2022).

[70] Bernd Braunecker et al. "Spin-selective Peierls transition in interacting one-dimensional conductors with spin-orbit interaction". In: Phys. Rev. B 82 (4 July 2010), p. 045127.

[71] S. Nadj-Perge et al. "Proposal for realizing Majorana fermions in chains of magnetic atoms on a superconductor". In: Phys. Rev. B 88 (2 July 2013), p. 020407.

[72] A. A. Zyuzin et al. "Correlations between Majorana Fermions Through a Superconductor". In: Phys. Rev. Lett. 111 (5 July 2013), p. 056802.

[73] Bas Nijholt et al. "*Adaptive*: parallel active learning of mathematical functions". In: 10.5281/zenodo.1182437 (2019).

[74] Piet W. Brouwer et al. "Topological superconducting phases in disordered quantum wires with strong spin-orbit coupling". In: Phys. Rev. B 84 (14 Oct. 2011), p. 144526.

[75] C. W. J. Beenakker et al. "Random-matrix theory of Andreev reflection from a topological superconductor". In: Phys. Rev. B 83 (8 Feb. 2011), p. 085413.

[76] Yashar Komijani and Ian Affleck. "Effect of disorder on the conductance of (non-) topological SN junctions". In: Journal of Statistical Mechanics: Theory and Experiment 2014.11 (Nov. 2014), P11017.

[77] L.Yu. "Bound State in Superconductors with Paramagnetic Impurities". In: Acta. Phys. Sin 21 (1965), p. 75.

[78] Hiroyuki Shiba. "Classical Spins in Superconductors". In: Prog. Theor. Phys. 40.3 (Sept. 1968), pp. 435–451.

[79] A. I. Rusinov. "On the Theory of Gapless Superconductivity in Alloys Containing Paramagnetic Impurities". In: Sov. Phys. JETP 29 (1969), p. 1101.

[80] Silas Hoffman, Jelena Klinovaja, and Daniel Loss. "Topological phases of inhomogeneous superconductivity". In: Phys. Rev. B 93 (16 Apr. 2016), p. 165418.

[81] Yoav Levine, Arbel Haim, and Yuval Oreg. "Realizing topological superconductivity with superlattices". In: Phys. Rev. B 96 (16 Oct. 2017), p. 165147.

[82] Christoph W Groth et al. "Kwant: a software package for quantum transport". In: New Journal of Physics 16.6 (June 2014), p. 063065.

[83] A. R. Akhmerov et al. "Quantized Conductance at the Majorana Phase Transition in a Disordered Superconducting Wire". In: Phys. Rev. Lett. 106 (5 Jan. 2011), p. 057001.

[84] I. C. Fulga et al. "Scattering formula for the topological quantum number of a disordered multimode wire". In: Phys. Rev. B 83 (15 Apr. 2011), p. 155429.

[85] Christopher Reeg, Daniel Loss, and Jelena Klinovaja. "Metallization of a Rashba wire by a superconducting layer in the strong-proximity regime". In: Phys. Rev. B 97 (16 Apr. 2018), p. 165425.

[86] Falko Pientka et al. "Topological Superconductivity in a Planar Josephson Junction". In: Phys. Rev. X 7 (2 May 2017), p. 021032.

[87] Omri Lesser et al. "Phase-induced topological superconductivity in a planar heterostructure". In: PNAS 118.27 (2021), e2107377118.

[88] Henry F. Legg, Daniel Loss, and Jelena Klinovaja. "Majorana bound states in topological insulators without a vortex". In: Phys. Rev. B 104 (16 Oct. 2021), p. 165405.

CHAPTER 4

Prevalence of trivial zero-energy sub-gap states in non-uniform helical spin chains on the surface of superconductors

Adapted from:
Richard Hess, Henry F. Legg, Daniel Loss, and Jelena Klinovaja
"Prevalence of trivial zero-energy sub-gap states in non-uniform helical spin chains on the surface of superconductors",
Phys. Rev. B **106**, 104503 (2022)

Helical spin chains, consisting of magnetic (ad-)atoms, on the surface of bulk superconductors are predicted to host Majorana bound states (MBSs) at the ends of the chain. Here, we investigate the prevalence of trivial zero-energy bound states in these helical spin chain systems. The existence of trivial zero-energy bound states can prevent the conclusive identification of MBSs and, given the limited tunability of atomic spin chain systems, could present a major experimental roadblock. First, we show that the Hamiltonian of a helical spin chain with varying non-uniform rotation rate between neighboring magnetic moments on a superconductor can be mapped to an effective Hamiltonian reminiscent of a ferromagnetic chain with strong Rashba spin-orbit coupling and with smooth non-uniform chemical potential, reminding a Rashba nanowire setups. Previously it has been found that trivial zero-energy states are abundant in nanowire systems with smoothly changing potentials. Therefore, we perform an extensive search for zero-energy bound states in helical spin chain systems with varying rotation rates. Although bound states with near zero-energy do exist for certain dimensionalities and rotation profiles, we find that zero-energy bound states are far less prevalent than in semiconductor nanowire systems with equivalent non-uniformities. In particular, utilising varying rotation rates, we do not find zero-energy bound states in the most experimentally relevant setup consisting of a one-dimensional helical spin chain on the surface of a three-dimensional superconductor, even for profiles that produce near zero-energy states in equivalent one- and two-dimensional systems. Although our findings do not rule them out, the much reduced prevalence of zero-energy bound states in long

non-uniform helical spin chains compared with equivalent semiconductor nanowires, as well as the ability to measure states locally via STM, should reduce the experimental barrier to identifying MBSs in such systems.

4.1 Introduction

The experimental realisation of Majorana bound states (MBSs) has become one of the most sought-after goals in modern condensed matter physics. The search for MBSs has largely been motivated by their exotic non-Abelian braiding statistics, which makes them a promising basis for fault tolerant quantum computation [1–5]. Despite this intense effort, however, there has been no conclusive observation of MBSs so far.

Topological $p_x + ip_y$ superconductors are predicted to host MBSs at the cores of vortices [1, 6]. However, since intrinsic p-wave superconductors turn out to be rare, the main experimental focus has been on engineering hybrid platforms based on proximity effect that can become topological superconductors. A wide variety of engineered systems have been proposed to host MBSs or chiral Majorana modes [5, 7–14] such as edge or surface states of topological insulators (TIs) [15], semiconductor nanowires [16–22], planar Josephson junctions [23–25], TI nanowires [26, 27], graphene-based systems [28–37], and many more.

Although many systems have been predicted to realise MBSs, to date, the conclusive experimental identification of MBSs has not been possible, largely due to trivial states that can mimic the experimental signatures of MBSs [38]. Most notable is the situation in semiconductor nanowires, which are perhaps the most mature experimental platform expected to host MBSs. Such systems consist of a nanowire with strong Rashba spin-orbit coupling that has been brought into proximity with a superconductor. It was predicted that a signature of MBSs is a zero-bias peak in differential-conductance measurements and that this peak is stable for a wide range of magnetic field strengths. Although such zero-energy signature has been observed in nanowires [39–42] and other platforms [43–48] it turned out that a zero-bias peak by itself is not a unique fingerprint of MBSs. In fact, it was shown that trivial Andreev bound states (ABSs) [49, 50] are expected to be abundant in nanowires [38]. These trivial states can also result in zero-bias peaks which mimic MBSs and they occur, for instance, due non-uniformities in the nanowire parameters [51–67]. Despite several further signatures of MBSs being proposed, due to the high prevalence of possible zero-energy modes, it remains unclear if a conclusive measurement of MBSs can be performed in nanowire systems.

Artificial magnetic structures, such as atomic chains, where adatoms are placed on the surface of a superconductor have also been predicted to host MBSs [68–81], with first signatures observed in the scanning tunneling microscope (STM) spectroscopy [44–47]. A single magnetic adatom on the surface of a superconductor leads to the formation of a Yu-Shiba-Rusinov (YSR) state, which is well studied in theory [82–90] and experiment [91–98]. Current experiments exploit an atom by atom construction technique to build the atomic chains, allowing great control over the chain length [98–104] compared to self-assembled chains [105–107]. Here we will focus on long chains of magnetic adatoms that possess a helical ordering [77]. Helical ordering of the magnetic moments of the adatoms can be mediated by Ruderman-Kittel-Kasuya-Yosida (RKKY) interaction [108–111] which should lead to a helix of magnetic moments with period π/k_F, where k_F denotes the Fermi momentum. Other mechanisms can also support helical ordering, for instance the

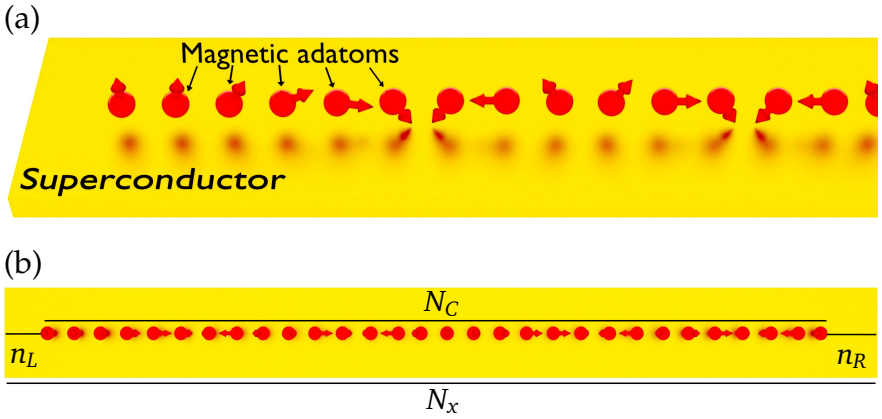

Figure 4.1: *Helical spin chain system:* (a) Magnetic adatoms (red) are placed on the surface of a bulk superconductor (yellow). The adatoms form a helical spin chain with a rotation rate that can vary along the chain. (b) Geometry of helical spin chain used in this manuscript (number of sites shown is not to scale). The full system has N_x sites in the x direction with magnetic adatoms deposited on N_C sites forming a helical spin chain. In general, the helical spin chain is embedded in the underlying superconductor with n_L sites on the left side of the system and n_R on the right. In addition we will consider one-, two-, and three-dimensional superconductors underlying the chain.

Dzyaloshinskii-Moriya interaction (DMI) [112]. Since local measurements can be performed on such atomic chains by utilising scanning-tunnelling microscopy techniques, the location of states can be very well established [47, 100, 101], a significant benefit over semiconductor systems. On the other hand, the topological transition in such chains is set by the exchange coupling strength, J, between the adatoms and the superconductor, which is not easily controlled. This lack of tunability makes exploring the phase space of a zero-energy bound state difficult and therefore, if trivial zero-energy states are as abundant in such chains as in nanowire systems, it would be even more difficult to conclusively identify MBSs.

In this paper we will investigate the prevalence of trivial zero-energy states due to non-uniformities in long helical spin chains. First, we apply the established mapping between the one-dimensional helical spin chain and the one-dimensional Rashba nanowire, following Refs. [75–77, 113], we generalize this mapping for non-uniform rotation rates. In particular, we find that the spatially varying rotation rates of the magnetic moments result in non-uniformities in the effective Hamiltonian that are similar to those that lead to the abundance of trivial zero-energy states in Rashba nanowires. Therefore, using this mapping as a basis, we will investigate if non-uniform rotation rates can also lead to an abundance of zero-energy modes in helical spin chains. Although bound states with near zero-energy do exist for certain dimensionalities and rotation profiles, including when the spin chain remains entirely trivial, for experimentally relevant systems we find that zero-energy bound states are far less prevalent in spin chains than semiconductor nanowire systems. Primarily this is due to the fact the helical chain is embedded in a superconductor

and also due to effects of the boundary.

This work is structured as follows: first, we investigate an effective one-dimensional continuum model for a helical spin chain with a smooth spatially varying rotation rate between adjacent magnetic moments on top of a superconductor. In Sec. 4.3 we introduce one-, two- and three-dimensional lattice models for the non-uniform helical spin chains. The topological phase diagram of a helical periodic one-dimensional spin chain is shown in Sec. 4.4 and, in addition, several non-uniform profiles of the rotation rate are suggested, which might potentially support the formation of trivial zero-energy sub-gap states. In Secs. 4.5, 4.6, and 4.7, we discuss the presence and absence of trivial zero-energy sub-gap states in one-, two- and three-dimensional systems for different types of rotation rate profiles. Finally, we conclude in Sec. 5.6. In addition, in App. 4.A, we study the disappearance of trivial zero-energy states in chains which are placed on the boundary of a two-dimensional superconductor. Furthermore, we consider the scenario of a chain deposited in the bulk of a three-dimensional superconductor instead on the surface, see App. 4.B.

4.2 Theory of a one-dimensional spin chain with spatially varying magnetization

In this section we show that the Hamiltonian of a helical spin chain, as shown in Fig. 4.1, can be mapped to an effective Hamiltonian that is reminiscent of a semiconductor nanowire brought into proximity with a superconductor. Surprisingly, despite this mapping and despite the fact that spatially varying potentials can easily be generated in the effective Hamiltonian, we will show in the remainder of the manuscript that trivial zero-energy bound states are far less abundant in helical spin chains than has been shown to occur in semiconductor Rashba nanowires.

To begin, we consider a helical spin chain placed on top of a superconductor. The effective one-dimensional (1D) model is described by the Hamiltonian $\mathrm{H_{1D}} = \int \mathrm{d}x\ \Psi^\dagger(x) H_{\mathrm{1D}} \Psi(x)$ in the basis

$$\Psi(x) = \left(c_{x,\uparrow}, \quad c_{x,\downarrow}, \quad c^\dagger_{x,\downarrow}, \quad -c^\dagger_{x,\uparrow} \right)^{\mathrm{T}}, \tag{4.1}$$

where the operator $c^\dagger_{x,\nu}$ ($c_{x,\nu}$) creates (annihilates) an electron at position x with spin ν. The Hamiltonian density is given by

$$H_{\mathrm{1D}} = \left(-\frac{\hbar^2}{2m}\nabla_x^2 - \mu \right) \tau_z + J(x)\mathbf{S}(x)\cdot\boldsymbol{\sigma} + \Delta_0 \tau_x, \tag{4.2}$$

where m is the effective mass, μ the chemical potential, Δ_0 is the superconducting gap, and $J(x)$ is the (position dependent) exchange coupling strength between the magnetic moments of the adatoms and the spins of the itinerant electrons. In addition, $\boldsymbol{\sigma} = (\sigma_x, \sigma_y, \sigma_z)^{\mathrm{T}}$ is the vector of Pauli matrices acting in spin space and τ_i are Pauli matrices acting in particle-hole space. Finally, the unit-vector $\mathbf{S}(x)$ determines the local direction of the magnetic moments of the adatoms that form the chain. We will consider magnetic textures along the chain of the form

$$\mathbf{S}(x) = \big(\cos[2\varphi(x)], \quad \sin[2\varphi(x)], \quad 0 \big), \tag{4.3}$$

such that the rotation of the magnetic moments in the xy-plane is described by the total angle $\varphi(x)$ which can be described by a non-linear function, assuming a non-uniform rotation. Applying the unitary transformation $U = e^{-i\varphi(x)\sigma_z}$, one can map the Hamiltonian of the helical chain, $H_{1\mathrm{D}}$, to that of a Rashba nanowire in a magnetic field $\tilde{H}$ [113], such that

$$\begin{aligned}\tilde{H} =& U^\dagger H_{1\mathrm{D}} U \\ =& -\frac{\hbar^2}{2m}\left(\nabla_x^2 - \left(\frac{\partial\varphi}{\partial x}\right)^2 - \left[i\frac{\partial\varphi}{\partial x}\nabla_x + i\nabla_x\frac{\partial\varphi}{\partial x}\right]\sigma_z\right)\tau_z \\ &+ J(x)\sigma_x + \Delta_0\tau_x - \mu\tau_z. \end{aligned} \tag{4.4}$$

When the rotation rate of the magnetic moments along the chain, which we define as $\Phi(x) \equiv \frac{\partial\varphi}{\partial x}$, is non-uniform then the transformed Hamiltonian, $\tilde{H}$, contains an effective coordinate dependent potential $\tilde{V}(x) = \hbar^2[\Phi(x)]^2/2m$ and also an effective coordinate dependent Rashba SOI

$$\begin{aligned}\tilde{H}_R(x) &= \frac{\hbar^2}{2m}[i\Phi(x)\nabla_x + i\nabla_x\Phi(x)]\sigma_z\tau_z \\ &= \frac{i}{2}\left[\alpha(x)\nabla_x + \nabla_x\alpha(x)\right]\sigma_z\tau_z, \end{aligned} \tag{4.5}$$

where we use the symmetrized from of the effective position-dependent Rashba SOI [114] with the strength given by $\alpha(x) = \hbar^2\Phi(x)/m$. The same unitary transformation U can in principle also be applied to higher-dimensional systems. This is because the kinetic terms that contain the derivative ∇_i, acting in the direction $i \neq x$ with $i \in \{y, z\}$, will commute with U. As a result, the one-dimensional helical magnetic structure can be mapped into a one-dimensional Rashba spin-orbit interaction term. We note that if the magnetic structure has a two-dimensional character, as, for example, it is the case for magnetic skyrmions, the direct mapping into a standard two-dimensional Rashba SOI term fails, giving rise to additional terms, which again could be used to engineer the topological phase [115–121]. The transformed Hamiltonian, $\tilde{H}$, is reminiscent of one-dimensional semiconductor nanowires and has the same ingredients that are required for topological superconductivity: Rashba SOI, a superconducting gap, and a Zeeman energy [16, 17]. Using this mapping we therefore see that, in the case of a constant rotation rate between adjacent magnetic moments along the chain, which means $\varphi(x) = k_r x$, the topological phase transition for the purely one-dimensional chain takes place at

$$J_C(k_r) = \sqrt{\Delta_0^2 + (\mu - \hbar^2 k_r^2/[2m])^2} \tag{4.6}$$

and depends on the spatial rotation period, which is set by $2\pi/(2k_r)$. If the magnetic moments of the magnetic adatoms are aligned by RKKY interaction ($k_r = k_F$), then the period is set to $\pi/k_r = \pi/k_F$ [68–70] and the system enters the topological phase at $J(k_F) = \Delta_0$. The topological phase transition is shifted to larger values of J for $k_r \neq k_F$.

Therefore, when the rotation rate of the one-dimensional helical chain is non-uniform, the above mapping is to an effective Hamiltonian that is reminiscent of a

one-dimensional semiconductor nanowire with spatially varying parameters. Such nanowires have been considered extensively and it has been shown that trivial zero-energy Andreev bound states (ABSs) are abundant in these systems [51–67] .

The existence of the mapping therefore suggests that trivial zero-energy states could potentially be as prevalent in helical spin chains as in nanowires, which would be a significant problem given the more limited tunability of parameters in the atomic chain compared to a nanowire. However, although the mapping for the one-dimensional case is rigorous, the two systems differ significantly in higher dimensions for the following reason: superconductivity in a semiconductor nanowire is present only in the region that is brought into proximity with a superconductor and the Zeeman energy is (approximately) constant throughout this region. In contrast, the helical spin chain is embedded in a superconductor and the exchange coupling energy – which maps to the Zeeman energy – is non-zero only close to the position of the magnetic adatoms. As a result, as we will show in the rest of this paper, while trivial zero-energy modes in a purely one-dimensional chain that is aligned with the end of the superconductor are as easily generated as this mapping suggests, the same is *not* true when the atomic chain is embedded in a superconductor, especially in the experimentally relevant scenario where the superconductor in which the chain is embedded is three-dimensional.

4.3 Lattice models of spin chain

One-dimensional system

In the previous section, we work in the continuum limit. In this section, we switch to the lattice description by discretizing the Hamiltonian, which will allow us later to solve the problem numerically. First, we construct a lattice Hamiltonian $H_{\mathrm{1D},L}$, corresponding to H_{1D} defined in Eq. (4.2). The lattice Hamiltonian $H_{\mathrm{1D},L}$ of the setup consisting of an atomic chain on the superconducting surface (see Fig. 4.1) is given by

$$H_{\mathrm{1D},L} = \sum_{n=1}^{N_x} \Bigg[\sum_{\nu,\nu'} c^\dagger_{n,\nu} (\{2t-\mu\}\delta_{\nu,\nu'} + J_n \left(\mathbf{S}_n \cdot \boldsymbol{\sigma}\right)_{\nu\nu'}) c_{n,\nu'} - \left(\sum_{\nu} t c^\dagger_{n,\nu} c_{n+1,\nu} + \Delta_0 c^\dagger_{n,\downarrow} c^\dagger_{n,\uparrow} + \mathrm{H.c.} \right) \Bigg], \tag{4.7}$$

where N_x denotes the total number of lattice sites and $t = \hbar^2/(2ma^2)$ denotes the matrix hopping element, which depends on the effective lattice constant a. We consider an exchange coupling strength of the form

$$J_n = J\left[\Theta(n-n_L) - \Theta(n-N_x+n_R)\right], \tag{4.8}$$

where n_L ($N_x - n_R$) is the site hosting the first (last) adatom and $\Theta(n)$ is the Heaviside step-function with $\Theta(0) = 0$ and the length of the chain of magnetic adatoms is given by $N_C = N_x - (n_R + n_L)$. Depending on the relative locations of the ends of

the chain and the system boundaries, we distinguish two different types of setups: 1) An *aligned* setup is defined as the following: an end of the chain coincides with a boundary of the system, such that $N_C = N_x$, [see Fig. 4.1(b)]. 2) In an *embedded* setup, in contrast, magnetic adatoms are located only along a subsection of the entire system and do not reach the system boundary. In particular, we will consider an embedded left end, such that $N_x \gg N_C$ and $n_R = 0$ [see Fig. 4.1(b)]. We will use the same nomenclature of aligned and embedded systems referring to setups in which the superconductor underlying the chain is two- or three-dimensional (see below).

We define the rotation rate, Φ_n, such that the helix has a period $\pi a/\Phi_n$, as

$$\Phi_n(\lambda) = \Phi_L + (\Phi_R - \Phi_L)\,\mathrm{sig}\left(\frac{2[n-n_0]}{\lambda}\right), \tag{4.9}$$

where we have used the sigmoid function $\mathrm{sig}(x) = \frac{1}{2}\left[1+\tanh(x/2)\right]$. The profile Φ_n describes a helix of magnetic moments which rotates with the period $\pi a/\Phi_L$ and $\pi a/\Phi_R$ on the left and right end of the chain, respectively. If the sign of Φ_L is the opposite of Φ_R, then the rotation direction changes and the system contains a domain wall. The parameter λ controls the width and smoothness of the transition between two sections of different rotation rate and the parameter n_0 parameterises the position of the transition. In the discretized model φ_n enters $\mathbf{S}(x)$ [see Eq. (4.3)] instead of $\varphi(x)$, where the angle φ_n relative to the magnetic moment located at $n = 1$ is given by

$$\varphi_n = \sum_{m=1}^{n} \Phi_m(\lambda) - \Phi_1. \tag{4.10}$$

The particular choice of a constant rotation rate, $\Phi_R = \Phi_L = \Phi$, results in the well known case of a helical spin chain with fixed rotation period ($\varphi_n = n\Phi - \Phi_1$). Consequently, the topological phase is defined by the condition [77]

$$\begin{aligned} J_C^{<}(\Phi) &= \sqrt{\Delta_0^2 + (|\mu - 2t| - 2t|\cos(\Phi)|)^2} < J \\ &< \sqrt{\Delta_0^2 + (|\mu - 2t| + 2t|\cos(\Phi)|)^2} = J_C^{>}(\Phi), \end{aligned} \tag{4.11}$$

see Fig. 4.2a. In the limit of small angles between magnetic moments, Φ, the prediction for the lower bound of the topological phase transition, $J_C^{<}$, corresponds to the analytic result, J_C, for the location of the bulk gap closing in the continuum system as discussed in the previous section [see Eq. (4.6)]. This can be shown explicitly by expanding the cosine function and using the definition of the matrix hopping element t as well as the relation $\Phi = k_r a$. We note that the choice $\Phi_{k_F} = k_F a$ results in the topological phase transition criterion $J_C^{<} = \Delta_0$, which is the lowest value of $J_C^{<}$ possible for any Φ.

Two- and three-dimensional systems

Here, we extend our model from Sec. 4.3 to higher dimensions, such that the chain is deposited on top of a two- or three-dimensional (2D, 3D) superconductor. The

Hamiltonian in this case has the form

$$H_{\kappa\mathrm{D}} = \sum_{j} \Bigg[\sum_{\nu,\nu'} c^{\dagger}_{j,\nu} \{ (2t\kappa - \mu)\delta_{\nu,\nu'} + J_j (\mathbf{S}_j \cdot \boldsymbol{\sigma})_{\nu,\nu'} \} c_{j,\nu'} - \Delta_0 c^{\dagger}_{j,\downarrow} c^{\dagger}_{j,\uparrow} - \Delta_0^{*} c_{j,\uparrow} c_{j,\downarrow} \Bigg] - \sum_{\langle j,j' \rangle,\nu} t c^{\dagger}_{j,\nu} c_{j',\nu}, \tag{4.12}$$

where $\kappa \in \{2, 3\}$ denotes the dimensionality of the model and the index j accounts for the x, y, and z coordinates of the corresponding lattice site. In particular, we choose $j = (n, m)$ and $j = (n, m, l)$ in two and three dimensions, respectively, and the number of sites in y (z) direction is N_y (N_z). The exchange coupling, for example in three dimensions, is given by $J_j = J_{n,m,l} = J_n \delta_{m,m_0} \delta_{l,l_0}$, where m_0 and l_0 denote the y and z position of the atomic chain, respectively. Here, J_n is the same as in the one-dimensional chain and the notation $\langle j, j' \rangle$ indicates a summation over nearest neighbouring sites. As discussed above, we also use the terms *aligned* and *embedded* to describe systems where $N_C = N_x$ and $N_C \ll N_x$, respectively. Finally we note that, since the atomic chain breaks translation symmetry in the directions perpendicular to the chain, momentum in these directions is not a good quantum number and the location of the topological phase transition can be expected to be different than that found in the equivalent purely one-dimensional system. We use the Python package Kwant for the implementation of the tight binding models [122].

4.4 Topological phase diagram and rotation rate profiles

In this section, we briefly discuss the topological phase diagram of the helical spin chain and suggest different rotation rate profiles that, based on the mapping to semiconductor nanowires (see Sec. 5.2), could lead to low energy trivial sub-gap states. First, we start with an aligned one-dimensional system and plot the energy difference $E_2 - E_1$ between the first excited state and the ground state for a chain with constant $\Phi_n \equiv \Phi$, such that sub-gap states other than MBSs or ABSs close to the gap edge, emerging for example from shifting the chemical potential away from the SOI energy [123], are not expected (see Fig. 4.2a). Although in the general case this quantity does not provide direct information about the topology of the phase, in a system with no other sub-gap states than MBSs, this energy difference is given by the finite-size level-spacing in the trivial phase and is very small. In contrast to that, in the topological phases, it determines the value of the topological mini-gap, which should be much larger than the level spacing (see, respectively, the dark red regions of Fig. 4.2a). As expected, the critical value of the continuum model J_C (yellow line Fig. 4.2a), agrees well for small values of the rotation rate Φ with the almost zero value of $E_2 - E_1$ and with $J_C^{<}$ (orange line Fig. 4.2a). The upper critical value of the lattice model, $J_C^{>}$, confines the topological phase space in the regime of strong J. For example, in the case of an antiferromagnetic alignment the topological phase is absent [77, 124, 125]. We also note that the interval spanned

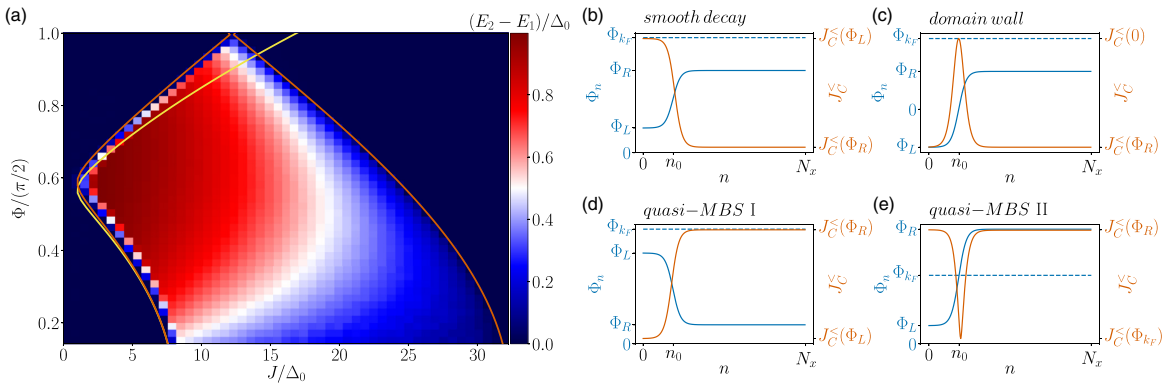

Figure 4.2: *Phase diagram and non-uniform rotation profiles:* (a): Phase diagram of a one-dimensional helical spin chain with constant rotation rate ($\Phi_n = \Phi = \text{const.}$), showing the energy difference $E_2 - E_1$ between the lowest energy state and the first excited state. Orange lines indicate the critical exchange couplings $J_C^<(\Phi)$ and $J_C^>(\Phi)$, which separate the topological phase from the trivial phase [see Eq. (4.11)], while the yellow line represents J_C [see Eq. (4.6)]. In the trivial phase, this energy difference is given by the finite-size quantization and very small, corresponding to dark blue color. For small rates J_C agrees well with $J_C^<$. Next, we consider spatially varying rotation rates, with constant rates at the long right section of the chain: (b-e) Different profiles of the rate Φ_n (blue) and the corresponding profile of $J_C^<(\Phi_n)$ (orange) along the atomic chain to be considered in this work. The blue dashed line indicates the value of Φ_{k_F} corresponding to a period π/k_F. Numerical parameters for the phase diagram: $t \approx 10$ meV, $N_x = N_c = 322$, $\Delta_0 = 1$ meV, $a = 3\,\text{Å}$, $\mu = 8$ meV.

by the values of $J_C^<(\Phi)$ and $J_C^>(\Phi)$ is maximal in case of ferromagnetic ordering. However, the system with ferromagnetic configuration stays trivial since the bulk gap does not reopen, for more details see Ref. [77].

We now define the different non-uniform rotation profiles that we will use in the remainder of the manuscript. In general, these non-uniform rotation rates will involve a transition between two different rotation rates in a short and long section of the atomic chain, mathematically described by the profile defined in Eq. (4.9). We refer to a section as *short* if its length is comparable or shorter than the smoothness parameter λ (see above) and a section as *long* if its length is larger than λ. Since the phase diagram shown in Fig. 4.2a verifies that the topological phase transition criterion $J_C^<$ is strongly dependent upon the rotation rate Φ_n between neighbouring magnetic moments, we can expect a rich variety of states arising due to these non-uniform profiles. Throughout we will consider only one transition region on the left end of the chain. However, most probably, both ends should be identical, such that there is also a trivial state on the right. We consider only one region such that we can demonstrate the difference between a uniform chain end and one with the transition region at the end.

The first non-uniform rotation rate profile we define is that of a *smooth decay*,

this is shown in Fig. 4.2b. In this profile, the magnetic moments rotate in the longer section of the chain with a rate $\Phi_R < \Phi_{k_F}$, as such this section of the chain obeys the topological phase transition criterion for exchange couplings larger than $J_C^<(\Phi_R)$. In addition, the magnetic moments in the short section, e.g. on the left side of the chain, rotate slower with a rate $\Phi_L < \Phi_R$ and, as a result, the topological phase transition criterion in this section is shifted to $J_C^<(\Phi_L)$ which is larger than $J_C^<(\Phi_R)$. Consequently, the entire system stays in the trivial regime for exchange couplings smaller than $J_C^<(\Phi_R)$ and any sub-gap state in this regime must have a trivial origin. An example of such a profile would be a ferromagnetic ordering of the magnetic moments close to the left end of the chain and a helical ordering on the right end. The consequences of this profile will be discussed in detail in Sec. 4.5.

Another rotation rate profile is one that contains a *domain wall* i.e. a change of the rotation direction, for example from clockwise to anticlockwise rotation. For instance, a rotation rate, which is negative in a short section on the left ($\Phi_L < 0$), but which takes the value $\Phi_R > 0$ with

$$\Phi_{k_F} > \Phi_R \geq |\Phi_L| \gg \frac{2\pi}{N_C} \tag{4.13}$$

in the longer right section of the atomic chain. The arguments from above apply also in this case and the topological phase transition criterion is shifted to values of the exchange coupling larger than $J_C^<(\Phi_R)$ in the region where the sign of Φ_n changes, see Fig. 4.2c. The entire system therefore stays trivial below for $J < J_C^<(\Phi_R)$ and any sub-gap states in this limit must be of trivial origin. We refer to Sec. 4.6 for a detailed study of the sub-gap states resulting from such a profile.

Next, we consider a similar setup as in the case of the smooth decay, however, for this profile $\Phi_R < \Phi_L < \Phi_{k_F}$ (see Fig. 4.2d). This choice has a significant impact on $J_C^<$, namely, the critical value of the exchange coupling for which the system obeys the topological phase transition criterion in this case is smaller for the left section with the fast rotating magnetic moments than for the long section of the chain with the slow rotating magnetic moments. Therefore, when $J_C^<(\Phi_L) \leq J < J_C^<(\Phi_R)$ the short section on the left of the atomic chain nominally could enter the topological regime. However, these MBSs will be strongly overlapping spatially and, thus, be hybridized. In Rashba nanowires zero-energy bound states arising due to a section of the system entering the topological regime have been termed as quasi-MBSs [38] and we therefore refer to this as the quasi-MBS profile. In fact, several other quasi-MBS profiles are possible. For example, if the rotation rate is set to $\Phi_L < \Phi_{k_F}$ in the short section on the left side of the chain and to $\Phi_R > \Phi_{k_F}$ in the longer section on the right side, such that the rotation rate changes smoothly between these sections, then at some site $n = \tilde{n}$ of the chain $\Phi_{n=\tilde{n}} = \Phi_{k_F}$ (see Fig. 4.2e). As such, a subsystem, namely the section where Φ_n grows, enters the topological regime for exchange couplings satisfying $J > \Delta$, $J < J_C^<(\Phi_L)$, and $J < J_C^<(\Phi_R)$. We will investigate quasi-MBS profiles in Sec. 4.7.

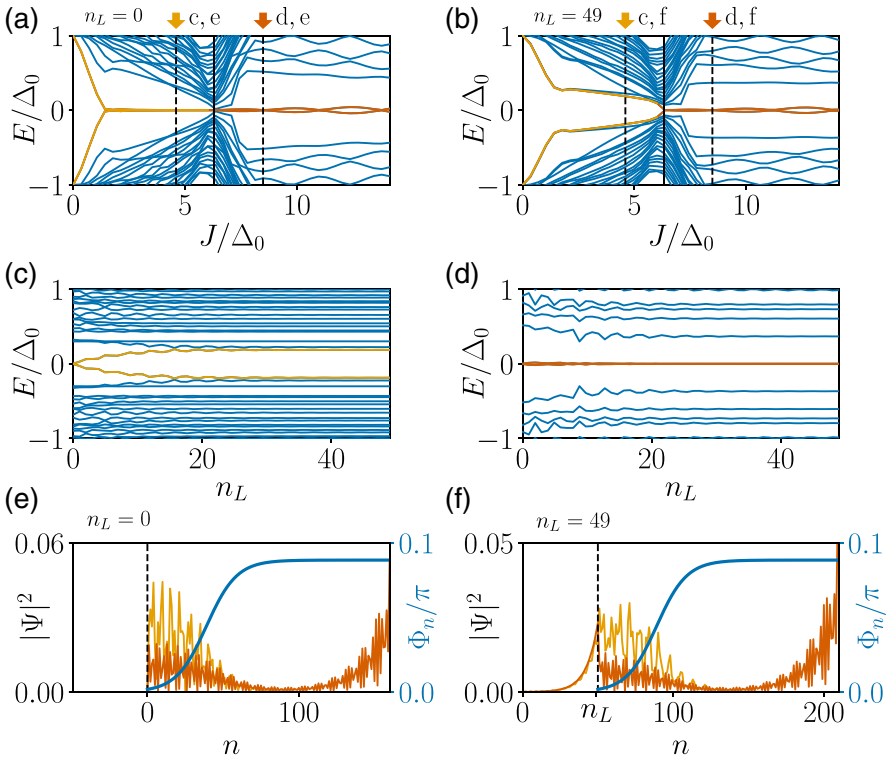

Figure 4.3: *Energy spectrum and probability density of the lowest energy state of a chain with a smooth decay rotation profile on a one-dimensional superconductor.* (a,b) Energy spectrum as a function of the exchange coupling J for (a) the aligned and (b) embedded systems. The black vertical solid line indicates the value $J = J_C^{<}(\Phi_R)$ at which the topological phase transition occurs. States in the completely trivial regime [$J < J_C^{<}(\Phi_R)$] are marked yellow, while the lowest sub-gap states in the topological regime [$J > J_C^{<}(\Phi_R)$] are marked orange. Higher energy states are shown in blue. The helical spin chain hosts trivial zero-energy states only in the aligned system but these states are continuously pushed away from zero energy as the number of sites without magnetic moments n_L on the left of the atomic chain grows. (c) [(d)] Evolution of the lowest trivial (yellow) [topological (orange)] sub-gap state as well as of the higher states as a function of the distance of the chain end from the system boundary at the exchange coupling strength indicated by the yellow [orange] arrows in panels (a) [(b)]. While the trivial sub-gap states split away from zero energy, see panel (c), the MBSs are stable and do not substantially change in energy, see panel (d). (e) [(f)] The probability densities of the trivial (yellow) and the topological (orange) lowest-energy states calculated at the exchange couplings indicated by the yellow (orange) arrows in panels (a) and (b) in case of an aligned [embedded] system. The blue line represents the rotation rate Φ_n between adjacent magnetic moments and the black dashed line indicates the end of the chain. Moreover, the probability densities show a clear difference between the MBSs and the trivial sub-gap states, and the latter are approximately confined in the left section. Parameters: $N_C = 160$, $t \approx 10$ meV, $\mu = 7$ meV, $\Delta = 1$ meV, $\Phi_L = 0$, $2\Phi_R = 0.1768\pi$, $\lambda = 20$, $n_0 = 40$, $a = 3$ Å, $n_R = 0$.

In summary the configurations, shown in Figs. 4.2b and 4.2c only host trivial states since the exchange coupling is always smaller than the topological phase transition criterion $J_C^<(\Phi_R)$. In contrast, short sections of the systems shown in Figs. 4.2d-4.2e could obey the topological phase transition criterion locally. We will see that in such profiles a subsystem hosts hybridized (quasi-)MBSs. We note that topology is defined for bulk systems, so in general the topological phase transition criterion, $J_C^<$, is not meaningful for a single site or small section of a chain. Nevertheless, interpreting the behaviour of energies and wavefunctions of sub-gap states in terms of the variation of the critical exchange coupling $J_C^<$, such that a section of the system enters the topological regime, agrees well with our numerical observations.

4.5 Smooth Decay

This section deals with trivial zero-energy states in the one-dimensional helical spin chain model described in Sec. 4.3 using the *smooth decay* rotation rate profile, as described in Sec. 4.4 (Fig. 4.2b). For this profile, in the long right section of the chain the rotation rate Φ_n between adjacent magnetic moments is approximately constant such that $\Phi_n \approx \Phi_R$, however, the rotation rate Φ_n decreases to zero close to the left end of the chain (see blue line in Figs. 4.3e and 4.3f).

One-dimensional model

The energy spectrum of the one-dimensional lattice model with a smooth decay rotation profile is shown in Fig. 4.3a (aligned) and Fig. 4.3b (embedded) as a function of exchange coupling J. In both cases we find that the bulk gap closes and reopens for $J \approx J_C^<(\Phi_R)$, indicated by a solid black vertical line. In the regime $J < J_C^<(\Phi_R)$ we find that sub-gap states appear. These sub-gap states must be entirely trivial in nature, since the topological phase transition criterion is not met for any section of the chain.

When the chain ends coincide with the boundaries of the superconductor (aligned system), the lowest energy sub-gap state is localized and pinned to zero energy over a range of exchange couplings (see Fig. 4.3a). Such a zero-energy bound state is reminiscent of an MBS, but here is entirely trivial. Since the exchange coupling $J < J_C(\Phi)$ does not satisfy the topological criterion in Eq. (4.11) for any Φ, the existence of such a zero-energy state is surprising and only arises here due to the non-uniformity of the rotation profile. However, when the chain is embedded into the superconductor, such that the length of the superconductor far exceeds the length of the chain, we find that the zero-energy pinning is lifted and the sub-gap states split away from zero energy (see Fig. 4.3b).

To further analyze the behavior of the low energy sub-gap states, we examine the transition from an aligned ($n_L = 0$) to an embedded ($n_L a \gg \xi$) system by adding lattice sites to the left of the atomic chain and by calculating the energy spectrum as a function of the distance n_L between the chain end and boundary

of the superconductor. Here, $\xi = \hbar v_F/\Delta_0$ denotes the superconducting coherence length with v_F being the Fermi velocity. The resulting energy spectra for an exchange coupling smaller than $J_C^<(\Phi_R)$, indicated by the yellow arrow, and for an exchange coupling larger than $J_C^<(\Phi_R)$, indicated by the orange arrow, are shown in Figs. 4.3c and 4.3d, respectively. This transition from the aligned to the embedded system shows that the trivial zero-energy state is continuously pushed away from zero energy as superconductor sites are added to the end of the chain. In addition, the next highest state decreases in energy such that the two lowest sub-gap states become approximately degenerate for a sufficiently long section without magnetic adatoms on the left of the chain (see Fig. 4.3c). In contrast, the zero-energy pinning of the MBS is essentially unaffected by an increase in n_L (see Fig. 4.3d). Analyzing the probability density $|\Psi(n)|^2$, see Figs. 4.3e and 4.3f, reveals that the trivial state and the left MBS tend to leak into the section without magnetic adatoms in the case of an embedded system. More specifically, the wavefunction $\Psi(n)$ decays exponentially into the section without magnetic moments with $|\Psi|^2 \sim e^{-2na/\xi}$ [126, 127].

Hence already in one dimension we observe that, in spite of the mapping of Sec. 5.2, the leakage of the lowest energy states of an atomic chain into the surrounding superconductor results in an increase in energy of that state. In general, mechanisms that suppress the leakage of the wavefunction into the section without magnetic adatoms can restore the zero-energy pinning of this lowest state. For instance, in one dimension, a scalar impurity at the end of the chain reduces the leakage and a strong impurity results in a lowest energy state that is again pinned close to zero energy (not shown).

Reducing the smoothness of the transition profile $\Phi_n(\lambda)$ via the parameter λ [see Eq. (4.9)], lifts the zero-energy pinning of the lowest sub-gap state in the topologically trivial regime. In contrast, the energies of the MBSs are unaffected by the smootheness of the profile $\Phi_n(\lambda)$. The exact form of the function $\Phi_n(\lambda)$ is actually not crucial for the existence of the zero-energy sub-gap states as long as $\Phi_n(\lambda)$ changes sufficiently smoothly between Φ_L and Φ_R. In particular, we find that λ needs to be larger than the rotation period of the magnetic moments on the right end of the atomic chain to obtain a sub-gap state with energy pinned to zero. Furthermore, the position n_0 in Eq. (4.9) of the smooth step should be placed at least twice the length of λ from the site of first magnetic adatom and the larger the value of n_0 the more sub-gap states enter the spectrum.

Trivial sub-gap states appear at finite values of exchange coupling. By analyzing our numerical simulations we find that their energy is only pinned to zero when the condition

$$\Delta_0 < J < J_C^<(\Phi_R) \tag{4.14}$$

holds. We can understand this behaviour in the picture outlined in Ref. 51 for semiconductor nanowires: when the exchange coupling J is larger than the superconducting gap, the superconducting correlation has an effective p-wave nature and below the critical exchange coupling $J_C^<(\Phi_R)$ two p-wave channels are present.

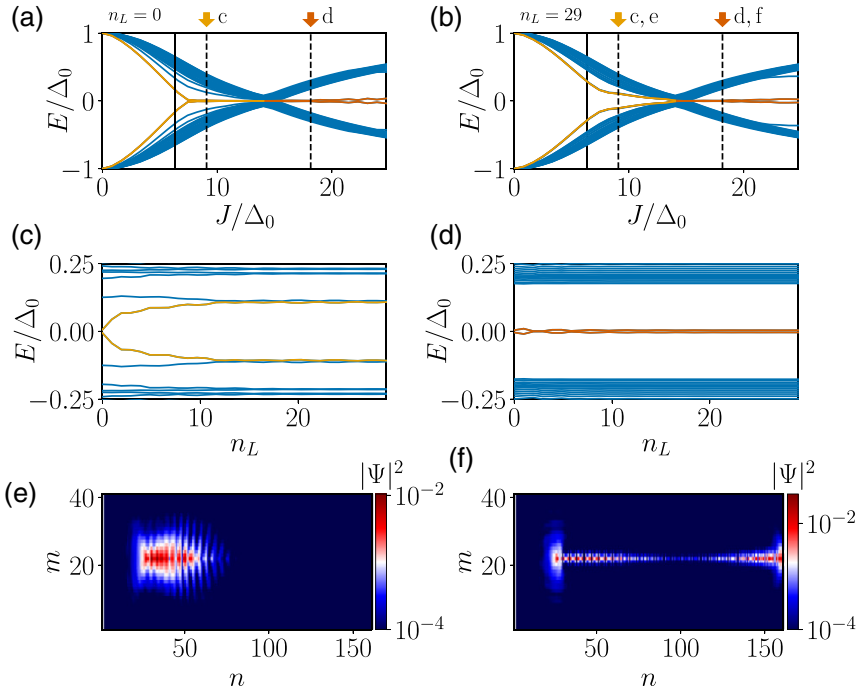

Figure 4.4: *Energy spectrum and probability density of the lowest energy state of a chain with a smooth decay rotation profile on a two-dimensional superconductor.* (a,b) Energy spectrum as a function of the exchange coupling J for (a) the aligned and (b) embedded systems. The black vertical solid line indicates the value $J = J_C^<(\Phi_R)$ in the analogous one-dimensional system, this does not match the actual bulk gap closing and reopening observed in two-dimensional setup. (a) The lowest sub-gap state has almost zero energy when the chain is aligned (b) but the state has finite energy when the chain is embedded. (c) [(d)] Evolution of the lowest trivial (yellow) [topological (orange)] sub-gap state as well as of the higher states as a function of the distance of the chain end from the system boundary at the exchange coupling strength indicated by the yellow [orange] arrows in panel (a). (c) The lowest trivial state is continuously pushed away from zero energy by adding more non-magnetic sites to the left of the end of the chain. (d) In contrast the energy of the MBSs is essentially unaffected by the number of non-magnetic sites at the end of the chain. (e) [f] The probability densities of the trivial (yellow) and the topological (orange) low-energy states calculated at the exchange couplings indicated by the yellow (orange) arrows in panels (a) and (b) in case of an aligned [embedded] system. The wavefunction of the lowest energy trivial sub-gap state is mostly localized at the section of the atomic chain with the slow-rotating magnetic moments but it leaks also slightly (strongly) in the x (y) direction parallel (perpendicular) to the chain into the section with no magnetic adatoms. In contrast, the probability density of the lowest state in the topological phase reveals two peaks at the ends of the chain due to the left and right MBS. The parameters are the same as in Fig. 4.3. We choose $N_y = 41$ and place the chain on the line $m_0 = 21$ along the y-direction.

The smooth change of the rotation rate, which maps to a smooth variation of po-

tential and induced SOI in the effective model, does not allow a coupling between the two channels and supports the formation of trivial zero-energy states. In contrast, an abrupt change in the spatial profiles couples the two channels and the sub-gap states are pushed away from zero energy. On the other hand, for $J > J_C^<(\Phi_R)$, the sub-gap states evolve into MBSs [51].

If the rotation rate is set to $\Phi_R = \Phi_{k_F}$ in the longer section of the chain, as predicted for an ordering mediated by the RKKY interaction [68, 75–81, 108–110], and if the magnetic moments deviate from the k_F ordering on the very left end of the chain, as $\Phi_L < \Phi_{k_F}$, then almost the entire system, except the section on the left, satisfies the topological phase transition criterion when $J_C(k_r = k_F) \geq \Delta_0$, see Eq. (4.6). Consequently, the interval of exchange coupling strengths for which trivial sub-gap states might appear shrinks to zero [see Eq. (4.14)]. Therefore, if the magnetic moments in the long right section of the chain form a spiral with period π/k_F, as RKKY interaction suggests, then no sub-gap states are present even in the case of an aligned system. In contrast, if the spin ordering deviates from $k_r = k_F$ in a long section of the chain, see for example Refs. [128], then the formation of zero-energy states of trivial nature is possible for the aligned system.

Two-dimensional model

We now consider a helical magnetic atomic chain placed on top of a two-dimensional superconductor, as presented in Sec. 4.3. We choose the same smooth profile for the rotation rate between adjacent magnetic moments as in the purely one-dimensional system discussed above. Many of our findings are the same as for the one-dimen-sional system. For instance, a smooth decay profile leads to sub-gap states with an energy close to zero over some range of exchange coupling strengths in the trivial phase in the case of an aligned system (see Fig. 4.4a). Extending the superconductor in the direction parallel to the chain (increasing n_L) lifts the zero-energy pinning of the trivial state, see Fig. 4.4c, in the same manner as in the embedded one-dimensional system. Moreover, the two lowest-energy states become almost degenerate in the trivial phase. Again, the energy of the MBSs is nearly independent of n_L (see Fig. 4.4d) as in the one-dimensional system.

One significant difference to the analogous one-dimensional system is that the exchange coupling strength for which the bulk gap closes and reopens is larger than in the one-dimensional system [129], see the black vertical solid line in Figs. 4.4a and 4.4b. This discrepancy can be understood due to the additional leakage of the wavefunction into the direction perpendicular to the chain (see wavefunction in Fig. 4.4f). Due to this leakage, low-energy states have a weaker overlap with the sites where a finite exchange coupling is present, therefore the effective exchange coupling strength decreases and the topological phase transition is shifted to higher exchange coupling strengths J. This effect is also reminiscent of the renormalization of the effective g-factor in Rashba or TI nanowires due to metallization caused by the coupling to a thin superconducting shell [130–133]. We note that a leakage of the wavefunction of the trivial sub-gap states in the perpendicular direction, see Fig. 4.4e, in the aligned system does not significantly change the zero-energy pin-

ning, while the leakage in the direction parallel of the chain in the embedded system does affect the energy of the sub-gap states.

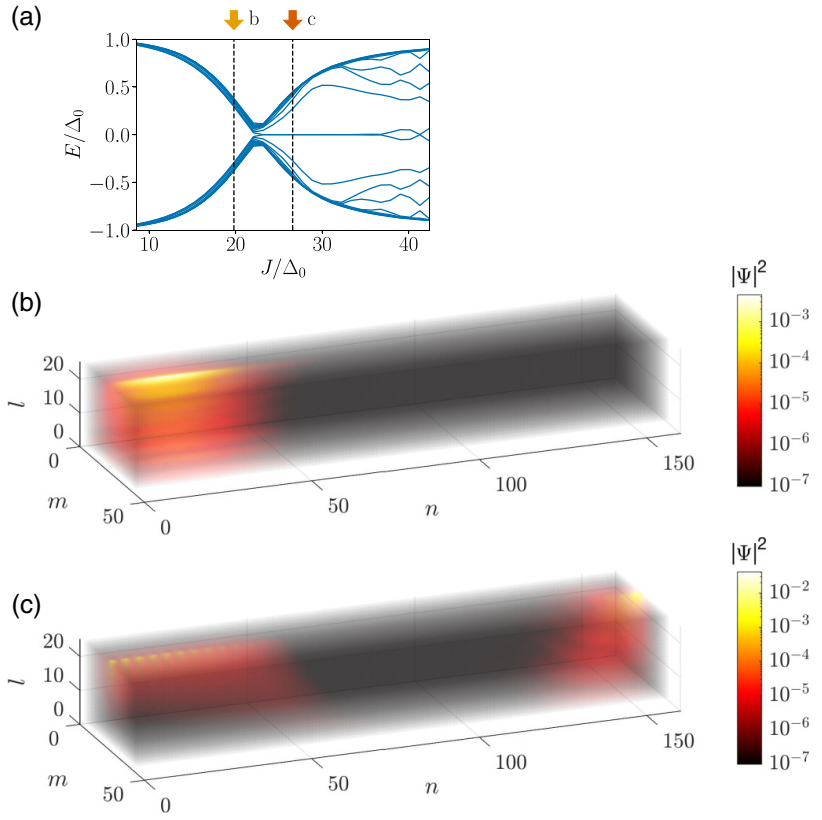

Figure 4.5: *Energy spectrum and probability density of the lowest energy state of a chain with a smooth decay rotation profile on a three-dimensional superconductor.* (a) Energy spectrum as a function of the exchange coupling J for the aligned systems. The system undergoes a topological phase transition indicated by the gap closing and reopening and the appearance of zero-energy MBSs. We do not find trivial zero-energy sub-gap states in this three-dimensional system. (b,c) Probability density of the lowest energy state in the trivial and the topological regime, respectively. The lowest state in the trivial regime is mostly localized in the section of the smooth change of the rotation rate. The probability densities are plotted for the exchange couplings strengths indicated by the yellow and orange arrow in panel (a). The probability density in (b) shows that the lowest state is localized in the region where the rotation rate changes, as expected from the one- and two-dimensional case, even though the state is energetically hardly separated from the bulk states. The MBSs are well separated and localized at the opposite ends of the chain. Again, their wavefuction is mostly located on the sites not covered by magnetic impurities, allowing to effectively diminish their localization length [73, 134]. The parameters are the same as in Fig. 4.3. In addition we choose $N_y = 41$, $m_0 = 21$, $N_z = 25$, and $l_0 = 1$.

In the most experimentally realistic setup of an embedded chain on the superconductor, we do not find any zero-energy trivial sub-gap states. We also note that, unlike in the one-dimensional system, even a single-site scalar impurity at the end of the chain is now not sufficient to restore the zero-energy pinning since, in two-dimensional systems, the confined state can bypass the impurity.

Three-dimensional model

Finally, we consider an atomic chain placed on the surface of a three-dimensional superconductor, utilising the model described in Sec. 4.3. This model is closest to realistic experimental set-ups, in which the adatoms are deposited on top of a bulk three-dimensional superconductor [100, 101, 112].

As was found in the two-dimensional model, also for the three-dimensional system there are no zero-energy states when the chain is embedded on the surface of the superconductor. Unlike the two-dimensional system, however, in the three-dimensional system we also do not find near zero-energy states when the chain end is aligned with the boundary of the superconductor. In particular, Fig. 4.5a shows the energy spectrum of an aligned system as a function of the exchange coupling. The gap closes and reopens for an exchange coupling strength J_C that is larger than observed in both the one-dimensional and two-dimensional systems. For coupling strengths below the value at which the gap closes we do not observe any zero-energy sub-gap states, even in the aligned system. We also note that the curvature of the bulk gap closing lines differs from the curvature of the same process in the two-dimensional superconductor (see Figs. 4.4a and 4.4b). After the gap closing, as expected, we find MBSs appear at the end of the chain.

In the trivial regime, i.e. before the closing of the bulk gap, of the aligned chain the probability density of the lowest state is bound to the section in which Φ_n smoothly changes as we observed in one- and two dimensional systems (see Fig. 4.5b), however the energy of this lowest state is essentially equal to that of the bulk gap. Both the lowest energy state in the trivial regime and the MBS decay exponentially into the bulk superconductor (see Figs. 4.5b and 4.5c).

We note that much of the behavior of the aligned three-dimensional system can be understood from the fact that the chain is placed on the surface of the three-dimensional superconductor and therefore states can scatter from the surface into the bulk of the superconductor (along the z-direction). To investigate the importance of a boundary of the system perpendicular to the chain, we construct an analogous system in two dimensions, where the chain has the same length as the superconductor in x direction ($N_C = N_x$) and in which the chain is placed along the boundary of the superconductor (see Appendix 4.A). In this scenario we also do not find trivial zero-energy sub-gap states, similar to the three-dimensional system. In contrast, when the chain is placed in the bulk of the superconductor rather than on the surface, then trivial sub-gap states with energies smaller than the bulk gap do appear (see Appendix 4.B). Both of these results highlight the importance of scattering from the boundary in pushing trivial zero-energy states to higher energies.

We would like to emphasize that numerical restrictions limit us to relatively small systems in three dimensions and we cannot therefore perform extensive nu-

merical investigations in such systems. Nonetheless, the disappearance of trivial zero-energy and sub-gap states in our three dimensional set-up, even for the aligned chain, indicates that the formation of trivial zero-energy sub-gap states is strongly suppressed when the chain is placed on top of a three-dimensional superconductor. Especially since zero-energy states do form in an aligned two-dimensional system of comparable width and length. As the most realistic experimental setup is an embedded chain on the surface of a three-dimensional superconductor we can conclude that there is a low prevalence of zero-energy sub-gap states due to a smooth decay rotation profile.

4.6 Domain wall

In this section, we will investigate the sub-gap states forming due to domain-wall rotation profiles. The results from the previous section show that the formation of trivial zero-energy states is unlikely when the length of the superconductor (x direction) exceeds the length of the chain and there is a smooth decay in rotation rate. However, sub-gap states due to a domain wall profile, i.e. a smooth change between a clockwise and anticlockwise rotation of the magnetic moments within the chain, can be expected to be largely independent of the relative position of the chain end and the superconductor boundary. Although it should be noted that, for this profile, low energy subgap states can be expected to form close to the domain wall rather than at ends of the chain, as is expected for MBSs.

One-dimensional model

First, utilising the one-dimensional model outlined in Sec. 4.3 we find that a chain with a domain wall profile does support trivial states with almost zero energy in both the case of an aligned (see Fig. 4.6a) and also an embedded chain (see Fig. 4.6b), which is in contrast to the system with the smooth decay profile, for which we did not observe trivial zero-energy states in the embedded case. In particular, within a domain wall profile, the rotation rate of magnetic moments is set by Eqs. (4.9) and (4.13) such that the rotation rate of the magnetic moments smoothly interpolates between $\Phi_L \ll -\frac{2\pi}{N_C}$ on the left side and $\Phi_R \gg \frac{2\pi}{N_C}$ on the right side of the chain. Here, we chose for simplicity $\Phi_L = -\Phi_R$, which means that the direction of the rotation changes along the atomic chain (see blue lines in Figs. 4.6e and 4.6f). As such, since the critical exchange coupling at which the gap closes is shifted to larger values for slower rotating magnetic moments, the chain is completely trivial for an exchange coupling below $J_C^<(\Phi_R)$ (see also Fig. 4.2c). Within this trivial regime, we find two sub-gap states – as well as their particle-hole partners – that have almost zero energy and the transition from the aligned to the embedded system does not substantially affect this zero-energy pinning (see Fig. 4.6c). Similar to the chain with a smooth decay, the two lowest sub-gap states of the embedded chain become almost degenerate in the case that the section without magnetic atoms to the left of the atomic chain is sufficiently long, such that the localization length of the states is

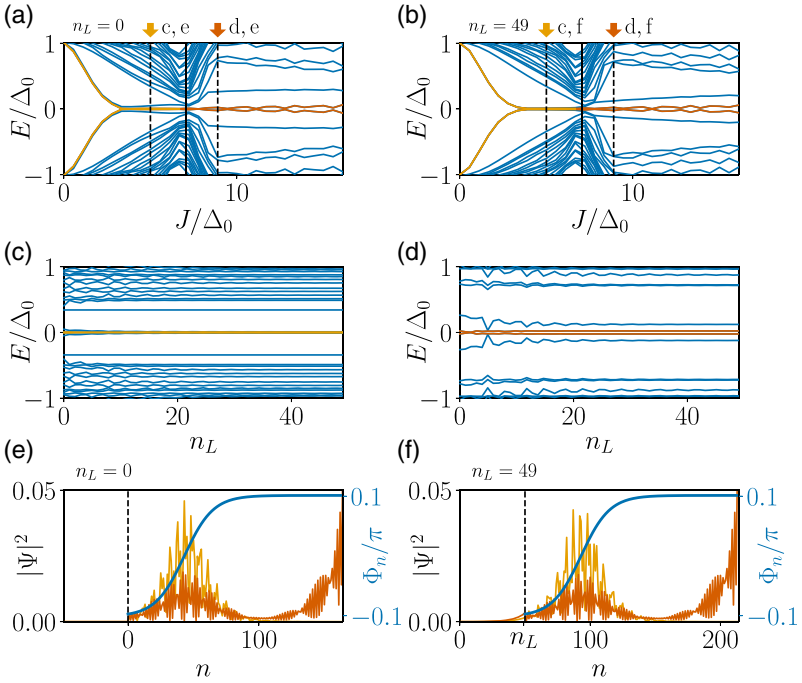

Figure 4.6: *Energy spectrum and probability density of the lowest energy state of a chain with a domain wall rotation profile on a one-dimensional superconductor.* The panels are arranged in the same manner as in Fig. 4.3. The energies of the trivial sub-gap states can be pinned to zero in case of (a) the aligned system and, in contrast to the previous system, also in case of (b) the embedded system. The domain wall allows the formation of a total of four MBSs, which hybridize and form multiple sub-gap states in the topological regime. (c,d) The trivial state (yellow) does not split away from zero when non-magnetic sites are added to the left of the helical spin chain and therefore behaves similarly to the lowest MBS (orange). (e,f) The wavefunction of the trivial state (and the left MBS) is mainly localized in the region where the direction of the rotation changes ($\Phi_n = 0$). The wavefunction profiles are similar in both cases. In particular, the wavefunction of the trivial state (yellow) is approximately zero in the section without magnetic adatoms. Parameters: $N_C = 164$, $t \approx 10$ meV, $\mu = 8$ meV, $\Delta = 1$ meV, $2\Phi_L = -0.2026\pi$, $2\Phi_R = 0.2026\pi$, $\lambda = 22$, $n_0 = 44$, $a = 3$ Å, $n_R = 0$.

much shorter than the length of the left section of the superconductor without any magnetic adatoms.

Further analyzing the wavefunction of the states in this trivial regime $J < J_C^<(\Phi)$, we find the maximum of the probability density of the sub-gap states is localized at the position of the sign change of Φ_n and that the probability density is almost zero in the region where the rotation rate reaches its maximal positive or maximal negative value (see blue line Fig. 4.6e). Adding more sites to the left of the chain does not substantially affect the energy spectrum since the weight of the wavefunction in the section without magnetic atoms is very small (see Fig. 4.6f). In the topological regime, i.e. after the closing and reopening of the bulk gap, we

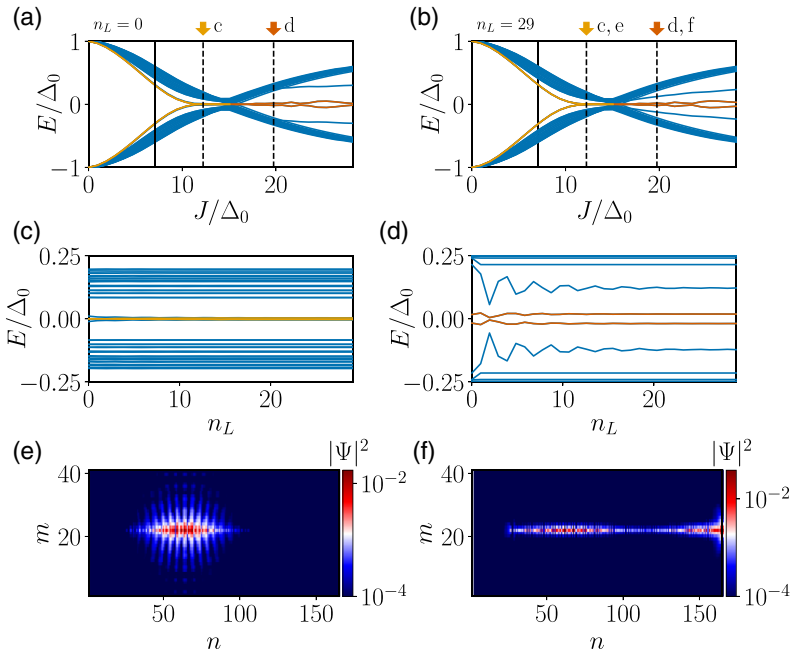

Figure 4.7: *Energy spectrum and probability density of the lowest energy state of a chain with a domain wall rotation profile on a two-dimensional superconductor.* The panels are arranged in the same manner as in Fig. 4.4. The lowest sub-gap state has almost zero energy when (a) the chain is aligned and also when (b) the chain is embedded. The black solid vertical line indicates $J_C^<$ in an analogous one-dimensional system, the line does not match with the actual bulk gap closing and reopening in two dimension system. The energy of the lowest state is neither affected in (c) the trivial nor in (d) the topological regime during the crossover from the aligned to the embedded system if the chain is long enough. (e) The wavefunction of the lowest energy trivial sub-gap state is mostly localized at the domain wall but also slightly leaks into the section with no magnetic adatoms perpendicular to the chain. In contrast in panel (f), the probability density of the lowest state in the topological phase reveals two additional peaks at the ends of the chain due to the left and right MBS. Here, for our choice of parameters, the MBSs hybridize strongly. The parameters are the same as in Fig. 4.6 and we chose $N_y = 41$ and $m_0 = 21$ to account for the two-dimensional system.

find the system hosts four MBSs. In particular, one MBS appears at each end of the chain and one MBS on each side of the domain wall. Depending on the length of the domain wall transition the MBSs closest to the domain wall can hybridize and form a finite-energy sub-gap state [114].

Two-dimensional model

Next, we consider the helical chain with the domain wall profile that is placed on top of a two-dimensional superconductor. The physical properties of the sub-gap states are similar to those found in one-dimensional system, namely trivial states

are pinned to zero-energy in both cases of an aligned and embedded chain (see Figs. 4.7a and 4.7b). The lowest energy states in the trivial regime before the bulk gap closes and reopens (see Fig. 4.7c), as well as in the topological regime after the closing and reopening of the bulk gap (see Fig. 4.7d), are unaffected by the value of n_L. Furthermore, as found in the one-dimensional system, the probability density of the near zero-energy sub-gap states is localized to the region of the smooth change of the rotation rate (see Fig. 4.7e). In the topological regime – after the reopening of the bulk gap – strongly overlapping MBSs appear, their probability density is maximal on the right end and in the region of the smooth transition (see Fig. 4.7f). We note that the wavefunction of the MBS only weakly leaks into the y-direction perpendicular to the chain, such that the wavefunction is confined very close to the position of the chain.

Three-dimensional model

In contrast to the one- and two-dimensional systems considered above, we find that a helical spin chain with a domain wall spin profile that is placed on the surface of a three-dimensional superconductor does not exhibit trivial near zero-energy states. The energy spectrum is shown in Fig. 4.8a. The MBSs appear after the reopening of the bulk gap but there are no sub-gap states in the trivial regime. This behaviour corresponds with a similar observation for the smooth decay profile with aligned boundaries (see Sec. 4.5). In the three-dimensional system, the chain is placed on the surface of the superconductor, thus, boundary effects such as scattering from the surface also affect the energy of the lowest states. Finally we note, as also observed in one- and two-dimensional systems, the probability density of the two lowest states in the topological regime after the bulk gap has closed, reveals the presence of a total of four MBSs, with two that are localized at the ends of the chain and on either side of the domain wall. The MBSs close to the domain wall partially hybridize (see Figs. 4.8b and 4.8c).

4.7 Quasi-MBS

In this section, we consider a chain in which only one section of the chain nominally obeys the topological phase transition criterion, see the discussion in Sec. 4.4 and Fig. 4.2d. In particular, we consider a chain in which the magnetic moments rotate with the rate Φ_R in the long right section of the chain but in the left short section the rotation rate between neighbouring magnetic moments increases smoothly up to Φ_L, with $\Phi_{k_F} > \Phi_L > \Phi_R$. The zero-energy sub-gap states that result from a system only partially obeying the topological phase transition criterion in a certain range of exchange couplings (see Sec. 4.7 for the specific values of J in the one-dimensional system) have been termed *quasi-MBSs* [38].

One-dimensional model

First, considering a one-dimensional system, we find the bulk gap closing and reopening appears at $J_C^{<}(\Phi_R)$. The shorter left section with the faster rotating

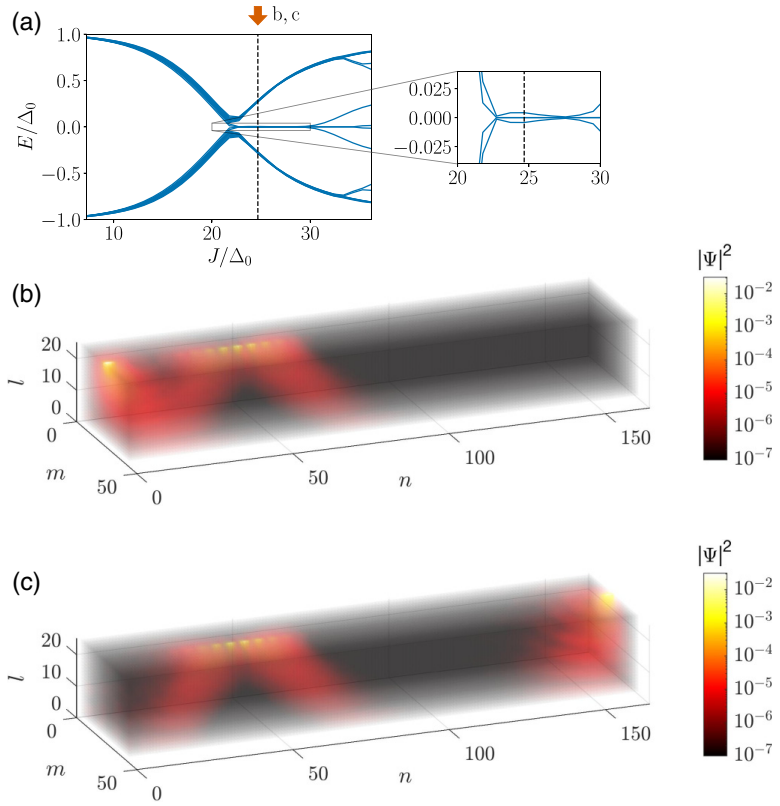

Figure 4.8: *Energy spectrum and probability density of the lowest energy state of a chain with a domain wall rotation profile on a three-dimensional superconductor.* The panels are arranged in the same manner as in Fig. 4.5. (a) No sub-gap states are present before the topological phase transition, indicated by the gap closing and reopening. In the topological regime, MBSs appear. The system hosts four MBSs: two on each side of the domain wall. A zoom into the panel reveals the slightly different energies of the two MBS pairs close to zero due to finite overlap between MBS wavefunctions. The probability density of (b) the second lowest and (c) lowest energy states in the topological phase. The probability densities are plotted for the exchange couplings strength indicated by the orange arrow in panel (a). The parameters are the same as in Fig. 4.6 and in addition we chose $N_y = 41$, $m_0 = 21$, $N_z = 25$, and $l_0 = 1$ to account for the y and z directions.

magnetic moments, however, obeys the topological phase transition criterion for $J_C^<(\Phi_L) < J < J_C^<(\Phi_R)$ (see Fig. 4.2d). As a result, the system contains a sub-gap state for exchange couplings smaller than $J_C^<(\Phi_R)$ which results from the presence of two hybridizing MBSs. The energy of this state is well pinned to zero over a range of exchange coupling strengths in both the aligned (see Fig. 4.9a) and in the embedded setup (see Fig. 4.9b). This effect is shown clearly in Fig. 4.9d where we observe that the energy of the lowest sub-gap states below and above $J_C^<(\Phi_R)$ remain close to zero as an increasing number of sites n_L without magnetic adatoms are added to the superconductor on the left of the system. In contrast to the pre-

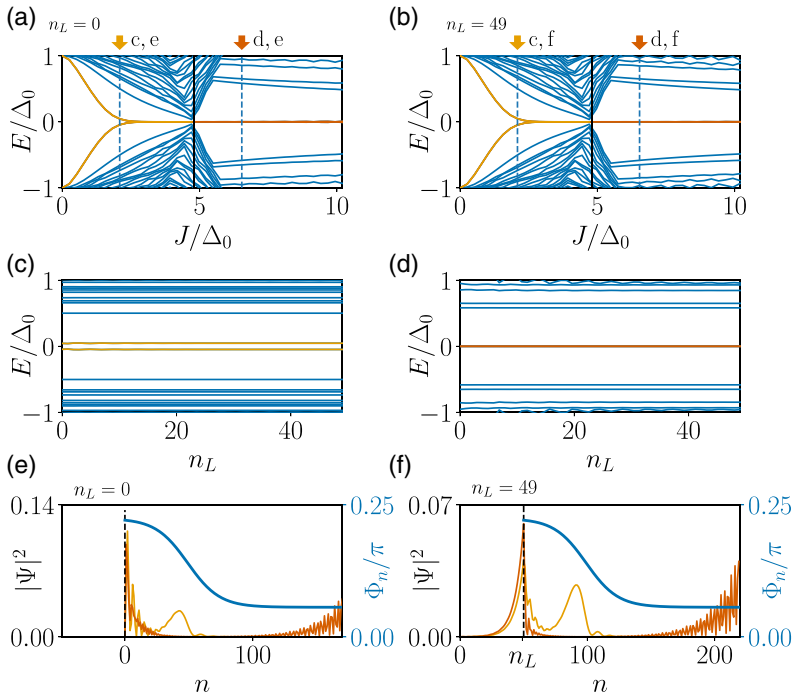

Figure 4.9: *Energy spectrum and probability density of the lowest energy state of a chain with a quasi-MBS rotation profile on a one-dimensional superconductor.* The panels are arranged in the same manner as in Fig. 4.3. The system hosts the so-called quasi MBSs (yellow) for (a) the aligned and (b) the embedded system. (c) [(d)] The energy of the quasi-MBS [the MBS] is nearly independent of the number of sites which are placed to the left of the chain, though the probability densities shown in panels (e) and (f) of the quasi-MBSs (yellow) and the MBSs (orange) are substantially shifted into the section without magnetic adatoms. The probability density reveals clearly that the quasi-MBS originates from hybridizing MBSs which form in the section of faster rotation. Parameters: $N_C = 170$, $t \approx 10$ meV, $\mu = 5$ meV, $\Delta = 1$ meV, $2\Phi_L = 0.4484\pi$, $2\Phi_R = 0.1121\pi$, $\lambda = 25$, $n_0 = 50$, $a = 3\,\text{Å}$, $n_R = 0$.

vious profiles we do not find a degeneracy of the two lowest energy states in the embedded system.

The spatial profile of wavefunctions of these sub-gap states reveals the MBS character of the quasi-MBSs. In particular, in the regime $J < J_C^<(\Phi_R)$, the probability density of the lowest state (yellow) has two separated peaks at the ends of the section that obeys the topological phase transition criterion (see Figs. 4.9e and 4.9f).

Increasing the exchange coupling to values of $J \approx J_C^<(\Phi_R)$ allows one to bring the entire chain into the topological regime. We find the quasi-MBSs transform into MBSs that are localised at the ends of the chain (see orange line in Figs. 4.9e and 4.9f). Other rotation rate profiles, which lead to a local reduction of the critical exchange coupling $J_C^<$, as suggested in Fig. 4.2e, support quasi-MBSs as well and lead to similar results as discussed in this section (not shown). We emphasize that the mechanism for zero-energy states in partially topological chains crucially differs from the one in fully trivial chains, see Secs. 4.5 and 4.6. However, similar to the

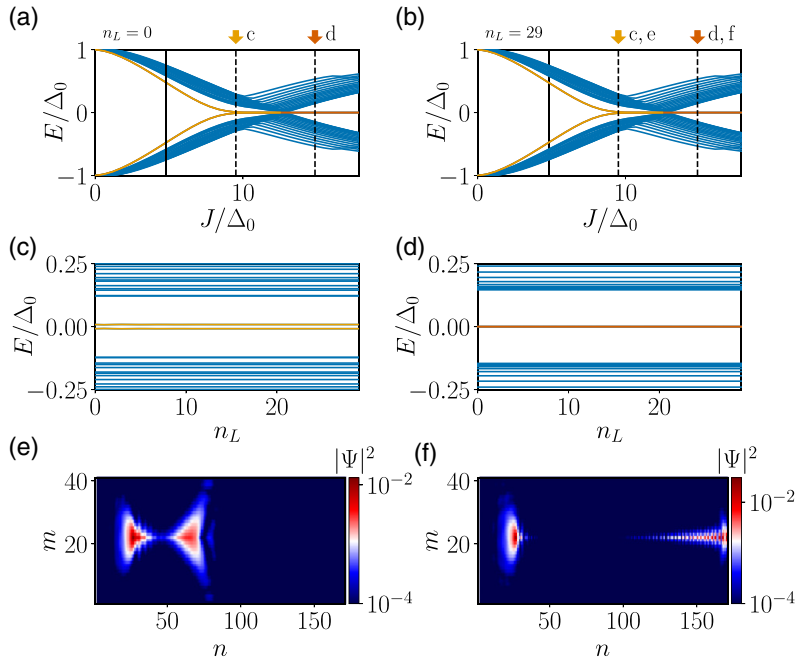

Figure 4.10: *Energy spectrum and probability density of the lowest energy state of a chain with a quasi-MBS rotation profile on a two-dimensional superconductor.* The panels are arranged in the same manner as in Fig. 4.4. The main results are similar to ones found for the one-dimensional model: the quasi-MBS energy is pinned close to zero in the case of (a) the aligned and (b) the embedded system. A calculation of the energy spectrum as a function of the length n_L of the left section without magnetic adatoms in (c) below and (d) above the bulk gap closing and reopening shows that the energies are basically not affected, in contrast, to the systems discussed in Secs. 4.5 and 4.6. The probability density for exchange couplings (e) smaller and (f) larger than the coupling corresponding to the bulk gap closing has a MBS character: The chain can partially enter the topological phase due to the increasing rotation rate of the magnetic moments in the left section of the chain. Consequently, MBSs appear at the ends of this short topological section and move to the ends of the chain with increasing exchange coupling. The parameters are the same as in Fig. 4.9 and in addition we chose $N_y = 41$ and $m_0 = 21$.

domain wall case, near zero-energy states appear in the partially topological chain independent of the boundary conditions for a purely one-dimensional system.

Two-dimensional model

The behavior of a two-dimensional system, consisting of a one-dimensional partially topological chain placed on top of a two-dimensional superconductor, agrees well with the properties of the simple one-dimensional model, presented in the previous subsection. In particular, the energy of the sub-gap states does not depend on n_L (see Figs. 4.10c and 4.10d) and the sub-gap states are pinned close to zero-energy over some range of the exchange coupling strength before the gap closes and re-

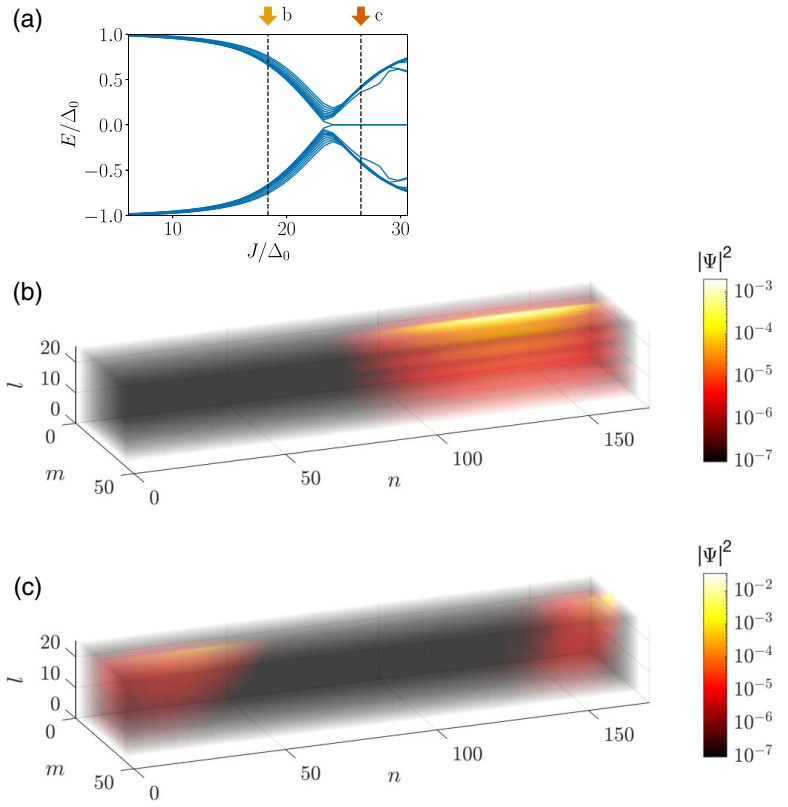

Figure 4.11: *Energy spectrum and probability density of the lowest energy state of a chain with a quasi-MBS rotation profile on a three-dimensional superconductor.* The panels are arranged in the same manner as in Fig. 4.5. (a) The system undergoes a topological phase transition indicated by the gap closing and reopening and the appearance of zero-energy MBSs. This three-dimensional system does not host any trivial zero-energy sub-gap states. Probability density of the lowest state energy in (b) the trivial and (c) the topological phase, respectively. Unlike the one- and two-dimensional systems, the lowest state in the trivial state is not localized in the region of the smooth change of the rotation rate. The probability densities are plotted for the exchange couplings strengths indicated by the yellow and orange arrow in panel (a). The parameters are the same as in Fig. 4.9 and in addition we choose $N_y = 41$, $m_0 = 21$, $N_z = 25$, $l_0 = 1$

opens (see Figs. 4.10a and 4.10b). A subsystem of the chain enters the topological regime for exchange couplings smaller than the value at which the bulk gap closing and reopening appears, with quasi-MBSs emerging at the ends of this subsystem (see Fig. 4.10e). The leakage of the wavefunction in parallel or perpendicular direction to neighbouring sites of the chain does not affect the zero-energy pinning. For sufficiently large exchange couplings the gap closes and reopens and the right MBS is pushed to the end of the chain (see Fig. 4.10f).

Three-dimensional model

Finally, we examine a helical chain with a quasi-MBS rotation rate profile as in Fig. 4.2d on top of a three-dimensional superconductor and use the same parameters for the chain as in the two-dimensional system. In contrast to the one- and two-dimensional systems we do not find near zero-energy states in this three-dimensional system, even though the parameters are the same. Indeed, the energy spectrum shows a clear bulk gap closing and reopening as a function of J with zero-energy MBSs present only after this closing and reopening (see Fig. 4.11a). The probability density of the lowest state in the trivial and the topological regime is shown in Figs. 4.11b and 4.11c, respectively. The lowest-energy trivial state is not bound to the region in which Φ smoothly changes and, in contrast to the lower dimensional systems, this lowest energy state is actually extended over the section in which the rotation angle is almost constant, suggesting it is not of quasi-MBS nature.

This result in combination with Secs. 4.5 and 4.6 suggest that the formation of trivial sub-gap states due to non-periodic rotations of the magnetic moments along the chain is unlikely in three-dimensional systems. We again note, however, that simulations in three dimensions are limited and that these results do not exclude the presence of trivial zero-energy sub-gap states, however, our results show that these states are less prevalent in three-dimensional systems than in one- and two-dimensional systems and far less abundant than in equivalent nanowire systems.

4.8 Conclusions

In this paper, we investigated the prevalence of trivial zero-energy bound states due to non-periodic helical spin chains of magnetic adatoms on the surface of superconductors. Generalizing the established unitary transformation between the helical spin chain and the Rashba nanowire, we mapped a spatially varying rotation rate on non-uniform Rashba SOI and a non-uniform potential in the transformed Hamiltonian. Since these spatially varying potentials, when sufficiently smooth,

Table 4.1: *Presence of trivial zero-energy states in different system configurations.* Models marked with the checkmark ✓ do support the formation of stable trivial zero-energy states. In set-ups with the cross × we did not find trivial-zero energy states, this however does not fully rule out their potential appearance if alternative scenarios are considered.

system	rotation rate profile	1d	2d	3d
aligned	*smooth decay*	✓	✓	×
aligned	*domain wall*	✓	✓	×
aligned	*quasi MBS*	✓	✓	×
embedded	*smooth decay*	×	×	×
embedded	*domain wall*	✓	✓	×
embedded	*quasi MBS*	✓	✓	×

are known to support the formation of trivial zero-energy sub-gap states in Rashba nanowires, the mapping therefore suggests that trivial zero-energy states in helical chains might be as abundant as in Rashba nanowires. However, unlike any realistic nanowire, the helical spin chain is installed on the surface of the superconductor. As such, although it is possible to use this mapping to generate some trivial zero-energy bound states for spin rotation profiles which mimic known mechanisms for trivial sub-gap states in Rashba nanowires, we found that such states are far less abundant in helical spin chains than in nanowires. In particular, for the most experimentally relevant setup of a helical spin chain on the surface of a three-dimensional superconductor we did not find zero-energy bound states for any rotation profile. Finally, in Table 4.1, we summarize our results for the appearance of trivial zero-energy sub-gap states in all examined system configurations.

Although we stress that our findings do not conclusively rule out the appearance of trivial zero-energy sub-gap states in helical spin chain systems due to non-uniformities, they clearly show that the same mechanisms that lead to an abundance of zero-energy bound states in Rashba nanowires do not result in equivalent issues in atomic chains, despite an apparent mapping between the two systems. Further mechanisms other than the variation of the rate Φ_n still can result in zero-energy sub-gap states. For instance, another mechanism has been suggested in Ref. 135: multiple YSR states, emerging from a magnetic chain on top of a superconductor, form a YSR band with van Hove singularities, visible in the LDOS. The energy of these singularities changes in the LDOS close to the chain ends and it can be tuned to zero for sufficiently strong exchange coupling.

We also want to emphasize that our findings are only relevant for long helical spin chains consisting of many rotation periods as, for instance, weakly coupled YSR states in short trivial ferromagnetic chains can be tuned close to zero energy for certain exchange coupling strengths [47, 100–102]. Nonetheless, it is a significant benefit that zero-energy bound states can be more conclusively identified as MBSs in helical spin chains compared to in semiconductor nanowires, especially since atomic chains have a reduced tunability in comparison to semiconductor nanowire devices and so the phase space of a purported MBS signal is more difficult to explore. Our findings coupled with other benefits of helical spin chains, such as the fact that states in atomic chains can be addressed very locally via STM measurements, should enable one to build more confidence that a given zero-energy mode is of topological origin rather than trivial in nature.

4.9 Acknowledgements

This project has received funding from the European Union's Horizon 2020 research and innovation programme under Grant Agreement No 862046 and under Grant Agreement No 757725 (the ERC Starting Grant). This work was supported by the Georg H. Endress Foundation and the Swiss National Science Foundation.

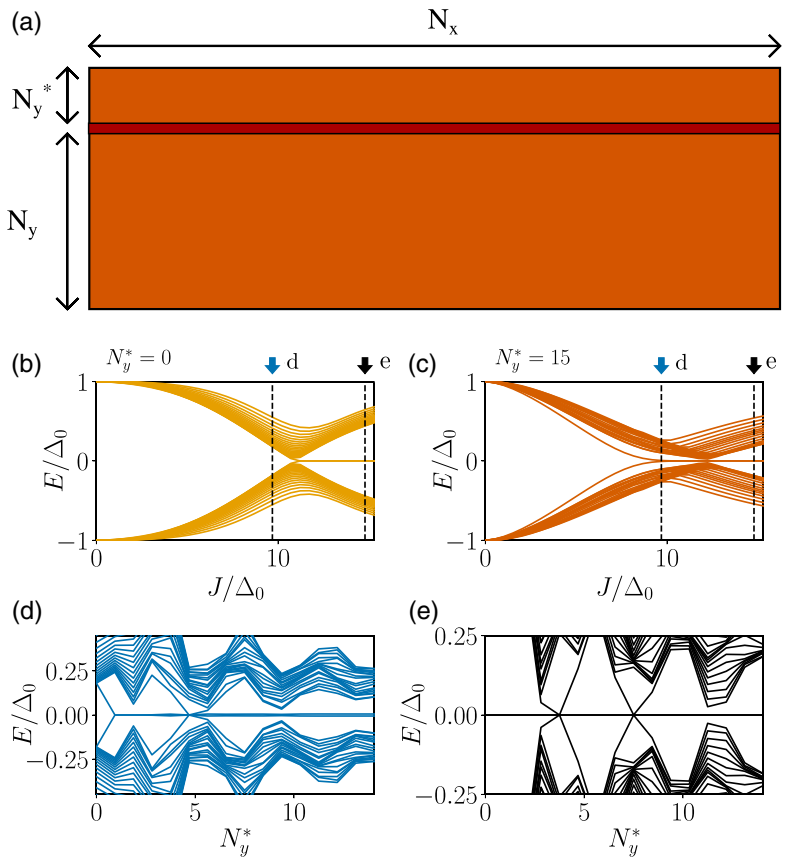

Figure 4.12: *Sketch and energy spectra of a chain, with a quasi-MBS rotation profile deposited at varying distances from the boundary in y direction of a two-dimensional superconductor.* (a) Schematic sketch of an atomic chain (red) deposited on a two-dimensional superconductor (orange). The length N_C of the atomic chain coincides with the total length N_x of the system, the chain is separated by a number of N_y^* sites from the boundary of the two-dimensional superconductor. (b,c) The energy spectrum of the system as a function of the exchange coupling for $N_y^* = 0$ and $N_y^* = 15$, respectively. (d,e) Energies as a function of N_y^* for an exchange coupling smaller and larger than the critical exchange coupling. The blue [black] arrow in panels (a) and (b) indicates the value of the exchange coupling used in panel (d) [(e)]. The trivial zero-energy state is present only if the chain is placed away for the boundary. The parameters are the same as in Fig. 4.10, except that we introduced the quantity N_y^*.

4.A Chain on the boundary of a two-dimensional system

In this Appendix, we vary the position m_0 of the atomic chain in two-dimensional systems. In particular, we place the chain on a boundary of a two-dimensional superconductor. This analysis is motivated by our finding in three-dimensional systems (see Secs. 4.5, 4.6, and 4.7) that the appearance of trivial zero-energy sub-gap states is suppressed compared to similar one- and two-dimensional systems where such states occur due to smooth variations of the rotation rates of neighbouring magnetic moments along the atomic chain. This effect is likely a result of the boundary conditions, since the atomic chain is placed on the surface of the three-dimensional superconductor. In the two-dimensional system, see Secs. 4.5, 4.6, and 4.7, however, we considered a chain in the bulk of the superconductor ($m_0 \approx N_y/2$). Placing the chain on the boundary of a two-dimensional superconductor should, therefore, lead to similar boundary effects as observed in three dimensions.

To further investigate the importance of boundary effects, we consider the model from Sec. 4.7, with identical parameters except that the chain is located at the boundary of the two-dimensional superconductor, $m_0 = 0$. The corresponding energy spectrum as a function of the exchange coupling J is shown in Fig. 4.12b. The bulk gap closing and reopening at a critical exchange coupling is accompanied by the appearance of MBSs at the ends of the chain. The system does not, however, host trivial zero-energy sub-gap states for J smaller than the critical exchange coupling.

Next, we extend the superconductor in y direction, by adding $N_y^* N_x$ sites, so that the atomic chain is not anymore positioned on the boundary of the two-dimensional system. We calculate the energies as a function of N_y^* for an exchange coupling smaller (see Fig. 4.12d) and larger (see Fig. 4.12e) than the coupling necessary for the bulk gap closing and reopening. In the first case, there are no zero-energy states for $N_y^* = 0$, however, for finite values of N_y^* a state with almost zero energy appears. Furthermore, the size of the superconducting gap changes, due to varying leakage of the wavefunctions to sites neighbouring the atomic chain. For sufficiently large values of N_y^* the gap and the zero-energy state stabilize. In contrast, when the entire atomic chain enters the topological regime, MBSs appear also for the choice $N_y^* = 0$ and are stable against changes of N_y^*. In both cases the size of the superconducting gap varies as a function of N_y^*, but it stabilizes for sufficient large values of N_y^*.

Finally, we plot the energy spectrum as a function of the exchange coupling J in the limit of large N_y^*, which means that the localization length of the states in y direction is shorter than the length aN_y^*, see Fig. 4.12c. For this case, we obtain almost the same spectrum as in Fig. 4.10a, as expected. In addition, we calculated the energies of the systems from Secs. 4.5 and 4.6 with $m_0 = 0$. In both cases, we did not find any trivial zero-energy sub-gap states in agreement with the results presented in Fig. 4.12. In conclusion, we find that placing the chain at the boundary of the superconductor, such that it is parallel to the chain, suppresses the formation of trivial zero-energy sub-gap states in two dimensions.

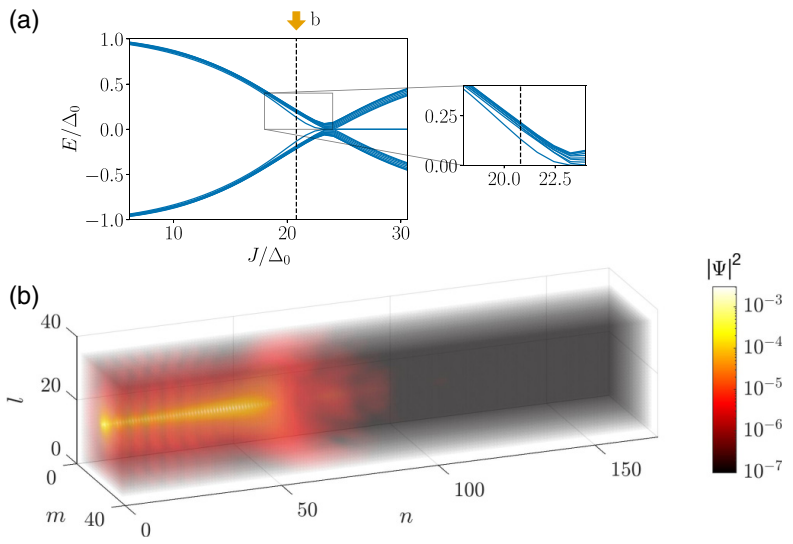

Figure 4.13: *Energy spectrum and probability density of the lowest energy state of a chain with a quasi-MBS rotation profile deposited in the bulk of a three-dimensional superconductor.* (a) The system hosts sub-gap states and a zoom into the figure reveals a clear separation of a sub-gap state from the bulk states. (b) Probability density of the sub-gap state at the exchange coupling indicated by the yellow arrow in panel (a). The trivial sub-gap state is localized in the region of smooth change of the rotation rate. The only changed parameters compared to Fig. 4.11 are the locations of the chain sites, such that $N_y = N_z = 35$ and $m_0 = l_0 = 17$.

4.B Chain in the bulk of a three-dimensional superconductor

In experiments, see e.g. Refs. [100, 101, 112], magnetic adatoms are deposited on the surface of a superconductor, therefore we consider in the main text only chains which are placed on the surface of a three-dimensional superconductor. Here, on the contrary, we study a chain *located fully inside the bulk* of a three-dimensional system. This particular situation cannot easily be realized in experiments, however, we study this scenario to gain further insights about the importance of boundary effects on the sub-gap state at the surface. In particular, a sub-gap state appears in this setup for exchange couplings smaller than the critical value at which the gap closes and reopens, see Fig. 4.13a. This sub-gap state is not pinned to zero energy, but it is separated in energy from the bulk gap, see the zoom on the right side, which is not the case for systems in which the chain is placed on the surface of the superconductor, cf. Secs. 4.5, 4.6, and 4.7. Furthermore, we note that the energy of the sub-gap state could potentially be pinned to zero for sufficiently large systems. Moreover, the state is localized in the region of smooth change of Φ, see Fig. 4.13b. These results in combination with Appendix 4.A clearly show that the relative position of the chain towards the superconductor boundary can strongly affect the energies of sub-gap states and, in particular, trivial zero-energy states are

suppressed when the chain is placed close to a boundary, such as the surface of a three-dimensional superconductor.

Bibliography

[1] N. Read and Dmitry Green. "Paired states of fermions in two dimensions with breaking of parity and time-reversal symmetries and the fractional quantum Hall effect". In: Phys. Rev. B 61 (15 Apr. 2000), pp. 10267–10297.

[2] T. Senthil and Matthew P. A. Fisher. "Quasiparticle localization in superconductors with spin-orbit scattering". In: Phys. Rev. B 61 (14 Apr. 2000), pp. 9690–9698.

[3] D. A. Ivanov. "Non-Abelian Statistics of Half-Quantum Vortices in p-Wave Superconductors". In: Phys. Rev. Lett. 86 (2 Jan. 2001), pp. 268–271.

[4] Chetan Nayak et al. "Non-Abelian anyons and topological quantum computation". In: Rev. Mod. Phys. 80 (3 Sept. 2008), pp. 1083–1159.

[5] Jason Alicea. "New directions in the pursuit of Majorana fermions in solid state systems". In: Rep. Prog. Phys. 75.7 (June 2012), p. 076501.

[6] G. E. Volovik. "Fermion zero modes on vortices in chiral superconductors". In: Journal of Experimental and Theoretical Physics Letters 70.9 (1999), pp. 609–614.

[7] Masatoshi Sato, Yoshiro Takahashi, and Satoshi Fujimoto. "Non-Abelian Topological Order in s-Wave Superfluids of Ultracold Fermionic Atoms". In: Phys. Rev. Lett. 103 (2 July 2009), p. 020401.

[8] Jay D. Sau et al. "Generic New Platform for Topological Quantum Computation Using Semiconductor Heterostructures". In: Phys. Rev. Lett. 104 (4 Jan. 2010), p. 040502.

[9] Masatoshi Sato, Yoshiro Takahashi, and Satoshi Fujimoto. "Non-Abelian topological orders and Majorana fermions in spin-singlet superconductors". In: Phys. Rev. B 82 (13 Oct. 2010), p. 134521.

[10] Jason Alicea. "Majorana fermions in a tunable semiconductor device". In: Phys. Rev. B 81 (12 Mar. 2010), p. 125318.

[11] C.W.J. Beenakker. "Search for Majorana Fermions in Superconductors". In: Annu. Rev. Condens. Matter Phys. 4.1 (2013), pp. 113–136.

[12] Rémy Pawlak et al. "Majorana fermions in magnetic chains". In: Progress in Particle and Nuclear Physics 107 (2019), pp. 1–19.

[13] Katharina Laubscher and Jelena Klinovaja. "Majorana bound states in semiconducting nanostructures". In: Journal of Applied Physics 130 (8 2021), p. 081101.

[14] Karsten Flensberg, Felix von Oppen, and Ady Stern. "Engineered platforms for topological superconductivity and Majorana zero modes". In: Nature Reviews Materials 6.10 (2021), pp. 944–958.

[15] Liang Fu and C. L. Kane. "Superconducting Proximity Effect and Majorana Fermions at the Surface of a Topological Insulator". In: Phys. Rev. Lett. 100 (9 Mar. 2008), p. 096407.

[16] Yuval Oreg, Gil Refael, and Felix von Oppen. "Helical Liquids and Majorana Bound States in Quantum Wires". In: Phys. Rev. Lett. 105 (17 Oct. 2010), p. 177002.

[17] Roman M. Lutchyn, Jay D. Sau, and S. Das Sarma. "Majorana Fermions and a Topological Phase Transition in Semiconductor-Superconductor Heterostructures". In: Phys. Rev. Lett. 105 (7 Aug. 2010), p. 077001.

[18] Suhas Gangadharaiah et al. "Majorana Edge States in Interacting One-Dimensional Systems". In: Phys. Rev. Lett. 107 (3 July 2011), p. 036801.

[19] Doru Sticlet, Cristina Bena, and Pascal Simon. "Spin and Majorana Polarization in Topological Superconducting Wires". In: Phys. Rev. Lett. 108 (9 Mar. 2012), p. 096802.

[20] Fernando Domıénguez, Fabian Hassler, and Gloria Platero. "Dynamical detection of Majorana fermions in current-biased nanowires". In: Phys. Rev. B 86 (14 Oct. 2012), p. 140503.

[21] Elsa Prada, Pablo San-Jose, and Ramón Aguado. "Transport spectroscopy of NS nanowire junctions with Majorana fermions". In: Phys. Rev. B 86 (18 Nov. 2012), p. 180503.

[22] Teemu Ojanen. "Topological π Josephson junction in superconducting Rashba wires". In: Phys. Rev. B 87 (10 Mar. 2013), p. 100506.

[23] Annica M. Black-Schaffer and Jacob Linder. "Majorana fermions in spin-orbit-coupled ferromagnetic Josephson junctions". In: Phys. Rev. B 84 (18 Nov. 2011), p. 180509.

[24] Falko Pientka et al. "Topological Superconductivity in a Planar Josephson Junction". In: Phys. Rev. X 7 (2 May 2017), p. 021032.

[25] Yanick Volpez, Daniel Loss, and Jelena Klinovaja. "Time-reversal invariant topological superconductivity in planar Josephson bijunction". In: Phys. Rev. Research 2 (2 June 2020), p. 023415.

[26] A. Cook and M. Franz. "Majorana fermions in a topological-insulator nanowire proximity-coupled to an s-wave superconductor". In: Phys. Rev. B 84 (20 Nov. 2011), p. 201105.

[27] Henry F. Legg, Daniel Loss, and Jelena Klinovaja. "Majorana bound states in topological insulators without a vortex". In: Phys. Rev. B 104 (16 Oct. 2021), p. 165405.

[28] Jelena Klinovaja, Suhas Gangadharaiah, and Daniel Loss. "Electric-field-induced Majorana Fermions in Armchair Carbon Nanotubes". In: Phys. Rev. Lett. 108 (19 May 2012), p. 196804.

[29] Jay D. Sau and Sumanta Tewari. "Topological superconducting state and Majorana fermions in carbon nanotubes". In: Phys. Rev. B 88 (5 Aug. 2013), p. 054503.

[30] Jelena Klinovaja, Gerson J. Ferreira, and Daniel Loss. "Helical states in curved bilayer graphene". In: Phys. Rev. B 86 (23 Dec. 2012), p. 235416.

[31] Annica M. Black-Schaffer. "Edge Properties and Majorana Fermions in the Proposed Chiral d-Wave Superconducting State of Doped Graphene". In: Phys. Rev. Lett. 109 (19 Nov. 2012), p. 197001.

[32] Jelena Klinovaja and Daniel Loss. "Giant Spin-Orbit Interaction Due to Rotating Magnetic Fields in Graphene Nanoribbons". In: Phys. Rev. X 3 (1 Jan. 2013), p. 011008.

[33] Jelena Klinovaja and Daniel Loss. "Spintronics in MoS_2 monolayer quantum wires". In: Phys. Rev. B 88 (7 Aug. 2013), p. 075404.

[34] Clément Dutreix et al. "Majorana fermions in honeycomb lattices". In: The Eur. Phys. J. B 87.12 (2014), p. 296.

[35] P. San-Jose et al. "Majorana Zero Modes in Graphene". In: Phys. Rev. X 5 (4 Dec. 2015), p. 041042.

[36] Benjamin T. Zhou et al. "Ising superconductivity and Majorana fermions in transition-metal dichalcogenides". In: Phys. Rev. B 93 (18 May 2016), p. 180501.

[37] C. Dutreix. "Topological spin-singlet superconductors with underlying sublattice structure". In: Phys. Rev. B 96 (4 July 2017), p. 045416.

[38] Elsa Prada et al. "From Andreev to Majorana bound states in hybrid superconductor–semiconductor nanowires". In: Nature Reviews Physics 2.10 (2020), pp. 575–594.

[39] V. Mourik et al. "Signatures of Majorana Fermions in Hybrid Superconductor-Semiconductor Nanowire Devices". In: Science 336.6084 (2012), pp. 1003–1007.

[40] M. T. Deng et al. "Anomalous Zero-Bias Conductance Peak in a Nb–InSb Nanowire–Nb Hybrid Device". In: Nano Lett. 12 (12 Dec. 2012), pp. 6412–6419.

[41] Anindya Das et al. "Zero-bias peaks and splitting in an Al–InAs nanowire topological superconductor as a signature of Majorana fermions". In: Nat. Phys. 8 (12 2012), pp. 887–895.

[42] H. O. H. Churchill et al. "Superconductor-nanowire devices from tunneling to the multichannel regime: Zero-bias oscillations and magnetoconductance crossover". In: Phys. Rev. B 87 (24 June 2013), p. 241401.

[43] Satoshi Sasaki et al. "Topological Superconductivity in $\mathrm{Cu}_x\mathrm{Bi}_2\mathrm{Se}_3$". In: Phys. Rev. Lett. 107 (21 Nov. 2011), p. 217001.

[44] Stevan Nadj-Perge et al. "Observation of Majorana fermions in ferromagnetic atomic chains on a superconductor". In: Science 346.6209 (2014), pp. 602–607.

[45] Michael Ruby et al. "End States and Subgap Structure in Proximity-Coupled Chains of Magnetic Adatoms". In: Phys. Rev. Lett. 115 (19 Nov. 2015), p. 197204.

[46] Rémy Pawlak et al. “Probing atomic structure and Majorana wavefunctions in mono-atomic Fe chains on superconducting Pb surface”. In: npj Quantum Information 2.1 (2016), p. 16035.

[47] Lucas Schneider et al. “Precursors of Majorana modes and their length-dependent energy oscillations probed at both ends of atomic Shiba chains”. In: Nature Nanotechnology 17.4 (2022), pp. 384–389.

[48] S. M. Albrecht et al. “Exponential protection of zero modes in Majorana islands”. In: Nature 531.7593 (2016), pp. 206–209.

[49] A. F. Andreev. “The thermal conductivity of the intermediate state in superconductors”. In: Sov. Phys. JETP 19 (5 Nov. 1964), p. 1228.

[50] A. F. Andreev. “Electron Spectrum of the Intermediate State of Superconductors”. In: Sov. Phys. JETP 22 (5 Feb. 1966), p. 455.

[51] G. Kells, D. Meidan, and P. W. Brouwer. “Near-zero-energy end states in topologically trivial spin-orbit coupled superconducting nanowires with a smooth confinement”. In: Phys. Rev. B 86 (10 Sept. 2012), p. 100503.

[52] Eduardo J. H. Lee et al. “Zero-Bias Anomaly in a Nanowire Quantum Dot Coupled to Superconductors”. In: Phys. Rev. Lett. 109 (18 Oct. 2012), p. 186802.

[53] Andrzej Ptok, Aksel Kobiałka, and Tadeusz Doma ński. “Controlling the bound states in a quantum-dot hybrid nanowire”. In: Phys. Rev. B 96 (19 Nov. 2017), p. 195430.

[54] Chun-Xiao Liu et al. “Andreev bound states versus Majorana bound states in quantum dot-nanowire-superconductor hybrid structures: Trivial versus topological zero-bias conductance peaks”. In: Phys. Rev. B 96 (7 Aug. 2017), p. 075161.

[55] Christopher Reeg et al. “Zero-energy Andreev bound states from quantum dots in proximitized Rashba nanowires”. In: Phys. Rev. B 98 (24 Dec. 2018), p. 245407.

[56] Fernando Peñaranda et al. “Quantifying wave-function overlaps in inhomogeneous Majorana nanowires”. In: Phys. Rev. B 98 (23 Dec. 2018), p. 235406.

[57] Christopher Moore, Tudor D. Stanescu, and Sumanta Tewari. “Two-terminal charge tunneling: Disentangling Majorana zero modes from partially separated Andreev bound states in semiconductor-superconductor heterostructures”. In: Phys. Rev. B 97 (16 Apr. 2018), p. 165302.

[58] C. Fleckenstein et al. “Decaying spectral oscillations in a Majorana wire with finite coherence length”. In: Phys. Rev. B 97 (15 Apr. 2018), p. 155425.

[59] Adriaan Vuik et al. “Reproducing topological properties with quasi-Majorana states”. In: SciPost Phys. 7 (2019), p. 061.

[60] Benjamin D. Woods et al. “Zero-energy pinning of topologically trivial bound states in multiband semiconductor-superconductor nanowires”. In: Phys. Rev. B 100 (12 Sept. 2019), p. 125407.

[61] Chun-Xiao Liu et al. "Conductance smearing and anisotropic suppression of induced superconductivity in a Majorana nanowire". In: Phys. Rev. B 99 (2 Jan. 2019), p. 024510.

[62] J. Chen et al. "Ubiquitous Non-Majorana Zero-Bias Conductance Peaks in Nanowire Devices". In: Phys. Rev. Lett. 123 (10 Sept. 2019), p. 107703.

[63] Christian Jünger et al. "Magnetic-Field-Independent Subgap States in Hybrid Rashba Nanowires". In: Phys. Rev. Lett. 125 (1 June 2020), p. 017701.

[64] Marco Valentini et al. "Nontopological zero-bias peaks in full-shell nanowires induced by flux-tunable Andreev states". In: Science 373.6550 (2021), pp. 82–88.

[65] Richard Hess et al. "Local and nonlocal quantum transport due to Andreev bound states in finite Rashba nanowires with superconducting and normal sections". In: Phys. Rev. B 104 (7 Aug. 2021), p. 075405.

[66] Pasquale Marra. "Majorana nanowires for topological quantum computation". In: Journal of Applied Physics 132.23 (Dec. 2022), p. 231101.

[67] Roshni Singh and Bhaskaran Muralidharan. "Conductance Spectroscopy of Majorana Zero Modes in Superconductor-Magnetic Insulating Nanowire Hybrid Systems". In: arXiv:2203.08413 (2022).

[68] Jelena Klinovaja et al. "Topological Superconductivity and Majorana Fermions in RKKY Systems". In: Phys. Rev. Lett. 111 (18 Nov. 2013), p. 186805.

[69] Bernd Braunecker and Pascal Simon. "Interplay between Classical Magnetic Moments and Superconductivity in Quantum One-Dimensional Conductors: Toward a Self-Sustained Topological Majorana Phase". In: Phys. Rev. Lett. 111 (14 Oct. 2013), p. 147202.

[70] M. M. Vazifeh and M. Franz. "Self-Organized Topological State with Majorana Fermions". In: Phys. Rev. Lett. 111 (20 Nov. 2013), p. 206802.

[71] Andreas Heimes, Panagiotis Kotetes, and Gerd Schön. "Majorana fermions from Shiba states in an antiferromagnetic chain on top of a superconductor". In: Phys. Rev. B 90 (6 Aug. 2014), p. 060507.

[72] Hoi-Yin Hui et al. "Majorana fermions in ferromagnetic chains on the surface of bulk spin-orbit coupled s-wave superconductors". In: Scientific Reports 5.1 (2015), p. 8880.

[73] Yang Peng et al. "Strong Localization of Majorana End States in Chains of Magnetic Adatoms". In: Phys. Rev. Lett. 114 (10 Mar. 2015), p. 106801.

[74] Andreas Heimes, Daniel Mendler, and Panagiotis Kotetes. "Interplay of topological phases in magnetic adatom-chains on top of a Rashba superconducting surface". In: New Journal of Physics 17.2 (Feb. 2015), p. 023051.

[75] T.-P. Choy et al. "Majorana fermions emerging from magnetic nanoparticles on a superconductor without spin-orbit coupling". In: Phys. Rev. B 84 (19 Nov. 2011), p. 195442.

[76] Ivar Martin and Alberto F. Morpurgo. "Majorana fermions in superconducting helical magnets". In: Phys. Rev. B 85 (14 Apr. 2012), p. 144505.

[77] S. Nadj-Perge et al. "Proposal for realizing Majorana fermions in chains of magnetic atoms on a superconductor". In: Phys. Rev. B 88 (2 July 2013), p. 020407.

[78] Falko Pientka, Leonid I. Glazman, and Felix von Oppen. "Topological superconducting phase in helical Shiba chains". In: Phys. Rev. B 88 (15 Oct. 2013), p. 155420.

[79] Falko Pientka, Leonid I. Glazman, and Felix von Oppen. "Unconventional topological phase transitions in helical Shiba chains". In: Phys. Rev. B 89 (18 May 2014), p. 180505.

[80] I. Reis, D. J. J. Marchand, and M. Franz. "Self-organized topological state in a magnetic chain on the surface of a superconductor". In: Phys. Rev. B 90 (8 Aug. 2014), p. 085124.

[81] Kim Pöyhönen et al. "Majorana states in helical Shiba chains and ladders". In: Phys. Rev. B 89 (11 Mar. 2014), p. 115109.

[82] L.Yu. "Bound State in Superconductors with Paramagnetic Impurities". In: Acta. Phys. Sin 21 (1965), p. 75.

[83] Hiroyuki Shiba. "Classical Spins in Superconductors". In: Prog. Theor. Phys. 40.3 (Sept. 1968), pp. 435–451.

[84] A. I. Rusinov. "On the Theory of Gapless Superconductivity in Alloys Containing Paramagnetic Impurities". In: Sov. Phys. JETP 29 (1969), p. 1101.

[85] Michael E. Flatté and Jeff M. Byers. "Local Electronic Structure of a Single Magnetic Impurity in a Superconductor". In: Phys. Rev. Lett. 78 (19 May 1997), pp. 3761–3764.

[86] Michael E. Flatté and Jeff M. Byers. "Local electronic structure of defects in superconductors". In: Phys. Rev. B 56 (17 Nov. 1997), pp. 11213–11231.

[87] M. I. Salkola, A. V. Balatsky, and J. R. Schrieffer. "Spectral properties of quasiparticle excitations induced by magnetic moments in superconductors". In: Phys. Rev. B 55 (18 May 1997), pp. 12648–12661.

[88] A. V. Balatsky, I. Vekhter, and Jian-Xin Zhu. "Impurity-induced states in conventional and unconventional superconductors". In: Rev. Mod. Phys. 78 (2 May 2006), pp. 373–433.

[89] Michael E. Flatté and David E. Reynolds. "Local spectrum of a superconductor as a probe of interactions between magnetic impurities". In: Phys. Rev. B 61 (21 June 2000), pp. 14810–14814.

[90] Silas Hoffman et al. "Impurity-induced quantum phase transitions and magnetic order in conventional superconductors: Competition between bound and quasiparticle states". In: Phys. Rev. B 92 (12 Sept. 2015), p. 125422.

[91] Ali Yazdani et al. "Probing the Local Effects of Magnetic Impurities on Superconductivity". In: Science 275.5307 (1997), pp. 1767–1770.

[92] Shuai-Hua Ji et al. "High-Resolution Scanning Tunneling Spectroscopy of Magnetic Impurity Induced Bound States in the Superconducting Gap of Pb Thin Films". In: Phys. Rev. Lett. 100 (22 June 2008), p. 226801.

[93] Michael Ruby et al. "Tunneling Processes into Localized Subgap States in Superconductors". In: Phys. Rev. Lett. 115 (8 Aug. 2015), p. 087001.

[94] Gerbold C. Ménard et al. "Coherent long-range magnetic bound states in a superconductor". In: Nat. Phys. 11.12 (2015), pp. 1013–1016.

[95] Michael Ruby et al. "Wave-Function Hybridization in Yu-Shiba-Rusinov Dimers". In: Phys. Rev. Lett. 120 (15 Apr. 2018), p. 156803.

[96] Felix Küster et al. "Correlating Josephson supercurrents and Shiba states in quantum spins unconventionally coupled to superconductors". In: Nat. Commun. 12.1 (2021), p. 1108.

[97] Dongfei Wang et al. "Spin-Polarized Yu-Shiba-Rusinov States in an Iron-Based Superconductor". In: Phys. Rev. Lett. 126 (7 Feb. 2021), p. 076802.

[98] Felix Küster et al. "Long range and highly tunable interaction between local spins coupled to a superconducting condensate". In: Nat. Commun. 12.1 (2021), p. 6722.

[99] Manuel Steinbrecher et al. "Non-collinear spin states in bottom-up fabricated atomic chains". In: Nat. Commun. 9.1 (2018), p. 2853.

[100] Howon Kim et al. "Toward tailoring Majorana bound states in artificially constructed magnetic atom chains on elemental superconductors". In: Science Advances 4.5 (2018), eaar5251.

[101] Lucas Schneider et al. "Topological Shiba bands in artificial spin chains on superconductors". In: Nat. Phys. 17 (8 2021), pp. 943–948.

[102] Felix Küster et al. "Non-Majorana zero energy modes in diluted spin chains proximitized to a superconductor". In: arXiv:2112.05708 (2021).

[103] Lucas Schneider et al. "Precursors of Majorana modes and their length-dependent energy oscillations probed at both ends of atomic Shiba chains". In: Nature Nanotechnology 17.4 (2022), pp. 384–389.

[104] Hao Ding et al. "Tuning interactions between spins in a superconductor". In: Proc. Natl. Acad. Sci. 118.14 (2021).

[105] Benjamin E. Feldman et al. "High-resolution studies of the Majorana atomic chain platform". In: Nat. Phys. 13.3 (2017), pp. 286–291.

[106] Sangjun Jeon et al. "Distinguishing a Majorana zero mode using spin-resolved measurements". In: Science 358.6364 (2017), pp. 772–776.

[107] Berthold Jäck, Yonglong Xie, and Ali Yazdani. "Detecting and distinguishing Majorana zero modes with the scanning tunnelling microscope". In: Nat. Rev. Phys. 3.8 (2021), pp. 541–554.

[108] M. A. Ruderman and C. Kittel. "Indirect Exchange Coupling of Nuclear Magnetic Moments by Conduction Electrons". In: Phys. Rev. 96 (1 Oct. 1954), pp. 99–102.

[109] Tadao Kasuya. "A Theory of Metallic Ferro- and Antiferromagnetism on Zener's Model". In: Prog. Theor. Phys. 16.1 (July 1956), pp. 45–57.

[110] Kei Yosida. "Magnetic Properties of Cu-Mn Alloys". In: Phys. Rev. 106 (5 June 1957), pp. 893–898.

[111] Bernd Braunecker, Pascal Simon, and Daniel Loss. "Nuclear magnetism and electron order in interacting one-dimensional conductors". In: Phys. Rev. B 80 (16 Oct. 2009), p. 165119.

[112] Matthias Menzel et al. "Information Transfer by Vector Spin Chirality in Finite Magnetic Chains". In: Phys. Rev. Lett. 108 (19 May 2012), p. 197204.

[113] Bernd Braunecker et al. "Spin-selective Peierls transition in interacting one-dimensional conductors with spin-orbit interaction". In: Phys. Rev. B 82 (4 July 2010), p. 045127.

[114] Jelena Klinovaja and Daniel Loss. "Fermionic and Majorana bound states in hybrid nanowires with non-uniform spin-orbit interaction". In: Eur. Phys. J. B 88.3 (2015), p. 62.

[115] Sho Nakosai, Yukio Tanaka, and Naoto Nagaosa. "Two-dimensional p-wave superconducting states with magnetic moments on a conventional s-wave superconductor". In: Phys. Rev. B 88 (18 Nov. 2013), p. 180503.

[116] Wei Chen and Andreas P. Schnyder. "Majorana edge states in superconductor-noncollinear magnet interfaces". In: Phys. Rev. B 92 (21 Dec. 2015), p. 214502.

[117] Guang Yang et al. "Majorana bound states in magnetic skyrmions". In: Phys. Rev. B 93 (22 June 2016), p. 224505.

[118] Utkan Güngördü, Shane Sandhoefner, and Alexey A. Kovalev. "Stabilization and control of Majorana bound states with elongated skyrmions". In: Phys. Rev. B 97 (11 Mar. 2018), p. 115136.

[119] Maxime Garnier, Andrej Mesaros, and Pascal Simon. "Topological superconductivity with deformable magnetic skyrmions". In: Communications Physics 2.1 (2019), p. 126.

[120] Stefan Rex, Igor V. Gornyi, and Alexander D. Mirlin. "Majorana bound states in magnetic skyrmions imposed onto a superconductor". In: Phys. Rev. B 100 (6 Aug. 2019), p. 064504.

[121] Eric Mascot et al. "Topological superconductivity in skyrmion lattices". In: npj Quantum Materials 6.1 (2021), p. 6.

[122] Christoph W Groth et al. "Kwant: a software package for quantum transport". In: New Journal of Physics 16.6 (June 2014), p. 063065.

[123] Yingyi Huang et al. "Metamorphosis of Andreev bound states into Majorana bound states in pristine nanowires". In: Phys. Rev. B 98 (14 Oct. 2018), p. 144511.

[124] Aksel Kobiałka, Nicholas Sedlmayr, and Andrzej Ptok. "Majorana bound states in a superconducting Rashba nanowire in the presence of antiferromagnetic order". In: Phys. Rev. B 103 (12 Mar. 2021), p. 125110.

[125] Sebastián A. Dıéaz et al. “Majorana bound states induced by antiferromagnetic skyrmion textures”. In: Phys. Rev. B 104 (21 Dec. 2021), p. 214501.

[126] Jelena Klinovaja and Daniel Loss. “Composite Majorana fermion wave functions in nanowires”. In: Phys. Rev. B 86 (8 Aug. 2012), p. 085408.

[127] E. Vernek et al. “Subtle leakage of a Majorana mode into a quantum dot”. In: Phys. Rev. B 89 (16 Apr. 2014), p. 165314.

[128] Michael Schecter, Mark S. Rudner, and Karsten Flensberg. “Spin-Lattice Order in One-Dimensional Conductors: Beyond the RKKY Effect”. In: Phys. Rev. Lett. 114 (24 June 2015), p. 247205.

[129] Andreas Theiler, Kristofer Björnson, and Annica M. Black-Schaffer. “Majorana bound state localization and energy oscillations for magnetic impurity chains on conventional superconductors”. In: Phys. Rev. B 100 (21 Dec. 2019), p. 214504.

[130] William S. Cole, S. Das Sarma, and Tudor D. Stanescu. “Effects of large induced superconducting gap on semiconductor Majorana nanowires”. In: Phys. Rev. B 92 (17 Nov. 2015), p. 174511.

[131] Christopher Reeg and Dmitrii L. Maslov. “Transport signatures of topological superconductivity in a proximity-coupled nanowire”. In: Phys. Rev. B 95 (20 May 2017), p. 205439.

[132] Christopher Reeg, Daniel Loss, and Jelena Klinovaja. “Metallization of a Rashba wire by a superconducting layer in the strong-proximity regime”. In: Phys. Rev. B 97 (16 Apr. 2018), p. 165425.

[133] Henry F. Legg, Daniel Loss, and Jelena Klinovaja. “Metallization and proximity superconductivity in topological insulator nanowires”. In: arXiv:2201.02918 (2022).

[134] A. A. Zyuzin et al. “Correlations between Majorana Fermions Through a Superconductor”. In: Phys. Rev. Lett. 111 (5 July 2013), p. 056802.

[135] Jay D. Sau and P. M. R. Brydon. “Bound States of a Ferromagnetic Wire in a Superconductor”. In: Phys. Rev. Lett. 115 (12 Sept. 2015), p. 127003.

CHAPTER 5

Josephson transistor from the superconducting diode effect in domain wall and skyrmion magnetic racetracks

Adapted from:
Richard Hess, Henry F. Legg, Daniel Loss, and Jelena Klinovaja,
"Josephson transistor from the superconducting diode effect in domain wall and skyrmion magnetic racetracks",
Phys. Rev. B 108, 174516 (2023)

In superconductors, the combination of broken time-reversal and broken inversion symmetries can result in a critical current being dependent on the direction of current flow. This phenomenon is known as superconducting diode effect (SDE) and has great potential for applications in future low-temperature electronics. Here, we investigate how magnetic textures such as domain walls or skyrmions on a racetrack can be used to control the SDE in a Josephson junction and how the SDE can be used as a low-temperature read-out of the data in racetrack memory devices. First, we consider a two-dimensional electron gas (2DEG) with strong spin-orbit-interaction (SOI) coupled to a magnetic racetrack, which forms the weak-link in a Josephson junction. In this setup, the exchange coupling between the magnetic texture and the itinerant electrons in the 2DEG breaks time-reversal symmetry and enables the SDE. When a magnetic texture, such as a domain wall or skyrmion enters the Josephson junction, the local exchange field within the junction is changed and, consequently, the strength of the SDE is altered. In particular, depending on the position and form of the magnetic texture, moving the magnetic texture can cause the SDE coefficient to change its sign, enabling a Josephson transistor effect with potentially fast switching frequencies. Further, we find that the SDE is enhanced if the junction length-scales are comparable with the length-scale of the magnetic texture. Furthermore, we show that, under certain circumstances, the symmetry breaking provided by particular magnetic textures, such as skyrmions, can lead to an SDE even in the absence of Rashba SOI in the 2DEG. Our results provide a basis for new forms of readout in low-temperature memory devices as well as demon-

strating how a Josephson transistor effect can be achieved even in the absence of an external magnetic field and intrinsic Rashba SOI.

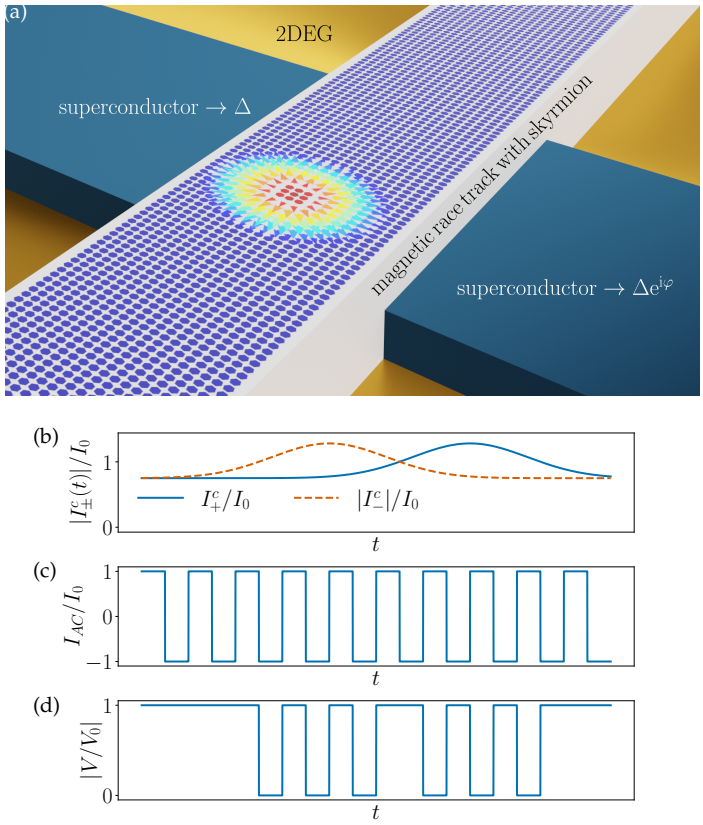

Figure 5.1: *Schematic setup of a Josephson junction sandwiching a magnetic racetrack*: (a) The superconductors, described by the order parameters Δ and $\Delta e^{i\varphi}$, so that the superconducting phase difference is given by φ, are shown in blue, while the racetrack is shown in white. A skyrmion (multi-colored points and arrows) is embedded in a ferromagnetic-out-of-plane background (dark blue dots). (b) The positive [negative] critical super current I^c_+ [I^c_-] changes as a function of time t when a magnetic texture like a domain wall or skyrmion passes through the system. (c) If an alternating current I_{AC} with amplitude I_0 is driven through the junction as a function of the time t, then the change of critical currents and SDE becomes visible in (d) the voltage response signal: The voltage drops if the alternating current is smaller than the critical supercurrents. Here, we normalized the voltage response signal by the voltage strength V_0, which is measured if I_{AC} is larger than the critical supercurrent in a given direction.

5.1 Introduction

One of the building blocks of semiconductor technology is the diode [1] that, due to inversion symmetry breaking, is characterized by different values of resistances for currents flowing in opposite directions and is the basic element required to build a transistor. A similar effect, the so-called *superconducting diode effect* (SDE) appears in superconductors and hybrid superconductor-semiconductor devices with broken time reversal and inversion symmetry [2–25]. In particular, the SDE results in critical currents that are dependent on the direction of current flow. As a con-

sequence, for a range of currents, the SDE results in a zero resistance state in one direction, but finite Ohmic resistance in the opposite direction.

The SDE can appear both in bulk superconductors and in Josephson junctions. Some prominent platforms that result in the SDE are artificial superconducting superlattices that lack an inversion symmetry center [26] and two-dimensional electron gases (2DEG) with strong spin orbit interaction (SOI) brought into proximity with a superconductor [27, 28]. In such setups, time-reversal symmetry is broken by an external magnetic field. The direction of the magnetic field is crucial and should couple to the inversion symmetry breaking term in the Hamiltonian [7], i.e. SOI, in order for a finite SDE to occur.

Recently very large SC diode efficiencies have been achieved, opening the pathway to significant potential technological applications [29, 30]. In addition to an element within future low temperature electronics, it has been proposed that the SDE can be used as a method to detect SOI strength in the presence of a superconductor [28, 31] and as a measure of whether a system has entered a topological phase for example in Rashba or TI nanowires [31, 32].

Another promising future technology is racetrack memory devices [33–35]. The basic idea of a racetrack memory is to store information using magnetic domains in a thin quasi-one-dimensional racetrack. One advantage of racetrack memory is that the device architecture does not rely on moving parts unlike, for instance, a hard disk drive. In a racetrack memory device, currents push magnetic domains along the racetrack [36], which can also enable a much faster read out of the stored data compared to other storage devices. In a standard racetrack setup, the magnetic domains are separated by finite size domain walls, within which the magnetization direction smoothly changes. Alternatively, however, these magnetic domains can be replaced by other spin textures such as magnetic skyrmions [37–40].

The low operating temperature of quantum computers, for instance, has recently resulted in significantly increased interest in electronic elements, both classical and quantum, that work at low temperatures. In particular, these low temperatures enable building basic electronic devices such as transistors and read/write components from superconductors. The use of superconductors in low-temperature electronics also opens up the potential for novel and potentially faster computational devices than room temperature equivalents [29].

In this paper, we consider the interplay of the SDE and magnetic textures on a racetrack. In particular, we show that the SDE can be controlled by magnetic domain walls or skyrmions moving on a racetrack that is sandwiched by a Josephson junction. The control of the SDE by the magnetic texture provides the basis for new low-temperature electronic components such as Josephson transistors as well as for new mechanisms for low-temperature read-out of data in racetrack memory devices. The schematic setup and functionality is shown in Fig. 5.1: A magnetic racetrack (white) is sandwiched by two superconductors (blue) placed on top of a substrate (yellow). Many proposed magnetic racetrack materials have itinerant electrons with strong SOI, however, if the racetrack material is insulating, it can be further coupled to a 2DEG with Rashba SOI to produce an SDE. In Fig. 5.1, the dots and arrows on top of the racetrack indicate the local magnetization. Here, for example, a magnetic skyrmion is embedded in a ferromagnetic background. The critical

currents associated with the Josephson junction are altered when a domain wall or skyrmion passes through the junction and therefore the critical currents also vary as a function of time, as shown schematically in Fig. 5.1c. If an alternating current is driven through the Josephson junction, see Fig. 5.1b, then a finite voltage occurs only when the magnitude of the current in a given direction is larger than the magnitude of the critical current in that direction, see Fig. 5.1d. This change of the voltage signal can serve as an indicator whether a magnetic texture like a domain wall or a skyrmion passes the junction. The fact that the SDE is strongly dependent on the position of the texture can also enable a Josephson transistor effect. Furthermore, importantly, we find that the length-scales such as the ratio between the Fermi wave length in the two-dimensional electron gas and the skyrmion size strongly influence the diode efficiency as a function of the position of the magnetic texture.

In the second part of this paper we consider Josephson junctions hosting racetracks with arbitrary smoothly spatially varying magnetic textures but now in the absence of Rashba SOI. Most proposals for the SDE in Josephson junctions rely on the presence of Rashba SOI in the 2DEG. However, it is known that non-uniform magnetic textures can map to a combination of a uniform exchange coupling field and some effective SOI [41–58]. A helical spin chain, for example, maps to a ferromagnetic chain with Rashba SOI [41, 59]. As such, we show that an intrinsic Rashba SOI in the 2DEG is not a necessary ingredient for the SDE or Josephson transistor effect in our setup and spatially-varying magnetic textures within the Josephson junction by themselves can be sufficient to result in the SDE.

This paper is organized as follows: First, in Sec. 5.2, we define a simple model describing a quasi-two-dimensional electron gas with exchange coupling to the magnetization of a racetrack and which is sandwiched by two superconductors forming a Josephson junction. In addition, we describe details about the how we numerically perform calculations of critical current. Second, in Sec. 5.3, we analyze the SDE for a ferromagnetic texture as a function of the chemical potential and the exchange coupling along the junction with a focus on sign changes of the diode efficiency. Next, in Sec. 5.4, we discuss the SDE for domain walls and skyrmions moving on the racetrack. We classify smooth magnetic textures in Sec. 5.5 and predict which texture-class can mediate a SDE without the need of explicit Rashba SOI in the 2DEG. Finally, we discuss the experimental realization and implications in Sec. 5.6. In Appendix 5.A, we present details on the gauge transformation used in Sec. 5.5 and, in Appendix 5.B, we choose three random examples from different classes of magnetic textures and calculate the corresponding SC diode efficiencies: these numerical results confirm the predictions made in Sec. 5.5. Last, in Appendix 5.C, we clarify notations used throughout the paper.

5.2 Model

We utilize an effective two-dimensional (2D) tight binding model to describe a Josephson junction with a normal section within which the exchange coupling to the magnetic racetrack occurs. The kinetic contribution H_{kin} to the full Hamiltonian

is given by

$$H_{\text{kin}} = -\sum_{\langle \mathbf{n},\mathbf{m}\rangle,\nu} t c^{\dagger}_{\mathbf{n},\nu} c_{\mathbf{m},\nu} + \sum_{\mathbf{n},\nu} (4t - \mu_{\mathbf{n}}) c^{\dagger}_{\mathbf{n},\nu} c_{\mathbf{n},\nu}, \tag{5.1}$$

where $t = \hbar^2/(2m_{\text{eff}}a^2)$ and $\mu_{\mathbf{n}}$ denote the hopping amplitude and the position dependent potential, respectively. Here, m_{eff} is the effective mass of the itinerant electrons and a is the lattice constant. Moreover, $\mathbf{n} = (n_x, n_y)$ [or $\mathbf{m} = (m_x, m_y)$] denote the coordinate of a lattice site and ν denotes the spin $\uparrow, \downarrow$ along the quantization axis, so that $c^{\dagger}_{\mathbf{n},\nu}$ ($c_{\mathbf{n},\nu}$) creates (annihilates) an electron with spin ν at the site $\mathbf{n}$. Here, the first sum runs over nearest neighbour sites as indicated by the notation $\langle \mathbf{n}, \mathbf{m}\rangle$. The superconducting pairing potential is modelled via

$$H_{\text{sc}} = \sum_{\mathbf{n}} \left(\Delta_{\mathbf{n}} c^{\dagger}_{\mathbf{n},\uparrow} c^{\dagger}_{\mathbf{n},\downarrow} + \Delta^{*}_{\mathbf{n}} c_{\mathbf{n},\downarrow} c_{\mathbf{n},\uparrow} \right), \tag{5.2}$$

where $\Delta_{\mathbf{n}}$ denotes the local superconducting pairing potential at site $\mathbf{n}$. The coupling between itinerant electrons and the magnetization texture is described by

$$H_J = \sum_{\mathbf{n},\nu,\nu'} J_{\mathbf{n}} \left[\boldsymbol{\sigma} \cdot \mathbf{S}_{\mathbf{n}} \right]_{\nu,\nu'} c^{\dagger}_{\mathbf{n},\nu} c_{\mathbf{n},\nu'}, \tag{5.3}$$

where $J_{\mathbf{n}}$ describes the exchange coupling strength between the spin $\boldsymbol{\sigma}$ of the itinerant electrons and the local magnetic moments

$$\mathbf{S}_{\mathbf{n}} = \begin{pmatrix} \cos[\vartheta(\mathbf{n})] \sin[\Phi(\mathbf{n})] \\ \sin[\vartheta(\mathbf{n})] \sin[\Phi(\mathbf{n})] \\ \cos[\Phi(\mathbf{n})] \end{pmatrix}, \tag{5.4}$$

which we treat classically. Here, $\Phi(\mathbf{n})$ and $\vartheta(\mathbf{n})$ are the polar and azimuthal angles, respectively, at the lattice site $\mathbf{n}$. Next, we account for Rashba SOI via

$$\begin{aligned} H_{\text{so}} = \alpha_l \sum_{n_x,n_y} \Big[& c^{\dagger}_{\downarrow,n_x-1,n_y} c_{\uparrow,n_x,n_y} - c^{\dagger}_{\downarrow,n_x+1,n_y} c_{\uparrow,n_x,n_y} \\ & + i \left(c^{\dagger}_{\downarrow,n_x,n_y-1} c_{\uparrow,n_x,n_y} - c^{\dagger}_{\downarrow,n_x,n_y+1} c_{\uparrow,n_x,n_y} \right) + \text{H.c.} \Big], \end{aligned} \tag{5.5}$$

with $\alpha_l = \alpha/(2a)$ the finite-difference version of the Rashba SOI strength α [60, 61]. The full Hamiltonian is then given by

$$H = H_{\text{kin}} + H_{\text{sc}} + H_J + H_{\text{so}}. \tag{5.6}$$

We define the parameter profiles as follows: The local superconducting pairing potential is described by

$$\Delta_{\mathbf{n}} = \Delta\Theta(N_L - n_x) + \Delta e^{i\varphi}\Theta(n_x - N_R), \tag{5.7}$$

where N_L (N_R) defines the position of the left (right) interface between superconducting and normal region, so that the width of the junction in terms of lattice sites

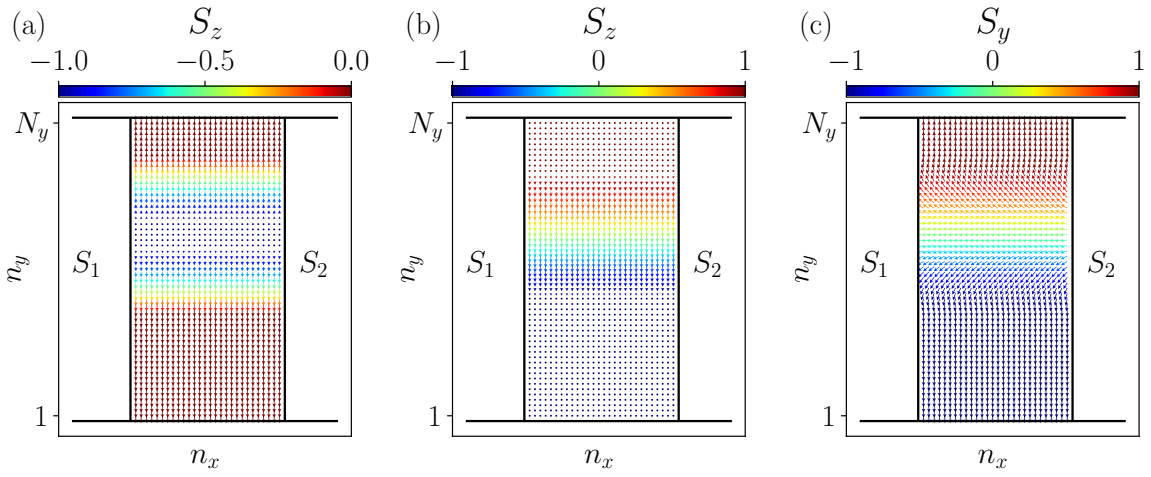

Figure 5.2: *Schematic representation of the domain wall profiles*: Here, S_1 and S_2 denote the left and right superconductor, the magnetization is only non-zero in between the superconducting regions. In particular, the arrows and the colorbars indicate the in-plane and out-of-plane orientation of the magnetic texture, except in panel (c), where the colorbar shows the S_y component, since the S_z component is zero. The domain wall described by the angles (a) $\vartheta_{dw,1}$ and $\Phi_{dw,1}$; (b) $\vartheta_{dw,2}$ and $\Phi_{dw,2}$; (c) $\vartheta_{dw,3}$ and $\Phi_{dw,3}$. We note that only the components pointing in y-direction contribute to the superconducting diode effect in our case. Parameters: $L_y = 2L_x = 140$ nm, $a = 2.5$ nm, and $\lambda_{dw}a = 70$ nm.

is set by $N_J = N_R - N_L$. The angle $\varphi \in [0, 2\pi)$ is the phase difference between left and right superconductor. Here, we used the Heaviside function Θ with the particular definition $\Theta(0) = 1$. Second, we define

$$J_{\mathbf{n}} = J[\Theta(N_R - n_x) - \Theta(N_L - n_x)], \tag{5.8}$$

so that the effective magnetization is only non-zero inside the junction and with a uniform exchange coupling strength, J, to the spins of the itinerant electrons. Finally, we define the local potential

$$\mu_{\mathbf{n}} = \mu + \gamma(\delta_{n_x,N_L} + \delta_{n_y,N_R}), \tag{5.9}$$

where we accounted for tunnel barriers at the superconductor normal (SN) interface. The symbols μ and γ denote the chemical potential and the barrier strength, while $\delta_{n,m}$ denotes the Kronecker delta.

Magnetization profiles

Here, we define the different types of magnetization profiles that will be utilized throughout the paper. Namely, various types of domains walls and skyrmions.

Domain walls

We will analyze three different profiles of magnetic domain walls. First, we consider a domain wall as described by $\vartheta_{dw,1}(n_y) = \frac{\pi}{2}$ and

$$\Phi_{dw,1}(n_y) = \begin{cases} \frac{\pi}{2}, & n_y \leq n_{dw}, \\ \frac{\pi(n_y - n_{dw})}{\lambda_{dw}} + \frac{\pi}{2}, & n_{dw} < n_y < \lambda_{dw} + n_{dw}, \\ \frac{3\pi}{2}, & n_y \geq \lambda_{dw} + n_{dw}, \end{cases} \tag{5.10}$$

where n_{dw} and λ_{dw} determine the y-coordinate of the first site of the domain wall and its size, respectively. This choice of $\Phi(n_y)$ models a magnetization out of plane at the center, $n_c = n_{dw} + \lambda_{dw}/2$, of the domain wall and it describes a magnetization parallel or anti-parallel to the y-direction for large distances ($|n_y - n_c| > \lambda_{dw}/2$) away from the domain wall center, see Fig. 5.2a. The substitution $\Phi_{dw,2}(n_y) \Rightarrow \Phi_{dw,1}(n_y) \pm \pi/2$ leads to a magnetization aligned out of plane for large distances away from the center of the domain wall, which is the second configuration analyzed in this paper. Finally, we define a domain wall with $\Phi_{dw,3}(n_y) = \frac{\pi}{2}$ and $\vartheta_{dw,3}(n_y) = \Phi_{dw,1}(n_y)$ modelling an in-plane magnetization aligned along the y-direction for large distances (larger than $\lambda_{dw}/2$) away from the domain wall center and aligned in x-direction at n_c, see Fig. 5.2a.

Skyrmions

In addition to magnetic domain walls, we consider Néel [62] and Bloch [63] type skyrmions. The Néel skyrmion is described by a polar angle of the form

$$\Phi_{ns}(\mathbf{n}) = \begin{cases} \pi & \text{if } r > \lambda_s, \\ \pi r/\lambda_s & \text{otherwise}, \end{cases} \tag{5.11}$$

where $n_{u,s}$ with $u \in \{x, y\}$ denotes the x- and y-coordinate of the center of the skyrmion and λ_s sets the length-scale of the skyrmion. Moreover, we introduced the quantity $r = \sqrt{(n_x - n_{x,s})^2 + (n_y - n_{y,s})^2}$ measuring the distance from the center of the skyrmion and the vector

$$\mathbf{r} = \begin{pmatrix} n_x - n_{x,s} \\ n_y - n_{y,s} \end{pmatrix} = \begin{pmatrix} r\cos[\vartheta_{ns}(n_x, n_y)] \\ r\sin[\vartheta_{ns}(n_x, n_y)] \end{pmatrix}, \tag{5.12}$$

which defines the azimuthal angle $\vartheta_{ns}(\mathbf{n})$ measured from the position of the skyrmion. The angle of the Bloch skyrmion is related to the Néel skyrmion angle via $\vartheta_{bs} \to \vartheta_{ns} - \frac{\pi}{2}$.

Calculation of the current

In this subsection, we present the details on the calculations of the supercurrents. The computation is mainly based on the Heisenberg equation of motion [64–66], which, in general, supports the computation of local currents. Here, however, we are mainly interested in the total current passing in x-direction through the system.

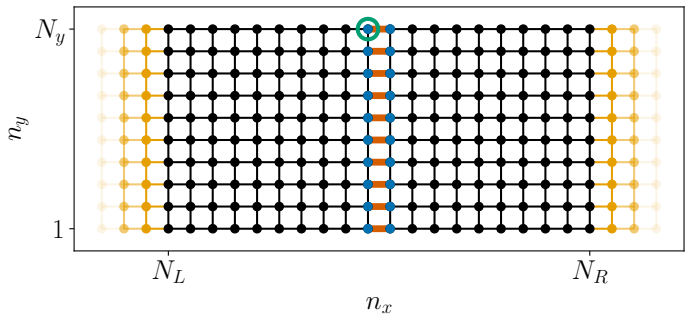

Figure 5.3: *Schematic illustration of the implemented tight binding model*: The normal region is represented by the black and blue sites, while the superconducting leads are represented by the yellow sites. The total current in x-direction is calculated by summing up the local currents on the red bonds between the blue colored sites. We note that the number of sites shown here does not match with the number of sites used in the actual calculations.

This total current is conserved inside the junction and therefore the total current does not depend on the x-coordinate, as long as it is located in the junction. In contrast, the calculation of the current inside the superconductor requires a self-consistent calculation of the superconducting order parameter to ensure current conservation, this however is not considered here, therefore we follow the calculations presented in Refs. [67–71].

The local current between two adjacent lattice sites $\mathbf{n}$ and $\mathbf{m}$ is given by

$$I_{\mathbf{n},\mathbf{m}} = 2\frac{ek_BT}{\hbar}\sum_{n=0}^{\infty}\mathrm{Im}\left\{\mathrm{Tr}\left[H_{\mathbf{n},\mathbf{m}}G_{\mathbf{m},\mathbf{n}}(i\omega_n) - H_{\mathbf{m},\mathbf{n}}G_{\mathbf{n},\mathbf{m}}(i\omega_n)\right]\right\}, \tag{5.13}$$

where k_B and T denote the Boltzmann constant and the temperature of the system, respectively [67–71]. Moreover, $H_{\mathbf{n},\mathbf{m}}$ [$G_{\mathbf{n},\mathbf{m}}$] is the submatrix of the Hamiltonian [Green's function] that connects the sites $\mathbf{n}$ and $\mathbf{m}$. In addition, $\omega_n = (2n+1)\pi k_BT$ are the fermionic Matsubara frequencies and the corresponding summation over n can be carried out numerically due to a fast convergence, which enables a truncation of the sum when the required accuracy is reached. Next, we define the total current $I_x = \sum_{\mathbf{n}\in\Upsilon} I_{\mathbf{n},\mathbf{n}+\mathbf{e}_x}$ in x-direction as the sum of all local currents through a cross section in y-direction in between two adjacent columns of sites. Here, $\mathbf{e}_x$ denotes the unit vector in x-direction. For example, the total current would be the sum of the all local currents flowing through the red bonds connecting the blue colored sites in Fig. 5.3. Here, we denote the set of sites to the left of the cross section as Υ, which corresponds to the left blue colored sites in Fig. 5.3.

Our numerical calculations are based on the Python package Kwant [72]. In most of the work, we discretize the normal region (black and blue colored sites in Fig. 5.3) and attach superconducting semi-infinite leads to the left and right (yellow colored sites in Fig. 5.3). These leads do not have any exchange field, $J = 0$. The length of the junction $L_y = N_y a$ is set by the number of sites along the y-direction. Although the actual width of the system with leads is infinite along the x-direction,

we will refer to system width as $L_x = N_J a$, i.e., the number of sites describing the width of the junction. Additionally, within the Kwant software, we attach virtual self-energy leads at the blue sites next to the cross section in order to compute the Green's function locally on these sites. A gauge transformation enables us to account for the superconducting phase difference via a complex phase added to the sub-matrix H_{LR} (H_{RL}). In order to improve the code efficiency we follow Ref. 67. In particular, we calculate the zero-phase Green's function for a given Matsubara frequency and afterwards we exploit the Dyson series to obtain the Green's function for finite phase difference φ. We exploit the same scheme to obtain the local density of states (LDOS), however, this time we calculate the retarded Green's function $G(\omega)$ for a normal frequency ω [instead for a Matsubara frequency $G(i\omega_n)$]

$$\rho(\omega, \mathbf{n}) = -\frac{1}{\pi}\mathrm{Tr}_{\mathbf{n}}\left\{\mathrm{Im}\left[G(\omega + i\kappa)\right]\right\}. \tag{5.14}$$

Here, $\mathrm{Tr}_{\mathbf{n}}$ indicates that we perform a partial trace, such that we only account for the Green's function submatrix associated with the site $\mathbf{n}$. Moreover, the parameter κ accounts for broadening, e.g., due to temperature. In this paper, we focus on the LDOS at the end of the cross section, in particular at the green encircled site.

In addition to the method described above, we implemented a separate tight-binding model, where we replace the superconducting leads by finite-size superconducting regions. We use this model to check our results for the LDOS and current. In these finite-size systems we consider the length of the superconducting regions to be larger than the superconducting coherence length ξ, meaning that $N_L a = (N_x - N_R)a > \xi$ holds, where N_x denotes this time the total number of sites in x-direction including the superconducting regions. The finite size of the system enables extraction of all eigenvalues and eigenvectors, so that we can compare the sub-gap eigenvalues with the peaks found in the LDOS calculation. Moreover, we compared selected results for the current obtained from the Heisenberg equation of motion, as described above, with the current obtained from the free energy, which is given by

$$I_x(\varphi) = -\frac{e}{\hbar}\sum_{n, E_n>0}\tanh\left(\frac{E_n}{2k_BT}\right)\frac{\partial E_n}{\partial \varphi}, \tag{5.15}$$

where E_n are the energies of the Hamiltonian as defined in Eq. (5.6) [73].

We note that the code performance is better in case of the first method based on the Green's function calculated in the infinite system compared to the second method, which is based on the eigenvalue calculation in finite-size systems. Therefore, most of the current calculations are based on the first method.

Finally, we introduce the directional dependent critical currents I_+^c and I_-^c that are the maxima and minima of the current phase relation for all phases $\varphi \in [0, 2\pi)$. These represent the critical current for current flow to the right and left, respectively. The corresponding diode efficiency is defined as

$$\eta = \frac{I_+^c - |I_-^c|}{(I_+^c + |I_-^c|)/2}. \tag{5.16}$$

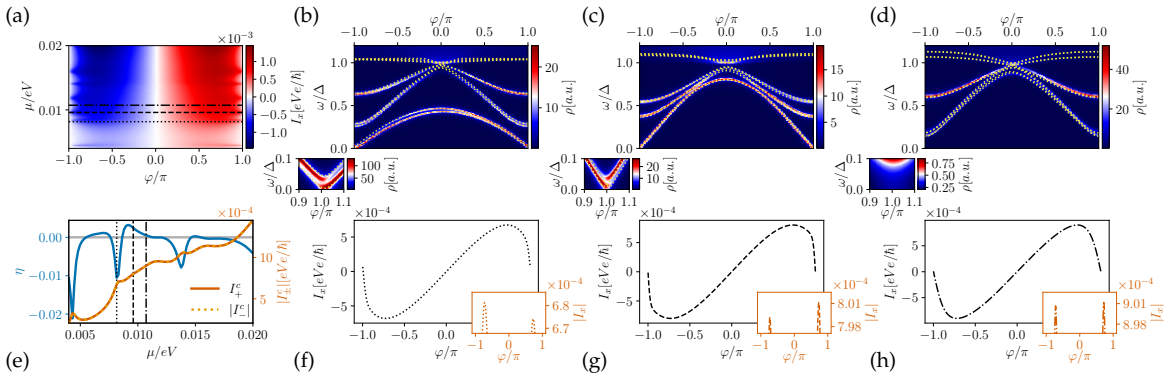

Figure 5.4: *SDE as a function of the chemical potential in case of an in-plane ferromagnetic texture*: (a) Supercurrent I_x as a function of the chemical potential μ and of the superconducting phase difference φ. (b-d) The LDOS, ρ, as a function of the superconducting phase difference φ. The values chosen for the chemical potentials are indicated by the (b) dotted, (c) dashed, and (d) dashed-dotted lines in panel (a). We compare the LDOS calculated at a single site at the end of the junction (with the position of the site chosen similar to the green encircled site in Fig. 5.3) found via Green's function method in the infinite system (with leads) with the low-energy energy spectrum (yellow dashed lines) obtained for a finite-size system in which the superconducting regions are longer than the coherence length (no superconducting leads). If the lowest energy state crosses zero energy, then the diode efficiency is non-zero, see panel (b) and (c). In contrast, if the lowest state does not cross zero energy, then the diode efficiency approaches almost zero, see panel (d). (e) Left [right] y-axis: diode efficiency [critical currents] as a function of the chemical potential. Here, the diode efficiency changes its sign, meaning that the diode can switch its polarity as a function of the chemical potential. (f-h) CPR for the position of the chemical potentials shown as in panels (b-d). The inset shows the modulus of the current and it reveals the diode polarity, which can hardly be read off from the bare CPR. Parameters: $L_y = 2L_x = 140$ nm, $m_{\text{eff}} = 0.023m_e$, $a = 2.5$ nm, $\Delta = 0.8$ meV, $J = 0.05$ meV, $\alpha = 0.05$ eVnm, and $\gamma = 32$ meV.

5.3 SDE for uniform ferromagnetic exchange coupling

Dependence on the chemical potential

In this section, we study the diode efficiency for a system with a uniform ferromagnetic exchange coupling oriented in parallel to the junction (y-direction in Fig. 5.3). This is done in order to find an optimal parameter range for the operation of the SC diode.

We note that, in principle, all ingredients for Majorana bound states (MBSs) in a planar Josephson junction are present, namely (Rashba) SOI due to broken inversion symmetry and exchange coupling, which acts as a local magnetic field, and a superconducting phase difference. Consequently, the appearance of a topological phase is a question of the chosen parameters [74–78]. In this work, however, we

focus on the case of $L_y \ll \xi_{sc}$, where ξ_{sc} denotes the superconducting coherence length, so that the system does not host well localized MBSs. We start our analysis by the calculation of the current as a function of the superconducting phase and the chemical potential, see Fig. 5.4a. We find that the current reveals oscillations as a function of the chemical potential. Additionally, the critical currents increase with growing μ, which can be partially explained with a higher transparency at larger μ. We estimate for the chosen parameters an average transparency of $\tau = 0.77$ and $\tau = 0.94$ at $\mu/\Delta = 10$ in absence of the exchange coupling for the cases $E_{so}/\Delta = 0$ and $E_{so}/\Delta = 0.47$, respectively. In particular, we fitted the current phase relation (CPR) with the formula [79]

$$I_x(\varphi) = \frac{A \sin(\varphi)}{\sqrt{1 - \tau \sin^2(\varphi/2)}}, \tag{5.17}$$

where A and τ serve as fit parameters [1].

We choose three values of the chemical potential, see the dotted, dashed and dotted-dashed lines in Fig. 5.4a, and plot the corresponding current phase relation in Figs. 5.4f-5.4h. The inset shows the modulus of the current, highlighting that there is a difference of the critical currents and also that this difference in critical currents depends on chemical potential. Here, the diode efficiency η is quite small due to the weak exchange coupling. This small exchange coupling was chosen in order to reduce the phase space of the topological phase. In general, if the transparency of the junction is reduced, then the topological phase shrinks for fixed finite exchange couplings [74]. However, as mentioned above, well localized Majorana bound states cannot form in junctions where the length (y-direction of Fig. 5.3) is short.

We also calculated the LDOS at one site located at the end of the junction (see e.g. the green encircled site in Fig. 5.3) by attaching superconducting leads as described in the Sec. 5.2. Here, we show only the positive energy range, see Figs. 5.4b-5.4d, a comparison with the energy spectrum (yellow dashed lines) calculated in a finite size system, in which we discretized the superconducting regions (no superconducting leads), reveals a good agreement. We find that the diode efficiency decreases when the lowest ABS is pushed to higher energies for superconducting phases close to π. A magnification of the low energy region reveals in particular that the lowest ABS energy is almost a linear function of φ close to $\varphi = \pi$ for systems with sizeable diode efficiency, indicating a high transparency mode [19]. In contrast, if the diode efficiency is almost zero, then the derivative of the lowest ABS energy vanishes close to $\varphi = \pi$. Finally, we calculated the diode efficiency and the critical currents as a function of the chemical potential, see Fig. 5.4e. Notably, the diode efficiency changes its sign multiple times, we attribute this behaviour partially to the behaviour of the lowest ABS, which is strongly influenced by the choice of the chemical potential. In principle, such a gate tunable SDE can be used as a Josephson transistor [16], below we will show that this is also possible simply by moving a magnetic texture along the racetrack.

[1] The additional factor of τ in Ref. [79], has been absorbed into the amplitude A.

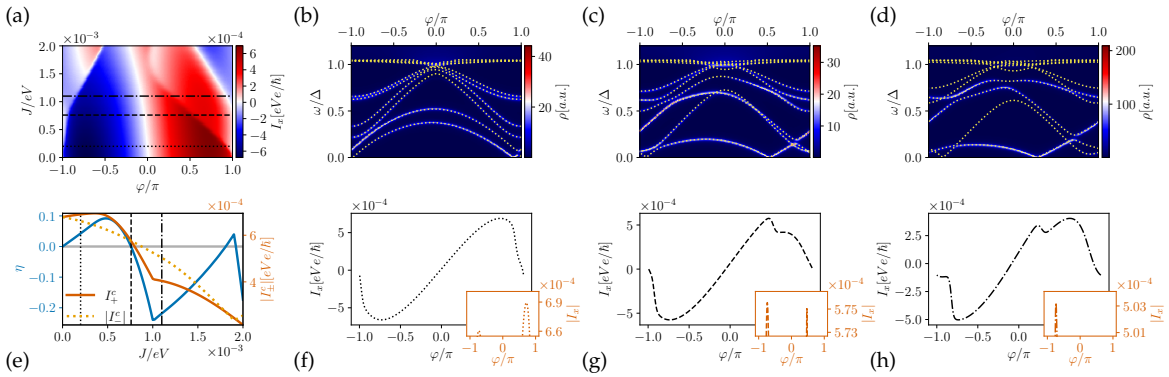

Figure 5.5: *SDE as a function of the exchange coupling strength in case of an in-plane ferromagnetic texture*: (a) Supercurrent I_x as a function of the exchange coupling J and of the superconducting phase difference φ. (b-d) The LDOS, ρ, as a function of the superconducting phase difference φ. The values chosen for the exchange coupling are indicated by the (b) dotted, (c) dashed, and (d) dashed-dotted lines in panel (a). We compare the LDOS at a single site at the end of the junction (with the position of the site chosen similar to the green encircled site in Fig. 5.3), calculated by using Green's function method in the infinite system (with leads) with the low energy spectrum (yellow dashed lines) of a finite-size system in which the superconducting regions are longer than the coherence length (no superconducting leads). The zero-energy crossing of the lowest energy state can lead to kinks in the CPR. (d) Left [right] y-axis: diode efficiency [critical currents] as a function of the exchange coupling. The diode can change its polarity. (f-h) The CPR for the exchange couplings as in panels (b-d). Parameters: $L_y = 2L_x = 140$ nm, $m_{\text{eff}} = 0.023m_e$, $a = 2.5$ nm, $\Delta = 0.8$ meV, $\alpha = 0.05$ eVnm, $\mu = 8.16$ meV, and $\gamma = 32$ meV.

Dependence on the exchange coupling J

Next, we study the current as a function of the exchange coupling strength J for the same ferromagnetic texture, i.e., pointing in y-direction, see Fig. 5.5. The critical currents decrease with growing exchange coupling strength. However, in general, the overall behaviour of the current is quite complicated due to the low energy sub-gap states, which we analyze in Figs. 5.5b-5.5d for three different values of J as indicated by the dotted, dashed and dashed-dotted line in panel Fig. 5.5a. If an ABS crosses zero energy, then the (central) derivative of the ABS energy with respect to the superconducting phase difference is not well defined since only the negative eigenvalues contribute to the ground state and therefore to the current phase relation. A different sign of left and right derivative can lead to jumps in the CPRs, see Eq. (5.15) and Figs. 5.5f-5.5h. These jumps, in turn, lead to strong changes in the diode efficiency including sign changes, as can be read out from the insets, which show the absolute value of the currents. The overall behaviour of the diode efficiency as a function of the exchange coupling is shown in Fig. 5.5e. For small values of J, the diode efficiency η increases approximately linearly with exchange coupling strength. In contrast, for large exchange coupling strengths, the diode

efficiency deviates from the linear behaviour and can even change its sign. In the linear regime, the lowest state crosses zero energy close to $\varphi = \pi$. At the exchange coupling associated with the sign change of the diode efficiency, the zero-energy crossing of the lowest state is pushed away from $\varphi = \pi$. Finally, we note that the SDE generally increases substantially for larger exchange couplings, in part due to the smaller critical currents, as long as the system is not fine-tuned to a chemical potential where the SDE vanishes completely.

Local supercurrents

So far, we have only considered the total supercurrent flowing in x-direction through the junction. Here, in contrast, we analyze the local supercurrents in x-direction as a function of the y-coordinate. With respect to Fig. 5.3, this means that we study the current on individual red bonds. In order to simplify the analysis, we set the exchange coupling J and the Rashba SOI α to zero, such that there is no SDE. It turns out that the current strength oscillates along the y-direction with an approximate period $\lambda_F/2$ set by the Fermi wavelength $\lambda_F \equiv 2\pi/k_F$, where k_F is the Fermi momentum. In Fig. 5.6a we analyze these current oscillation for two different values of the chemical potential.

To connect the LDOS to the current, we note that Eq. (5.13) can be rewritten in terms of the eigenenergies and wavefunctions. This explains the oscillatory behavior of the current with respect to chemical potential, since the wave functions of the ABSs exhibit oscillations in y-direction set by the Fermi wavelength. In order to quantify the direct correlation between oscillations of the wave functions and of the current, we integrate the LDOS over energy window inside the superconducting gap:

$$\varrho(\mathbf{n}) = \int_0^{\Delta} \rho(\omega, \mathbf{n}) \mathrm{d}\omega, \tag{5.18}$$

which also captures the dependence on the superconducting phase difference. In terms of the schematic picture shown in Fig. 5.3, this means that we consider the LDOS along the left column of blue sites. The integrated LDOS, which takes all sub gap states into account, reveals a similar oscillation pattern as in the current, see Fig. 5.6b.

Finally, we note that the oscillations of the current as a function of position can affect the critical currents in systems with finite-size magnetic texture like domain walls or skyrmions. In fact, the ratio between the Fermi wavelength and the spatial extent of the magnetic defect, in our case $\lambda_s a$ or $\lambda_{dw} a$, plays a central role. For example, if $\lambda_s a \gg \lambda_F$, then the effect of the spatial oscillation gets averaged out and have less impact on the diode efficiency as a function of position of the magnetic texture.

5.4 SDE for a texture moving on a racetrack

We now consider what happens to the SDE when a given magnetic texture moves along the portion of the racetrack that forms the normal section of the Josephson

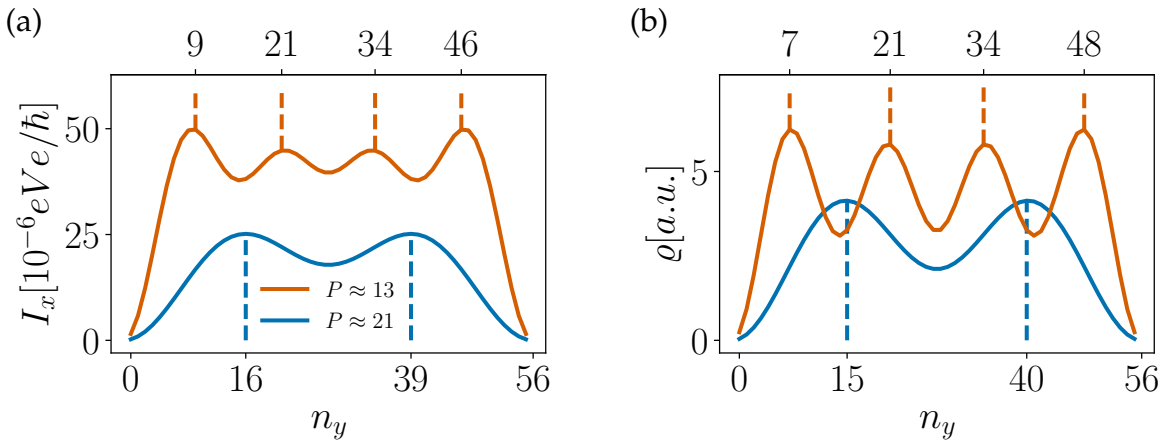

Figure 5.6: *Spatial oscillations in the distribution of local supercurrents:* (a) Local currents as a function of the y-coordinate n_y. The red and blue curve correspond to systems with different chemical potential and therefore different Fermi momenta, which determine the oscillation period P (in units of a). We find that the spatial separation of the peaks agrees well with the analytic prediction of the oscillation period set by the Fermi wavelength. (b) Energy-integrated LDOS [see Eq. (5.18)] along a column of sites to the left of the cross section through which we calculated the current. The oscillation profile of LDOS matches quite well with the profile of the local supercurrents. Parameters: $L_y = 2L_x = 140$ nm, $m_{\text{eff}} = 0.023m_e$, $a = 2.5$ nm, $\Delta = 0.8$ meV, $J = 0$ meV, $\alpha = 0$ eVnm, $\gamma = 0$ meV, and $\mu = 15$ ($\mu = 6$) meV for the red (blue) graph.

junction. We will see that the nature of the magnetic texture and its position within the junction can significantly modify the diode efficiency, η, and even change its sign. As a result, the magnetic texture can be detected by these modifications in the SDE as it moves through the junction or, conversely, moving a magnetic texture through the junction can be used to change the sign of the diode efficiency and therefore create a Josephson transistor effect.

Domain walls

We first study the SDE due to a magnetic domain wall moving through the Josephson junction. First, we consider a magnetic texture as defined by the angle profiles $\Phi_{dw,1}$ and $\Theta_{dw,1}$ and calculate the current as a function of the superconducting phase difference and of the position of the domain wall, see Fig. 5.7a. The phases associated with the positive and negative critical currents as well as the phase associated with zero current change as a function of the position of the domain wall. More importantly, the direction of the exchange field of the magnetic texture reverses when the domain wall passes through the junction and, consequently, the direction of the SDE also inverts, resulting in a Josephson transistor effect. This behaviour manifests itself in a diode efficiency that changes its sign when the domain wall passes through the center of the system ($\approx N_y/2$), see Fig. 5.7b. The sign change and the value $\eta = 0$ for a system with the domain wall in the middle is enforced by sym-

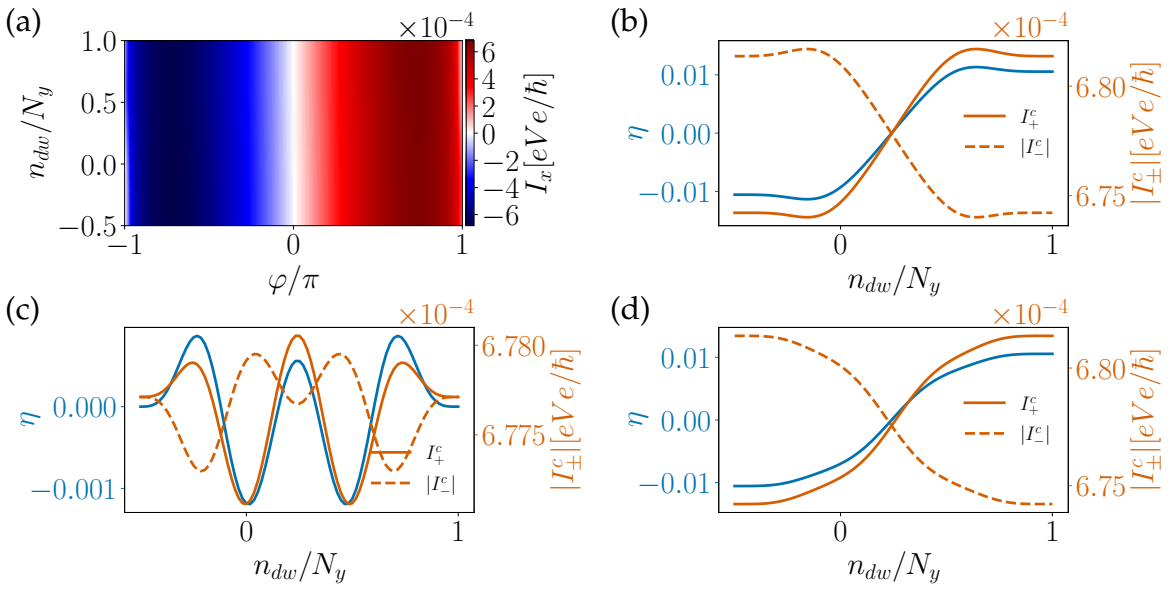

Figure 5.7: *The CPR and diode efficiency as a function of the position of the domain wall:* (a) Supercurrent as a function of phase difference φ and the position of the domain wall n_{dw}. Panels (a) and (b) correspond to the domain wall profile $\Phi_{dw,1}$, while panels (c) and (d), correspond to the profiles $\Phi_{dw,2}$ and $\Phi_{dw,3}$, respectively. (b,c,d) Critical currents $I^c_\pm$ and diode efficiency η as a function of n_{dw}. The diode changes its sign for the magnetic textures considered in (a,b) and (d). In contrast, when the magnetization is out of plane far away from the domain wall (c), then the SDE appears only when the domain wall enters the junction and we observe additional oscillations of the diode efficiency when the domain wall moves through the system. Parameters: $L_y = 2L_x = 140$ nm, $m_{\text{eff}} = 0.023m_e$, $\mu = 8.16$ meV, $a = 2.5$ nm, $\Delta = 0.8$ meV, $J = 0.05$ meV, $\alpha = 0.05$ eVnm, $\gamma = 32$ meV, and $\lambda_{dw}a = 70$ nm.

metry. Moreover, we note that as the domain wall moves through the system, the magnitude of the critical currents change significantly.

In general, the physics of the system are strongly determined by the magnetization direction: Repeating the same calculation with an out-of-plane magnetization far away from the domain wall, as defined by $\Phi_{dw,2}$ and $\Theta_{dw,2}$, reveals a different behavior, see Fig. 5.7c. In particular, if the domain wall is far away from the junction, then the out-of-plane magnetization does not result in a diode effect and consequently the diode efficiency is zero.

The overall behaviour of the diode efficiency as a function of the domain wall position exhibits several sign changes. In a simple picture, one might expect that the diode efficiency first increases when the domain wall moves into the junction until the whole domain wall entered the system. The efficiency would be constant until the domain wall starts to leave the junction. However, the calculated diode effect exhibits a more complex behaviour, see Fig. 5.7c. The diode efficiency does at first grow and is almost constant when the domain wall is located in the middle of the junction, due to the symmetry of the system. However, η exhibits in total four sign changes as the domain wall moves through the junction. We attribute this be-

haviour to the wavefunctions of the ABSs in the junction. As discussed above, the ABSs in the junction exhibit spatially dependent oscillations along the y-direction, resulting in both a probability density and current changes that depends locally on the y-coordinate. Consequently, the diode efficiency can change, including sign changes and associated Josephson transistor effect, if the spatial extent of the domain wall $\lambda_{dw}a$ is of the same order as the Fermi wavelength λ_F. Although for numerical ease we utilized a low chemical potential with large λ_F, in practice, many proposed racetrack materials are good metals [34, 35] such that $\lambda_F \gg \lambda_{dw}a$ and these multiple sign changes would not be expected.

Next, we note that the magnitude of the diode efficiency, η, for the particular choice of magnetization set by $\Phi_{dw,2}$ and $\Theta_{dw,2}$, strongly depends on the ratio between the length of the domain wall and the length of the junction, which are set by λ_{dw} and N_y, respectively. In particular, the longer the junction compared to the domain wall the smaller the superconducting diode efficiency of the whole junction. This is why we chose junctions which are just a few times longer than λ_{dw} and avoid the regime $N_y \gg \lambda_{dw}$.

Finally, we studied a junction with a magnetization as defined via $\Phi_{dw,3}$ and $\Theta_{dw,3}$, see Fig. 5.7d. This junction behaves similar to the first considered set-up with $\Phi_{dw,1}$ and $\Theta_{dw,1}$. In particular, $|\eta|$ is constant until the domain wall enters the junction, then it decreases until the domain wall reaches the center of the junction at which point a sign change in η occurs and $|\eta|$ increases until the domain wall exits the junction.

Skyrmions

We now repeat a similar analysis for the domain wall setups studied above but instead for racetracks hosting skyrmions. First, we note that we only consider skyrmions with a ferromagnetic background aligned in z-direction (out of plane). Therefore, there is no diode effect if a skyrmion is not in the junction ($n_{y,s} \leq -\lambda_s/2$), see Fig. 5.8. Considering first Néel skyrmions moving on a racetrack, when the skyrmion enters the junction the tilted magnetization close to the skyrmion core leads to a finite SDE, see Fig. 5.8a. The strength of this effect strongly depends on the ratio between λ_s and N_y, as in the case of the second domain wall configurations with $\Phi_{dw,2}$ and $\Theta_{dw,2}$ studied above. As above, these spatial oscillations of η are set by the Fermi wavelength and result in a complicated behaviour that can exhibit several sign changes of η, see Fig. 5.8a.

Finally, we consider a Bloch skyrmion with a magnetization as defined in Sec. 5.2, see Fig. 5.8b. The general behaviour is quite similar to the Néel skyrmion and in general we do not find a substantial difference in the diode efficiency response caused by the two types of skyrmionic texture.

5.5 SDE in Josephson junctions without Rashba SOI

So far we have explicitly incorporated Rashba SOI in our model via Eq. (5.5). Here, instead, we remove the Rashba SOI and investigate which type of magnetic texture

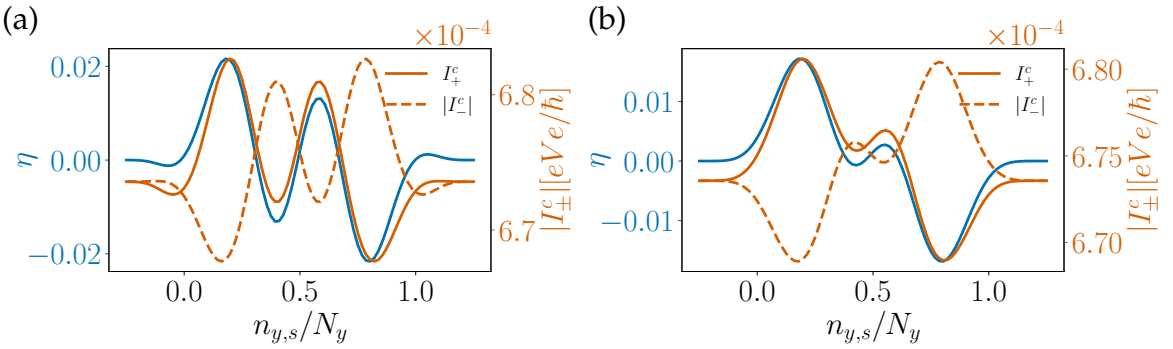

Figure 5.8: *Diode efficiency as a function of the position of the skyrmion:* Critical currents $I^c_\pm$ and diode efficiency η as a function of $n_{y,s}$ for (a) [(b)]: Néel [Bloch] skyrmion. The diode efficiency strongly depends on the position of the Néel or Bloch skyrmion and there are certain positions, depending on the system configurations, where $|\eta|$ is maximized. If there is no skyrmion inside the junction, then there is no SDE ($\eta = 0$) since the background magnetization is out of plane. Parameters: $L_y = 2L_x = 140$ nm, $m_{\text{eff}} = 0.023m_e$, $\mu = 8.16$ meV, $a = 2.5$ nm, $\Delta = 0.8$ meV, $J = -0.2$ meV, $\alpha = 0.05$ eVnm, and $\gamma = 32$ meV, and $\lambda_s a = 35$ nm.

can support a SDE by itself. In order to answer this question, we first consider the continuum Hamiltonian

$$H = \int \mathrm{d}x\, \mathrm{d}y\, \Psi^\dagger(\vec{r})\mathcal{H}(\vec{r})\Psi(\vec{r}), \tag{5.19}$$

where $\Psi^\dagger(\vec{r}) = (\Psi^\dagger_{\vec{r},\uparrow}, \Psi^\dagger_{\vec{r},\downarrow}, \Psi_{\vec{r},\downarrow}, -\Psi_{\vec{r},\uparrow})$ is a vector composed of the field operators $\Psi^\dagger_{\vec{r},\uparrow}$ ($\Psi_{\vec{r},\uparrow}$) and $\Psi^\dagger_{\vec{r},\downarrow}$ ($\Psi_{\vec{r},\downarrow}$) which create (annihilate) a particle at the position $\vec{r} = (x, y)$ with spin up or down, respectively. The Hamiltonian density is given by

$$\begin{aligned}\mathcal{H}(\vec{r};\varphi_{\vec{r}}) &= -\frac{\hbar^2}{2m}(\nabla_x^2 + \nabla_y^2)\tau_z \\ &+ \Delta_{\vec{r}}(\tau_x \cos\varphi_{\vec{r}} + \tau_y \sin\varphi_{\vec{r}}) + J\tau_0 \vec{S}_{\vec{r}}(\Phi_{\vec{r}}, \vartheta_{\vec{r}}) \cdot \vec{\sigma},\end{aligned} \tag{5.20}$$

where σ_j and τ_j are Pauli-matrices acting in spin space and particle hole space respectively, and $\Delta_{\vec{r}}$ is real. As in Eq. (5.4), the spin texture is finite only within the normal section and using spherical coordinates such that

$$\vec{S}_{\vec{r}}(\Phi_{\vec{r}}, \vartheta_{\vec{r}}) = [\cos(\vartheta_{\vec{r}})\sin(\Phi_{\vec{r}}), \sin(\vartheta_{\vec{r}})\sin(\Phi_{\vec{r}}), \cos(\Phi_{\vec{r}})] \tag{5.21}$$

and $\vec{\sigma} = (\sigma_x, \sigma_y, \sigma_z)$ the vector of Pauli matrices. Both the angles $\Phi_{\vec{r}}$ and $\vartheta_{\vec{r}}$ as well as the superconducting phase difference $\varphi_{\vec{r}}$ can depend on position $\vec{r} = (x, y)$ of a given spin of the texture.

Although we are interested in cases where an SDE does occur in the absence of Rashba SOI, we first point out that there are several spin textures where symmetries still do not allow the system to support an SDE. For instance, if the angles $\vartheta_{\vec{r}}$ and $\Phi_{\vec{r}}$ are constant then all spins are parallel, so the system breaks only time reversal symmetry. The absence of Rashba SOI in the 2DEG means that there is no

coupling between spin-space and real space, allowing for arbitrary rotations in spin space. As a consequence, the combination of time-reversal symmetry, $\mathcal{T} = i\sigma_y\tau_0\mathcal{K}$, where $\mathcal{K}$ is complex conjugation, with a rotation in spin-space by π around an axis in the plane perpendicular to the direction of the spins, $\mathcal{R}_\pi$, results in the identity $\mathcal{R}_\pi\mathcal{T}\mathcal{H}(\vec{r};\varphi_{\vec{r}})(\mathcal{R}_\pi\mathcal{T})^\dagger = \mathcal{H}(\vec{r};-\varphi_{\vec{r}})$. This implies that all eigenenergies satisfy $E_n(\varphi) = E_n(-\varphi)$, however, since the current is given by the derivative of eigenenergies with respect to the phase difference, see Eq. (5.15), this identity means that the current must satisfy $I(\varphi) = -I(-\varphi)$ and therefore no SDE can occur since $I^c_+ = |I^c_-|$.

In fact, more generally, if all spins lie in a plane, then the combination of a π rotation around the axis defining the plane and time reversal symmetry will result in the same identity and the absence of an SDE. For instance, if all spins lie in the xz-plane then a rotation in spin-space about the y-axis, such that $\mathcal{R}_\pi = \sigma_y$, will also result in the identity $\mathcal{R}_\pi\mathcal{T}\mathcal{H}(\vec{r};\varphi_{\vec{r}})(\mathcal{R}_\pi\mathcal{T})^\dagger = \mathcal{H}(\vec{r};-\varphi_{\vec{r}})$ which ensures the absence of an SDE. As such, in the absence of Rashba SOI, a simple domain wall will not result in an SDE since it only rotates in a single plane.

Additionally, we note that spatial symmetries can also result in a similar identity that will forbid an SDE. Namely, for our setup we are interested in currents in the x-direction i.e. across the junction. If the spin-texture, $\vec{S}_{\vec{r}}(\Phi_{\vec{r}},\vartheta_{\vec{r}})$, only depends on the y-coordinate then the transformation $\vec{r} = (x,y) \to \vec{r}' = (-x,y)$ gives again $H(\vec{r}';\varphi_{\vec{r}'}) = H(\vec{r};-\varphi_{\vec{r}})$, where we used the fact the phase $\varphi_{\vec{r}}$ only varies in the x-direction and that, without loss of generality, the phase can be taken to be of opposite in sign in the left and right superconducting sections of the junction.

We now demonstrate that an SDE is allowed in the absence of Rashba SOI. First, since the superconducting terms are unaffected by the following transformations and for the ease of discussion, we set $\Delta_{\vec{r}} = 0$ everywhere in the BdG Hamiltonian presented in Eq. (5.20). Next, apply the gauge transformation $U_1 = e^{-i(\vartheta_{\vec{r}}/2-\pi/4)\sigma_z}$ via $\tilde{\mathcal{H}} = U_1^\dagger\mathcal{H}U_1$. This transformation rotates the magnetic texture around the z-axis into the yz-plane. Subsequently, we apply the second gauge transformation $U_2 = e^{i(\Phi/2-\pi/4)\sigma_x}$ as $\mathcal{H}' = U_2^\dagger\tilde{\mathcal{H}}U_2$ and obtain

$$\begin{aligned}\mathcal{H}' =& \frac{-\hbar^2}{2m}\sum_{x_j\in\{x,y\}}\left[\left(\frac{\partial^2}{\partial x_j^2} - \frac{1}{4}\left\{\frac{\partial\vartheta}{\partial x_j}\right\}^2 - \frac{1}{4}\left\{\frac{\partial\Phi}{\partial x_j}\right\}^2\right)\sigma_0\right.\\ &\left. -i\left\{\frac{\partial}{\partial x_j}\Lambda_{x_j}(x,y) + \Lambda_{x_j}(x,y)\frac{\partial}{\partial x_j}\right\}\right] + J\sigma_y,\end{aligned} \tag{5.22}$$

where

$$\Lambda_{x_j}(x,y) = \frac{1}{2}\left[\cos(\Phi)\sigma_y + \sin(\Phi)\sigma_z\right]\frac{\partial\vartheta}{\partial x_j} - \frac{1}{2}\frac{\partial\Phi}{\partial x_j}\sigma_x, \tag{5.23}$$

see Appendix 5.A for a detailed derivation. In this new basis, after the unitary transformation has been applied, the exchange coupling term, namely the term proportional to J, is ferromagnetic. This modification of the exchange coupling field, however, results in new effective SOI term and a non-uniform chemical potential [41–46, 59]. As discussed extensively above, SOI and a ferromagnetic background coupling to the direction of that SOI is the key ingredient that can enable an SDE.

Φ	ϑ	$\mathcal{R}_\pi\mathcal{T}$	$x \to -x$	SDE$[I_x]$
$\Phi = \frac{\pi}{2}$	$\vartheta = \text{const.}$	✓	✓	×
$\Phi = \frac{\pi}{2}$	$\vartheta = \vartheta(x)$	✓	×	×
$\Phi = \frac{\pi}{2}$	$\vartheta = \vartheta(y)$	✓	✓	×
$\Phi = \frac{\pi}{2}$	$\vartheta = \vartheta(x,y)$	✓	×	×
$0 \neq \Phi = \text{const.} \neq \frac{\pi}{2}$	$\vartheta = \text{const.}$	✓	✓	×
$0 \neq \Phi = \text{const.} \neq \frac{\pi}{2}$	$\vartheta = \vartheta(x)$	×	×	✓
$0 \neq \Phi = \text{const.} \neq \frac{\pi}{2}$	$\vartheta = \vartheta(y)$	×	✓	×
$0 \neq \Phi = \text{const.} \neq \frac{\pi}{2}$	$\vartheta = \vartheta(x,y)$	×	×	✓
$\Phi = \Phi(x)$	$\vartheta = \text{const.}$	✓	×	×
$\Phi = \Phi(x)$	$\vartheta = \vartheta(x)$	×	×	✓
$\Phi = \Phi(x)$	$\vartheta = \vartheta(y)$	×	×	✓
$\Phi = \Phi(x)$	$\vartheta = \vartheta(x,y)$	×	×	✓
$\Phi = \Phi(y)$	$\vartheta = \text{const.}$	✓	✓	×
$\Phi = \Phi(y)$	$\vartheta = \vartheta(x)$	×	×	✓
$\Phi = \Phi(y)$	$\vartheta = \vartheta(y)$	×	✓	×
$\Phi = \Phi(y)$	$\vartheta = \vartheta(x,y)$	×	×	✓
$\Phi = \Phi(x,y)$	$\vartheta = \text{const.}$	✓	×	×
$\Phi = \Phi(x,y)$	$\vartheta = \vartheta(x)$	×	×	✓
$\Phi = \Phi(x,y)$	$\vartheta = \vartheta(y)$	×	×	✓
$\Phi = \Phi(x,y)$	$\vartheta = \vartheta(x,y)$	×	×	✓

Table 5.1: *SDE resulting from magnetic textures in a model lacking explicit Rashba SOI:* We classify different textures via their angles Φ and ϑ and check which symmetries are present in the corresponding class to predict whether a SDE is possible. If the spins lie in a plane, then the symmetry $\mathcal{R}_\pi\mathcal{T}$ forbids a SDE. Similar if the texture is not a function of the x-coordinate, then the SDE is suppressed in x-direction. Both symmetries have to be broken to allow a SDE. Here, we indicate the presence [absence] of the symmetries and the SDE with a checkmark [cross]. We note that fine-tuned symmetries, e.g. spatial rotational symmetry, can also result in the absence of an SDE and that, even when symmetry allowed, the magnitude of the SDE is not guaranteed to be large.

Given that a sufficiently complex spin-texture transforms to an effective SOI with ferromagnetic background, it is clear that this can result in an SDE, as long as it is not symmetry forbidden. In Table 5.1 we give all possible forms of spin-textures and indicate whether or not an SDE is allowed in the absence of Rashba SOI as well as whether or not the symmetries discussed above are present. We note, even if allowed by the general symmetries discussed above, fine-tuning of the position of magnetic textures can result in the absence of an SDE due to, e.g., spatial rotational symmetries.

To provide a concrete example of a spin texture where an SDE is allowed, we consider skyrmionic textures. In this case both the angles $\vartheta_{\vec{r}}$ and $\Phi_{\vec{r}}$ are a function of x and y-coordinates and therefore the texture can in principle support a SDE, see Fig. 5.9 where we consider a Néel skyrmion. However, the position of the skyrmion

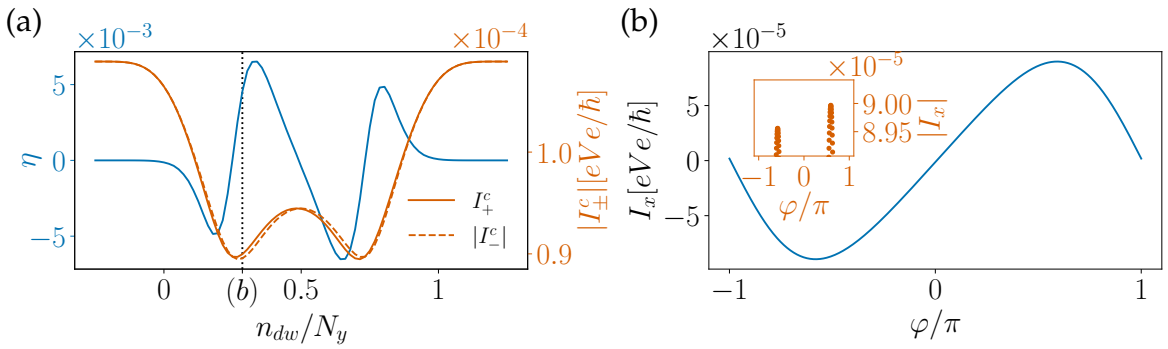

Figure 5.9: *Diode efficiency as a function of the position of the Néel skyrmion in a system without Rashba SOI:* (a) Diode efficiency η as a function of the position of the skyrmion n_{dw}. (b) The CPR and the modulus of the current (shown in the inset) indicate the different critical currents. The CPR is calculated for the skyrmion position as indicated in panel (a). In the inset we plot the data points and do not connect them to show that the resolution of the superconducting phase is indeed high enough to resolve the difference in the critical currents. Parameters: $L_y = 2L_x = 140$ nm, $m_{\text{eff}} = 0.023m_e$, $\mu = 5$ meV, $a = 2.5$ nm, $\Delta = 1$ meV, $J = 1$ meV, $\alpha = 0$ eVnm, $\gamma = 32$ meV, and $\lambda_s a = 35$ nm.

plays a crucial role and the SDE can vanish at certain symmetry points, for example if the skyrmion is placed exactly in the middle of the junction, see Fig. 5.9a. Comparing the Néel and Bloch type skyrmion we find that the polar angle Φ agrees for both textures and the azimuthal angle ϑ can be mapped from the Néel skyrmion to the Bloch skyrmion via the shift $\vartheta \to \vartheta - \pi/2$. The effective SOI, in Eq. (5.22), however, depends only on the derivative of ϑ, but not on the actual value. Consequently, the effective SOI is the same for both configurations, which we also checked numerically. This is also evident from unitary spin rotations around the z axis of the original Hamiltonain $\mathcal{H}$ presented in Eq. (5.20), which leave the energy spectrum unchanged. If we add Rashba SOI to the system, then the gauge transformation acting on this additional Rashba term yields an explicit dependence of the transformed Hamiltonian on the angle ϑ, not only on its derivative, therefore the SDE effect differs for the two types of skyrmions if Rashba SOI is present, as was shown in Fig. 5.8.

Finally we note that the transformation we utilize to map a varying magnetic texture to an effective SOI is quite general, however, we require that the derivatives of the angles are well-defined, such that the angles should be smooth functions of the coordinates x and y. Therefore, we explicitly do not consider certain classes of magnetic textures such as domain walls with $\lambda_{dw} \to 0$ or antiferromagnetic structures.

5.6 Discussion

We have shown how a highly controllable SDE can be achieved in a Josephson junction where the normal section is a racetrack hosting magnetic textures, such

as domain walls or skyrmions. In particular, the positions of the magnetic texture alters the efficiency of the SDE and can even change its sign, enabling a Josephson transistor effect. First, we showed that a system containing Rashba-like spin-orbit interaction enables a high degree of control that can be exerted on the SDE, depending on the location of the magnetic textures. The ratio between the size of a magnetic texture and the dimensions of the Josephson junction plays an important role in determining the maximal strength of the SDE. We also showed that certain textures, such as skyrmions, can enable an SDE even in the absence of Rashba SOI in the itinerant charge carrier material and classified some magnetic textures where this is possible.

Our results show that the interplay between magnetic textures and the SDE is an exciting playground for future low-temperature electronics. For instance, this effect could be used to create a superconducting transistor that is controlled by magnetic textures rather than gates. Furthermore, the effects discussed here could be the basis for a low-temperature readout scheme of racetrack memory devices that can be used as components in cryogenic or quantum computers.

5.7 Acknowledgements

We thank Joel Hutchinson and Maximilian Hünenberger for useful conversations. This project has received funding from the European Union's Horizon 2020 research and innovation programme under Grant Agreement No 862046 and under Grant Agreement No 757725 (the ERC Starting Grant). This work was supported by the Georg H. Endress Foundation and the Swiss National Science Foundation. During the preparation of this paper, Ref. [25] appeared on arXiv also proposing the idea that complex magnetic textures in the absence of an explicit Rashba SOI can be sufficient to mediate an SDE.

5.A Gauge Transformation

Derivation of the rotated Hamiltonian

In this Appendix, we present the detailed derivation of the Hamiltonian in Eq. (5.22). Starting point is the Hamiltonian from Eq. (5.20), which we split into the kinetic term

$$H_0 = -\frac{\hbar^2}{2m}(\nabla_x^2 + \nabla_y^2)\sigma_0 \tag{5.24}$$

and the exchange term

$$H_{Ex} = J\left\{\sin(\Phi)\left[\cos(\vartheta)\sigma_x + \sin(\vartheta)\sigma_y\right] + \cos(\Phi)\sigma_z\right\}. \tag{5.25}$$

These terms transform under the unitary gauge transformation $U_1 = e^{-i(\vartheta/2-\pi/4)\sigma_z}$ as

$$U_1^\dagger H_{Ex} U_1 = J\left[\sin(\Phi)\sigma_y + \cos(\Phi)\sigma_z\right], \tag{5.26}$$

and

$$U_1^\dagger[\nabla_{x_j}^2\sigma_0]U_1 = \left[\nabla_{x_j}^2 - \frac{1}{4}\left(\frac{\partial\vartheta}{\partial x_j}\right)^2\right]\sigma_0 - i\left[\frac{\partial\vartheta}{\partial x_j}\nabla_{x_j} + \frac{1}{2}\frac{\partial^2\vartheta}{\partial x_j,^2}\right]\sigma_z, \tag{5.27}$$

where $x_j \in \{x, y\}$, respectively. Combining the results yields

$$\begin{aligned} U_1^\dagger\mathcal{H}U_1 =& -\frac{\hbar^2}{2m}\sum_{x_j\in\{x,y\}}\left\{\left[\nabla_{x_j}^2 - \frac{1}{4}\left(\frac{\partial\vartheta}{\partial x_j}\right)^2\right]\sigma_0 - i\left[\frac{\partial\vartheta}{\partial x_j}\nabla_{x_j} + \frac{1}{2}\frac{\partial^2\vartheta}{\partial {x_j}^2}\right]\sigma_z\right\} \\ &+ J\left[\sin(\Phi)\sigma_y + \cos(\Phi)\sigma_z\right]. \end{aligned} \tag{5.28}$$

Next, we apply the second gauge transformation $U_2 = e^{i(\Phi/2-\pi/4)\sigma_x}$ on the exchange coupling term like

$$U_2^\dagger\left[\sin(\vartheta)\sigma_y + \cos(\vartheta)\sigma_z\right]U_2 = \sigma_y \tag{5.29}$$

to map the system on a ferromagnet with a magnetization in y-direction. The last term in Eq. (5.28) transforms as

$$U_2^\dagger\sigma_z U_2 = \sin(\Phi)\sigma_z + \cos(\Phi)\sigma_y, \tag{5.30}$$

while the first derivative term takes the form

$$U_2^\dagger\nabla_x\sigma_z U_2 = \frac{1}{2}\frac{\partial\Phi}{\partial x}\left[\cos(\Phi)\sigma_z - \sin(\Phi)\sigma_y\right] + \left[\sin(\Phi)\sigma_z + \cos(\Phi)\sigma_y\right]\nabla_x. \tag{5.31}$$

The combination of the results presented in Eqs. (5.30) and (5.31) allows us to rewrite those terms as a position dependent SOI, please note the symmetrized form which ensures the hermiticity of the term [80]

$$\begin{aligned} &\frac{\partial\vartheta}{\partial x_j}\left[U_2^\dagger\sigma_z\left(\nabla_{x_j}U_2\right) + U_2^\dagger\sigma_z U_2\nabla_{x_j}\right] + \frac{1}{2}\frac{\partial^2\vartheta}{\partial x_j^2}U_2^\dagger\sigma_z U_2 \\ =&\nabla_{x_j}\left[\frac{1}{2}\frac{\partial\vartheta}{\partial x_j}\left(\sin(\Phi)\sigma_z + \cos(\Phi)\sigma_y\right)\right] + \left[\frac{1}{2}\frac{\partial\vartheta}{\partial x_j}\left(\sin(\Phi)\sigma_z + \cos(\Phi)\sigma_y\right)\right]\nabla_{x_j}. \end{aligned} \tag{5.32}$$

The second derivative takes the form

$$U_2^\dagger\nabla_{x_j}^2\sigma_0 U_2 = \nabla_{x_j}^2 - \frac{1}{4}\left[\frac{\partial\Phi}{\partial x_j}\right]^2 + i\frac{1}{2}\left(\nabla_{x_j}\frac{\partial\Phi}{\partial x_j} + \frac{\partial\Phi}{\partial x_j}\nabla_{x_j}\right)\sigma_x. \tag{5.33}$$

Finally, the Hamiltonian is given by

$$\begin{aligned} U_2^\dagger U_1^\dagger\mathcal{H}U_1U_2 =& -\frac{\hbar^2}{2m}\sum_{x_j\in\{x,y\}}\left\{\left(\frac{\partial^2}{\partial x_j^2} - \frac{1}{4}\left[\frac{\partial\Phi}{\partial x_j}\right]^2 - \frac{1}{4}\left[\frac{\partial\vartheta}{\partial x_j}\right]^2\right)\sigma_0\right. \\ &\left. - i\left[\frac{\partial}{\partial x_j}\Lambda_{x_j}(x,y) + \Lambda_{x_j}(x,y)\frac{\partial}{\partial x_j}\right]\right\} + J\sigma_y \end{aligned} \tag{5.34}$$

with

$$\Lambda_{x_j}(x,y) = \frac{1}{2}\frac{\partial\vartheta}{\partial x_j}\left[\sin(\Phi)\sigma_z + \cos(\Phi)\sigma_y\right] - \frac{1}{2}\frac{\partial\Phi}{\partial x_j}\sigma_x. \tag{5.35}$$

Last, we note that the strength of the appearing SOI term does not depend on the strength of the exchange coupling, instead it is only a function of the angles ϑ and Φ or their derivatives with respect to the x- or y-coordinate.

5.B Magnetic textures and the SDE

In Sec. 5.5, we discuss which magnetic textures support a SDE, here we numerically study the underlying conditions and confirm the analytic results. First, we consider a texture that changes in x-direction since the angle $\vartheta = g(n_x)$ depends explicitly on the x-coordinate. Here, the function $g(n_{x_j}) = n_{x_j}\pi/\lambda_m$ with $n_{x_j} = n_x$ or $n_{x_j} = n_y$ is linear for simplicity and the length-scale λ_m, measured in lattice sites, sets the rotation-period of the magnetic texture. Our choice $\Phi = \frac{\pi}{3}$ forces the spins into a conical rotation, so that the texture is not confined to a plane. From our analytic analysis we expect a SDE is in principle possible for this case. Indeed, the current-phase relation and in particular the absolute value of the current reveals a finite SDE in x-direction, see Fig. 5.10. In contrast, if $\vartheta(n_y) = g(n_y)$ varies instead in y-direction, then the SDE is suppressed, since the current does not experience any non-uniformity in x-direction. Last, we prepare a texture lying in a plane, with $\Phi = g(n_x)$ and $\vartheta = \frac{\pi}{3}$, see the last column in Fig. 5.10, the corresponding current is odd-symmetric with respect to φ and does therefore not support a SDE as predicted.

5.C Position of domain walls and skyrmions

In this section, we clarify the meaning of negative values of the domain wall or skyrmion centre position, see for example Fig. 5.7. We emphasize that the junction has only N_y sites in y-direction but we move the domain wall or skyrmion so that only a finite part of it enters the junction, as illustrated in Fig. 5.11, which shows the in-plane magnetization of three system configurations hosting skyrmions: In the first configuration we chose $n_{y,s} = -\lambda_s/2$ so that only a small part of the skymrion is inside the junction. For $n_{y,s} = 0$, only the half of a skyrmion has entered the junction. Last, the case $n_{y,s} = \lambda_s$ describes the scenario in which the whole skyrmion just entered the junction. Finally we note that the same logic applies also to the case $n_{dw} > N_y$ [$n_{y,s} > N_y$]. We note that the definitions of the position of the domain wall and the skyrmion are different: While the skyrmion position $n_{y,s}$ is measured from the center of the skyrmion, the domain wall position is measured from the beginning of the domain wall, see the definitions in Eqs. (5.10) and (5.11).

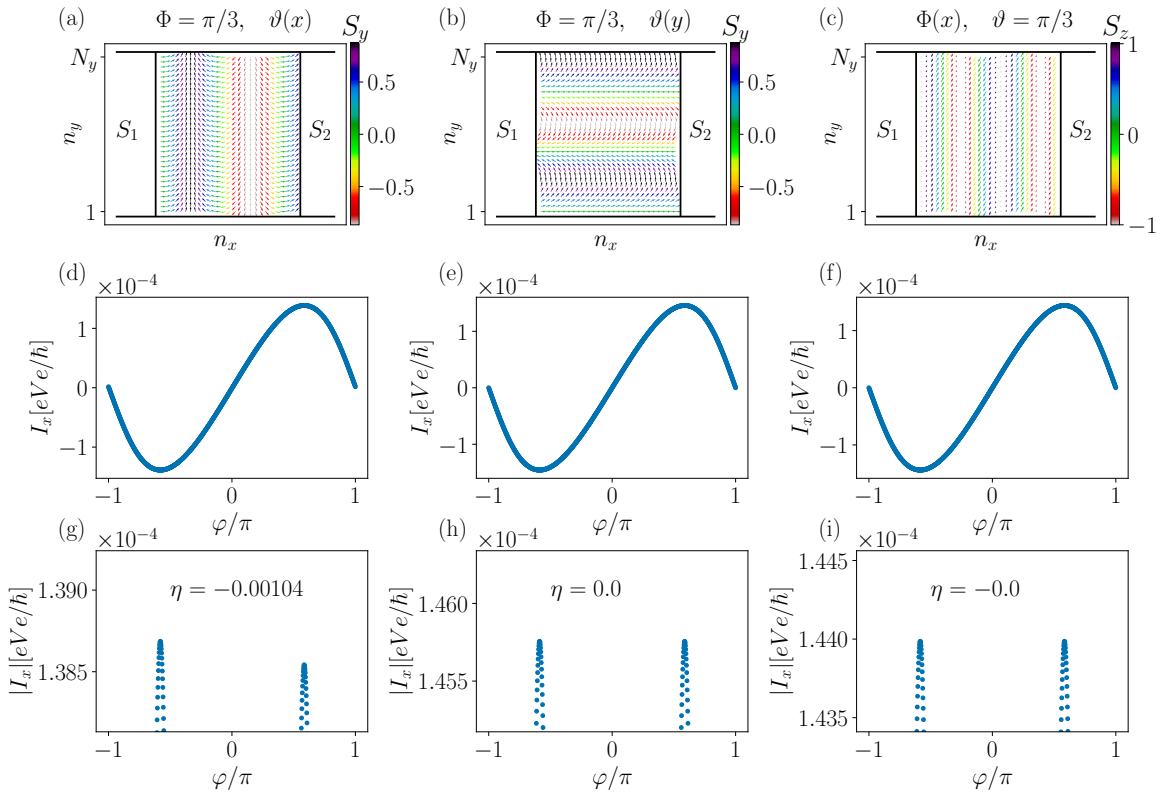

Figure 5.10: *Magnetic textures and the SDE without Rashba SOI*: First row: magnetic textures (a)[b] conical rotation parallel [perpendicular] to the direction of current flow and (c) magnetic texture confined to a plane. Second row: current phase relations corresponding to the magnetic textures. Third row: absolute value of the current as function of the superconducting phase and associated diode efficiency. The first texture yields a SDE, while the others do not, this is in agreement with our analytic analysis. Parameters: $(L_x, L_y) = (70, 80)$ nm, $m_{\text{eff}} = 0.023 m_e$, $\mu = 5$ meV, $a = 2.5$ nm, $\Delta = 1$ meV, $J = 1$ meV, $\alpha = 0$, $\lambda_m a = 20$ nm, and $\gamma = 32$ meV.

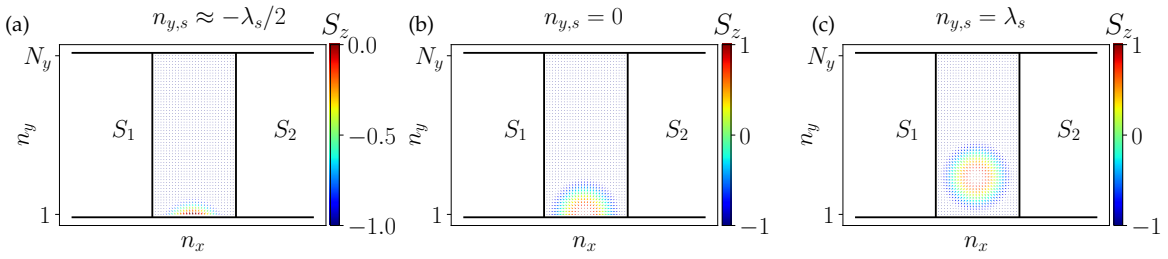

Figure 5.11: *Different positions of a Néel skyrmion*: (a) The skyrmion moved partially into the junction. (b) Half of the skyrmion entered the junction. (c) The whole skyrmion is fully in the junction. The arrows indicate the in-plane direction of the magnetic moments, while the color-code illustrates the local out of plane magnetization. The superconducting regions S_1 and S_2 have with potentially different superconducting phases. The black lines serve as guide lines for the eye to distinguish the normal and superconducting regions and to highlight the system boundaries. Parameters: $L_y = 2L_x = 140$ nm, $a = 2.5$ nm, and $\lambda_s a = 35$ nm.

Bibliography

[1] Ferdinand Braun. "Ueber die Stromleitung durch Schwefelmetalle". In: Annalen der Physik 229.12 (Jan. 1875), pp. 556–563.

[2] G. L. J. A. Rikken and E. Raupach. "Observation of magneto-chiral dichroism". In: Nature 390.6659 (1997), pp. 493–494.

[3] G. L. J. A. Rikken, J. Fölling, and P. Wyder. "Electrical Magnetochiral Anisotropy". In: Phys. Rev. Lett. 87 (23 Nov. 2001), p. 236602.

[4] Ryohei Wakatsuki et al. "Nonreciprocal charge transport in noncentrosymmetric superconductors". In: Science Advances 3.4 (2017), e1602390.

[5] Shintaro Hoshino et al. "Nonreciprocal charge transport in two-dimensional noncentrosymmetric superconductors". In: Phys. Rev. B 98 (5 Aug. 2018), p. 054510.

[6] Kenji Yasuda et al. "Nonreciprocal charge transport at topological insulator/superconductor interface". In: Nature Communications 10.1 (2019), p. 2734.

[7] Noah F. Q. Yuan and Liang Fu. "Supercurrent diode effect and finite-momentum superconductors". In: Proceedings of the National Academy of Sciences 119.15 (2022), e2119548119.

[8] F. Qin et al. "Superconductivity in a chiral nanotube". In: Nature Communications 8.1 (2017), p. 14465.

[9] Rubén Seoane Souto, Martin Leijnse, and Constantin Schrade. "Josephson Diode Effect in Supercurrent Interferometers". In: Phys. Rev. Lett. 129 (26 Dec. 2022), p. 267702.

[10] James Jun He, Yukio Tanaka, and Naoto Nagaosa. "A phenomenological theory of superconductor diodes". In: New Journal of Physics 24.5 (May 2022), p. 053014.

[11] Heng Wu et al. "The field-free Josephson diode in a van der Waals heterostructure". In: Nature 604.7907 (2022), pp. 653–656.

[12] Jiang-Xiazi Lin et al. "Zero-field superconducting diode effect in small-twist-angle trilayer graphene". In: Nature Physics 18.10 (2022), pp. 1221–1227.

[13] Muhammad Nadeem, Michael S. Fuhrer, and Xiaolin Wang. "Superconducting Diode Effect – Fundamental Concepts, Material Aspects, and Device Prospects". In: arXiv:2301.13564 (2023).

[14] Akito Daido, Yuhei Ikeda, and Youichi Yanase. "Intrinsic Superconducting Diode Effect". In: Phys. Rev. Lett. 128 (3 Jan. 2022), p. 037001.

[15] Artem Kononov et al. “One-Dimensional Edge Transport in Few-Layer WTe2”. In: Nano Letters 20.6 (June 2020), pp. 4228–4233.

[16] G. P. Mazur et al. “The gate-tunable Josephson diode”. In: arXiv:2211.14283 (2022).

[17] Yasen Hou et al. “Ubiquitous Superconducting Diode Effect in Superconductor Thin Films”. In: Phys. Rev. Lett. 131 (2 July 2023), p. 027001.

[18] S. Ili ć and F. S. Bergeret. “Theory of the Supercurrent Diode Effect in Rashba Superconductors with Arbitrary Disorder”. In: Phys. Rev. Lett. 128 (17 Apr. 2022), p. 177001.

[19] C Baumgartner et al. “Effect of Rashba and Dresselhaus spin–orbit coupling on supercurrent rectification and magnetochiral anisotropy of ballistic Josephson junctions”. In: Journal of Physics: Condensed Matter 34.15 (Feb. 2022), p. 154005.

[20] Ya. V. Fominov and D. S. Mikhailov. “Asymmetric higher-harmonic SQUID as a Josephson diode”. In: Phys. Rev. B 106 (13 Oct. 2022), p. 134514.

[21] Margarita Davydova, Saranesh Prembabu, and Liang Fu. “Universal Josephson diode effect”. In: Science Advances 8.23 (2022), eabo0309.

[22] Banabir Pal et al. “Josephson diode effect from Cooper pair momentum in a topological semimetal”. In: Nature Physics 18.10 (2022), pp. 1228–1233.

[23] Lorenz Bauriedl et al. “Supercurrent diode effect and magnetochiral anisotropy in few-layer NbSe2”. In: Nature Communications 13.1 (2022), p. 4266.

[24] Abhishek Banerjee et al. “Control of Andreev Bound States Using Superconducting Phase Texture”. In: Physical Review Letters 130.11 (Mar. 2023).

[25] A. Sinner et al. “Superconducting Diode sensor”. In: arXiv:2306.11145 (2023).

[26] Fuyuki Ando et al. “Observation of superconducting diode effect”. In: Nature 584.7821 (2020), pp. 373–376.

[27] Christian Baumgartner et al. “Supercurrent rectification and magnetochiral effects in symmetric Josephson junctions”. In: Nature Nanotechnology 17.1 (2022), pp. 39–44.

[28] Neda Lotfizadeh et al. “Superconducting Diode Effect Sign Change in Epitaxial Al-InAs Josepshon Junctions”. In: arXiv:2303.01902 (2023).

[29] Heng Wu et al. “The field-free Josephson diode in a van der Waals heterostructure”. In: Nature 604.7907 (2022), pp. 653–656.

[30] Carlo Ciaccia et al. “Gate Tunable Josephson Diode in Proximitized InAs Supercurrent Interferometers”. In: arXiv:2304.00484 (2023).

[31] Henry F. Legg, Daniel Loss, and Jelena Klinovaja. “Superconducting diode effect due to magnetochiral anisotropy in topological insulators and Rashba nanowires”. In: Phys. Rev. B 106 (10 Sept. 2022), p. 104501.

[32] Henry F. Legg et al. “Parity protected superconducting diode effect in topological Josephson junctions”. In: arXiv:2301.13740 (2023).

[33] Stuart S. P. Parkin, Masamitsu Hayashi, and Luc Thomas. "Magnetic Domain-Wall Racetrack Memory". In: Science 320.5873 (2008), pp. 190–194.

[34] Kwang-Su Ryu et al. "Chiral spin torque at magnetic domain walls". In: Nature Nanotechnology 8.7 (2013), pp. 527–533.

[35] Stuart Parkin and See-Hun Yang. "Memory on the racetrack". In: Nature Nanotechnology 10.3 (2015), pp. 195–198.

[36] A. Yamaguchi et al. "Real-Space Observation of Current-Driven Domain Wall Motion in Submicron Magnetic Wires". In: Phys. Rev. Lett. 92 (7 Feb. 2004), p. 077205.

[37] X. Z. Yu et al. "Skyrmion flow near room temperature in an ultralow current density". In: Nature Communications 3.1 (2012), p. 988.

[38] J. Sampaio et al. "Nucleation, stability and current-induced motion of isolated magnetic skyrmions in nanostructures". In: Nature Nanotechnology 8.11 (2013), pp. 839–844.

[39] R. Tomasello et al. "A strategy for the design of skyrmion racetrack memories". In: Scientific Reports 4.1 (2014), p. 6784.

[40] Jan Mueller. "Magnetic skyrmions on a two-lane racetrack". In: New J. Phys. 19 (2017), p. 025002.

[41] Bernd Braunecker et al. "Spin-selective Peierls transition in interacting one-dimensional conductors with spin-orbit interaction". In: Phys. Rev. B 82 (4 July 2010), p. 045127.

[42] T.-P. Choy et al. "Majorana fermions emerging from magnetic nanoparticles on a superconductor without spin-orbit coupling". In: Phys. Rev. B 84 (19 Nov. 2011), p. 195442.

[43] Ivar Martin and Alberto F. Morpurgo. "Majorana fermions in superconducting helical magnets". In: Phys. Rev. B 85 (14 Apr. 2012), p. 144505.

[44] S. Nadj-Perge et al. "Proposal for realizing Majorana fermions in chains of magnetic atoms on a superconductor". In: Phys. Rev. B 88 (2 July 2013), p. 020407.

[45] Sho Nakosai, Yukio Tanaka, and Naoto Nagaosa. "Two-dimensional p-wave superconducting states with magnetic moments on a conventional s-wave superconductor". In: Phys. Rev. B 88 (18 Nov. 2013), p. 180503.

[46] Wei Chen and Andreas P. Schnyder. "Majorana edge states in superconductor-noncollinear magnet interfaces". In: Phys. Rev. B 92 (21 Dec. 2015), p. 214502.

[47] Guang Yang et al. "Majorana bound states in magnetic skyrmions". In: Phys. Rev. B 93 (22 June 2016), p. 224505.

[48] Suhas Gangadharaiah et al. "Majorana Edge States in Interacting One-Dimensional Systems". In: Phys. Rev. Lett. 107 (3 July 2011), p. 036801.

[49] Jelena Klinovaja, Peter Stano, and Daniel Loss. "Transition from Fractional to Majorana Fermions in Rashba Nanowires". In: Phys. Rev. Lett. 109 (23 Dec. 2012), p. 236801.

[50] Jelena Klinovaja et al. "Topological Superconductivity and Majorana Fermions in RKKY Systems". In: Phys. Rev. Lett. 111 (18 Nov. 2013), p. 186805.

[51] Jelena Klinovaja and Daniel Loss. "Giant Spin-Orbit Interaction Due to Rotating Magnetic Fields in Graphene Nanoribbons". In: Phys. Rev. X 3 (1 Jan. 2013), p. 011008.

[52] Bernd Braunecker and Pascal Simon. "Interplay between Classical Magnetic Moments and Superconductivity in Quantum One-Dimensional Conductors: Toward a Self-Sustained Topological Majorana Phase". In: Phys. Rev. Lett. 111 (14 Oct. 2013), p. 147202.

[53] M. M. Vazifeh and M. Franz. "Self-Organized Topological State with Majorana Fermions". In: Phys. Rev. Lett. 111 (20 Nov. 2013), p. 206802.

[54] Chen-Hsuan Hsu et al. "Antiferromagnetic nuclear spin helix and topological superconductivity in ^{13}C nanotubes". In: Phys. Rev. B 92 (23 Dec. 2015), p. 235435.

[55] Stefan Rex, Igor V. Gornyi, and Alexander D. Mirlin. "Majorana bound states in magnetic skyrmions imposed onto a superconductor". In: Phys. Rev. B 100 (6 Aug. 2019), p. 064504.

[56] Maxime Garnier, Andrej Mesaros, and Pascal Simon. "Topological superconductivity with deformable magnetic skyrmions". In: Communications Physics 2.1 (2019), p. 126.

[57] Eric Mascot et al. "Topological superconductivity in skyrmion lattices". In: npj Quantum Materials 6.1 (2021), p. 6.

[58] Sebastián A. Dıéaz et al. "Majorana bound states induced by antiferromagnetic skyrmion textures". In: Phys. Rev. B 104 (21 Dec. 2021), p. 214501.

[59] Richard Hess et al. "Prevalence of trivial zero-energy subgap states in nonuniform helical spin chains on the surface of superconductors". In: Phys. Rev. B 106 (10 Sept. 2022), p. 104503.

[60] Masatoshi Sato, Yoshiro Takahashi, and Satoshi Fujimoto. "Non-Abelian Topological Order in s-Wave Superfluids of Ultracold Fermionic Atoms". In: Phys. Rev. Lett. 103 (2 July 2009), p. 020401.

[61] Olesia Dmytruk, Daniel Loss, and Jelena Klinovaja. "Pinning of Andreev bound states to zero energy in two-dimensional superconductor- semiconductor Rashba heterostructures". In: Phys. Rev. B 102 (24 Dec. 2020), p. 245431.

[62] Stefan Heinze et al. "Spontaneous atomic-scale magnetic skyrmion lattice in two dimensions". In: Nature Physics 7.9 (2011), pp. 713–718.

[63] X. Z. Yu et al. "Real-space observation of a two-dimensional skyrmion crystal". In: Nature 465.7300 (2010), pp. 901–904.

[64] Akira Furusaki. "DC Josephson effect in dirty SNS junctions: Numerical study". In: Physica B: Condensed Matter 203.3 (1994), pp. 214–218.

[65] A. Martıén-Rodero, F. J. Garcıéa-Vidal, and A. Levy Yeyati. "Microscopic theory of Josephson mesoscopic constrictions". In: Phys. Rev. Lett. 72 (4 Jan. 1994), pp. 554–557.

[66] A. Levy Yeyati, A. Martıén-Rodero, and F. J. Garcıéa-Vidal. "Self-consistent theory of superconducting mesoscopic weak links". In: Phys. Rev. B 51 (6 Feb. 1995), pp. 3743–3753.

[67] V. P. Ostroukh et al. "Two-dimensional Josephson vortex lattice and anomalously slow decay of the Fraunhofer oscillations in a ballistic SNS junction with a warped Fermi surface". In: Phys. Rev. B 94 (9 Sept. 2016), p. 094514.

[68] Kun Zuo et al. "Supercurrent Interference in Few-Mode Nanowire Josephson Junctions". In: Phys. Rev. Lett. 119 (18 Nov. 2017), p. 187704.

[69] Folkert K. de Vries et al. "h/e Superconducting Quantum Interference through Trivial Edge States in InAs". In: Phys. Rev. Lett. 120 (4 Jan. 2018), p. 047702.

[70] Christian Baumgartner et al. "Supercurrent rectification and magnetochiral effects in symmetric Josephson junctions". In: Nature Nanotechnology 17.1 (2022), pp. 39–44.

[71] Wolfgang Himmler et al. "Supercurrent interference in HgTe Josephson junctions". In: arxiv2211.06702 (2022).

[72] Christoph W Groth et al. "Kwant: a software package for quantum transport". In: New Journal of Physics 16.6 (June 2014), p. 063065.

[73] Jorge Cayao et al. "Majorana splitting from critical currents in Josephson junctions". In: Phys. Rev. B 96 (20 Nov. 2017), p. 205425.

[74] Falko Pientka et al. "Topological Superconductivity in a Planar Josephson Junction". In: Phys. Rev. X 7 (2 May 2017), p. 021032.

[75] Michael Hell, Martin Leijnse, and Karsten Flensberg. "Two-Dimensional Platform for Networks of Majorana Bound States". In: Phys. Rev. Lett. 118 (10 Mar. 2017), p. 107701.

[76] Antonio Fornieri et al. "Evidence of topological superconductivity in planar Josephson junctions". In: Nature 569.7754 (2019), pp. 89–92.

[77] Hechen Ren et al. "Topological superconductivity in a phase-controlled Josephson junction". In: Nature 569.7754 (2019), pp. 93–98.

[78] Melina Luethi et al. "Planar Josephson junctions in germanium: Effect of cubic spin-orbit interaction". In: Phys. Rev. B 107 (3 Jan. 2023), p. 035435.

[79] M. Titov and C. W. J. Beenakker. "Josephson effect in ballistic graphene". In: Phys. Rev. B 74 (4 July 2006), p. 041401.

[80] Jelena Klinovaja and Daniel Loss. "Fermionic and Majorana bound states in hybrid nanowires with non-uniform spin-orbit interaction". In: Eur. Phys. J. B 88.3 (2015), p. 62.

Acknowledgments

First, I would like to thank my supervisors, Prof. Dr. Jelena Klinovaja and Prof. Dr. Daniel Loss, who made this PhD possible. I got to know Jelena and Daniel as brilliant physicists, and it was a pleasure for me to learn from them. Most important, Jelena and Daniel always supported me and guided me well through the difficult times of my PhD. Moreover, they made the whole PhD a great and pleasant experience: Jelena gave me the opportunity to visit many conferences at amazing places. In fact, I traveled a lot, not only in Switzerland but also to Italy, Greece, Germany, and Hungary. And beside the actual work, I enjoyed the BBQs on the roof terrace and even more our group retreats to Engelberg. These group activities, however, were so great because of the individual group members. Therefore, I would like to thank my colleagues. You helped me when I was struggling with physics, and I learned a lot from you. It was a great experience to be surrounded by so many extremely talented people and to benefit from your expertise. In particular, I would like to thank Dr. Henry Legg. We had amazing collaborations, which ended up in the four papers listed in this thesis. Henry, I really enjoyed our discussions, and I will always be thankful for your support! It was a good day when we started the first project. Moreover, I would like to thank Dr. Katharina Laubscher for her valuable feedback on this thesis. Katharina, your comments helped me very much to improve the manuscript.

In principle, I would like to individually thank every actual and former group member in this acknowledgement. However, I decided to break with this conventional approach and instead list the activities that we did together. So I hope you will remember the time we spent together while reading this: we played badminton, did cross-fit, swam in the Rhine, went hiking and bouldered. Apart from sports, we visited many restaurants, often went to the cinema, had a weekly James Bond movie session, celebrated some birthdays, and went a couple of times to Bar Rouge. Moreover, we visited Colmar and Strasbourg; we watched the big firework on the Swiss National Day, and we went to the Floss festival and the Basler Fasnacht. Thank you for these wonderful memories.

I would also like to thank Prof. Dr. Annica Black-Schaffer for becoming a member of my PhD examination committee.

Last, I would like to thank my family, in particular my sister Maria-Carina for her support and my parents, to whom I dedicate this thesis. Without you, Mom and Dad, I would not have been able to do this PhD. You gave me the necessary inspiration and motivation.